Influence of liquid properties and process parameters on nanoelectrospray behaviour in both continuous and pulsed voltage operation

Rebecca Erica Jean Hill

A thesis submitted for the degree of Doctor of Philosophy

University of East Anglia

Engineering, School of Mathematics

November 2020

Abstract

Nanoelectrospray (nES) is a technique where liquid ejection is controlled purely by the applied voltage. A systematic study into the effect of the liquid properties and process parameters, on nES behaviour has been conducted. Testing was performed using both a continuous and pulsed voltage, where both pulsation and stable cone-jet modes were observed.

In continuous voltage operation the pulsation frequency (f) increases linearly with the applied voltage. Plotting the effect of the emitter outer diameter (OD) on the pulsation frequency against the magnitude of the field strength above the onset for pulsations (E_{step}), it was found that the data collapsed giving the same $\mathrm{d}f/\mathrm{d}E_{\text{step}}$. In pulsation mode the charge emitted is influenced by each process parameter, with a greater charge being emitted for a higher viscosity and larger emitter OD, but smaller in relation to a higher conductivity.

In pulsed voltage operation, the magnitude of the applied voltage is important in determining the spray mode and on controlling a single ejection. The combination of parameters was found to influence the formation time and the ejected volume, where the volume increased with the magnitude of the voltage pulse. The emitter-to-substrate distance (ESD) has an effect on the height and width of the current transient, with the greatest ESD giving the smallest ejected volume. The maximum ESD to achieve a discrete droplet is dependent on the combination of viscosity, conductivity, and emitter OD.

Contents

List of Figures

List of Tables

Nomenclature

A_1 - Constant

Bo_e - Electrical bond number

c_v - Vapour concentration

d - Distance between deposits

d_0 - Characteristic length

D - Diffusion coefficient

D_c - Duty cycle

d_d - Electrospray drop diameter

D_{drop} - Diameter of spherical droplet

d_i - Emitter inner diameter

d_j - Jet diameter

d_m - Characteristic length

d_n - Emitter outer/meniscus anchoring diameter

D_{print} - Printed droplet diameter

E - Electric field strength

E_0 - Characteristic electric field

E_n^i - Normal inner electric field

E_n^o - Normal outer electric field

E_t - Tangential electric field

E_{pulse} - Magnitude of electric field (pulsed voltage)

E_{step} - Magnitude of electric field (continuous voltage)

$f(\epsilon)$ - Scaling law function

f - Pulsation frequency

f_c - Capillary frequency

f_p - Ejection frequency (pulsed voltage)

f_V - Pulsed voltage frequency

h_d - Droplet height

H - Emitter-to-substrate distance

I - Current

I_0 - Characteristic current

I_{ave} - Average current during a pulsation cycle

I_b - Conduction current

I_{base} - Base current

I_{charge} - Current during liquid replenishment

I_{min} - Minimum cone-jet current

I_{on} - Current during liquid ejection

I_{peak} - Peak current

I_s - Cone surface current

k_i/k_v - Constants

L - Length of pipe section

m - Mass

M - Molar mass

m_{pe} - Electric pressure sensitivity

m_Q - Flow rate sensitivity

Molar_c - Molar concentration

n - Number of pulsation events

n_d - Number of measurements

N - Electrical bond number

P_c - Surface tension pressure

P_D - Externally applied pressure

P_e - Electric pressure

P_T - Total driving pressure

P_v - Vapour pressure

q - Charge

Q - Liquid flow rate

q_0 - Characteristic charge

Q_0 - Characteristic flow rate

Q_{ave} - Average flow rate

Q_{c} - Cone formation rate

Q_{jet} - Flow rate through the jet

Q_{min} - Minimum flow rate for cone-jet mode

Q_{nom} - Nominal flow rate

Q_{on} - Cone-jet onset flow rate

q_{R} - Rayleigh charge limit on a droplet

R - Resistance to flow

r_c - Emitter radius

r_{curve} - Radius of curvature at the apex of the meniscus

r_d - Contact radius of droplet on a substrate

R_e - Reynold's number

R_G - Gas constant

RH - Relative humidity

r_i - Emitter inner radius

r_j - Jet radius

r_n - Anchoring radius

r_o Emitter outer radius

R_Ω - Electrical resistance

r_s - Cross-sectional radius of cone surface

R_T - Total resistance to flow

R_x - Radial direction

S - Standard error

s - Stage speed

t - Time between ejected droplets

T - Temperature

$t_{1,2,3}$ - Time positions on current transients

t_n - Time at last pulse

T_{form} - Pulse formation time

t_{p1} - Time at first pulse

u_s - Axial velocity

v - Liquid volume

V - Voltage

V_1 - Base/resting voltage

V_2 - Ejection voltage

V_{applied} - Applied voltage

v_{drop} - Volume of spherical droplet

v_{est} - Estimated volume

V_o - Cone-jet mode onset voltage

V_{onset} - Pulsation onset voltage

v_{print} - Volume from printed droplet

V_{pulse} - Magnitude of pulsed voltage

V_{step} - Magnitude of voltage above onset (continuous)

$v_{\text{transient}}$ - Volume calculated from current transient

%wt - Weight percentage of solution

δ - Inverse of the dimensionless flow rate

δ_μ - Viscous dimensionless parameter

Γ - Non-dimensional parameter, electrical to surface tension forces

σ - Standard deviation

σ_{charge} - Charge density

τ_e - Charge relaxation time

τ_h - Hydrodynamic time

τ_{off} - Time between ejections

τ_{on} - On-time of an ejection

τ_p - Total period of a pulsation event

τ_{stress} - Tangential stress

θ - Droplet contact angle

θ_0 - Cone half angle

θ_{plume} - Spray angle

Liquid properties

ϵ - Liquid permittivity

γ - Surface tension

K - Liquid conductivity

μ - Liquid viscosity

ρ - Liquid density

Physical constants

ϵ_0 - Permittivity of free space ($8.85\text{x}10^{-12}$ C^2 N^{-1} m^{-2})

R_G - Gas constant (8.31 J mol^{-1} K^{-1})

Acknowledgements

I thank my primary supervisor, Dr Matthew Alexander, for introducing me to electrospray, for passing on his specialist knowledge and for his guidance throughout this project. I also thank my secondary supervisor, Dr Richard Purvis, for initial discussions on producing a MATLAB® code for data analysis, and for mathematical and fluids guidance throughout. I also thank both of my supervisors for supporting me remotely throughout a difficult time of writing my thesis during a pandemic.

I thank Andy for his support and helping sort issues in the lab and for answering all of my lab based questions. I also thank Dave and Nick in the electronics workshop for making numerous electrical cables and fixing equipment when it went wrong, and thanks to Gareth and Stuart in the mechanical workshop for numerous engineering support tasks.

A big thank you goes to my family and friends, especially my mum and dad for all their support and for being there for me every step of the way, my brother Matt and Hannah.

1

Introduction

Electrospray is a technique where liquids are ejected via different spray modes such as dripping, microdripping, pulsations and cone-jet. In forced flow electrospray the flow rate is controlled by a syringe pump, and unforced/nanoelectrospray the flow rate is modulated by the applied voltage. The application and increase in the applied voltage causes transitions between the spray modes (Cloupeau and Prunet-Foch [1994]; Juraschek and Röllgen [1998]; Jaworek and Krupa [1999b]). The spray modes produced also depend on the balance between the liquid properties, emitter geometry, flow rate and emitter-to-substrate distance.

The most studied mode of electrospray is cone-jet mode, which occurs within a certain range of voltage and flow rate values (Collins et al. [2007]; Bober and Chen [2011]; Yu et al. [2016]). The shape of the cone is known as the Taylor cone, which when the pressures are in equilibrium forms a half angle of 49.3° (Taylor [1964]). In this mode liquid is continually ejected via a jet which emanates from the apex of the cone, and breaks up into a spray of droplets. Scaling laws for stable cone-jet mode have been derived linking the flow rate and the current, along with scaling for the minimum flow rate, current and drop size (De La Mora and Loscertales [1994]; De La Mora [1996]; Ganan-Calvo et al. [1997]). Due to the spray of disperse droplets that cone-jet mode produces, it is used in electrospray mass spectrometry for producing gas-phase ions (Van Berkel and Kertesz [2007]), for printing of thin films (Jaworek and Sobczyk [2008]) and interconnects for electrical devices (Wang et al. [2009]; Wang and Stark [2010b]).

The pulsation electrospray mode which is described as an intermittent cone-jet, has shown promise in being used for high resolution printing. On the application of a constant voltage, the frequency of the pulsations depends on the balance

between the liquid properties and process parameters, and also increases with an increase in the applied voltage (Juraschek and Röllgen [1998]; Parvin et al. [2005]; Paine et al. [2007a]; Wang and Stark [2011]). It has been shown that by setting the speed of the stage underneath the emitter, these intermittent ejections can be used to print an array of droplets (Park et al. [2008]; Barton et al. [2010]). This process has limitations in relation to the controllability of each ejection. It has been shown that by applying a voltage pulse using a voltage waveform, the ejections can be controlled by varying the magnitude of the voltage pulse, the frequency and the duty cycle. Pulsed voltage electrospray has shown promise for applications such as printing of biological microarrays (Kim et al. [2010]), DNA printing (Park et al. [2008]) and quantum dots for LED devices (Kim et al. [2015]).

Nanoelectrospray is an experimental method which operates without the use of pumps to control and fix the flow rate but is where the flow rate is influenced by the applied voltage. The sensitivity of the change in the flow rate with voltage depends on the balance between the applied voltage, liquid properties and emitter geometry. It has been shown that the flow rate increases linearly with the applied voltage (Alexander et al. [2006]; Smith et al. [2006a]; Ryan et al. [2014]) and is suggested that the flow rate follows that of Poiseuille flow. Compared to forced flow, nanoelectrospray has shown promise in that it allows for smaller flow rates, drop volumes, and reduces the cost as no pumps are required. Understanding the effect that each parameter has on achieving the smallest flow rates and volumes is important to utilising this technology.

1.1 Thesis aims and objectives

The aim of this project is to further the understanding of nanoelectrospray in both continuous and pulsed voltage operation, and gain further understanding as to how varying liquid properties (viscosity and conductivity), emitter geometry and emitter-to-substrate distance affect how the ejection process can be utilised and

controlled. This has been done by varying each of the parameters systematically, and combining measurements from the recorded current transients, along with physically printed droplets to show how the measurements from the transients and the droplets compare. The current transients have been used to calculate the flow rate and ejected volume at emitter-to-substrate distances where a droplet was not achievable.

1.2 Thesis structure

The chapters in this thesis are:

Chapter 2 details relevant literature on the basis of electrospray technology, and distinguishes between different experimental methods such as forced flow and unforced/nanoelectrospray. The different spray modes have been characterised, with key importance on the effect of parameters on the pulsations, and methods used to control liquid ejection for drop-on-demand printing.

Chapter 3 gives a detailed description of the methods used to produce the solutions, and measurements of the liquid properties, along with the experimental methods used for continuous and pulsed voltage operation. Sections are also included on data analysis and processing of the current transients.

Chapter 4 compares the difference between measurements of the pulsation frequency, from physically printed droplets and from the current transients. It also includes a discussion on processing the current transients to calculate the flow rate, and therefore the ejected volume, which were compared against physically printed droplets to deduce the scaling law to be used in consecutive chapters.

Chapter 5 gives the experimental results from a systematic study into the effects that viscosity, conductivity, and emitter geometry have on the natural

pulsations in nanoelectrospray. The effects that each individual parameter has on the pulsation frequency, the shape of the current transients, along with using the scaling law to calculate the effect on the flow rate and therefore the ejected volume.

Chapter 6 introduces the effect that pulsing the voltage has on nanoelectrospray pulsations, at an emitter-to-substrate distance of 1.0 cm. Again a systematic study of varying the viscosity, conductivity, and emitter geometry were used to understand the effect that each parameter has on controlling and isolating a single ejection event.

Chapter 7 investigates the effect of the emitter-to-substrate distance on controlling and isolating a single ejection event. This is followed by the effect that the viscosity, conductivity, and emitter geometry have on the maximum emitter-to-substrate distance at the highest V_2 voltage, to achieve an individual droplet on the substrate, and the effect of each of the parameters on the printed deposits.

Chapter 8 gives the conclusions presented in this work, along with future work that could be done to build upon findings in this thesis.

2

Literature review

2.1 Electrospray technology

Electrospray is a technique used to spray/deposit conductive liquids. Applying a high voltage to either the emitter or the collector/substrate, while the other is grounded or at a lower potential, liquid is ejected in the form of a droplet, or a spray which is produced from a jet at the apex of the meniscus. The application of the voltage in turn produces an electric field. This field adds an electrical pressure to the meniscus given by

$$P_e = \frac{\epsilon_0 E^2}{2}, \tag{2.1.1}$$

where ϵ_0 is the permittivity of free space and E is the electric field strength. Liquid is ejected when the electrical pressure overcomes the pressure from the surface tension,

$$P_c = \frac{2\gamma}{r_{\text{curv}}}, \tag{2.1.2}$$

where r_{curv} is the radius of curvature at the apex of the meniscus (Juraschek and Röllgen [1998]). The polarity of the ions built up at the surface of the meniscus depends on the polarity and direction of the applied voltage. For example if a positive voltage is applied to the emitter, and the collector is grounded, positive ions will be measured at the collector, whereas if a negative voltage was applied negative ions would be measured. Figure 2.1 shows an example of cone-jet mode electrospray that is used to produce a spray of charged droplets.

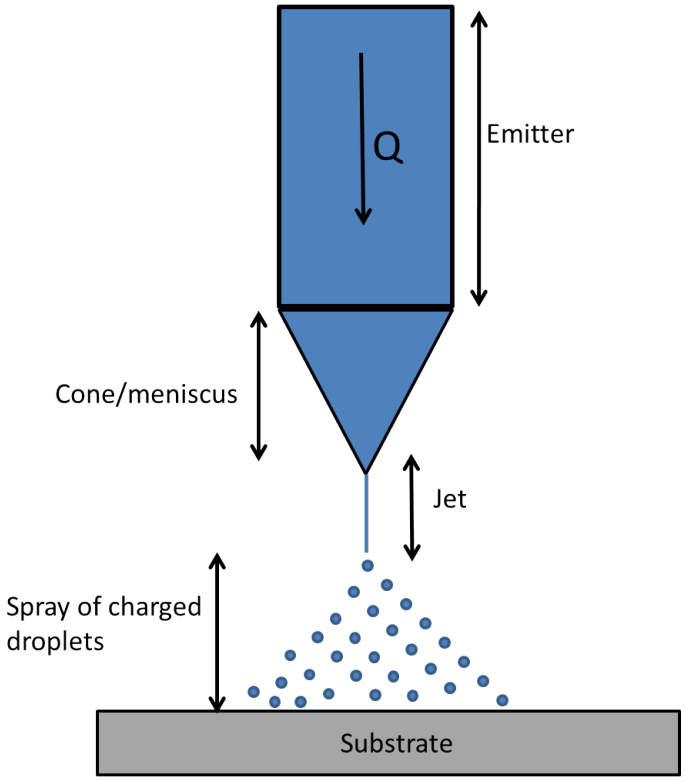

Figure 2.1: Cone-jet mode diagram.

2.2 Flow rate control

In electrospray there are two methods in which the flow rate can be controlled. This is either done by setting the flow rate to be constant, for example by using a syringe pump, or by allowing the flow rate to be controlled by the applied voltage, for example by using a pipe feed network with a constant pressure head.

2.2.1 Forced flow

Forced flow has been more frequently studied and is where a syringe pump is used to produce a constant flow rate. The flow rate is constant even when a voltage is applied. When no voltage is applied liquid is still ejected from the emitter, as the flow of liquid produces a drop which detaches once the gravitational force overcomes the surface tension. This process will continue repeatedly until the syringe pump is turned off, or no liquid remains.

2.2.2 Unforced/Nanoelectrospray

Unforced/nanoelectrospray is where the flow rate of the system is modulated by the applied voltage. In the absence of an applied voltage if the external pressures applied to the system are greater than the surface tension, liquid is ejected, there is an initial flow rate which has been termed Q_{nom} and is the nominal flow rate (Smith et al. [2006a], Ryan et al. [2009]). Even though there is an initial flow rate, unforced electrospray is different to forced flow due to the variation in flow rate with the applied voltage.

Nanoelectrospray (nES), where the name comes from the nL s^{-1} flow rates that are achieved (Wilm and Mann [1996]; Gibson et al. [2009]). The main difference between nES and unforced is that Q_{nom}=0 nL s^{-1}, meaning there is no initial starting flow rate. In this case there are no pumps and the flow rate is fully controlled by the applied voltage, and no liquid is ejected until the electrical forces overcome the surface tension. The voltage at which ejections occur is the onset voltage (V_{onset}) which depends on the liquid properties (mainly the surface tension), and the other set-up parameters (emitter geometry and emitter-to-substrate distance).

2.2.2.1 Flow rate to voltage sensitivity in unforced electrospray

In unforced/nanoelectrospray the flow rate response varies with the applied voltage. It is important to understand how the system will respond to the change in voltage, to find the optimal set-up conditions required for what is to be achieved. In terms of electrospray printing, it can be used to determine the combination of parameters which will achieve the smallest resolution droplet.

Extensive research has been performed using unforced electrospray, where an initial flow rate has been set by either applying a constant gas pressure to the system (Smith et al. [2006b]), or via a gravity fed reservoir (Ryan et al. [2009]). In both of these cases an initial flow rate (Q_{nom}) was set when no voltage was

applied, where the onset flow rate for cone-jet mode (Q_{on}) was shown to increase with an increase in Q_{nom} (Smith et al. [2006a]). It has been reported that Q increases linearly with the applied voltage (V) in pulsations (Ryan et al. [2014]), cone-jet mode (Smith et al. [2006a]; Smith et al. [2006b]; Ryan et al. [2009]) and multi-jet (Ryan et al. [2014]), where the gradient of the graph has been termed m_Q (Smith et al. [2006a]), given by

$$m_Q = \frac{\mathrm{d}Q}{\mathrm{d}V}. \tag{2.2.1}$$

The rate at which the flow rate varies with the applied voltage has been shown to be influenced by a number of parameters. Early investigations by Smith et al. [2006b] showed that at Q_{nom} values from 4 to 50 nL s^{-1}, m_Q decreased from 0.82 to 0.28 nL s^{-1} kV^{-1}. A later study by Smith et al. [2006a] concluded that m_Q was relatively independent of Q_{on}, with Q_{on} ranging from 7.98 to 62.26 nL s^{-1} kV^{-1} the average m_Q value measured was 2.4±0.2 nL s^{-1} kV^{-1}. The difference in observations being put down to the resolution of the in-line flow rate measurements, going from 0.03 nL s^{-1} in Smith et al. [2006b] to 0.001 nL s^{-1} in Smith et al. [2006a]. Ryan et al. [2009] showed that over the Q_{nom} range ∼25 to 160 nL s^{-1} a constant m_Q of 5.39±0.34 nL s^{-1} kV^{-1} was measured. These results conclude that as long as all other parameters are constant, varying Q_{nom} has little effect on the sensitivity of the flow rate to voltage.

Taking Q_{on} into account and starting to investigate other parameters such as the conductivity, viscosity, and emitter geometry (ID=inner diameter and OD=outer diameter) the response of the flow rate to voltage was shown to differ for each of these properties. It has been shown that for Q_{nom} values 25±5 and 50±5 nL s^{-1}, m_Q is largely independent of the conductivity of the solution (Smith et al. [2006b]). This was then again investigated over a larger range of Q_{on} values where by plotting $(m_Q/Q_{\text{on}})\%$ against Q_{on} it was again shown that m_Q is independent of the conductivity in cone-jet mode (Smith et al. [2006a]).

Another liquid property that was briefly investigated was that of viscosity, where it was shown that the lower viscosity ethylene glycol solution (21 cP) achieved a higher $(m_Q/Q_{\text{on}})\%$ compared to the triethylene glycol (40 cP) solution which has a higher viscosity (Smith et al. [2006a]). To try and understand the effect of this parameter on the flow through the system, it was assumed that the liquid would behave as a Newtonian fluid flowing through a pipe network. To determine how the fluid would behave it was assumed that it would follow the Poiseuille equation (Smith et al. [2006a]), where the resistance (R) and total resistance (R_T) to flow are given by

$$R = \frac{8\mu L}{\pi {r_i}^4}, \tag{2.2.2}$$

$$R_T = R_1 + R_2 + R_3 + ... + R_n, \tag{2.2.3}$$

where μ is the viscosity, L is the length of the pipe section, r_i is the inner radius of the pipe system, and the total resistance is the sum of the different pipe sections. Taking into account the driving pressure to the system the flow rate can be calculated by

$$Q = \frac{P_T}{R_T}. \tag{2.2.4}$$

Smith et al. [2006a] split the driving pressure P_T into two terms, P_D which is from the back pressure applied to the reservoir, and P_e which relates to the pressure from the applied voltage and therefore the electric field (Smith et al. [2006a]). The equation to estimate the flow rate has then been rewritten in the form of

$$Q = \frac{P_D + P_e}{R_T}. \tag{2.2.5}$$

Since P_D is constant and P_e is dependent on the applied voltage/field strength, by taking

$$\frac{dP_e}{dV} = \frac{dQ}{dV} R_T = m_{\text{pe}}, \tag{2.2.6}$$

the effect of the electric pressure from the applied voltage on the flow rate sensitivity can be calculated (Smith et al. [2006a]). Taking Equation 2.2.6 and

plotting $(m_{\mathrm{pe}}/Q_{\mathrm{on}})\%$ for the different viscosity data, it was shown that the data collapsed, which showed that by taking the resistance to flow into account the effect of viscosity could be removed (Smith et al. [2006a]). These above equations have been used to investigate the effect that other variables have on the flow rate sensitivity mainly in cone-jet mode, but also in pulsations and multi-jet.

It has been shown that the properties of the emitter and extractor distance have an effect on the values of both m_Q and m_{pe}, where initially it was shown that decreasing the size of the emitter ID caused an increase in the value of m_{pe} (Smith et al. [2006a]), however it was not clear as to whether it was due to the ID or the OD. Therefore, tests were performed where the ID and the OD of the system were investigated separately by keeping the other constant (Ryan et al. [2009]); Ryan et al. [2014]). It was shown that if the ID was below about 250 μm, there was a decrease in m_Q, however if m_{pe} was calculated then there was shown to be no effect of the emitter geometry, which was suggested to be down to the change in the resistance to flow from decreasing the ID (Ryan et al. [2009]). On the other hand in terms of the OD it was shown that decreasing the OD, m_Q and therefore m_{pe} increased (Ryan et al. [2009]; Ryan et al. [2014]). Results have also shown that decreasing the distance of the extractor causes an increase in the value of m_Q (Ryan et al. [2012]; Ryan et al. [2014]). Combining this with the OD Ryan et al. [2014] showed that the smaller emitter not only had a larger m_Q at the smaller extractor distance, but also had a larger m_Q due to having a smaller OD.

This work has concluded that some parameters do not affect the sensitivity of flow rate to applied voltage such as Q_{nom}, Q_{on} and the conductivity, where as other variables such as the viscosity and the emitter ID can be removed if the sensitivity of the electric pressure with voltage is measured, removing the effect of the resistance to flow (Smith et al. [2006a]; Ryan et al. [2009]). Other parameters such as the OD and extractor distance can have quite a large effect on the behaviour (Ryan et al. [2009]; Ryan et al. [2012]; Ryan et al. [2014]). This therefore shows that to get an optimal system all of these variables need to

be taken into account.

2.3 Electrospray modes

In electrospray the liquid can be ejected from the emitter in different ways, whether this be from detachment of liquid drops from the emitter, or from the formation of a jet at the apex of the cone. Much attention has been invested into understanding the fundamentals which govern the ejection process. Understanding the interplay between liquid properties (viscosity, conductivity, surface tension), emitter geometry, voltage and flow rate is vital to understanding the electrospray process.

Zeleny [1917] observed the first modes, which were described in terms of how the meniscus shape changed and liquid ejected. Over the years from then classification has been given to the different forms of ejection. Cloupeau and Prunet-Foch [1994] wrote a review describing each of the different modes under the names that had been given to distinguish them, such as dripping and microdripping. Building on from just having names to describe each of the different forms of ejection, Jaworek and Krupa [1999b] classed the modes into two groups. Group 1 consisted of modes such as dripping, microdripping and spindle. These were grouped due to ejections coming from the meniscus. Group 2 consisted of an oscillating (pulsed) jet, cone-jet and multi-jet, where liquid was ejected from the formation of a jet.

Many of these modes were initially characterised from imaging the meniscus and observing how it broke up. However, this was later built on by measuring the current. Initial work was performed by Juraschek and Röllgen [1998] where three modes were characterised. These modes were where liquid was ejected via a jet and were termed axial mode I, axial mode II and axial mode III. Axial mode I was defined as a pulsation mode made up of high and low frequency pulsations, axial mode II as a pulsed jet with a constant frequency, and axial mode III as cone-jet

mode. In a later study, Verdoold et al. [2014] built on this by measuring current data for other modes such as dripping, microdripping and spindle to name a few. Here it was shown that each of the different modes had distinguishable current traces.

There is still some discrepancy between the naming/characterisation of each of the spray modes. Imaging the jet is useful in that it shows the shape of the meniscus and the wetting properties. However, current measurements can add another way to help distinguish the mode being observed. This can help the operator make appropriate adjustments to get the spray mode required. Below is a description of the key spray modes. It is to be noted that all spray modes will not necessarily be observed, as each of the modes depends on the combination of liquid properties, emitter geometry, flow rate and voltage.

2.3.1 Dripping

Dripping mode is where droplets much larger than the emitter are produced, especially when no voltage is applied (Zeleny [1917]; Cloupeau and Prunet-Foch [1994]). With no voltage/electric field present, the droplet is emitted from the exit of the emitter when the gravitational force overcomes the surface tension. The size of the drops therefore have a constant volume and are regular in size (Cloupeau and Prunet-Foch [1994]). Figure 2.2 shows a schematic of the ejection process in dripping mode.

Applying a low voltage (small electric field) introduces an electrical force to help overcome the surface tension. Drops produced in the electric field are still spherical in shape (Jaworek and Krupa [1999b]), they just have a smaller volume and a larger emission frequency (Cloupeau and Prunet-Foch [1994]; Ryan et al. [2014]). The electric field reduces the surface tension due to a slight build-up of charge on the liquid surface. The frequency has been shown to range from a few Hz to kHz, with the frequency being highly dependent on the liquid properties, and the emitter diameter/wetting characteristics (Cloupeau

and Prunet-Foch [1994]). In unforced electrospray Ryan et al. [2014] showed that the flow rate in dripping is independent of the applied voltage, and this was due to the combination of a reduced drop volume and increased frequency. At relatively high voltages a secondary droplet can be produced if the charge of the initial droplet is half the Rayleigh limit (Jaworek and Krupa [1999b]) as given by

$$q_{\mathrm{R}} = \pi(8\gamma\epsilon_0 d_d^3)^{1/2}, \tag{2.3.1}$$

where d_d is the droplet diameter (cited in De La Mora [1996]; Ganan-Calvo et al. [1997]).

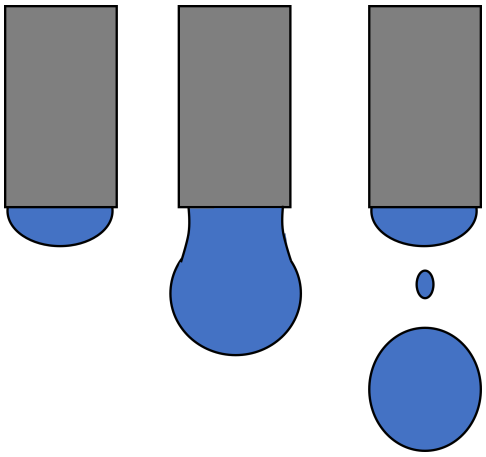

Figure 2.2: Stages of dripping mode.

Majority of the descriptions of dripping mode come from imaging of the meniscus and are therefore a visual representation. Verdoold et al. [2014] went onto link the observation with measured current data. Here it was shown that a very small constant current was measured. This is mainly due to the small charge to mass ratio. Majority of the ejection in dripping mode will be liquid rather than charged ions.

2.3.2 Microdripping

Microdripping occurs at a voltage increase higher than that required for dripping. The key difference between the two modes is that in microdripping the droplet is produced from an elongated jet (Cloupeau and Prunet-Foch [1994]; Verdoold

et al. [2014]). Imaging of the ejection has shown that the jet has a rounded apex, where over time the top of the jet near the emitter pinches off to form a single drop (Cloupeau and Prunet-Foch [1994]; Jaworek and Krupa [1999b]; Verdoold et al. [2014]). The droplets are very regular and uniform. In general the size of the drops are smaller than the emitter and can have frequencies of a few kHz (Cloupeau and Prunet-Foch [1994]; Juraschek and Röllgen [1998]). In microdripping it has been shown that plots of the pulsation frequency can be made dimensionless in relation to the capillary frequency given by

$$f_c = \sqrt{\frac{\gamma}{\rho d_o^3}}, \tag{2.3.2}$$

(Hijano et al. [2015]). Figure 2.3 shows a diagram of the stages of droplet production in microdripping.

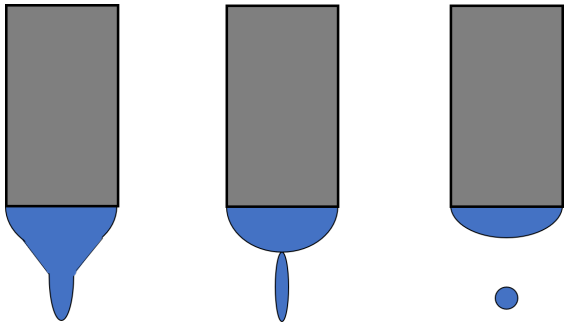

Figure 2.3: Stages of microdripping.

Along with a description of the microdripping process through visual observation, Verdoold et al. [2014] measured current data. The current against time plot showed that the pulses were quite broad at a few ms in duration. After the initial rise of the current, the data showed a small peak followed by a dip, which was then followed by another peak larger than the first. The dip corresponded to the elongating of the jet before it started to narrow, with the second peak corresponding to when the drop had pinched off (Verdoold et al. [2014]). Therefore, giving a different method to distinguish this mode. Figure 2.4 shows an example sketch of a microdripping transient similar to that observed by Verdoold et al. [2014].

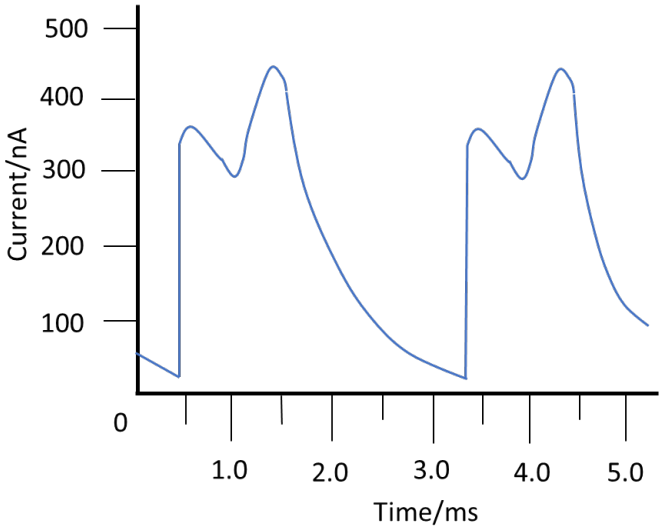

Figure 2.4: Sketch of the shape of a current transient that could be observed during the microdripping ejection process.

2.3.3 Spindle

Spindle produces a long thread of liquid from a conical shaped meniscus, Figure 2.5 shows an example of a spindle breakup. It has been commented on being a combination of jet breakup and volume detachment similar to the dripping modes (Cloupeau and Prunet-Foch [1994]). The thread has been shown to be irregular in shape (Jaworek and Krupa [1999b]; Verdoold et al. [2014]). Even though the frequency of the ejections can be regular, the size of the drops are not necessarily uniform (Cloupeau and Prunet-Foch [1994]).

Verdoold et al. [2014] measured the current data that linked to this mode of spraying. The trace showed two gradients in the current with time, where the second became steeper on approaching the peak. This part of the current data with time corresponded to the elongation of the thread. The peak corresponded to the detachment of the thread. After the detachment the current was shown to vertically decrease, with a then decrease in the gradient while a secondary droplet was ejected (Verdoold et al. [2014]). Figure 2.4 shows an example sketch of a spindle transient similar to that observed by Verdoold et al. [2014].

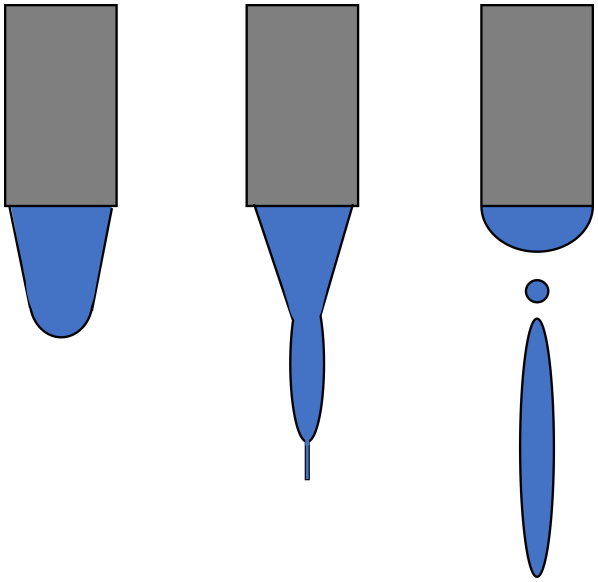

Figure 2.5: Stages of spindle.

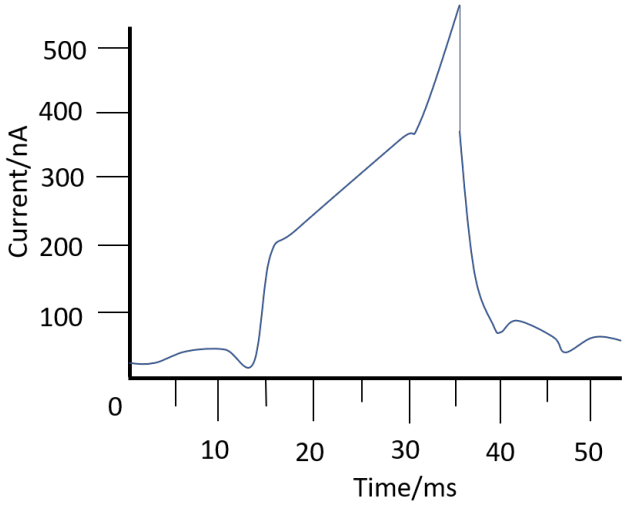

Figure 2.6: Sketch of the shape of a current transient that could be observed during the spindle ejection process.

2.3.4 Pulsations

Pulsations occur when there is an imbalance between the supplied and ejected flow rate. Liquid is ejected via a jet at the apex of a conical meniscus. The ejections are intermittent and very regular (Cloupeau and Prunet-Foch [1994]). Figure 2.7 shows an example of the meniscus deforming into a jet to eject a droplet or droplets, before collapsing again to build-up the lost liquid and charge for the next ejection. The frequencies over which this intrinsic mode can oscillate

has been shown to range from a few Hz to tens and hundreds of kHz (Paine et al. [2007a]).

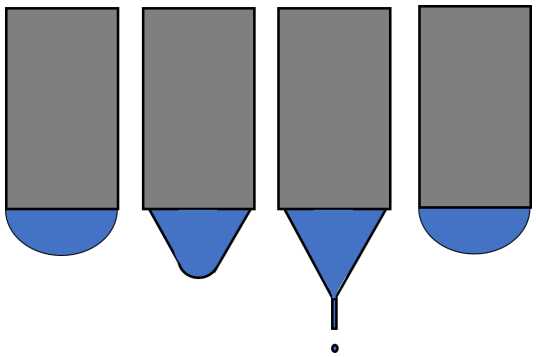

Figure 2.7: Stages of the pulsation mode ejection process.

In forced flow electrospray Juraschek and Röllgen [1998] observed two different types of pulsation, which were characterised from the current measurements recorded, as well as being linked to images of the meniscus. These modes were termed axial spray mode I and axial spray mode II. Axial mode I was characterised by having low frequency pulsations at a few to tens of Hz, which were made up of a packet of ejections at a few kHz. The amplitude of each ejection event was not constant, Figure 2.8 shows an example of a mode I ejection process. On imaging the meniscus, Juraschek and Röllgen [1998] observed that liquid was being ejected only during the peak of the pulse, and was related to the build-up and collapse of the entire meniscus. Later work by Marginean et al. [2007] described this mode as being a transition between dripping and axial mode II.

Axial mode II ejections were distinguished by the current measurements producing pulses with a constant amplitude, which were only made up of high frequency pulsations. Juraschek and Röllgen [1998] observed that in this mode the liquid was being ejected from the apex of the meniscus. Axial modes I and II were also shown to be produced in nanoelectrospray (Alexander et al. [2006]; Paine et al. [2007a]). From analysis of the current during an ejection event in nanoelectrospray a subset of mode II was discovered, which was named mode IIb (Alexander et al. [2006]; Paine et al. [2007a]). This mode was set apart from

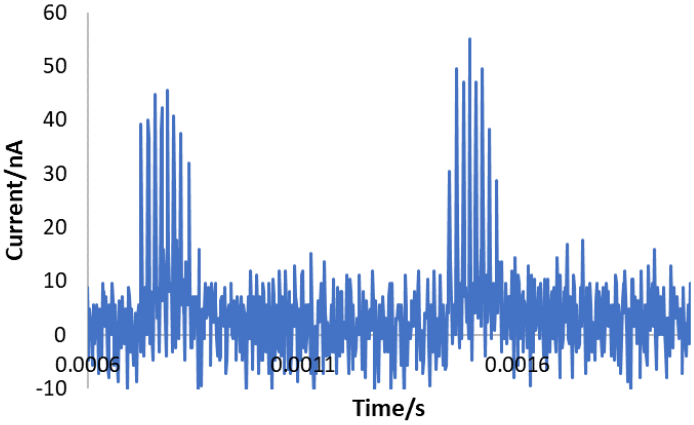

Figure 2.8: Example of a mode I ejection current transient.

mode II by the reduction in the current measured during the ejection process with increase in the applied voltage.

To build on the understanding of the pulsations, Paine et al. [2007a] and Stark et al. [2014] came up with methods for analysing specific parts of the current transients. The pulsation cycle was broken up into liquid ejection and liquid replenishment phases. The value of the current in relation to the peak current (I_{peak}) was used to distinguish between ejection and replenishment. Liquid ejection was defined by Paine et al. [2007a] as being when

$$I > 0.25(I_{\text{peak}} - I_{\text{base}}) + I_{\text{base}}, \tag{2.3.3}$$

where I_{base} is the current at the base of the pulse before the ejection starts. Stark et al. [2014] described ejections as being when the current was greater than 25% of I_{peak}. The advantage of the definition by Paine et al. [2007a] is that if the current does not have an I_{base}=0 nA the points calculated will be on the trace. When the current was less than either of these descriptions the liquid/charge was being replenished ready for the next ejection.

The average current I_{ave} during an entire pulsation event was defined as

$$I_{\text{ave}} = \frac{\int_{t_1}^{t_3} I dt}{t_3 - t_1}, \tag{2.3.4}$$

where t_1 is the time at the start of the pulse and t_3 is the start of the next pulsation cycle at 25% of I_{peak} (pulse period $\tau_{\text{p}} = t_3 - t_1$) (Stark et al. [2014]). The current was then split up into two components, that relating to liquid ejection

$$I_{\text{on}} = \frac{\int_{t_1}^{t_2} I dt}{t_2 - t_1}, \tag{2.3.5}$$

and that of liquid replenishment

$$I_{\text{charge}} = \frac{\int_{t_2}^{t_3} I dt}{t_3 - t_2}, \tag{2.3.6}$$

where t_2 relates to the time on the right hand side of the peak where the current is 25% of I_{peak}. The time of ejection (on-time) $\tau_{\text{on}} = t_2 - t_1$ and the time to replenish (off-time) $\tau_{\text{off}} = t_3 - t_2$. Figure 2.9 shows a current transient similar to that given by Stark et al. [2014] showing each of the time values and positions, the current line at 9.70 nA represents where $I = 0.25(I_{\text{peak}} - I_{\text{base}}) + I_{\text{base}}$.

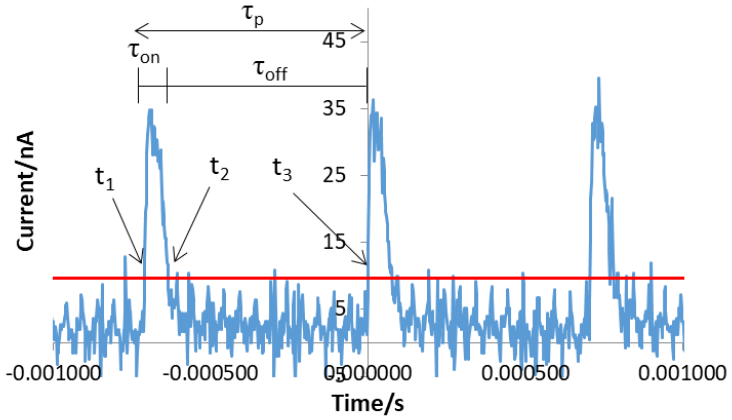

Figure 2.9: Current transient showing positions of t_1, t_2 and t_3 for calculating τ_{on}, τ_{off} and τ_{p}.

Due to the stability of the pulsations, and large range over which the pulsations can be operated, they have shown promise for applications such as high resolution printing, electrospray mass spectrometry and drug delivery. There is however still a lot that needs to be studied, especially in relation to the effect that process parameters have on controlling the pulsations, and the flow rate in nanoelectrospray.

2.3.4.1 Effect of parameters on pulsation transitions

The applied voltage plays a key part in the pulsations that are observed. As with the other spray modes the voltage not only increases the frequency, but also causes transitions from one mode to another. Juraschek and Röllgen [1998] showed that at a constant flow rate of 2 μL min^{-1}, with an emitter ID of 110 μm and OD of 240 μm that the production of mode I and mode II depended on both the concentration of KBr and the applied voltage. Results showed that at 2.3 to 2.4 kV, mode I ejections were observed at concentrations from 10^{-8} to 10^{-6} mol L^{-1}. On further increase in the concentration the results differed. At 2.4 kV, a concentration of 10^{-5} mol L^{-1} was required to enter mode II, whereas at 2.3 kV at this concentration the pulsations were still in mode I. At 2.3 kV, a concentration of 10^{-3} mol L^{-1} was needed to enter mode II, a difference in two orders of magnitude. At 2.6 to 2.8 kV, Juraschek and Röllgen [1998] showed that only mode II ejections were produced for each concentration, before entering a different spray mode.

Parvin et al. [2005] also used a constant flow rate of 2 μL min^{-1}, with an emitter ID of 130 μm and OD of 260 μm, where both mode I and mode II pulsations were observed. The solutions tested were 50% MeOH (methanol) at 1.40 μS cm^{-1} and 50% ACN (acetonitrile) at 0.61 μS cm^{-1}. Both modes producing similar trends in going from mode I to mode II, with the key difference being in that the higher conductivity 50% MeOH solution produced higher frequency pulsations.

In nanoelectrospray as discussed in Section 2.2.2 the voltage is not only important for the pulsation mode/frequency, it is also important in overcoming the surface tension to initiate spraying, especially in conditions where there is no initial flow rate. Similar to that in forced flow the production of mode I depends highly on the balance of process parameters. Alexander et al. [2006] performed tests using two different solutions, water with a conductivity of $\sim$7x10^{-3} S m^{-1} on a 10 to 15 μm emitter, and triethylene glycol (TEG) with a conductivity of $\sim$2x10^{-2} S m^{-1} on a 50 μm emitter. In both of these experiments axial mode I was not observed,

whereas the TEG solution transitioned from mode II to mode IIb, where a change in the rate of increase in the frequency was observed.

Work by Paine et al. [2007a] observed the first mode I pulsations in nanoelectrospray, but only under certain conditions. Using a water solution with conductivity of 8x10^{-4} S m^{-1} on a 30 μm emitter, mode I ejections were shown to increase in frequency with the voltage, and produce a larger number of pulsations per ejection event. The same was also observed using ethylene glycol, but only on an emitter of 150 μm, where only two pulsations per ejection event were recorded. Paine et al. [2007a] suggested that there were certain requirements to achieve this mode which were linked to the liquid properties and emitter size. Since these ejections were only observed on the lowest viscosity solution it was suggested that a low hydraulic resistance causes this mode.

2.3.4.2 Effect of parameters on the Pulsation frequency

Understanding the effect of process parameters on the pulsation frequency is of importance to be able to utilise the spray in the most efficient way, depending on the application, such as for mass spectrometry, printed electronics, and biological microarrays. Applications of electrospray are discussed in more detail in a later section. For many applications the ink/solution used has specific requirements, such as needing a high salt content or a high viscosity. Understanding the behaviour that varying each parameter has on the pulsations, can help the operator in producing an optimised system for that set-up.

Effect of the applied voltage on the pulsation frequency

The trend observed in majority of cases in relation to the frequency, is that as the voltage increases so does the pulsation frequency. However, the relationship

between the voltage and frequency has been shown to differ depending on the set-up conditions. The pulsation frequency has been shown in both forced and unforced electrospray to increase linearly up to a point where the frequency plateaus off at the highest voltage, before entering into another spray mode (Juraschek and Röllgen [1998]; Parvin et al. [2005]; Wang and Stark [2011]). Alexander et al. [2006] showed that for a water solution at $\sim$7x10^{-3} S m^{-1} on a 10 μm emitter, there was a sudden jump between low frequency pulsations and high frequency pulsations, where the transient for the high frequency oscillations represented a sine wave.

Other reports have shown a linear relationship between the frequency and the applied voltage (Alexander et al. [2006]; Paine et al. [2007a]; Wang and Stark [2010c]). In going from mode II to mode IIb ejections, the effect of the voltage on the frequency was shown by an increase in the rate of change of the frequency with the voltage (Alexander et al. [2006]; Stark et al. [2014]).

Pulsation frequency scaling

Scaling laws have been produced to estimate the maximum frequency which should be achievable experimentally. Chen et al. [2006] developed scaling based upon the relationship between the frequency (f), flow rate (Q) and volume ejected (v), where

$$f \sim \frac{Q}{v} \sim \frac{KE^2}{\epsilon\mu L}\left(\frac{\rho d_i^5}{\gamma}\right)^{1/2}, \tag{2.3.7}$$

where, ϵ is the liquid permittivity and d_i is the inner diameter of the emitter. In this scaling and what was previously discussed in Section 2.2.2, it has been suggested that the flow rate in nanoelectrospray follows that of Poiseuille flow given by

$$Q \approx Q_c \sim \frac{\pi d_i^4}{128\mu L}\left(\frac{\epsilon_0 E_0^2}{2} - \frac{2\gamma}{d_i} + \Delta P\right), \tag{2.3.8}$$

where Q_c is the cone formation rate (Chen et al. [2006]).

Choi et al. [2008] derived scaling for the maximum frequency by relating the competition between the electrical forces and the surface tension. The scaling was also produced from using the relationship between the jet diameter and the anchoring diameter of the meniscus to the emitter.

$$d_j \sim \sqrt{\frac{\gamma}{\epsilon_0}} \frac{\sqrt{d_n}}{E}, \tag{2.3.9}$$

where d_j is the jet diameter and d_n is the anchoring diameter of the meniscus at the emitter. Choi et al. [2008] used the scaling given by Marginean et al. [2006] which related the frequency from the Rayleigh capillary wave equation, at the lowest excitation given by

$$f^2 \approx \frac{2}{\pi^2} \frac{\gamma}{\rho r_n^3}, \tag{2.3.10}$$

where r_n is the anchoring radius. Assuming that a jet is produced when γd_n is roughly similar to $\epsilon_0 (E d_j)^2$, linking this with Equation 2.3.9, Choi et al. [2008] came up with the scaling for the frequency as

$$f \propto \left(\frac{\epsilon_0^3}{\rho^2 \gamma} \right)^{1/4} \left(\frac{E^{3/2}}{d_n^{3/4}} \right), \tag{2.3.11}$$

where here the electric field from a point plane set-up was used and given by

$$E = \frac{4V}{d_n \ln(\frac{8H}{d_n})}. \tag{2.3.12}$$

In forced flow electrospray the frequency of the oscillations have been shown to be related to the balance between the supplied flow rate (Q_s) and the minimum flow rate ($Q_{\min}$) (Bober and Chen [2011]), where

$$Q_{\min} = \frac{\gamma \epsilon}{\rho K}, \tag{2.3.13}$$

(Ganan-Calvo et al. [1997]). Two different types of oscillation were described, oscillating jet where the entire cone oscillates, and chocked jet which is where the liquid is ejected from the apex of the cone (Bober and Chen [2011]). In oscillating

cone jet $Q_s \geq Q_{\min}$, where the frequency was scaled to that given by Equation 2.3.2 (Bober and Chen [2011]). In the chocked jet regime $Q_s \leq Q_{\min}$, where the frequency of oscillations was given as

$$f \sim \frac{Q_s}{Q_{\min}} f_c. \tag{2.3.14}$$

Results showed that at low flow rates below 20 nL s^{-1} the frequency increased with Q_s, whereas above here the frequency was largely constant. Therefore, showing that at large flow rates the frequency is independent of the flow rate. Bober and Chen [2011] experimentally showed that using different conductivity solutions of ethylene glycol, ranging from 1.80 to 14.5 μS cm^{-1}, that plotting the frequency against $Q_s/Q_{\min}$ the data collapsed, with a transition between the two modes at $Q_s/Q_{\min}$=1. It was later stated that the $Q_{\min}$ scaling and frequency scaling was not valid for high viscosity solutions such as glycerol.

Effect of viscosity on the pulsation frequency

The effect of viscosity on the pulsation frequency has not been widely studied, especially using a systematic approach. General trends observed show that having a higher viscosity solution reduces the frequency of the pulsations (Paine et al. [2007a]; Guo et al. [2018]). The scaling law by Chen et al. [2006] suggests that the maximum frequency and viscosity scale as $f \sim \mu^{-1}$, this scaling was based on the Poiseuille equation as discussed in the previous section. A deionised water solution with a conductivity of 0.9x10^{-4} S m^{-1} was used, where the viscosity of water is ∼1 cP.

Effect of conductivity on the pulsation frequency

The conductivity has been shown to cause an increase in the frequency. In forced flow at a flow rate of 2 μL min^{-1} Juraschek and Röllgen [1998] showed that the pulsation frequency increased slightly with an increase in KBr concentration,

ranging from 10^{-8} to 10^{-2} mol L^{-1}.

In nanoelectrospray it has been shown that the pulsation frequency can increase rather substantially with conductivity over the voltage range tested. Taking triethylene glycol solutions at conductivities of 2.4x10^{-3} to 3.3x10^{-2} S m^{-1} on a 15 μm emitter, Paine et al. [2007a] showed that for a linear increase with voltage the rate of change of frequency with voltage ($\mathrm{d}f/\mathrm{d}(V_a - V_0)$) was greater for the highest conductivity solution, where V_a was the applied voltage and V_0 the voltage at which steady pulsations occurred. Increasing the conductivity from 2.4x10^{-3} to 3.3x10^{-2} S m^{-1} increased the value of $\mathrm{d}f/\mathrm{d}(V_a - V_0)$ from 0.0098 to 0.0352 kHz V^{-1}. The same observation was shown by Wang and Stark [2010c] over a smaller variation in conductivity, from 42 to 50 mS m^{-1} using a 30 μm emitter, results showed an increase in $\mathrm{d}f/\mathrm{d}V$ from 1.699 to 3.758 kHz V^{-1}. The conductivity of the solutions by Wang and Stark [2010c] are in the range of the highest conductivity by Paine et al. [2007a]. At this conductivity range there is a clear magnitude difference between the values of $\mathrm{d}f/\mathrm{d}V$ measured, which will be down to variations in other parameters. The emitter size used by Paine et al. [2007a] is half of that used by Wang and Stark [2010c], along with a variation in surface tension from 45.5 to 66.6 mN m^{-1}. The largest variation in set-up parameters between the two data sets is that of the emitter-to-substrate distance, from 3 mm used by Paine et al. [2007a] to 250 μm used by Wang and Stark [2010c].

As described earlier and shown in Figure 2.9, the pulsations can be split up into liquid ejection which relates to τ_{on} and liquid/charge replenishment during τ_{off}. In nanoelectrospray pulsations, it has been observed that a higher conductivity solution reduces the length of time that liquid is ejected (Paine et al. [2007a]; Stark et al. [2014]), where for a conductivity range from 2.98x10^{-3} to 0.2319 S m^{-1} Stark et al. [2014] reported τ_{on} to decrease linearly with increased conductivity.

In the charge replenishment stage Stark et al. [2014] showed that the total charge transferred was independent of both the applied voltage and the conductivity.

Taking the frequency and plotting against the off-time current (I_{charge}) a linear response was shown, where each of the data sets collapsed onto each other. It was therefore suggested that the conductivity was not a dominating factor to the mechanisms controlling the relationship between the frequency and I_{charge} (Stark et al. [2014]).

Some studies have proposed scaling laws to relate the frequency and the liquid conductivity. Equation 2.3.7 suggests that the frequency scales with the conductivity as $f \sim K$ (Chen et al. [2006]). Experimentally from observation of printed drop volumes on the substrate, at a range of conductivities from 2 to 10 μS cm^{-1}, Guo et al. [2018] found that the frequency was proportional to $K^{0.58}$. The main difference between the two works was that Chen et al. [2006] used an emitter with an inner diameter of 50 μm compared to a 160 μm diameter used by Guo et al. [2018].

Effect of emitter geometry on the pulsation frequency

The pulsation frequency has been shown to produce a larger frequency when a smaller emitter is used (Marginean et al. [2006]; Paine et al. [2007a]). The frequency scaling given by Equation 2.3.7, suggests that the frequency scales with the emitter diameter by $f \sim d_i^{5/2}$, suggesting an increase in the maximum frequency with increased emitter size. Choi et al. [2008] on the other hand gives the maximum frequency as $f \sim d_n^{-3/4}$, suggesting a reduction in the maximum frequency. The difference between the two scaling laws as discussed before is the calculation in the field strength and the derivations of the scaling laws. Chen et al. [2006] used the field equation for the field between two plates ($E = V/H$), where H is the spacing between the plates, and Choi et al. [2008] used the equation for a point plane geometry taking into account the size of the emitter. In deriving the scaling Chen et al. [2006] used the relationship between the flow rate and the volume of a pulsation, whereas Choi et al. [2008] took into account the electric field required to overcome the surface tension and initiate liquid ejection. Since

the electric field equation was related to the emitter diameter, Choi et al. [2008] plotted log of the frequency against $E/d_n^{1/2}$, and compared data to that from Juraschek and Röllgen [1998] and Chen et al. [2006]. The scaling was validated in that each of the sets of data showed a linear increase in log f with $\log(E/d_n^{1/2})$, with $\log(\mathrm{d}f/\mathrm{d}(E/d_n^{1/2}))$ equalling 3/2 giving $\left(E/d_n^{1/2}\right)^{3/2}$ which was shown to be in agreement with Equation 2.3.11 (Choi et al. [2008]).

2.3.4.3 Effect of parameters on the flow rate

In unforced/nanoelectropsray the flow rate is modulated by the applied voltage, as discussed in Section 2.2.2 in relation to cone-jet mode. Similar observations of the effect of voltage and set-up parameters have been shown in pulsations.

Recent studies relating the flow rate to the voltage have been performed where the flow rate has been measured during the ejection process (Alexander et al. [2006]; Paine et al. [2007a]). In tests by Alexander et al. [2006], Smith et al. [2006a] and Ryan et al. [2014] the flow rate was measured using an in line pressure transducer, based on the Poiseuille equation. The system was calibrated for each solution, where the liquid was collected over a fixed length of time. This was then weighed out giving the volumetric flow rate. The pressure drop (ΔP) was measured, where this process was performed for a range of flow rates to get the dependence of the pressure with the volumetric flow rate. It was stated that the volumetric flow rate is linearly proportional to the pressure drop, which agrees with that of Poiseuille.

Alexander et al. [2006] and Stark et al. [2014] suggested that the average flow rate (Q_{ave}) measured using an in-line flow rate sensor, and the average flow rate through the jet (Q_{jet}) can be related by

$$Q_{\mathrm{jet}} \sim \frac{Q_{\mathrm{ave}}}{\tau_{on} f}. \tag{2.3.15}$$

Stark et al. [2014] showed that Q_{jet} increased with the voltage during mode II

ejections, but then produced a peak where the flow rate started to decrease again during mode IIb ejections.

Effect of viscosity on nanoelectrospray flow rate

There have been few systematic studies experimentally measuring the effect of the viscosity on the flow rate in nanoelectrospray pulsations. It has been suggested before in Section 2.2.2 that in nanoelectrospray the flow rate can be described by Poiseuille flow, where $Q \sim \mu^{-1}$. In both scaling laws by Chen et al. [2006] and Choi et al. [2008] where a constant back pressure was applied to the liquid, it was suggested that the flow rate could be estimated using the Poiseuille relation. Guo et al. [2018] observed that increasing the viscosity decreased the pulsation frequency and increased the ejected volume, it was suggested that the reduction in frequency was due to a decrease in the supplied flow rate, where the supplied flow rate was suggested as being equivalent to that given by Poiseuille type flow. This is suggesting that for an increase in viscosity it would be expected that there will be a decrease in the flow rate.

Effect of conductivity on nanoelectrospray flow rate

There have not been many systematic studies describing the effect of conductivity on the flow rate response. Using ethylene glycol (EG), with a conductivity of 0.23 S m^{-1}, and 1-ethyl-3-methylimidazolium tetrafluoroborate (EMI BF_4) at a conductivity of 1.40 S m^{-1}, Ryan et al. [2014] showed that the EMI BF_4 had a flow rate in pulsations at least 10 times smaller than that of ethylene glycol. Tests were performed on the same size emitter at 50 μm. Guo et al. [2018] suggested that if the flow rate follows that of Poiseuille it is not affected by the conductivity and that the flow rate is kept constant, from the balance between the volume and frequency. These tests were also performed over a small conductivity range from 2 to 10 μS cm^{-1}. However, compared to the tests by Ryan et al. [2014] these conductivities are several orders of magnitude smaller, also a much larger emitter

size with an ID of 160 μm and OD of 260 μm were used.

Effect of emitter geometry on nanoelectrospray flow rate

It was discussed in Section 2.2.2 how the emitter inner and outer diameter affected the flow rate in unforced/nanoelectrospray during cone-jet mode ejections. It was shown that both the emitter ID and OD affected the flow rate sensitivity. However, the ID in the electric pressure sensitivity was shown to have no effect as the resistance was accounted for (Ryan et al. [2009]). Ryan et al. [2014] built upon this work further, this time taking into account three spray modes on the effect of $\mathrm{d}Q/\mathrm{d}V(m_Q)$. It was shown that pulsed mode, cone-jet mode, and multi-jet showed little to no variation in the effect of the flow rate sensitivity, where in these tests emitters with an ID ranging from 150 to 650 μm and OD from 200 to 1600 μm were used. Results of this study were discussed in Section 2.2.2.1, where the results are in agreement with Ryan et al. [2009], which showed that m_Q increased with emitter ID up to $\sim$300 μm before becoming constant. Whereas it was shown that a larger emitter OD caused a reduction in m_Q (Ryan et al. [2014]). In other words this result is showing that the flow rate sensitivity is independent of the spray mode, relating pulsations to cone-jet mode, therefore the same effects as discussed in Section 2.2.2 should be valid.

2.3.4.4 Effect of parameters on the ejected volume

The volume of an ejection is important especially in relation to high resolution printing. The volume can be altered in both forced flow and unforced/nanoelectrospray.

Chen et al. [2006] derived a scaling for the minimum volume that should be achievable during a pulsation event. This scaling was deduced from using the minimum flow rate ($Q_{\min}$) given by De La Mora [1996], along with the on-time

of the pulsation. The minimum flow rate was given by

$$Q_{\min} = \frac{\gamma \tau_e}{\rho}, \tag{2.3.16}$$

where τ_e is the charge relation time ($\tau_e = \frac{\epsilon \epsilon_0}{K}$). The scaling for the volume was given as

$$v \sim Q_{\min} \Delta t \sim (d_i d_m)^{3/2}, \tag{2.3.17}$$

where d_m is a characteristic length given by

$$d_m \sim \left(\frac{\gamma \tau_e^2}{\rho} \right)^{1/3}, \tag{2.3.18}$$

(De La Mora [1996]).

The volume ejected during a single pulsation event has been shown to be related to Q_{ave} over many pulsations, and relates to the frequency by

$$v_{\text{pulse}} = \frac{Q_{\text{ave}}}{f}, \tag{2.3.19}$$

where Q_{ave} was the average flow rate measured using an in-line flow rate monitor (Paine et al. [2007b]). This has come from the assumption that mass is only lost during the on-time of the ejection. Another method used in this study to determine the volume ejected by a pulse came from using the transients measured using a fast current amplifier, along with scaling laws (De La Mora and Loscertales [1994]; De La Mora [1996]). Paine et al. [2007b] used the current scaling for cone-jet mode given by De La Mora and Loscertales [1994], where when rearranged for the volume gives

$$v_{\text{est}} = \frac{\tau_{\text{on}} \epsilon}{\gamma K} \left(\frac{I_{\text{DC}}}{f(\epsilon)} \right)^2, \tag{2.3.20}$$

where I_{DC} was calculated by integrating under the current transient to calculate the charge per cycle, then by dividing by the number of pulsation events, and $f(\epsilon)$ is from the scaling and is a function given by De La Mora and Loscertales

[1994].

Effect of viscosity on the ejected volume

The effect of viscosity on the ejected volume during a pulsation event has been shown to produce a larger volume for a higher viscosity solution (Guo et al. [2018]). Guo et al. [2018] performed tests over a range of viscosities from 30 to 100 cP. At a viscosity of 30 cP volumes of ∼45 to 55 pL were achieved, compared to ∼65 to 125 pL at 111 cP. Guo et al. [2018] suggested that the supplied flow rate followed Poiseuille, and therefore an increase in the drop volume, and reduction in supplied flow rate caused the reduction in the frequency. In these experiments there was an air supply connected to a syringe adding an additional pressure.

Effect of conductivity on the ejected volume

The volume ejected during an ejection was given by Chen et al. [2006], where Equation 2.3.17 showed that the volume was related to the minimum flow rate, which is related to the conductivity by $Q_{\min} \sim K^{-1}$. Equation 2.3.17 can also be written as

$$v \sim \left(\frac{\gamma \epsilon \epsilon_0}{K \rho}\right) \Delta t, \tag{2.3.21}$$

which gives $v \sim K^{-1}$. Guo et al. [2018] carried out experiments over a range of viscosities from 40 to 60 cP, at conductivities ranging from 2 to 10 μS cm^{-1}. Averaging the power law exponent through each data set, Guo et al. [2018] concluded that the volume was related to $K^{-0.60}$. As discussed for the flow rate, Guo et al. [2018] suggested that the supplied flow rate was not dependent upon the conductivity, however the ejected volume was. It was shown that as the conductivity increased a smaller droplet was printed, with volumes ranging from ∼100 to 130 pL at 2 μS cm^{-1}, compared ranging from ∼28 to 62 pL at 10 μS cm^{-1}. It was shown that the frequency and volume were interrelated, and since the frequency increased by $K^{0.58}$ and the volume decreased by $K^{-0.60}$, it

followed that these would cancel to give a constant flow rate.

Not performing any tests where current transients were measured, Guo et al. [2018] used the Poiseuille equation along with the equation for the tangential stress and the current scaling by De La Mora [1996] to show that the shear stress was related to K^{-1}. It was suggested that by having a higher conductivity the shear stress on the outer surface of the meniscus would reduce the acceleration of the surface, and therefore eject a smaller volume. In turn reducing the diameter of the jet.

Effect of emitter geometry on the ejected volume

Equation 2.3.17 gives scaling for the minimum volume that should be achievable when ejecting using the pulsations, where it is shown that $v \sim d_i^{3/2}$ (Chen et al. [2006]). Using Equations 2.3.19 and 2.3.20 Paine et al. [2007b] calculated the volumes from data by Alexander et al. [2006] and Paine et al. [2007a] and showed that the ejected volume increased with an increase in the emitter diameter, from approximately 2 fL on a $\sim$5 μm emitter to 120 fL on a $\sim$120 μm.

2.3.5 Cone-jet mode

Cone-jet mode is the most studied mode of electrospray. Early work by Zeleny [1917] observed that under certain voltage and hydrostatic pressure conditions, a thin jet was produced from the apex of the meniscus. Taylor [1964] showed that if the electrostatic pressure and pressure from the surface tension were in equilibrium and at a specific voltage, the half angle of the cone was 49.3°. Cloupeau and Prunet-Foch [1989] showed that cone-jet mode could come in at least two forms, one where there is a clear distinction between the meniscus and the thin jet at the apex (Figure 2.10a), the other where there was less distinction and a wide jet was formed (Figure 2.10b).

As with the other spray modes, cone-jet mode has also been shown to have a

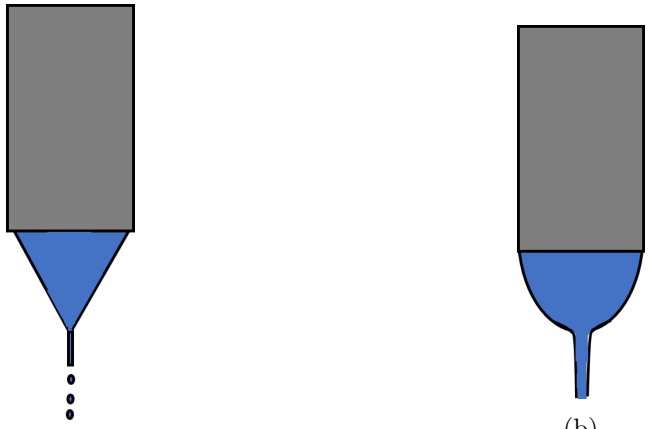

Figure 2.10: Schematic showing two different examples of jet characteristics in cone-jet mode.

distinguishable current transient. On increasing the voltage in pulsations, when cone-jet mode is entered the individual pulsations cease leaving behind a constant current. Figure 2.11 shows an example of a current transient measured during cone-jet mode, similar to those observed by Juraschek and Röllgen [1998] and Verdoold et al. [2014]. Another name given to this mode of electrospray is axial mode III (Juraschek and Röllgen [1998]).

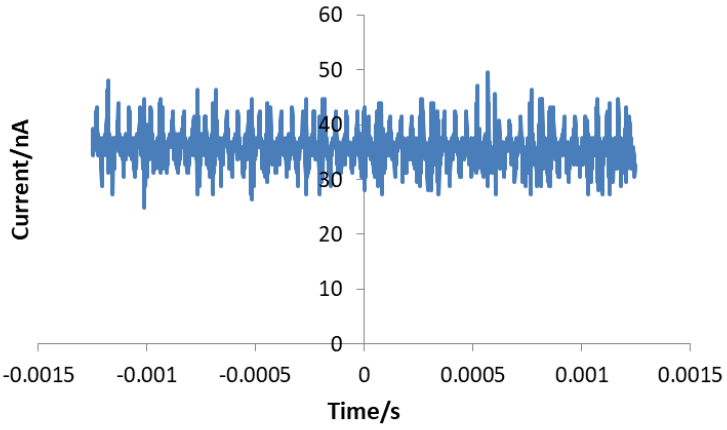

Figure 2.11: Current transient measured during cone-jet mode.

It has been shown that there is a stability window of applied voltages and flow rates over which cone-jet mode can be achieved (Bober and Chen [2011]; Collins et al. [2007]; Yu et al. [2016]). The onset voltage for cone-jet mode has been given

by

$$V_O = A_1 \left[\frac{2\gamma r_c \cos\theta_0}{\epsilon_0}\right]^{1/2} \ln\left(\frac{4H}{r_c}\right), \tag{2.3.22}$$

where A_1 is a constant, θ_0 is the half angle of the cone, and r_c is the radius of the emitter (Smith [1986]). Experimental and theoretical studies have suggested equations for calculating the minimum flow rate, where $Q_{\min}$ depends on the properties of the solution. Scaling for the minimum flow rate given by Fernández De La Mora was given by Equation 2.3.16, where τ_e is the relaxation time

$$\tau_e = \frac{\epsilon\epsilon_0}{K}, \tag{2.3.23}$$

(De La Mora [1996]). Gañán-Calvo gave the equation for the minimum flow rate as

$$Q_{min} \sim (\epsilon - 1)^{1/2} \left(\frac{\gamma\epsilon_0}{\rho K}\right), \tag{2.3.24}$$

(Ganan-Calvo et al. [1997]). The difference between the two is that Ganan-Calvo et al. [1997] has $(\epsilon - 1)^{1/2}$, instead of just ϵ.

2.3.5.1 Theoretical aspects of cone-jet formation

Numerous theoretical studies in electrospray have been based around cone-jet mode, where the formation of a Taylor cone (Taylor [1964]) has been used to understand the equations governing the dynamics of the cone and liquid ejections. If the charge relaxation time give by Equation 2.3.23 is less than the hydrodynamic time (Zhang and Basaran [1996])

$$\tau_h = \frac{r_O^3}{\pi Q}, \tag{2.3.25}$$

where r_O is the outer radius of the emitter, and Q is the liquid flow rate (Zhang and Basaran [1996]), a charged layer which has a thickness that is in the order of Debye lengths is produced at the liquid-air interface of the meniscus (Ganan-Calvo et al. [1997]; Barrero et al. [1999]).

The meniscus starts to deform due to the Coulomb repulsion between the ions at the liquid-air interface, and from the stresses on the surface of the meniscus from the electric field. There are two components to the electric field on the surface of the meniscus, which are the normal and tangential fields. Figure 2.12 shows an example of the different field components for a cone shape meniscus, similar to those given by Smith [1986] and Higuera [2004]. Both the normal and tangential fields produce Maxwell stresses on the meniscus. The tangential electric stress on the surface of the meniscus gives the charged layer the momentum to move towards the apex of the cone, deforming the shape of the meniscus. The tangential stress is given by

$$\tau_{\text{stress}} = \epsilon_0(E_n^o - \epsilon E_n^i)E_t, \tag{2.3.26}$$

where E_n^o and E_n^i refer to the outer (o) and inner (i) fields normal to the surface, and E_t refers to the tangential field (Melcher and Taylor [1969]; Barrero et al. [1999]). The charge layer on the surface causes the field within the meniscus to be reduced leading to $\epsilon E_n^i < E_n^o$, therefore the tangential stress can be written as

$$\tau_{\text{stress}} = \epsilon_0 E_n^o E_t, \tag{2.3.27}$$

(Melcher and Taylor [1969]; Barrero et al. [1999]).

There are also two components to the current. That due to conduction through the bulk of the solution

$$I_b = 2\pi K \int_0^{r_s} E_x^i r \mathrm{d}r, \tag{2.3.28}$$

where E_x^i is the internal field in the axial direction within the liquid (Ganan-Calvo [1997]; Higuera [2004]), and the current along the surface which is given by

$$I_s = 2\pi r_s u_{\text{s}} \sigma, \tag{2.3.29}$$

where r_s is the cross sectional radius of the surface (Higuera [2004]) and u_{s} is the

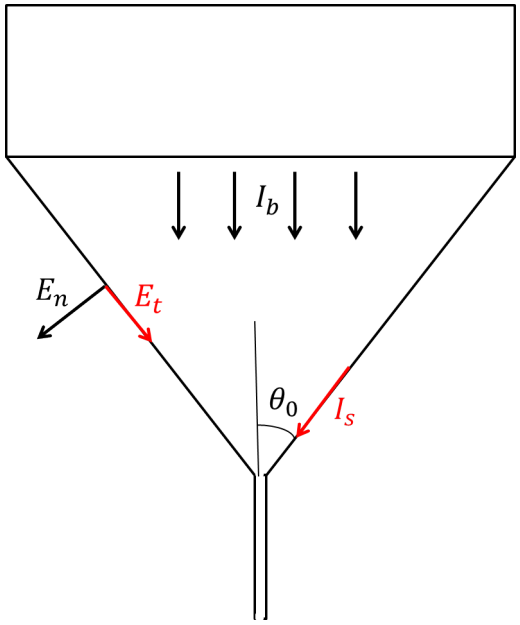

Figure 2.12: Electrospray cone diagram showing normal and tangential fields, and current positions.

axial velocity (Ganan-Calvo et al. [1997]). The axial velocity is given by

$$u_{\mathrm{s}} = \frac{Q}{\pi r_j^2}, \tag{2.3.30}$$

where σ_{charge} is the charge density at the surface of the meniscus, which can be written as

$$\sigma_{\mathrm{charge}} = \epsilon_0 E_n^o, \tag{2.3.31}$$

(Ganan-Calvo et al. [1997]; De La Mora and Loscertales [1994]). The tangential field has been given by

$$E_t = \frac{I_b}{2\pi K R_x^2 (1 - \cos\theta_0)}, \tag{2.3.32}$$

where R_x is the radial direction (Smith [1986]).

2.3.5.2 Formation of the jet and jet breakup

Once the forces from the electric field and the coulombic repulsion from the accumulated surface charge overcome the surface tension at the apex of the cone, a thin jet is produced which has a surface charge. Scaling for the diameter of the

jet has been given by

$$d_j \sim \left(\frac{Q\epsilon\epsilon_0}{K}\right)^{1/3}, \tag{2.3.33}$$

which suggests that the jet diameter is not dependent on the viscosity of the solution (De La Mora and Loscertales [1994]; De La Mora [1996]).

The length of the jet before breakup depends on the liquid properties, flow rate and the radius of the jet. Wang et al. [2012] showed that increasing the conductivity of the solution from a molar concentration of 0.13 to 1.68 mM the length of the jet decreased, as the angle of the spray when the jet broke up increased. It was shown that $\tan(\theta_{\text{plume}}) = \text{Molar}_C^{1/2}$, where θ_{plume} is the angle of the spray at breakup, and Molar_C is the molar concentration.

Ismail et al. [2018] developed two scaling laws to estimate the breakup length for both the viscid and inviscid limit. The experimental parameters were selected so that each of the experiments would exhibit varicose breakup, which was limited to a conductivity range from 0.1 to 10 μS cm^{-1}. The scaling for the jet length required the radius of the jet, where the radius was calculated using the scaling given by Gañán-Calvo [2004] where

$$r_j = \left(\frac{\rho Q^3 \epsilon_0}{\gamma K}\right)^{1/6}, \tag{2.3.34}$$

where this scaling is valid for

$$\alpha_\rho >> \alpha_\mu^{1/4}, \qquad\qquad \alpha_\rho/(\epsilon - 1) >> 1, \tag{2.3.35}$$

where $\alpha_\rho = \rho K Q/\gamma\epsilon_0$ and $\alpha_\mu = K^2\mu^3 Q/\epsilon_0^2\gamma^3$ (Gañán-Calvo [2004]; Ganán-Calvo et al. [2018]). Solutions with viscosities ranging from 1 to 976 cP, and emitters with ODs between 30 and 250 μm were tested.

In the viscid limit the scaling for the breakup length of the jet was given as

$$L_b = k_v \frac{6\mu}{Z_v}, \tag{2.3.36}$$

where

$$Z_v = \left[\left(\frac{\rho \gamma^5 \epsilon_0}{Q^3 K} \right)^{1/6} - \frac{1}{4\pi} \left(\frac{\rho^2 \gamma K}{\epsilon_0} \right)^{1/3} \right], \tag{2.3.37}$$

and k_v is a constant. Plotting L_b/d_n against $6\mu/Z_v d_n$ all data collapsed to give k_v as 7 except those where the electrical Reynold's number given by

$$Re = \left[\frac{(\rho^5 Q^3 \gamma K)}{(\mu \epsilon_0)} \right]^{1/6}, \tag{2.3.38}$$

was greater than 5. Therefore, this scaling did not fit for solutions with low viscosity.

Taking the condition where the solution is inviscid the scaling for the length of breakup was given by

$$L_b = k_i \frac{6\mu}{Z_i}, \tag{2.3.39}$$

where again k_i is a constant and

$$Z_i = \left[\left(\frac{\gamma^5 \epsilon_0}{\rho^5 Q^9 K} \right)^{1/6} - \frac{1}{4\pi} \left(\frac{\gamma K}{\rho Q^3 \epsilon_0} \right)^{1/3} \right]^{1/2}. \tag{2.3.40}$$

Plotting L_b/d_n against $6/Z_i d_n$ for the low viscosity solutions the data also collapsed to give k_i as 7.

It was concluded that the length of the jet is independent of the voltage and the emitter diameter, as this is greater than the jet radius. That if $Re < 0(1)$, $L_b = 6\mu/Z_v$ and if $Re > 0(1)$ then $L_b = 6\mu/Z_i$, for these experiments the threshold limit is when $Re \simeq 5$.

There are two different modes in which the jet breaks up as shown in Figure 2.13, either via varicose instabilities which is an on-axis form of breakup, and whipping/kink instabilities which causes the jet to curve during breakup (Cloupeau and Prunet-Foch [1994]; Xia et al. [2019]).

Varicose breakup is where at some distance along the jet, surface waves of wavelength $\lambda = u_s/f$ (Wei et al. [2002]) produce regular droplets which pinch

off from the jet, where the diameter of the droplet is related to the diameter of the jet by

$$d_d = 1.9 d_j, \tag{2.3.41}$$

(De La Mora [1996]). Figure 2.13a shows an example of this mode of jet breakup, where the on axis regular breakup of droplets is beneficial for electrospray printing which requires stable reproducible ejections.

Whipping/kink instabilities can be produced at high voltages, and if the jet has a high surface charge. The charge on the surface can allow lateral instabilities on the jet causing the jet to curve as the jet is stretched as shown in Figure 2.13b, this causes production of irregular droplets hence the reason why this mode is less desirable for printing applications.

(a) Varicose jet breakup (b) Whipping mode

Figure 2.13: Schematic showing two forms of jet breakup, varicose and whipping.

Xia et al. [2019] showed that there is a transition between varicose and whipping which can be characterised using the following non-dimensional parameters

$$\Gamma = \frac{\epsilon_0 E_n^2 r_j}{\gamma} = \frac{\sigma_{\text{charge}}^2 r_j}{\epsilon_0 \gamma}, \tag{2.3.42}$$

(Hartman et al. [2000]) which is the ratio between the electrical and surface tension forces, and the electrical bond number given by

$$Bo_e = \frac{\epsilon_0 E^2 d_n}{\gamma}, \tag{2.3.43}$$

which accounts for the ratio between the electric force from the applied voltage and surface tension forces. For a range of solutions with conductivities from 0.01 to 490 μS cm^{-1} results showed a transition of Γ for each solution, with varicose breakup occurring at smaller values of Γ. It was observed that the transition was independent of Bo_e but was dependent on the viscosity. On imaging the jet, when using a constant flow rate of 46 nL s^{-1} when the voltage was increased only varicose instabilities were observed. However, when applying a constant head pressure and increasing the voltage, the flow rate increased from 40 to 66 nL s^{-1} where a transition from varicose to whipping was observed. Xia et al. [2019] concluded that the transition between the two modes was independent of the applied voltage but was dependent on the liquid properties and the flow rate.

The viscous dimensionless parameter given by

$$\delta_\mu = \left(\frac{\rho \epsilon_0 \gamma^2}{K \mu^3} \right)^{1/3}. \tag{2.3.44}$$

(Ganan-Calvo et al. [1997]; Gañán-Calvo et al. [2013]) relates the forces due to inertia and viscosity, where viscosity becomes important when $\delta_\mu < 1$. By using the dimensionless values given by Equations 2.3.42 and 2.3.44 a general function termed G was given by

$$G = \Gamma^a \delta_\mu^b. \tag{2.3.45}$$

Xia et al. [2019] calculated values for a and b from the experimental data by plotting Γ^2 against δ_μ. When $\delta_\mu < 1$, $G = \Gamma^2 \delta_\mu^{-0.33}$, and when $\delta_\mu > 1$, $G = \Gamma^2$, where the transition from varicose to whipping was shown to be when G was approximately 145 and 165, as there is uncertainty in transitioning from varicose to whipping.

Once the jet has broken up the main droplets that detach from the jet have a surface charge, where the maximum charge that a droplet can hold is given by the Rayleigh limit (Equation 2.3.1). Gañán-Calvo et al. [2016] developed scaling laws based on the first droplet ejected from the jet. Experiments were performed using a droplet suspended from a copper disk above another disk electrode 10 mm away.

A constant voltage was applied to the top disk for a set length of time. The scaling law for the charge of the first ejected droplet were calculated from numerical simulations. The dimensionless charge was shown to scale as $q/q_0 = 0.2\zeta_q$, where the charge $q_0 = \epsilon_0 E_0 d_0^2$, characteristic length $d_0 = (\gamma\epsilon_0^2/\rho K^2)^{1/3}$, electric field $E_0 = (\gamma/d_0\epsilon_0)^{1/2}$, and $\zeta_q = \delta_\mu^{-2/3}\epsilon^{7/12}$.

Due to evaporation the charge stays constant however the size of the droplet decreases, this causes the droplet to breakup into smaller drops, which produces a plume of sprayed droplets, hence the name electrospray.

2.3.5.3 Current and flow rate scaling laws

Scaling laws have been produced based on experimental results and theoretical aspects of electrohydrodynamic theory governing electrospray behaviour. Different scaling laws have been proposed to link the measured current to the flow rate, and other liquid properties.

The main scaling laws for cone-jet mode electrospray have been derived by De La Mora and Loscertales [1994] and Ganan-Calvo et al. [1997]. Fernández De La Mora derived scaling laws based on whether a solution was polar or non-polar, which were distinguished by the conductivity of the liquid. Liquids with a conductivity greater than 10^{-5} S m^{-1} were classed as polar, and non-polar liquids had a conductivity less than 10^{-6} S m^{-1} (De La Mora [1996]). The scaling for the current and flow rate of a polar solution was given by

$$I = f(\epsilon)\left(\frac{\gamma K Q}{\epsilon}\right)^{1/2}, \tag{2.3.46}$$

where $f(\epsilon)$ is a function given by De La Mora and Loscertales [1994], where it was shown that when the permittivity was greater than 40, $f(\epsilon)$=18. The minimum current scaled as

$$I_{\min} = f(\epsilon)\gamma\left(\frac{\epsilon_0}{\rho}\right)^{\frac{1}{2}}. \tag{2.3.47}$$

It was concluded that the above scaling could be applied to electrospray pulsations

if the charge relaxation time (τ_e) was much smaller than the duration of the pulsation event (De La Mora [1996]).

Ganan-Calvo et al. [1997] proposed scaling laws based on the different behaviours due to the viscosity and the conductivity of the solution. Two scaling laws were derived, one for high viscosity and high conductivity solutions, and one for low viscosity and low conductivity solutions. The scaling law to use for a given solution was determined by a dimensionless parameter given by $\delta_\mu \delta^{1/3}$ where

$$\delta = \frac{\gamma \epsilon_0}{\rho K Q} = \frac{Q_0}{Q} \tag{2.3.48}$$

and δ_μ is given by Equation 2.3.44. If $\delta_\mu \delta^{1/3}$ <1 then the current scaling was given as

$$\frac{I}{I_0} = 6.2 \left[\frac{Q}{(\epsilon - 1)^{1/2} Q_0} \right]^{1/2} - 2.0, \tag{2.3.49}$$

and if $\delta_\mu \delta^{1/3}$ >1 then the following scaling was followed

$$\frac{I}{I_0} = 11.0 \left(\frac{Q}{Q_0} \right)^{1/4} - 5.0. \tag{2.3.50}$$

The characteristic current (I_0) and flow rate (Q_0) are given by

$$I_0 = \left(\frac{\epsilon_0 \gamma^2}{\rho} \right)^{1/2}, \qquad Q_0 = \frac{\gamma \epsilon_0}{\rho K}. \tag{2.3.51}$$

In the scaling laws by Ganan-Calvo et al. [1997] the difference in scaling was explained by the difference in the effect that the tangential stress has on the jet. In the high viscosity and high conductivity regime it was suggested that the velocity of the liquid in the bulk was the same as the velocity of the liquid on the surface of the jet, which can be described by a one dimensional model. In the low viscosity and low conductivity regime the layer on the surface of the jet was accelerated faster than that of the bulk of the solution.

A later study by Gañán-Calvo [2004] identified different regimes for electrospraying in cone-jet mode, along with the scaling between the drop

diameter, and the current and flow rate. The different regimes were classed by the dominance of difference forces and the ones of importance are:

- IE: Inertia and electrostatic suction

$$I = (\gamma K Q)^{1/2}, \tag{2.3.52}$$

  and d/r_j were given by Equation 2.3.34 and the criteria for this regime given by Equation 2.3.35.

- IP: Inertia and polarization

$$I = \left(\frac{\rho K^2 Q^2}{(\epsilon - 1)\epsilon_0}\right)^{1/2}, \qquad d = \left(\frac{\rho \epsilon_0 Q^3}{\gamma K}\right)^{1/6}, \tag{2.3.53}$$

  The criteria for this regime is given by $1 >> \alpha_\rho/(\epsilon - 1) >> \alpha_\mu/(\epsilon - 1)^4$.

- VE: viscous and electrostatic suction

$$I = (\gamma K Q)^{1/2}, \qquad d = \left(\frac{\mu \epsilon_0^2 Q^3}{\gamma K^2}\right)^{1/8}, \tag{2.3.54}$$

  The criteria for this regime is given by $\alpha_\rho << \alpha_\mu^{1/4}, \alpha_\mu/(\epsilon - 1)^4 >> 1$.

- VP: Viscous and polarization

$$I = \left(\frac{\mu^3 K^3 Q^2}{(\epsilon - 1)^4 \gamma^2 \epsilon_0^2}\right)^{1/2}, \qquad d = \left(\frac{\mu Q}{(\epsilon - 1)\gamma}\right)^{1/2}, \tag{2.3.55}$$

  The criteria for this regime is given by $\alpha_\rho/(\epsilon - 1) << \alpha_\mu/(\epsilon - 1)^4 << 1$.

2.3.6 Other modes

At higher voltages other modes have been distinguished, such as multi-jet (Cloupeau and Prunet-Foch [1994]), this mode consists of multiple jets in which the number of jets increases with the applied voltage. The jets are also emitted from the rim of the emitter, if the voltage is large enough (Cloupeau and

Prunet-Foch [1994]; Jaworek and Krupa [1999b]). Figure 2.14 shows an example of multi-jet, with two jets and multiple jets that would be produced from the rim at higher voltages.

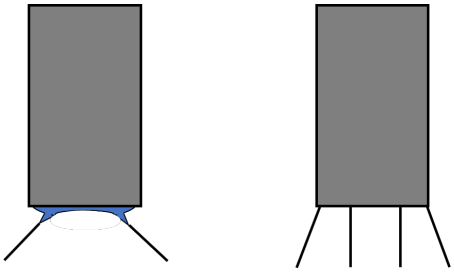

Figure 2.14: Examples of multi-jet.

At very high voltages corona discharge can occur, and it is common when using liquids with high viscosity or high surface tension. If discharge occurs before stable cone-jet it can stop this mode from occurring as discharge reduces the electric field strength (Cloupeau and Prunet-Foch [1994]).

2.4 Applications of electrospray

Electrospray technology is becoming more widely researched in relation to being used for printing applications, such as to produce biological microarrays (Kim et al. [2010]), DNA printing (Park et al. [2008]) and quantum dots for LED devices (Kim et al. [2015]). This technology has shown potential in being able to produce deposits in the micron to sub-micron scale and being able to print inks with a range of liquid properties.

Conventional ink-jet printing is the most common additive drop-on-demand printing technique used in many applications, due to the non-contact nature of the method, along with the high accuracy of the deposition. However, the main limitation is due to the high pressure required to eject the droplets. This limits the size of the emitter diameter which is around 40 to 60 μm, due to smaller emitters becoming blocked (Stringer and Derby [2009]; Famili et al. [2011]). The size of the drops scale with the emitter diameter and are typically limited

to 20 to 50 μm (Derby [2010]). The main constraints are with the viscosity and surface tension of the liquid. The recommended range for printing is to have a viscosity of 1 to 25 cP, and a surface tension of 25 to 50 mN m^{-1} (Cummins and Desmulliez [2012]).

This is where electrospray has significant advantages, as it has been shown to have the ability to overcome the limitation of ink-jet, such as being able to print inks with viscosities greater than 1000 cP (Jayasinghe and Edirisinghe [2002]; Carter et al. [2014]). In nanoelectrospray there are no pumps needed to drive the flow of the liquid, it is entirely controlled by the voltage. Emitter sizes as small as 1 to 2 μm have been used to print biological samples with diameters ranging from 1.00 to 4.50 μm (Shigeta et al. [2012]).

2.4.1 Continuous voltage printing

Constant DC voltage printing utilises the pulsations as described in Section 2.3.4, where liquid is ejected at a constant frequency depending on the liquid properties, emitter geometry, flow rate and applied voltage. To print individual droplets using the pulsations, the distance between deposits depends on the pulsation frequency, and the speed of the stage. The relationship between the speed of the stage (s) and the distance between deposits (d) is given by

$$s = \frac{d}{t}, \tag{2.4.1}$$

where t is the time between ejections. The frequency is inversely proportional to the time between ejections, making the frequency of pulsations equal to

$$f = \frac{s}{d}. \tag{2.4.2}$$

Printing inks containing DNA strands to produce biological microarrays, Park et al. [2008] showed how linking the natural pulsation frequency with the speed

of the stage, could be used to print individual droplets. Using a 2 μm emitter, a pulsation frequency of approximately 5 Hz and a stage speed on 20 μm s^{-1}, drop sizes of 2.00 μm were achieved. Increasing the pulsation frequency to approximately 50 Hz and a stage speed of 200 μm s^{-1}, drops of 3.00 μm were printed. Barton et al. [2010] also utilised the natural pulsations to print using a solution of glycerol and water. Using a 5 μm emitter, droplets with a diameter of 2.80 μm were achieved. Here droplets smaller than the emitter were produced, but as stated for the behaviour of the pulsations, the size of the deposits depend on the combination of liquid properties, emitter geometry, flow rate and emitter-to-substrate distance.

Limitations of printing using the pulsations, are that the frequency of the ejections is limited to the frequency range that can be achieved for the given set-up parameters used. Also, the operator does not have full control of where droplets are printed, the deposition is reliant on the frequency of the ejections. It has been previously mentioned that due to continuous ejections, the position of the droplets is not as controlled as when a pulsed voltage is applied (Park et al. [2008]; Barton et al. [2010]).

2.4.2 Pulsed voltage printing

Pulsed/switched voltage electrospray allows the operator to control the duration and the exact position of each ejection, compared to continuous voltage operation, making this process drop-on-demand. Different methods to control the change in voltage have been used, from varying the voltage by increasing and decreasing the emitter-to-substrate distance (Moerman et al. [2001]), to varying the applied voltage using a generated waveform (Mishra et al. [2010]; Laurila et al. [2017]; Phung et al. [2017]). Different waveforms have been used to produce ejections, from a square wave TTL signal (Paine et al. [2007b]; Mishra et al. [2010]), to a trapezoidal wave (Phung et al. [2017]), and using a signal which increases the voltage in more than one step (Rahman et al. [2011]).

The properties of the pulse used to initiate the ejections is important in controlling the speed of the ejection, and the number of ejections (Alexander et al. [2006]; Paine et al. [2007b]; Yuan et al. [2015]; Yuan and Xiong [2018];). The key parameters to control are the magnitude of the voltage switch, along with the frequency and duty cycle of the pulse. Understanding the effects of the magnitude of the voltage switch, the duration of the pulse, and the effect that the liquid properties and process parameters have on the print speed and resolution, are important to this technology being used in applications such as high resolution printing.

Effect of the applied voltage

Discussed in Section 2.3 different spray modes are observed depending on the applied voltage. The same has been shown for pulsed voltage operation in both forced and unforced/nanoelectrospray, where again the spray modes observed are dependent on the set-up parameters. It has been shown that when the duration of the pulsed voltage is kept constant, increasing the magnitude of the pulsed voltage causes transitions in the spray mode, for example dripping, pulsations, cone-jet and spindle mode (Wang and Stark [2010a]; Lee et al. [2012a]; Lee et al. [2012b]; Wang and Stark [2014]).

The magnitude of the voltage has also been shown to be important in the time it takes from the switching of the voltage to the first ejection. Figure 2.15 shows an example of a TTL signal switching from V_1 to V_2, where V_1 is the initial bias voltage and V_2 is the ejection voltage. Previous literature has shown that at a constant value of V_1, increasing V_2 reduces the time it takes for the first ejection to occur, or it reduces the formation time (T_{form}) (Paine et al. [2007b]; Paine [2009]; Lee et al. [2012b]; Obata et al. [2015]). Increasing the value of V_1 causes a larger V_2 voltage to be applied to initiate ejections. Paine [2009] showed that increasing V_1 from 0 to 1.000 kV, the V_2 voltage required to achieve an initial ejection at 9 ms increased from approximately 1.180 to 1.280 kV. By increasing

the value of V_1, the formation time decreased at a quicker rate with increase in V_2. Taking the electrical bond number given by

$$N = \frac{\epsilon_0 V^2}{r_c \gamma \left(\ln\left(1 + \frac{2H}{r_c}\right)\right)^2}, \tag{2.4.3}$$

which was modified from the electrical bond number given by Zhang and Basaran [1996], Paine [2009] plotted a $\log - \log$ plot of the formation time against the jump in electrical bond number which is given by

$$\Delta N = N_2 - N_1, \tag{2.4.4}$$

where N_2 is the bond number at V_2, and N_1 is the bond number at V_1. It was shown that when V_1 >1.100 kV the data fitted to a power law. The formation time varied with the jump in bond number given by

$$T_{\text{form}} = p\Delta N^q, \tag{2.4.5}$$

where p and q were shown to be linearly related to V_1, where p was inversely related and q directly related (Paine [2009]).

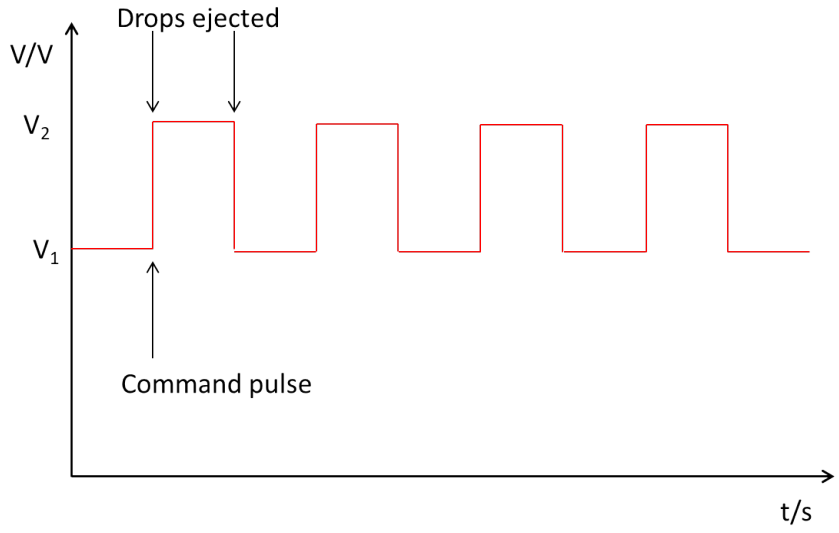

Figure 2.15: TTL signal for liquid ejection.

Applying a pulsed voltage to achieve pulsations similar to those discussed in

Section 2.3.4, it has been shown in previous studies that the magnitude of the applied voltage can be used to control the number of ejections (Paine et al. [2007b]; Mishra et al. [2010]). Early work by Paine et al. [2007b] using nanoelectrospray, showed that applying a pulsed voltage at a constant frequency of 1 Hz, and at a duration of 1 ms, increasing the voltage of the pulse increased the number of ejections per voltage switch. Similar was observed by Mishra et al. [2010], where this time the emitter was held at an initial bias voltage. At approximately the same pulse duration it was shown that a switching magnitude ($V_2 - V_1$) of 0.160 kV produced a single ejection, whereas a switching of 0.340 kV produced four ejections. Controlling the number of ejections is important for drop-on-demand printing, as the number of ejections isolated per switch of the voltage will affect the volume of the ejection.

The frequency of the pulsed voltage

The frequency of the pulsed voltage controls the length of the voltage pulse, and the time between consecutive switches of the voltage. It has been shown that using the pulsation mode as discussed in Section 2.3.4, applying a low frequency to the voltage switch allows for a voltage pulse long enough that multiple ejections occur (Paine et al. [2007b]; Yuan et al. [2015]; Yuan and Xiong [2018]). It has been shown in both forced and unforced/nanoelectrospray, that the frequency of ejection (f_p) increases with an increase in the frequency of the pulsed voltage (f_V), up to a point where the frequency of the ejections cannot keep up with the frequency of the pulsed voltage (Kim et al. [2008]; An et al. [2014]; Yuan and Xiong [2018]; Kim et al. [2018]; Zhu et al. [2019]). Drop-on-demand is achieved when $f_p = f_V$, as a single ejection is produced per voltage pulse (An et al. [2014]; Yuan and Xiong [2018]; Kim et al. [2018]; Zhu et al. [2019]).

2.4.2.1 Print resolution

The resolution of the deposit is vital in many applications as previously discussed, different methods have been used to calculate the size of the ejected deposit. It was shown previously by Equation 2.3.19 that the volume of a transient pulse or the volume of the deposited droplet is related to the flow rate and the frequency (Paine et al. [2007b]; Kim et al. [2008]). It was also shown by Equation 2.3.20, that the volume can be estimated from the scaling laws using the current measured during the ejection process (Paine et al. [2007b]). Paine et al. [2007b] showed that estimating volumes using the current transients and scaling laws, was a good method for when the flow rate could not be directly measured, where the volumes from Equation 2.3.19 were 81 to 297 fL, compared to 89 to 131 fL calculated using Equation 2.3.20. It was shown that the order of magnitude was the same, just that the estimation from the transients and scaling laws gave an underestimate.

Yogi et al. [2001] gave an equation for calculating the drop volume based on the diameter and height of the deposit, given by

$$v_{\text{print}} = \pi \left(\left(\frac{r_d^2 h_d}{2} \right) + \left(\frac{h_d^3}{6} \right) \right), \tag{2.4.6}$$

where r_d is the radius of the droplet on the substrate and h_d is the height of the droplet. Both Paine et al. [2007b] and Kim et al. [2008] used this equation to calculate drop volumes and diameters. Paine et al. [2007b] showed that using this equation along with an estimate for the density of the solid and liquid, the volume of the deposits ranged from 1.1 to 2.8 fL, where the current transients gave a volume estimate of 0.9 to 1.3 fL. Paine et al. [2007b] showed good agreement between different methods for estimating drop volumes, however it was suggest that more is required over a wider range of emitter sizes, and liquid properties to determine how reliable Equation 2.3.20 is for estimating the drop volumes. Kim et al. [2008] used Equation 2.4.6 to compare the drop diameters measured from those printed, to those calculated using the equation. Results showed good

agreement between the two with the drop diameter being related to the frequency by

$$D_{\text{print}} \sim f^{1/3}, \tag{2.4.7}$$

this relationship was also observed by Yuan et al. [2015].

Other researchers have derived theoretical models for predicting the drop diameter, based on the conservation of the ejected droplet to the droplet that spreads on the surface (Park et al. [2014]; Qian et al. [2018]). The diameter of the droplet ejected from the meniscus has been given by

$$D_{\text{drop}} = \left(\frac{6}{\pi} v_{\text{drop}}\right)^{1/3}, \tag{2.4.8}$$

(Qian et al. [2018]). Once the drop hits the substrate and has spread the drop will have a different diameter to that of the initial ejected droplet, however the volume ejected is conserved. The diameter of the printed droplets has been calculated using the spherical cap equation given by

$$v_{\text{print}} = \frac{\pi r_d^3 (1 - \cos\theta)^2 (2 + \cos\theta)}{3 \sin^3\theta}, \tag{2.4.9}$$

where θ is the contact angle between the droplet and the substrate (McHale et al. [2005]; Qian et al. [2018]). The ratio between the diameter of the drop on the substrate and the initial droplet has been given by

$$\frac{D_{\text{print}}}{D_{\text{drop}}} = \left(\frac{4 \sin^3\theta}{(1 - \cos\theta)^2 (2 + \cos\theta)}\right)^{1/3}, \tag{2.4.10}$$

where D_{print} is calculated from the spherical cap equation (Park et al. [2014]; Qian et al. [2018]). By equating Equations 2.4.8 and 2.4.10, and that $v_{\text{drop}} = QD_c/f$, where in relation to printing D_c is the duty cycle, the printed drop diameter has been shown to be theoretically predicted by

$$D_{\text{print}} = \left(\frac{24 \sin^3\theta Q D_c}{\pi f (1 - \cos\theta)^2 (2 + \cos\theta)}\right)^{1/3}. \tag{2.4.11}$$

Park et al. [2014] used forced flow electrospray in pulsed cone-jet mode at a range of flow rates, duty cycles, and contact angles, where good agreement was shown between the physical drop diameters and those theoretically calculated. Qian et al. [2018] showed the same using unforced electrospray where the flow rate was suggested to follow that of Poiseuille flow.

Printing using cone-jet mode

In a few studies pulsed voltage refers to switching into cone-jet mode (Kim et al. [2008]; Kim et al. [2010]). It has been shown that the size of the deposit decreases with an increase in the frequency of the pulsed voltage, and a decrease in the duty cycle (Kim et al. [2008]; Wang and Stark [2010b]; Park et al. [2014]). In cone-jet mode once the jet has formed, liquid is ejected during the duration of the voltage pulse. Varying the pulsed voltage frequency from 2.5 to 25 Hz, in forced flow electrospray at a flow rate of 3 nL s^{-1}, Kim et al. [2008] achieved prints with diameters ranging from 95 to 210 μm, using an emitter with ID=200 μm and OD=500μm, at an emitter-to-substrate distance of 1 mm. Also in forced flow but at a flow rate between 1 and 4 μL min^{-1}, Park et al. [2014] used an emitter with ID=50 μm, where varying the frequency of the pulsed voltage from 200 to 300 Hz diameters of $\sim$58 to 78 μm were achieved at a contact angle of 35°, whereas diameters of $\sim$38 to 56 μm were achieved at a contact angle of 75°. The largest drop diameters being printed at the lowest pulsed voltage frequency. Similar ranges were also achieved when varying the duty cycle, and these were printed at an emitter-to-substrate distance of 200 μm.

Another important parameter previously discussed is that of the applied voltage, where the size of the deposit has been shown to increase with the applied voltage (Kim et al. [2010]; Wang and Stark [2010a]; Wang and Stark [2010b]). In forced flow using a 30 μm emitter, Kim et al. [2010] showed that varying the voltage from 0.800 to 1.200 kV at a constant frequency of 10 Hz, deposits with diameters ranging from 8 to 20 μm were achieved when the emitter-to-substrate distance

was 100 μm. In nanoelectrospray using a 4 μm emitter at a range of voltages from 0.500 to 0.800 kV, at an emitter-to-substrate distance of 125 μm and a spray duration of 200 ms, spray diameters ranged from 120 to 185 μm were deposited (Wang and Stark [2010b]). Still using a 4 μm emitter at an emitter-to-substrate distance of 200 μm, using a 100 ms duration pulse at voltages between 0.800 and 1.000 kV spray diameters ranging from 120 to 125 μm were achieved. Using a 20 μm emitter at an emitter-to-substrate distance of 125 μm voltages of 0.925 and 0.975 kV produced spray deposits of 108 to 125 μm, where a voltage of 1.025 kV produced a spray area of over 250 μm.

These results suggest that the size of the deposit not only depends on the emitter geometry and the applied voltage, but also on the frequency of the pulsed voltage, the emitter-to-substrate distance and the flow rate. It has been shown that in cone-jet mode a range of deposits can be produced depending on these process parameters, which can allow for a range of deposit sizes. Printing using cone-jet mode can be useful in applications such as for printing tracks for electronic devices (Wang et al. [2009]; Wang and Stark [2010b]), and for thin film deposition (Jaworek and Sobczyk [2008]).

Printing using the pulsations

As discussed previously the number of ejections per application of the voltage pulse depends on the natural pulsation frequency of the meniscus, compared to the frequency of the pulsed voltage. In constant voltage electrospray it was discussed in Section 2.3.4 how the pulsation frequency of the meniscus varied with different liquid properties and emitter geometry. In pulsed voltage operation, it has been shown that by increasing the voltage a range of drop sizes can be produced, due to the increase in frequency, and therefore an increase in the number of ejections (Paine et al. [2007b]; Mishra et al. [2010]; An et al. [2014]). Increasing the duration of the voltage pulse, Mishra et al. [2010] produced drop sizes ranging from 6 to 22 μm using an emitter with an ID=5 μm, which showed

the ability to vary print resolution using one set of parameters.

In both forced and unforced/nanoelectrospray it has been shown that when a single pulsation is isolated to print each deposit, the diameter of each ejection decreases with an increase in the frequency of the pulsed voltage (An et al. [2014]; Yuan et al. [2015]; Yuan and Xiong [2018]; Zhu et al. [2019]). General trends have shown that in forced flow electrospray an increase in the flow rate produces a larger deposit (Yuan et al. [2015]; Yuan and Xiong [2018]), along with an increase in emitter geometry and voltage (Yuan and Xiong [2018]). In unforced electrospray Carter et al. [2014] observed that the drop volume decreased for an increase in the applied voltage, in these tests a single voltage pulse was applied and a current transient recorded for each ejection, an emitter with an ID=30 μm was used at an emitter-to-substrate distance of 200 μm.

High resolution printing in unforced/nanoelectrospray has shown that droplets less than 10 μm can be achieved, by isolating a single ejection for each droplet. It has been shown that high resolution can be achieved using a range of liquids such as solutions containing functional protein material (Shigeta et al. [2012]; Poellmann and Johnson [2013]), DNA samples (Park et al. [2008]) and by using a range of process parameters. To achieve these high resolution droplets emitters with diameters less than 5 μm have been used, which has required droplets to be printed at emitter-to-substrate distances at 50 μm or below (Mishra et al. [2010]; Shigeta et al. [2012]; Sutanto et al. [2012]). In relation to the emitter size and droplet diameter, Paine et al. [2007b] achieved prints with diameters of 1.40 μm using a 4 μm emitter, compared to Shigeta et al. [2012] where printing with a 2 μm emitter achieved droplets ranging from 1.00 to 4.50 μm, and a 1 μm emitter achieved droplets in the range of 1.10 to 1.90 μm.

Smaller emitters have shown that greater print resolution can be achieved, which is beneficial for printing of biological microarrays, which requires a large number of small droplets per unit area (Park et al. [2008]). However, there are limitations in relation to the emitter-to-substrate distances required, especially for use in

an industrial process, as this allows for little variation and displacement in the substrate.

However, there are still limitations to using electrospray for printing applications. In forced flow, since liquid is continually being supplied to the meniscus, the voltage needs to be pulsed constantly at a given frequency to achieve a printed array. It has been previously shown that to achieve a single ejection $f_p = f_V$ (An et al. [2014]; Yuan and Xiong [2018]; Kim et al. [2018]; Zhu et al. [2019]), where the frequency range depends on the combination of liquid properties and process parameters. In unforced/nanoelectrospray the operator has more control over the ejection process. If Q_{nom} is 0 nL s^{-1}, or small enough that when no voltage is applied there are no ejections, as long as V_1 is below the onset voltage ejections only occur when V_2 is applied. Due to there being no liquid ejection when the voltage is set to V_1, it allows a single voltage pulse to be applied (Paine [2009]; Carter et al. [2014]) without ejections continuing afterwards and producing another unwanted deposition.

Nanoelectrospray has shown that it has advantages due to the low flow rates and smaller volumes that can be achieved, which enhances print resolution, along with an increase in the sensitivity. The benefit that this has shown over forced flow is that no pumps are required and smaller samples can be used. However, in nanoelectrospray the operator loses control over the flow rate. Knowing how this flow rate will respond is beneficial to understanding the effect on the drop volume and charge. The process in understanding the interplay between each of the set-up variables (liquid properties, emitter geometry etc) is vital to achieving a stable ejection.

3

Experimental methods

The purpose of this study is to further the understanding of the interplay between liquid properties and geometry on nanoelectrospray behaviour, using a systematic approach. This chapter explains the experimental set-up and methods used to perform the experiments and analyse the data.

3.1 Solution preparation and characterisation

To enable the variation of liquid properties, viscosity and conductivity, a suitable combination of liquids was required to enable each of these parameters to be altered individually. The solutions chosen had to enable a deposit to be left on the substrate, whether this be a dried residual or a droplet. This was required to measure the size of the printed droplets afterwards.

Glycerol and water solutions were used to vary the viscosity, as it allowed little variation in the surface tension. At a temperature of 20 °C the surface tension is approximately 72.8 mN m^{-1} for water and 63.4 m Nm^{-1} for glycerol (Harrison and Ellis [1984]). Glycerol also has a low evaporation rate which allowed the droplets to be imaged on the substrate after printing. It has been assumed that if the droplets do not unpin from the substrate, then the diameter is the same as when the droplets were printed, allowing the volume to be calculated.

Solutions of glycerol (Analytical reagent grade >= 99 %, Fischer Scientific) and water (18 MΩ cm pure water) were produced using a range of wt:wt of glycerol to water, to achieve a range of viscosities from around 2.5 to 156 cP. The mass of water was initially decided, and the mass of glycerol required to achieve a certain

viscosity was calculated by using the following equations

$$\%\text{wt} = \left(\frac{\text{Mass of solute}}{\text{Mass of solution}}\right) 100, \tag{3.1.1}$$

$$m_{\text{glycerol}} = \frac{(\frac{\%\text{wt}_{\text{glycerol}}}{100}) \times m_{\text{water}}}{1 - (\frac{\%\text{wt}_{\text{glycerol}}}{100})}, \tag{3.1.2}$$

where m is the mass and wt is the weight.

Different molar concentrations of sodium iodide (NaI) and water were used to alter the conductivity of the solutions. Majority of the NaI and water solutions were made using an initial concentration, which was then diluted. An initial molar concentration of 0.7 M was produced by weighing out 5.25 g of sodium iodide (anhydrous, free-flowing, Redi- Dri$^{\text{TM}}$, ReagentPlus®, >=99%, Sigma-Aldrich®). The amount of NaI required to achieve this molar concentration was calculated by

$$m_{\text{solid}} = \text{Molar}_C \times v_{\text{Water}} \times M, \tag{3.1.3}$$

where Molar_C is the molar concentration required, v_{Water} is the volume of water (mL), and M is the molar mass of the solid, which in this case is NaI which is 149.89 g mol^{-1}. The NaI was poured into a 50 mL volumetric flask, which was filled with ultra pure water. After the NaI had fully dissolved, 5 mL of the 0.7 M concentration was pipetted into a 50 mL volumetric flask and water added to dilute the solution to 0.07 M. Taking 5 mL of each of the molar concentrations above, the dilutions were performed until a 0.0007 M solution was achieved.

The solutions were made by initially weighing out the glycerol into a glass beaker, where the beaker and the glycerol were then weighed. Different volumes/masses of ultra-pure water and NaI solutions were added to the glycerol to achieve the required viscosity and conductivity. A percentage error was allowed at each conductivity, with an error of ±10% at 6 and 60 μS cm^{-1}, and ±5% at 600 μS cm^{-1}. To achieve these conductivities for each viscosity, tests were performed by adding different amounts of ultra-pure water, and concentrations of NaI solutions to determine the amounts of each required. This

would enable solutions to be reproduced.

Each solution was mixed for 15 minutes using a magnetic stirrer to ensure the solutions were fully combined, then each solution was left for 1 hour before measuring the conductivity to make sure that any excess heat/energy added during stirring was removed, also each solution would have been idle before testing was performed.

3.1.1 Measuring the liquid properties

3.1.1.1 Viscosity and density

The viscosity was measured using an Anton Parr rolling ball viscometer (Lovis 2000 M/ME). Depending on the viscosity of the solution measured depended on the capillary needed to measure that solution, where a steel ball was used in each of the tests. A glass capillary with a diameter of 1.5 mm was used to measure viscosities below 20 cP, and a 1.8 mm capillary was used to measure viscosities above 20 cP but below 200 cP.

The measurements were taken using the flow through method, approximately 5 mL of each solution was pushed through a hole in the side of the viscometer where it went through a glass tube visualised on the screen. The liquid then went through the feed system through the capillary and out through another feed tube into the waste bin. In filling the system the solution needed to be pushed through slowly, especially for the higher viscosity solutions. It was important not to get any air bubbles in the capillary, as this could disturb the movement of the ball. Once the system was filled the density was automatically calculated and displayed on the screen. In each of these experiments the angle at which the capillary was tilted was 45°, and the temperature was 20°C. The equipment was set to run where the time for the ball to travel from one end of the capillary to the other was measured. If the times were reproducible then approximately 4 measurements were recorded, otherwise the machine would run approximately 8 measurements.

The dynamic viscosity was then recorded once all the measurements had been taken.

3.1.1.2 Conductivity

The conductivity of the solutions was measured using a Jenway 4510 conductivity meter and a Jenway Micro-volume conductivity probe. The probe was placed into each solution which was swirled around for 1 minute, to remove any residue water that may have been left in the probe, also to make sure that the solution had fully filled the probe and there were no air bubbles. The solution was then left to stand for 1 minute where the conductivity and temperature were recorded. The conductivity of the solutions was measured at temperatures between 20 and 23 °C. Table 3.1 gives the conductivity of each molar concentration, and Figure 3.1 shows a plot of the conductivity against the concentration of NaI. The conductivity of the 0.7 M solution was not high enough to achieve 600 μS cm^{-1} at 60 and 111 cP, therefore molar concentrations of 2.0 and 3.5 M were produced.

Concentration/(M)	Conductivity/(S m^{-1}) $\sim$ (22 to 23) $^{\circ}C$
3.5	14.7
2.0	9.69
0.7	4.48 $\pm$ 0.15
0.07	0.596 $\pm$ 0.029
0.007	0.0752 $\pm$ 0.0072
0.0007	0.00830 $\pm$ 0.00037

Table 3.1: Liquid concentration and conductivities.

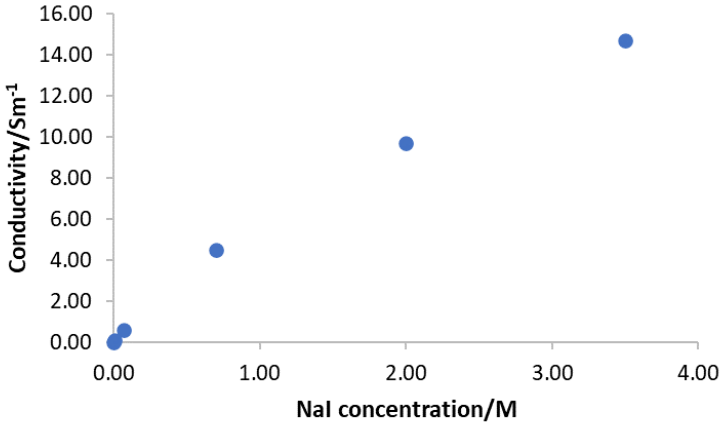

Figure 3.1: Conductivity against concentration of NaI to water.

3.1.1.3 Surface Tension

The surface tension values have been calculated using the following equation

$$\gamma_{\text{solution}} = \%wt_{\text{glycerol}}\gamma_{\text{glycerol}} \times \%wt_{\text{water}}\gamma_{\text{water}}, \tag{3.1.4}$$

where γ is the surface tension (Takamura et al. [2012]). This equation is being used to estimate the surface tension as very basic solvents are being tested. It is being assumed that the amount of NaI added is small enough that there should not be a large effect on the surface tension predicted.

Huang et al. [2013] investigated the effect of NaI concentrations on the surface tension of both glycerol and water, with concentrations ranging from 0.0 to 2.0 M. Plotting the ratio of the solutions with salt to the pure solvent between 0.0 to 2.0 M, the ratio of the surface tensions for glycerol went from 0.00 to 1.75 and was said to increase much less than pure water (Huang et al. [2013]). In the solutions tested in the present work, the amount of each NaI solution used at each conductivity is significantly less than that of both the glycerol and pure water used by Huang et al. [2013]. At 600 μS cm^{-1} for both the 67 and 156 cP solutions a concentration of 2.0 and 3.5 M were used, however for each solution this was diluted when added to the glycerol. Therefore, the concentration of

the actual solution tested will be smaller than the concentration added, due to dilution.

3.1.1.4 Dielectric constant

The dielectric constant was not measured directly but the values given in Association et al. [1963] were used, where Table 3.2 gives the values used from the paper. Association et al. [1963] does not give a dielectric constant value for 85% glycerol. Plotting the dielectric constant against $\%wt$ of glycerol as shown in Figure 3.2, the dielectric constant extracted from the line of best fit, gives a value of 49.97 at 85%.

% by wt of glycerol	Dielectric constant (20 °C)
30	71.77
70	57.06
80	52.27

Table 3.2: Dielectric constant for each % wt of glycerol

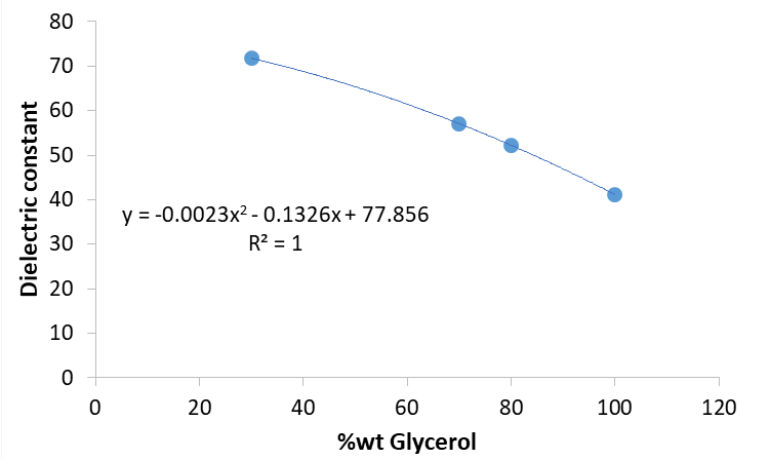

Figure 3.2: Dielectric constant against % wt of Glycerol.

3.1.1.5 Contact Angle

The contact angle was measured by initially taking images using a camera and a back light, making sure that the drops contact line and edges were clearly visible.

Droplets with a volume of 2 μL were deposited using a pipette, and it has been assumed that the droplets which are printed have got the same contact angle. The droplets were allowed to fully spread on the substrate before imaging, as this would happen to the droplets after being printed. The images were then processed using the contact angle plugin (Contact Angle.jar) in ImageJ® (Brugnara [2004-2006]), which required the image to be inverted 180 °. Points were selected on the edge of the droplet and the manual points procedure used to find the outline, before the contact angle was calculated.

3.1.1.6 Solution properties

Table 3.3 at the end of this chapter gives the masses of glycerol, water and NaI solution used to make each viscosity and conductivity solution tested, along with the liquid properties.

3.2 Electrospray experimental set-up and testing procedure

Nanoelectrospray tests were carried out using a borosilicate glass capillary/emitter (Fivephoton Biochemicals™) with a base outer diameter of 1.50 mm, and a wall thickness of 0.17 mm. The emitters had been pulled to a short taper. In these experiments emitters with an OD of 10, 20 and 40 μm were used, with a tolerance of 3 μm. The filled emitter was positioned inside a three way stainless steel swagelok® union with $\frac{1}{8}$ inch fittings, which was held in place using a vespel ferrule (SGE). Through the top of the three way union was a metal pin which was submerged in the liquid, where the top of the pin was positioned just above where the emitter started to taper.

Connected to the side of the three way union was a piece of tubing (PFA special tubing natural) which allowed pressure to be applied to the system. The three

way union was positioned and tightened in an acrylic arm which was connected to a Thorlabs manual translation stage (Thorlabs 0 to 25 mm). The manual stage allowed for vertical adjustment relative to the substrate, allowing the emitter-to-substrate distance (ESD) to be altered. The Thorlabs optical post (P300/M-∅ 1.5") was connected to a vibration table (Thorlabs-nexus) as any form of movement could cause the set-up to move which could affect the print.

Positioned directly underneath the emitter holder were two motorised stages to allow movement in the x and y direction (Thorlabs DDSM100 along with a TBD101 and KBD101 controller). The stages were connected to a computer where they were controlled by APT controller software. A silicon wafer (VIRGINIA SEMICONDUCTOR) was used as the substrate, and was cleaned with ultra pure water and isopropanol at the start of each experiment. The substrate was positioned on top of a plate which was fixed to the stages. A piece of foil was connected to the substrate to allow the transients to be measured. A crocodile clip was connected to the foil which was then connected to a current amplifier (Laser components, Femto DLPCA-200), where the gain was set depending on the magnitude of the measured current to either 10^6 or 10^7 V A^{-1}. The signal from the amplifier was sent into an oscilloscope (Tektronix, TBS 1064) where the traces could be observed and recorded.

The high voltage was applied to the metal pin submerged within the liquid via a crocodile clip, which was connected either to a single high voltage supply (FuG) or to the output from the high voltage switch (DEI PVX-4140 pulse generator). The high voltage switch required two high voltage power supplies, one to supply V_1 (base voltage or resting voltage) and the other to supply V_2 (ejection voltage). To pulse the voltage from V_1 to V_2 a square wave TTL signal trigger, with an amplitude of +5 V was applied to the gate of the switch where the rising edge caused the pulse in voltage. The square wave pulse was generated from a LabVIEW code, and output through a national instruments DAQ card (NI 6221) into a wave-function generator (TTi-TG2000 20MHz DDS), and into the gate of the high voltage switch. The wave-function generator was required because

the rise time straight from the DAQ card, was not fast enough to gate the high voltage switch.

An LED light source (PRIOR) or a constant strobe light (Opto engineering LTSCHP1W-W), along with a strobe controller (Gardasoft RT260F-20) were used for initial inspection of the emitter tip, the meniscus, and to visualise deposition onto the substrate. The light source was positioned on one side of the emitter and a CCD camera (JAI GO 5000m USB) with lens (Optem) was positioned directly opposite. The camera and lens were held on an x-y-z translation stage to allow imaging of the emitter at a range of distances from the substrate. Figure 3.3 shows a schematic of the set-up along with an image of the equipment.

3.2.1 Nanoelectrospray tests

The glass emitter was filled using a low/zero dead volume union, with a 2.5 mL syringe (Plastipak) connected to one end, and a piece of capillary feed (Polymicro technologies, TSP250350-AVVBO4A) connected to the other. Initially the solution was drawn up into the syringe and inverted before being connected to the union, where liquid was pushed (still inverted) out through the capillary feed. This was done to remove any air bubbles that could be trapped. The capillary feed was placed as far down into the emitter as possible while the liquid was being expelled from the syringe. While the solution was being expelled, the capillary feed was being slowly withdrawn until a 3.0±0.1 cm head height marker on the emitter was reached. The length of the emitters ranged from 4.0±0.1 cm to 5.5±0.1 cm, therefore 3.0 cm was chosen to fit with the constraints of the emitter length, to make sure there would be enough solution to perform the pulsation and printing tests, as well as to have a consistent starting height of liquid throughout. The same metal pin was used for each test which displaced the liquid to a height of 4.0 to 4.4±0.1 cm. Once filled the emitter was tightened into the union as described in Section 3.2. A syringe was

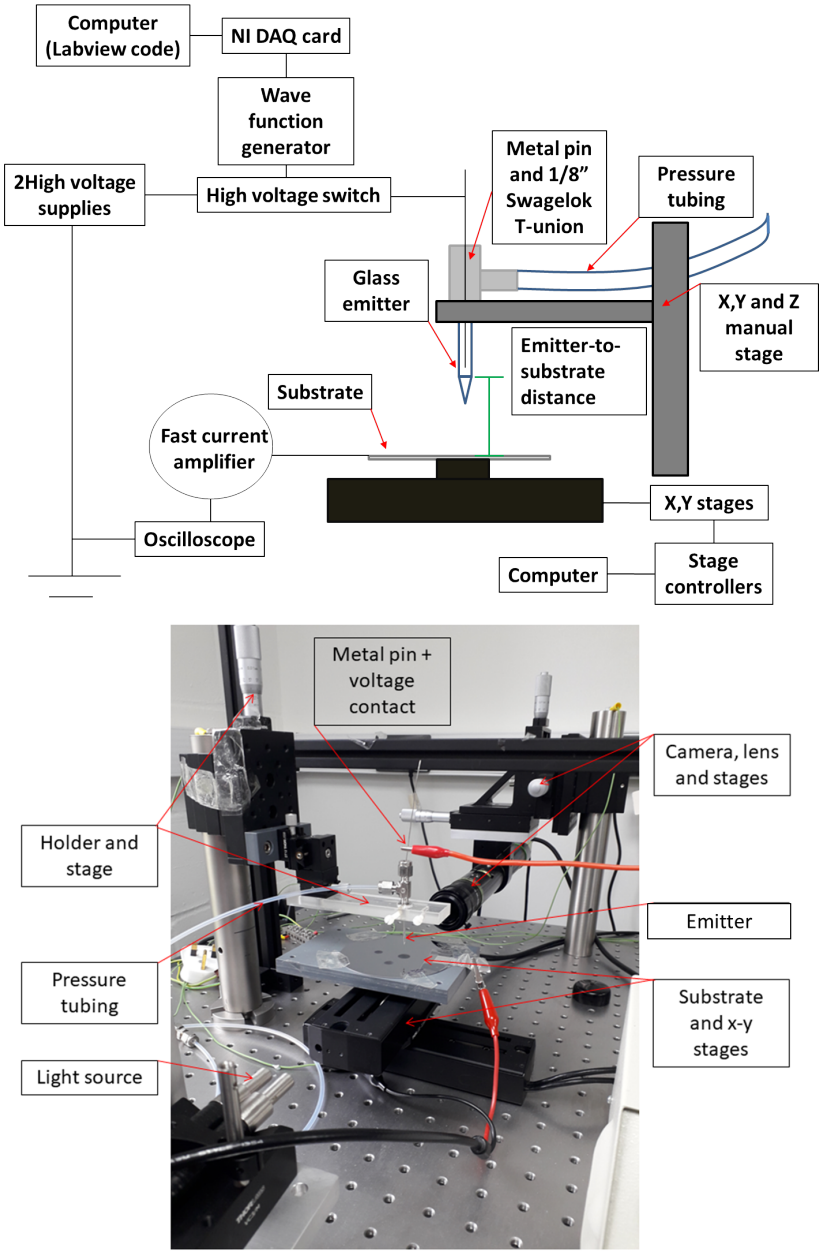

Figure 3.3: Schematic and image of experimental set-up.

placed on the end of the pressure tubing to force through a few drops to remove any possible air bubbles. The syringe was then removed, otherwise an unknown pressure would be applied to the system. The union was then placed into the holder and the connections made as described above. Before tests were performed the emitter was examined and liquid sprayed to check there were no blockages.

3.2.1.1 Natural pulsations

Natural pulsations were recorded mainly at an ESD of 1.0±0.1 cm, where this distance was not set using the camera but was measured manually using a ruler. This distance was chosen because the pulsations were recorded above a stationary substrate, which caused a thin non-uniform layer of liquid to build-up over time. It was assumed that due to the thickness of the build-up of liquid being much smaller than the ESD, at no more than approximately 500 μm, there should be little effect on the gap size and therefore the magnitude of the field strength. The voltage from the back of the power supply was connected directly to the metal pin submerged in the solution. The voltage applied had a positive polarity, therefore measuring positively charged ions. The voltage was slowly increased until the first irregular ejections were observed on the oscilloscope, this was taken as the onset voltage and used to calculate V_1. The voltage was slowly increased and traces of the pulsations recorded until cone-jet mode was entered or before discharge. Figure 3.4 shows an example of the transients at a range of voltages, where it shows an increase in the pulsation frequency with voltage, until cone-jet mode was entered.

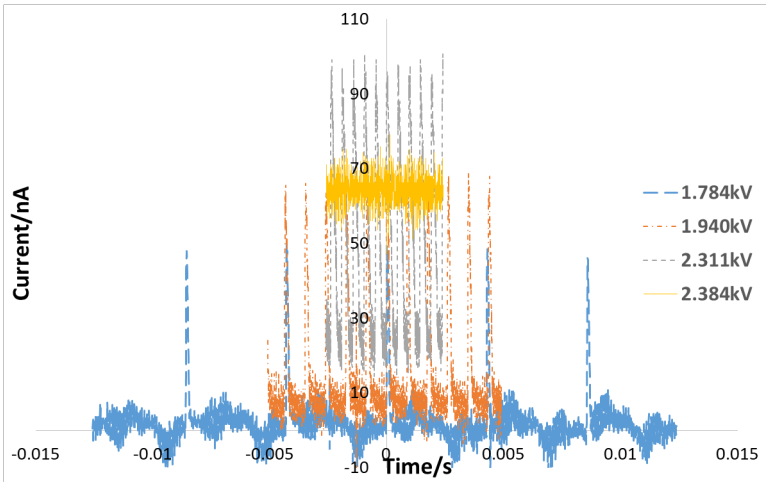

Figure 3.4: Natural pulsations and cone-jet mode with applied voltage.

Using a 60 cP solution at 6 μS cm^{-1} on a 40 μm emitter, the pulsations were recorded at a range of ESDs from 1.0±0.1 cm to 205 μm. The ESD was set by using markers that had been applied to the computer monitor at a range of

distances, with a zero position for the substrate. The lens was set to a constant magnification and the markers were used for positioning the substrate and emitter during the experiments to provide a rough positioning. A small amount of liquid was deposited onto the substrate or the previous ESD deposit was used to allow the substrate to be visible and positioned (Figure 3.5), before being moved for the next set of tests. An image was captured for each experiment to accurately measure the ESD. At the same magnification as the experiments were recorded, an image was taken of a graticule with a line of width 0.076 mm (76 μm). This image was processed in ImageJ® and the number of pixels making up the line was measured as this was needed for calibrating each image. Setting the scale in ImageJ® by using the number of pixels and 76 μm, the number of pixels per μm were calculated, this allowed the ESD to be measured directly in ImageJ® giving the distance in μm.

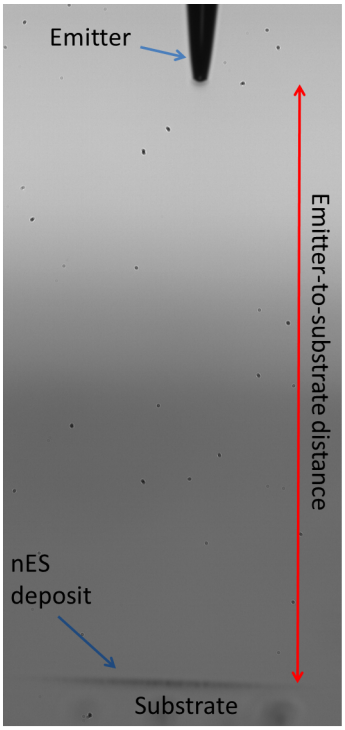

Figure 3.5: Emitter-to-substrate distance measurements below 1.0±0.1 cm.

It should be noted that at each ESD in the natural pulsations the current transients were recorded using a stationary substrate, at distances of 1100 μm and below there was a build-up of a spherical droplet when recording the

current transients. Liquid accumulation could potentially cause variation in the structure and magnitude of the electric field which can intern affect the flow rate, especially at smaller ESD values of a few hundred microns, and at higher voltages close to cone-jet mode. To minimise the effect that a build-up would have on the field strength, the current transients were measured as soon as the pulsations on the oscilloscope were stable. Before the next voltage was applied, the stage was moved to a new position, the power supply turned on to quickly recorded the transients before a substantial build-up could occur.

Printing in the natural pulsations used the same method as above, with the main difference being that once the voltage had been set on the power supply, the stage was moved at a continuous speed of 50 mm s^{-1}, allowing the drops to be deposited separately on the substrate. At the start of each test, before moving the stages the voltage was turned on to record a current transient as discussed above, which could be used later to compare the transient with the actual printed droplets. Transients could not be recorded during printing as the movement of the stage increased the noise picked up by the amplifier reducing the quality of the current transients. The main reason for this was to understand the effect of the ESD on pulsation behaviour, also to compare the values calculated from the pulses from the current transients recorded in relation to the actual droplets deposited.

3.2.1.2 Pulsed voltage operation

Initially pulsed voltage operation was performed using a stationary substrate at an ESD of 1.0 cm. The onset voltage as discussed in Section 3.2.1.1 was used to calculate V_1 which was set to 5% below the onset voltage. The voltage at which the natural pulsations were recorded was used as a guide for setting V_2, where V_2 was set to be a few hundred volts above onset to allow the initial voltage pulse to enter cone-jet mode (if the parameters of the set-up allowed this). Each voltage pulse was investigated using a single pulse where the voltage switch was pulsed

by manually running the LabVIEW program. The TTL signal was initially set to a frequency of 100 Hz and a duty cycle of 50% unless stated otherwise. The V_2 voltage was slowly decreased and transients recorded until only natural pulsations were observed, as shown by the example in Figure 3.6. The V_2 value as shown by Figure 3.6c was the condition classed as the highest voltage that could be pulsed to achieve only natural pulsations.

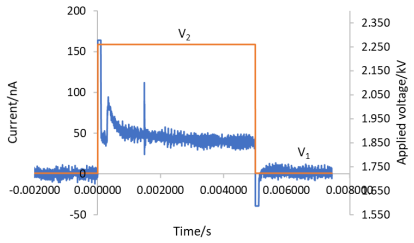

(a) Cone-jet mode switching, V_2=2.260 kV.

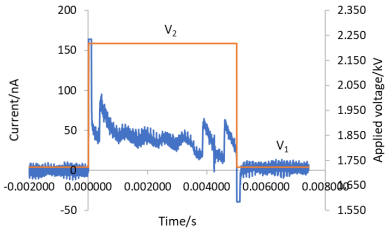

(b) Cone-jet mode then pulsations, V_2=2.218 kV.

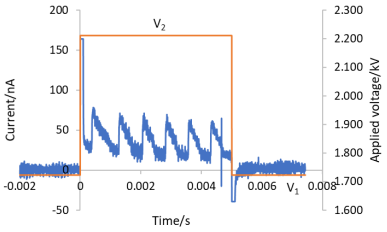

(c) Pulsations, V_2=2.211 kV.

Figure 3.6: Example of the effect of reducing V_2 on the current transient observed when V_1=1.723 kV.

In a limited number of conditions when reducing the V_2 voltage pulsations were observed before cone-jet mode, Figure 3.7 shows an example of a condition in which this was observed. However, V_2 was still reduced to find the condition when only pulsations were observed at a frequency of 100 Hz and duty cycle of 50 % unless stated otherwise, this was done to have a consistent condition for the highest V_2 voltage.

The frequency and the duty cycle were then altered to isolate a single reproducible ejection, as shown in Figure 3.8. At each ESD once the highest voltage for pulsations had been measured, V_2 was slowly decreased and the frequency and duty cycle altered to still achieve a single ejection, until there were no ejections observed when the frequency was again 100 Hz and the duty cycle at 50%.

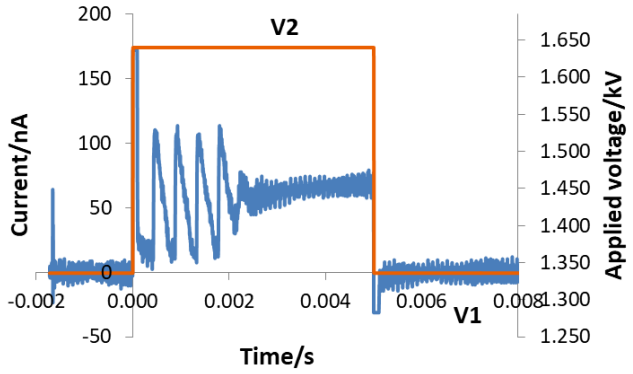

Figure 3.7: Example of the effect of reducing V_2 when pulsations are observed before cone-jet mode, V_1= 1.336 kV and V_2= 1.640 kV.

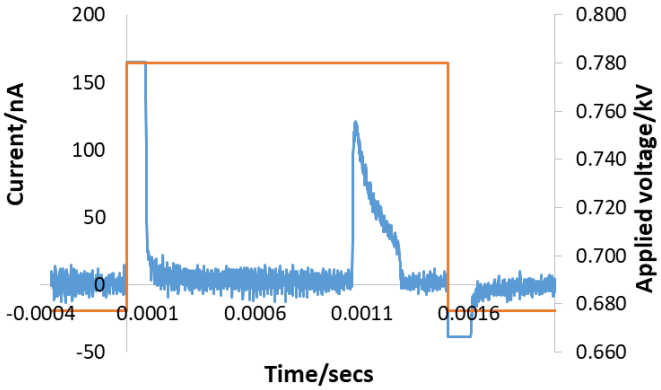

Figure 3.8: Single ejection transient, V_1= 0.677 kV and V_2= 0.780 kV.

The ESD was altered using the method described in Section 3.2.1.1, where at each ESD the same process of varying V_2 was performed to observe the effect of the voltage magnitude on the ejection process and on isolating a single ejection. A stationary substrate was also used at an ESD of 1447±2 μm and 1095±2 μm, as it was clear from visualising the substrate with the camera that only a thin layer of liquid was built-up after multiple pulsed voltage events, Figure 3.5 shows an example of this. It was therefore assumed as with 1.0 cm that this would have little effect on the field structure and strength.

At an ESD of 504±2 μm and below, when measuring the onset voltage a deposit was sometimes observed on the substrate but not observed on the oscilloscope. This could be due to the onset voltage being taken as the first irregular ejection observed, and possibly being too quick at such a short distance to observe on

the oscilloscope at the same time as monitoring the physical image. Therefore, the onset was taken from the time the first small deposit was observed from the image from the camera.

At 504±2 μm and below the build-up on the substrate was monitored carefully as this was where multiple ejections could produce a spherical droplet. If the size of the droplet was becoming significant the substrate was moved to a new position. The same voltage was pulsed to check the ejection process was not affected by the build-up, or if the substrate had already been moved the voltage was reduced to record the next ejection process.

If the ESD was small enough, and an individual drop was observed on the substrate, the highest V_2 voltage for pulsations was found and the frequency and duty cycle altered to isolate a single ejection. A row of 10 drops were deposited, where the stages were moved a set distance of 50 or 100 μm between each ejection, as this was the minimum distance to consistently separate neighbouring droplets. After printing the substrate was removed and imaged using a Nikon ECLIPSE LV150N microscope to determine whether the maximum ESD had been found, also to avoid large amounts of evaporation between printing and imaging. In pulsed voltage operation the drops were printed and imaged within no longer than 15 minutes. The printed deposits showed different characteristics depending on the ESD and other process parameters, as to whether the jet had broken-up into a spray or not.

As discussed in Section 2.3.5.2 the mode in which the jet breaks-up (varicose or whipping) is important to the production of the droplet especially in relation to high resolution printing. In these experiments the jet was not imaged due to not having the required high speed camera and light system to gain clear visualisation of the jet. A few assumptions have been made during the printing process and how the droplets were produced:

- If there was a non-uniform area of dispersed droplets produced as in Figure

3.9, it was assumed that the jet had broken-up into a spray before reaching the substrate.

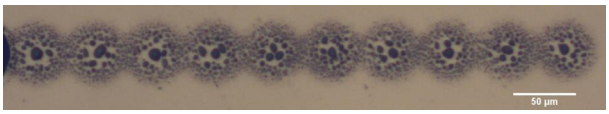

Figure 3.9: Uniform spray area.

- If there was a droplet in the centre with droplets around the edge, then the jet had possibly broken-up into a spray and the central drops coalesced as shown in Figure 3.10.

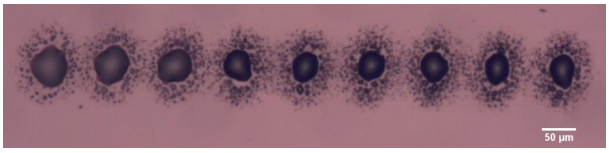

Figure 3.10: Central droplet with a large amount of satellite droplets.

- If there were droplets to one side of a single deposit then it was assumed that this could be from a form of whipping of the jet, as shown in Figure 3.11, due to the small amount of satellite droplets to one side this condition was taken as the maximum ESD.

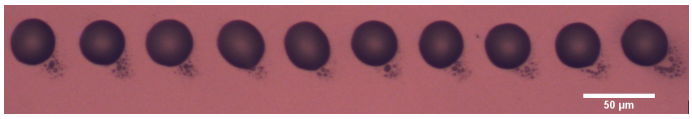

Figure 3.11: Central droplet with satellite droplets on one edge.

- If there was a discrete drop as in Figure 3.12 then the jet either impinged the substrate, or a varicose ejection produced the droplet.

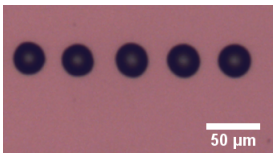

Figure 3.12: Discrete droplets.

After finding the position for the maximum ESD the distance was reduced to 191±1 μm and 82±2 μm. These ESDs were selected because they were close enough to print a discrete drop as shown in Figure 3.12 for majority of the range of variables tested. Starting from the maximum V_2 voltage a row of 5 to 10 drops were printed moving the substrate between each drop and recording the current transient for each ejection event. The V_2 voltage was then reduced using the method described for other ESDs, where a row of discrete droplets was printed at each voltage.

3.2.2 Test analysis

This section discusses how the data has been analysed, by either using the current transient or from the droplets printed onto the substrate.

3.2.2.1 Natural pulsations-Constant voltage

Current transients

Figure 3.13 shows an example current transient for the natural pulsations, where t_{p1} and t_n refer to the time at the peak of the first pulse, and the time at the peak of the last pulse. If n is the number of pulses from t_{p1} to t_n, the frequency is calculated using

$$f = \frac{1}{(t_n - t_{p1})/(n-1)}. \tag{3.2.1}$$

The average current (I_{ave}) measured from the current transients is also shown in Figure 3.13, where this has been calculated from averaging the current values between t_{p1} and t_n, and is given by Equation 2.3.4. The current during liquid ejection (I_{on}) has been calculated from integrating under the pulse between t_1 and t_2, and is given by Equation 2.3.5. The current during the off-time (I_{charge}) has been calculated from integrating under the transient between t_2 and t_3, and is given by Equation 2.3.6. In some conditions the current at the base of the

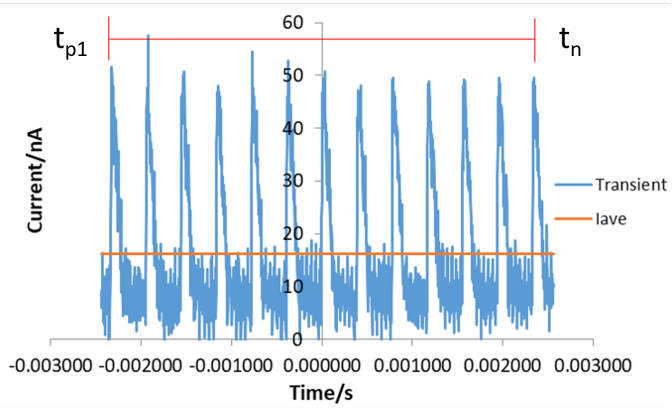

Figure 3.13: Transient of pulsations showing the measurement of the frequency.

ejection (I_{base}) was non-zero, to account for this in the calculation of the on-time (τ_{on}), Equation 2.3.3 was used as the criteria for when liquid was ejected.

The data output from the oscilloscope was in the form of a .csv file which consisted of the settings on the oscilloscope, along with two columns of data made up of 2500 data points, with one column for the time values and the other the amplitude/voltage. For each applied voltage the data points making up four pulses were saved into new separate .csv files, making sure that there were data points before the start and end of the pulsation. This was to ensure the entire pulse was captured. A MATLAB® code was developed to analyse the transients where the data was run through processing a single applied voltage condition at a time.

The original oscilloscope data was run through the code where the criteria given by Equation 2.3.3 was used in relation to the voltage, using V_{peak} and V_{base}, where I_{peak} was calculated by dividing the voltage by the amplification (V A^{-1}). Starting from V_{peak} the MATLAB® program examined the data to find the start and end of the pulse, where these times were termed t_1 and t_2 as shown in Figure 3.14, and were used to calculate the on-time.

Using the positions of t_1 and t_2 each of the voltage values between were converted to current as described above, and the data point numbers converted to the corresponding time values from the original .csv file. The trapezium method

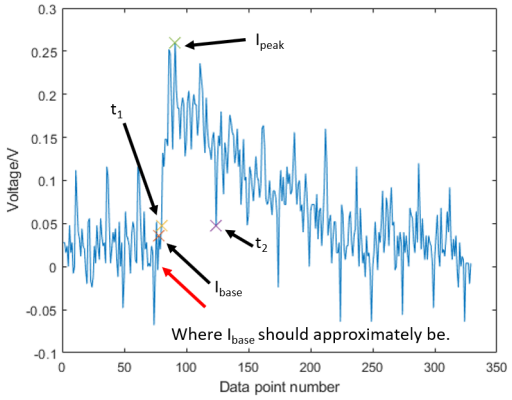

Figure 3.14: Original current transient pulse and positions required for calculating the on-time and ejected charge.

was then used to integrate between t_1 and t_2 to calculate the ejected charge (q). Figure 3.15 shows the original data along with the part of the pulse that was integrated. The charge was divided by the on-time to calculate I_{on}, which was then used along with the scaling laws to calculate the average flow rate through the jet, and therefore the ejected volume. The drop volume has been calculated from

$$v_{\text{transient}} = Q_{\text{jet}} \tau_{\text{on}}, \tag{3.2.2}$$

where $v_{\text{transient}}$ is the volume from the current transient.

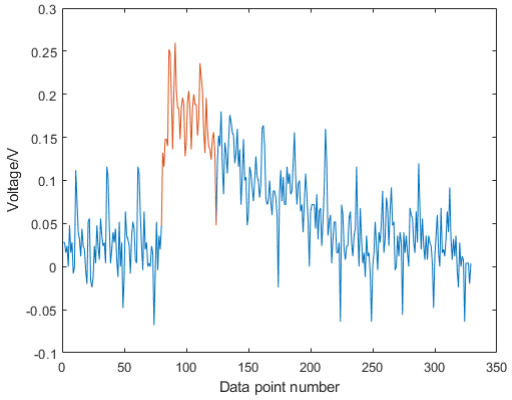

Figure 3.15: Original trace along with an overlap of where the transient was integrated under to calculate the charge and therefore I_{on}.

Figure 3.14 shows an example of a pulse where a substantial amount of noise was picked up by the amplifier. To remove the issue of noise on finding positions within the trace to calculate the on-time and charge, the original

current transient was smoothed using Savitzky-Golay filtering. Two smoothing techniques were tested, this method and using a moving average. Using the Savitzky-Golay filtering gave more control over the amount of smoothing by altering the number of data points smoothed over, along with the polynomial of the smoothing. The values varied depending on the trace from 10 to 21 data points, and a polynomial of 2 to 8. This depended on the number of data points that made up the pulsation event. At lower frequencies due to a short on-time there were far fewer data points making up the pulse, approximately 10 to 12 compared to higher frequencies which consisted of more than 50 data points. This meant at lower voltages a smaller number of data points and a larger polynomial were required. Plotting the smoothed trace on top of the original transient as shown in Figure 3.16 meant that the amount of smoothing could be monitored, making sure that the majority of the original transient shape was kept.

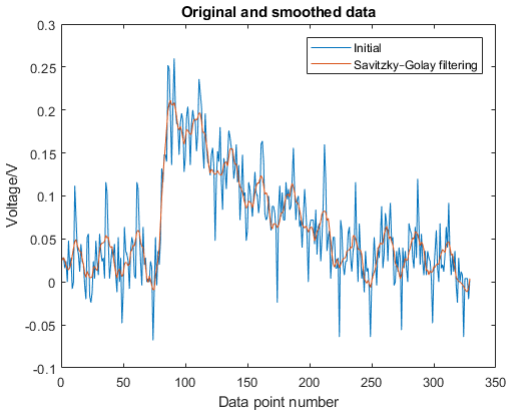

Figure 3.16: Original and smoothed data using Savitzky-Golay filtering.

The smoothed trace was used to find positions t_1 and t_2, then the original trace was used to calculate the charge and current a described above. Figure 3.17 shows the original trace overlapped with the part of the trace where the integration took place. Comparing Figure 3.17 to Figure 3.15 it shows that by smoothing the data to find the positions for the on-time, more of the transient gets captured, giving a more accurate representation of the pulsation event, and therefore better calculation of parameters.

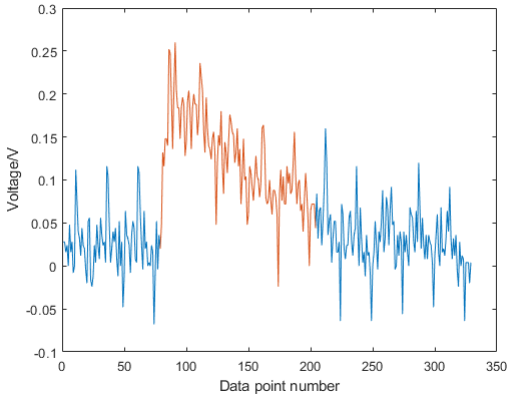

Figure 3.17: Original trace along with an overlap of where the transient was integrated under to calculate the charge and therefore I_{on}, where the positions were found using the smoothed data.

Printed droplets

From observations of printed droplets on the substrate, the frequency can be calculated from knowing, the speed of the stage and the distance between consecutive deposits, where the distance is shown in Figure 3.18. The frequency from the printed drops was calculated from measuring the distance between 20 to 40 drops, with the larger number of measurements being from higher voltages due to smaller spacing. The average distance was calculated for each of the voltage conditions, where this distance was used with the stage speed to calculate the time/frequency using Equations 2.4.1 and 2.4.2. The printed drop volume was calculated using the spherical cap equation given by Equation 2.4.9, where the diameter of each drop was measured in ImageJ®, and each image was initially calibrated using the method given in Section 3.2.1.1 for each magnification.

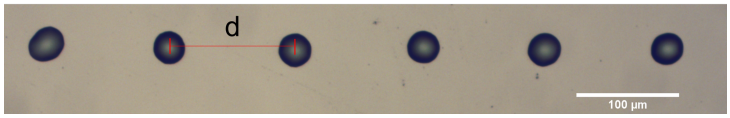

Figure 3.18: Measuring the distance between the printed droplets to measure the pulsation frequency.

3.2.2.2 Pulsed voltage operation

In pulsed voltage operation the current transients were also analysed but this time using a different inbuilt MATLAB® code, as in pulsed voltage operation the time for the first ejection (formation time) needed to be measured. As with the natural pulsations when a constant voltage was applied, the transients were analysed in relation to the original voltage data from the oscilloscope, and converted to current where required for the charge and current values. The main parameters to indicate are the top of the initial square pulse, which is where the voltage pulse was initiated, I_{peak}, I_{on} and the positions for determining the on-time of the pulse.

Figure 3.19 shows a pulsed voltage example, where the transient has not been smoothed. Figure 3.19a shows the positions used for calculating the on-time and therefore the charge ejected and I_{on}. To calculate the on-time Equation 2.3.3 was modified where the criteria for the falling edge of the pulse and liquid ejected was given when

$$I > 0.15(I_{\text{Peak}} - I_{\text{Base}}) + I_{\text{Base}}. \tag{3.2.3}$$

The reason that the falling edge has now been taken as 0.15 rather than 0.25, is because on the falling edge of the pulse it does not show a recharging current before the next ejection, especially when a single pulse was isolated as shown in Figure 3.19, and in some conditions taking 0.25 did not capture a lot of the transient. The flow rate and volume were then calculated using the same method as described for pulsations. Figure 3.19a shows that I_{base} is slightly higher than the base of the pulse and that t_2 has been taken from the noise of the transient rather than from the main part of the pulse.

Figure 3.19b highlights where the data has been integrated to calculate the charge ejected. Due to the position of t_2 it is shown that a large proportion of the pulse is missed in the calculation. To overcome the issue of t_2 being taken from the noise, the trace was smoothed. Figure 3.20 shows the smoothed data along with

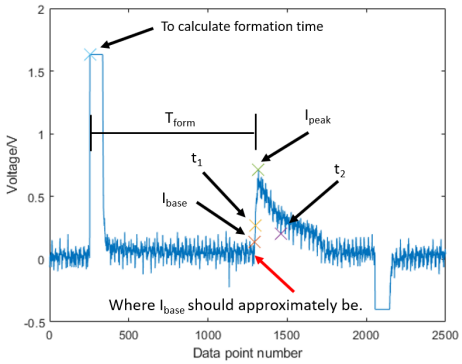

(a) Original current transient and position of points for calculations.

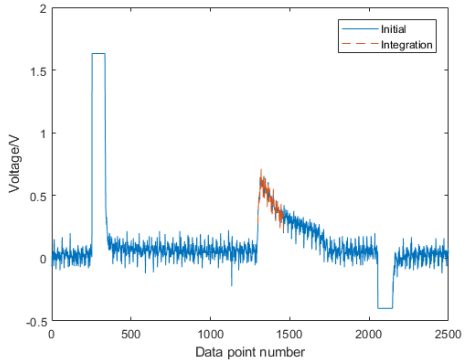

(b) Showing the original trace along with an overlap of where the transient was integrated under to calculate the charge and therefore I_{on}.

Figure 3.19: Analysing pulsed voltage data using MATLAB® when the current transient has not been smoothed.

where the data was integrated to calculate the charge. Compared to Figure 3.19b, Figure 3.20b shows that from using the smoothed trace, to find the positions of t_1 and t_2 more of the transient is captured in the calculation of the charge.

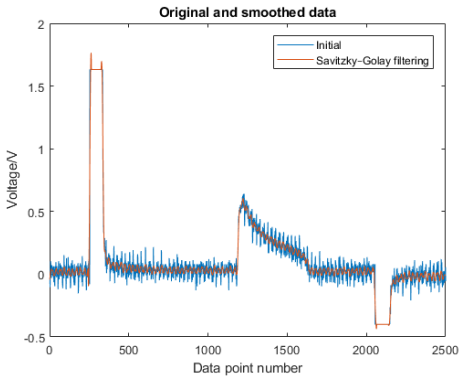

(a) Original and smoothed data using Savitzky-Golay filtering.

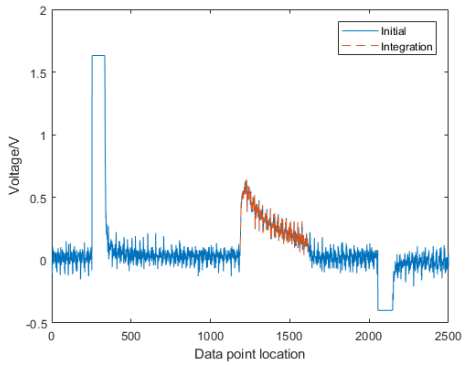

(b) Showing the original trace along with an overlap of where the transient was integrated under to calculate the charge and therefore I_{on}.

Figure 3.20: Analysing pulsed voltage data using MATLAB® when the current transient has been smoothed.

3.3 Error analysis

This section shows the methods used to calculate the errors throughout the results sections of this thesis. When multiple measurements have been taken the standard error has been calculated using

$$S = \frac{\sigma}{\sqrt{n_d - 1}}, \tag{3.3.1}$$

where σ is the standard deviation and n_d is the number of measurements. This includes parameters such as the current, on-time, flow rate, emitted charge, the frequency and multiple measurements for making the solutions. If there are two measurements then the error has been calculated by taking the difference between the two values and halving it.

For calculations where the value has been calculated from two measurements, for example the volume from the transients, which is calculated from Q_{jet} and τ_{on}, the error has been calculated using

$$|\frac{\delta a}{a}| = \sqrt{\left(\frac{\delta b}{b}\right)^2 + \left(\frac{\delta c}{c}\right)^2}, \tag{3.3.2}$$

where in this example a=$v_{\text{transient}}$, b=Q_{jet} and c=τ_{on}.

The errors for the physically printed droplets have been calculated by using the spherical cap equation (Equation 2.4.9) and taking partial derivatives with respect to r_b and θ. The error in the volume of the droplet is given by

$$\delta v = \sqrt{\left|\frac{2}{r_b}\delta r_b\right|^2 + \left|\left(\frac{-\sin\theta}{(2+\cos\theta)} + \frac{2\sin\theta}{(1-\cos\theta)} - \frac{3}{\sin\theta}\right)\delta\theta\right|^2}. \tag{3.3.3}$$

Errors have been included in the graphs where possible, in majority of cases an error bar is not visible because the magnitude of the error is smaller than the data point.

Solution	Mass of glycerol (g)	Pure water (g)	NaI + water (g)	μ (cP)	K (μS cm^{-1})	ρ (kg m^{-3})	γ (mN m^{-1})	Contact angle $^\circ$
2.5 cP - 6 μS cm^{-1}	6.4401 ± 0.0011	12.0222 ± 0.0066	2.8622 ± 0.0393 (0.00007 M)	2.482 ± 0.017	5.93 ± 0.31	1073 ± 1	68.16*	44.78 ± 2.17
2.5 cP - 60 μS cm^{-1}	6.4412 ± 0.0057	14.4847 ± 0.0308	0.3228 ± 0.0302 (0.07 M)	2.454 ± 0.005	55.3 ± 1.4	1073 ± 1	68.16*	48.22 ± 1.72
2.5 cP - 600 μS cm^{-1}	6.4160 ± 0.0001	10.4464 ± 0.0002	4.4759 ± 0.0002 (0.07 M)	2.559 ± 0.001	617 ± 1	1075 ± 1	68.16*	57.44 ± 0.48
23 cP - 6 μS cm^{-1}	11.6742 ± 0.0001	3.3605 ± 0.0002	1.6135 ± 0.0002 (0.007 M)	23.04 ± 0.01	6.32 ± 0.01	1181 ± 1	66.15*	33.65 ± 0.18
23 cP - 60 μS cm^{-1}	23.3522 ± 0.0111	6.5474 ± 0.0029	3.4039 ± 0.0063 (0.07 M)	22.67 ± 0.04	55.7 ± 1.3	1182 ± 1	66.15*	46.03 ± 1.29
23 cP - 600 μS cm^{-1}	11.6580 ± 0.0001	2.6634 ± 0.0002	2.4448 ± 0.0002 (0.7 M)	24.01 ± 0.02	594 ± 1	1194 ± 1	66.15*	48.13 ± 0.34
60 cP - 6 μS cm^{-1}	20.0273 ± 0.0155	4.3810 ± 0.0008	0.5952 ± 0.0019 (0.07 M)	59.75 ± 0.59	5.81 ± 0.29	1209 ± 1	65.20*	46.84 ± 1.23
60 cP - 60 μS cm^{-1}	20.0184 ± 0.0073	4.2652 ± 0.0029	0.7469 ± 0.0007 (0.7 M)	60.03 ± 0.02	61.0 ± 0.7	1211 ± 1	65.20*	45.76 ± 1.54
67 cP - 600 μS cm^{-1}	19.9333 ± 0.0001	1.9790 ± 0.0002	3.7200 ± 0.0002 (2.0 M)	67.15 ± 0.07	595 ± 1	1239 ± 1	65.20*	35.10 ± 0.98
111 cP - 6 μS cm^{-1}	28.3197 ± 0.0001	3.6646 ± 0.0002	1.2951 ± 0.0002 (0.07 M)	111.0 ± 0.01	6.14 ± 0.01	1222 ± 1	64.73*	35.06 ± 0.88
111 cP - 60 μS cm^{-1}	28.3723 ± 0.0040	3.1445 ± 0.1653	1.9567 ± 0.1797 (0.7 M)	110.0 ± 1.2	61.87 ± 1.42	1227 ± 1	64.73*	48.26 ± 0.51
156 cP - 600 μS cm^{-1}	28.3182 ± 0.0001	0.0000 ± 0.0002	6.9122 ± 0.0000 (3.5 M)	156.3 ± 0.1	575 ± 1	1290 ± 1	64.73*	

Table 3.3: Solution properties for glycerol, water and NaI solutions.

4

Comparison of transients and deposits

This chapter is going to briefly discuss the link between the pulsations from the current transients and actual deposited droplets, and compare how well the calculated values of frequency, flow rate and volume from the current transients relate to the physical measurements.

4.1 Pulsation frequency

Comparing the pulsation frequency between the transients and the physical droplets is discussed in this section, the method for this was described in Chapter 3, Section 3.2.1.1. Figure 4.1 shows droplets printed at an emitter-to-substrate distance (ESD) of 205 μm at a range of applied voltages, where the stage was moved at a speed of 50 mm s^{-1}. Figure 4.1 shows that as the voltage increases the distance between the printed drops decreases and therefore the frequency increases.

Transients were measured above a stationary substrate as discussed in Section 3.2.1.1 for each of the applied voltages that were printed, and have been analysed using the method discussed in Section 3.2.2.1. Figure 4.2 shows how the frequency from the transients compares to the printed drops. The frequency from the current transients was calculated over four or more pulsations. The error has been measured over four individual pulses and the percentage error of the average readings calculated, with the maximum error being around 1%. The errors in Figure 4.2 are within the data points.

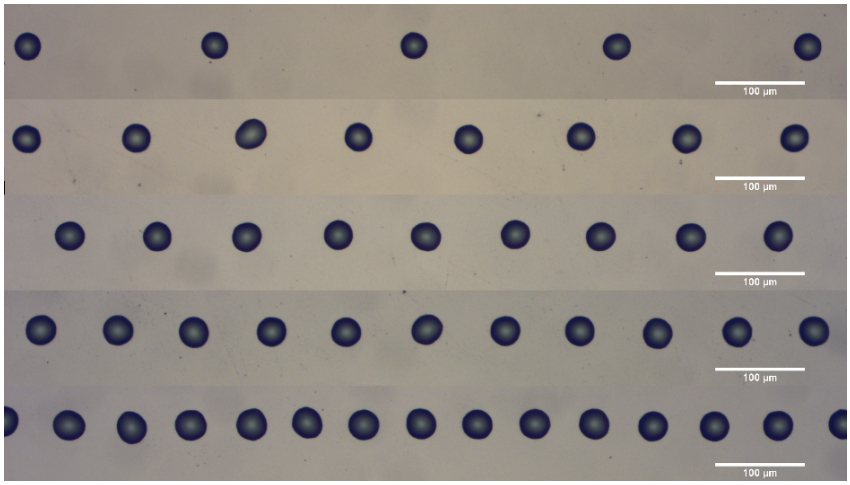

Figure 4.1: Droplets of glycerol and water at 60 cP, 6 μS cm^{-1} on a 41.97 μm emitter, printed at an emitter-to-substrate distance of 205 μm. Applied voltages from the top are V = 1.082, 1.091, 1.102, 1.111, 1.130 kV, with a stage speed of 50 mm s^{-1}.

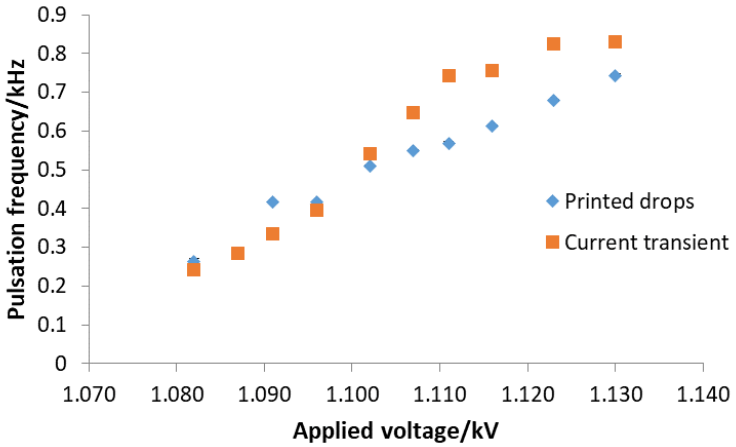

Figure 4.2: Pulsation frequency against applied voltage at an emitter-to-substrate distance of 205 μm, using a 60 cP solution, at 6 μS cm^{-1} and 41.97 μm emitter.

Figure 4.2 shows good correlation between the pulsation frequency measured from the transients and printed drops up to a voltage of 1.111 kV, after this the pulsation frequency from the transients increases slightly, which could suggest that the build-up is becoming substantial enough to increase the field strength and therefore the flow rate, where both of these would cause an increase in the pulsation frequency. To minimise the amount of build-up the transients were recorded as soon as they were stable. For the printed deposits, the stage was moving, therefore avoiding drop coalescence and build-up.

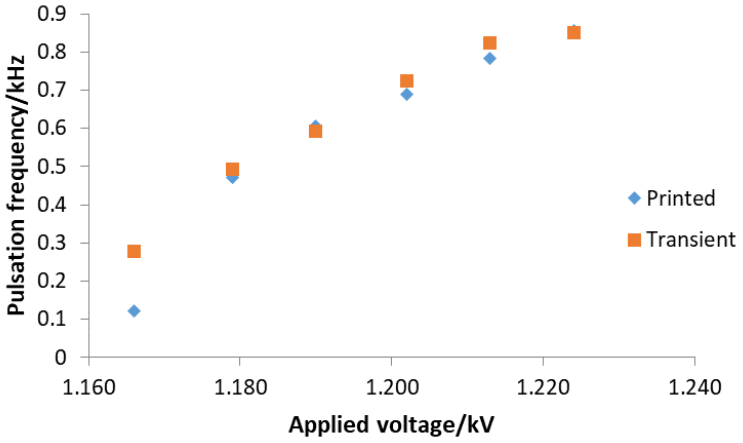

Figure 4.3: Pulsation frequency against applied voltage at an emitter-to-substrate distance of 295 μm, using a 60 cP solution, at 6 μS cm^{-1} and 41.97 μm emitter.

Figure 4.3 shows another example of comparing the current transient frequency over a stationary substrate, with those from individual printed droplets at an ESD of 295 μm. Results show that the frequency from the current transients are in agreement with those from the printed droplets, this suggests that by being further away from the substrate the transients can be recorded without the build-up having an effect on the field strength, by using the measures discussed in Section 3.2.1.1. This therefore confirms Equation 2.4.2, as the time between deposits is the same as the time between ejections calculated from the transients.

4.2 Droplet evaporation

In these experiments the drop volumes from the physically printed droplets have come from imaging the drops from above as shown in the previous section, and using Equation 2.4.9 for the volume of a spherical cap. In Section 3.1 it was discussed that glycerol was used to vary the viscosity, because it would leave a deposit on the substrate which could be imaged. However, between the time of printing the droplets and the time of imaging, it is understood that there will be some form of evaporation.

A simple approximation for the evaporation of sessile droplets with a pinned

contact line is given by

$$-\frac{\mathrm{d}m}{\mathrm{d}t} = \pi r_d D(1 - RH)c_v(0.27\theta^2 + 1.30), \tag{4.2.1}$$

where D is the diffusion coefficient, RH is the relative humidity, θ is the drop contact angle, and c_v is the vapour concentration (Hu and Larson [2002]). The rate of change of volume is given by

$$-\frac{\mathrm{d}v}{\mathrm{d}t} = -\frac{\mathrm{d}m}{\mathrm{d}t}\frac{1}{\rho}. \tag{4.2.2}$$

The vapour concentration has been calculated from

$$c_v = \frac{MP_v}{R_G T}, \tag{4.2.3}$$

assuming that the ideal gas law is obeyed, where M is the molecular weight, P_v is the vapour pressure, R_G is the gas constant and T is the temperature in Kelvins (Erbil [2012]). Table 4.1 gives the values for glycerol and water used in Equation 4.2.3.

Properties at 20°C	Water	Glycerol
M (g mol^{-1})	18.02 [a]	92.1 [b]
P_v (Pa)	2340[a]	0.020 [b]
D (m^2 s^{-1})	2.61x10^{-5} [c]	9.00x10^{-5} [b]

Table 4.1: Properties of water and glycerol. References: a=Harrison and Ellis [1984], b=Ray et al. [1991] and c=Hu and Larson [2002].

The average relative humidity at which these experiments were performed is 42±2%, and the average initial contact angle is 44.04±2.34°. A range of volumes from 0.20 to 9.00 pL are being considered to estimate the evaporation time as this is the volume range over which drops were printed. The approximate drop diameters printed for these volumes are 14 μm at 0.20 pL, 26 μm at 2.00 pL, 36 μm at 4.00 pL, and 46 μm at 9.00 pL. Using Equation 4.2.1, Table 4.2 gives the estimates for the evaporation rates for a droplet of water and glycerol at each

of the drop diameters. Table 4.2 shows that the evaporation rate of water is several orders of magnitude larger than that of the glycerol, therefore it is being assumed that during the time between printing and imaging, the water will have evaporated from each droplet leaving only the glycerol on the substrate.

Droplet diameter/μm	Water/pL s^{-1}	Glycerol/pL s^{-1}
14	8.45	$1.04x10^{-4}$
26	15.7	$1.87x10^{-4}$
36	21.7	$2.59x10^{-4}$
46	55.5	$3.30x10^{-4}$

Table 4.2: Estimates for the evaporation rate for drops of water and glycerol at a range diameters.

After the water has evaporated, assuming that the droplet has a pinned contact line, the contact angle will reduce. Hu and Larson [2002] showed that at a contact angle less than 40°, the evaporation rate was relatively constant. Using the evaporation rates for a droplet of pure glycerol in Table 4.2, Figure 4.4 shows the estimated time it should take for a given %wt of glycerol to evaporate from the substrate, where the % was taken from the initial volume. It is shown that the 0.20 pL droplet has the smallest evaporation times between 10 and 28 minutes. This suggests that a 30% glycerol droplet might have evaporated before being imaged. Figure 4.5 shows an example of printed droplets with a 30% glycerol content, where the average volume measured was 0.070±0.003 pL. Figure 4.5 clearly shows that after no longer than 13 minutes the droplets are still visible and have only slightly unpinned at a few points around the edge of the droplets. This suggests that Equation 4.2.1 gives an underestimate for the evaporation time. However, evaporation is a complex process and from these experiments there are too many unknowns, such as how the height of the drop/volume, contact angle and humidity around the drop change during the evaporation process to have a more accurate estimate of the total evaporation time. All of the other volumes at 30% glycerol have evaporation times greater than 53 minutes. This suggests that even with a glycerol content of 30%, there should be little evaporation of the

glycerol left on the substrate between printing and imaging, which should give a relatively accurate calculation of the ejected volume.

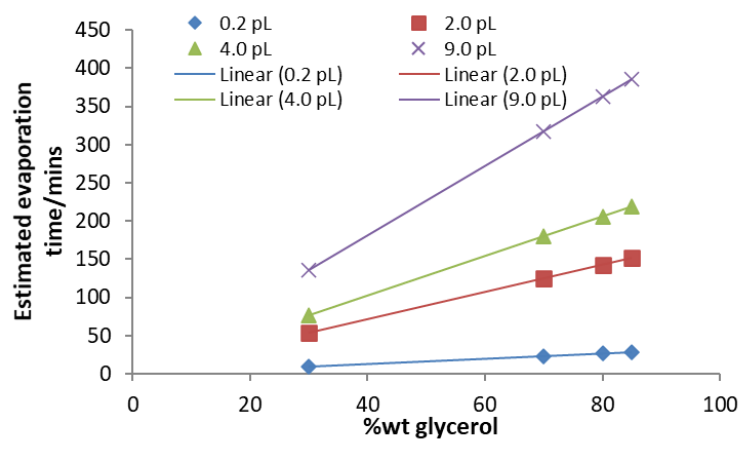

Figure 4.4: Estimation of evaporation times against %wt glycerol, where the amount of glycerol to evaporate is the percentage of the initial volume given.

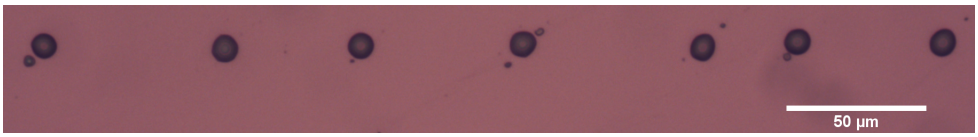

Figure 4.5: Printed glycerol and water droplets at 2.5 cP, 60 μS cm^{-1}, on a 10 μm emitter.

It has also been assumed that as the droplet evaporates during the time between printing and imaging the droplet, the triple contact line will stay pinned, therefore the initial ejected volume can be calculated using the diameter and the initial contact angles in Table 3.3. It has been shown that the evaporation of a single solution droplet happens in two stages (David et al. [2007]; Bormashenko et al. [2011]; Nguyen et al. [2012]), whereas for binary mixtures the evaporation process can consist of three stages (Sefiane et al. [2003]). Stage one has been shown to be where the contact line is pinned and the contact angle decreases, and stage two is where the contact line decreases, and the contact angle is either constant or reduces (David et al. [2007]; Bormashenko et al. [2011]; Nguyen et al. [2012]). Figure 4.6 shows an example of the change in drop shape during evaporation when the contact line is pinned (Figure 4.6a), and when the contact line unpins and the contact angle is constant (Figure 4.6b). The pinning of the droplet has been shown to be dependent on the thermal properties of the substrate (David

et al. [2007]), the contact angle, and whether the substrate is a metal or polymer (Bormashenko et al. [2011]). From the times given for the evaporation of glycerol for a range of volumes given in Figure 4.4, it is being assumed that the contact line will remain pinned for all of the solutions tested.

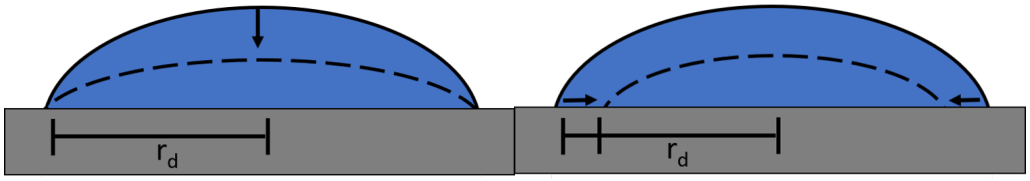

(a) Stage one example of drop evaporation when the contact line is pinned and the contact angle reduces.

(b) Stage two example of drop evaporation when the contact angle is constant and the radius has reduced.

Figure 4.6: Schematic showing examples of how the shape of the printed droplet could change during the evaporation process.

4.3 Electrospray scaling laws for estimating the ejected volume

This section focuses on how the scaling laws in Section 2.3.5.3 can be used to calculate the flow rate and volume from the current transients, in comparison to the physically printed droplets. Data is going to be compared when printing using a constant voltage and a pulsed voltage.

4.3.1 DC voltage operation

The method used to print using a constant voltage was described in Section 3.2.1.1, where a stationary substrate was used to record the transients, and the substrate moved at 50 mm s^{-1} to print the individual droplets. In these experiments a 60 cP solution with a conductivity of 6 μS cm^{-1}, on a 41.97 μm emitter was used. Between the first row of drops being printed at an ESD of 205 μm and the last row being printed at 295 μm, the first drops were imaged after approximately 60 minutes with the last drops being imaged at a time approaching 150 minutes. The smallest drops printed had a volume of

approximately 2.00 pL, and a maximum volume of 3.40 pL, Figure 4.5 suggests that the time for evaporation is around 140 to 200 minutes, which is close to the time the last drops were imaged. As discussed above the estimates for the evaporation time are suggested to be an underestimate. The last row of droplets printed were still visible and relatively circular in shape suggesting little change in diameter and therefore evaporation of the glycerol.

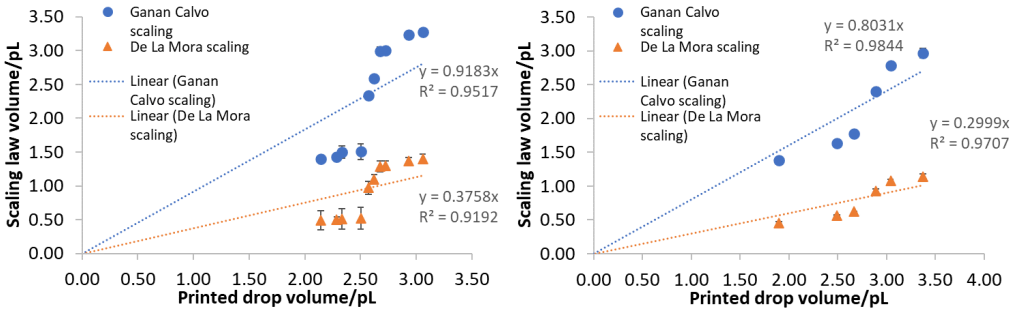

(a) 205 μm. (b) 295 μm.

Figure 4.7: Scaling law volumes against printed volumes at an emitter-to-substrate distance of 205 and 295 μm using a 60 cP solution at 6 μS cm^{-1}, on a 41.97 μm emitter.

Figure 4.7 shows the volume calculated from the scaling laws by De La Mora and Loscertales [1994] and Ganan-Calvo et al. [1997] using the current transients against the printed drop volume at an ESD of 205 and 295 μm. Each data point represents a different operation voltage and has come from averaging over multiple printed droplets and pulses from the current transient. A linear trend has been fitted through the data and the intercept set to 0, as the ideal relationship would be that the scaling law volume equals the printed drop volume. When no liquid is printed there will also be no spike in the current transient that corresponds to an ejection event to calculate the volume.

Figure 4.7a shows that at an ESD of 205 μm, at a printed volume of 2.50 pL (1.111 kV), there is an increase in the volume calculated from the current transients which was discussed in relation to the difference in pulsation frequency in Section 4.1. It was suggested that the build-up of liquid on the stationary substrate caused an increase in the field strength, which in turn increased the flow rate, which could explain the sudden increase in volume. In

Figure 4.7b at an ESD of 295 μm the data does not show a clear increase in the volume calculated from the scaling laws compared to that at an ESD of 205 μm, suggesting the build-up has little effect on the calculated volume.

Results show that at both ESDs there is a correlation with R^2 >0.90 between the two volumes, with R^2 increasing with an increase in the ESD. In majority of the pulsation work an ESD of 1.0 cm has been used, therefore Figure 4.7 suggests that due to the relatively high correlation at 295 μm the scaling laws should be able to provide a scale for the flow rate and volume. Figure 4.7 shows that the scaling laws at 295 μm give an underestimate for the ejected volume with the scaling by De La Mora and Loscertales [1994] being 3.3 times smaller, and the scaling by Ganan-Calvo et al. [1997] being 1.3 times smaller. Therefore, the scaling law by Ganan-Calvo et al. [1997] gives a closer estimate to the actual printed volume.

4.3.2 Pulsed voltage operation

The method used to print in pulsed voltage operation was described in Section 3.2.1.2, where a single droplet was printed and the transient recorded for that droplet, and so the possibility of liquid build-up under the emitter was avoided. The droplets were imaged no longer than 15 minutes after printing, and as discussed in Section 4.2 there should be little effect of evaporation especially at 23 cP and above. Figure 4.8 shows the data for a range of printed volumes at a range of viscosities (2.5, 23, 60 and 111 cP), on a range of emitter ODs (10, 20 and 40 μm), and the volumes calculated from the scaling laws by De La Mora and Loscertales [1994] and Ganan-Calvo et al. [1997] as given in Section 2.3.5.3.

Each of the data sets comprises of a range of pulsed voltages, where for multiple ejections at the same voltage each drop and scaling law volume have been plotted individually. Plotting a linear trend through each of the data sets as described in the previous section, results in Figure 4.8 show the same result as in Figure 4.7 in that the scaling by Ganan-Calvo et al. [1997] gives a closer estimate than that by

De La Mora and Loscertales [1994]. In pulsed voltage operation it is shown that as the viscosity increases the volume measured from the scaling law gets closer to that from the printed volume, increasing from 0.10 times the printed volume at 2.5 cP to 0.45 at 111 cP.

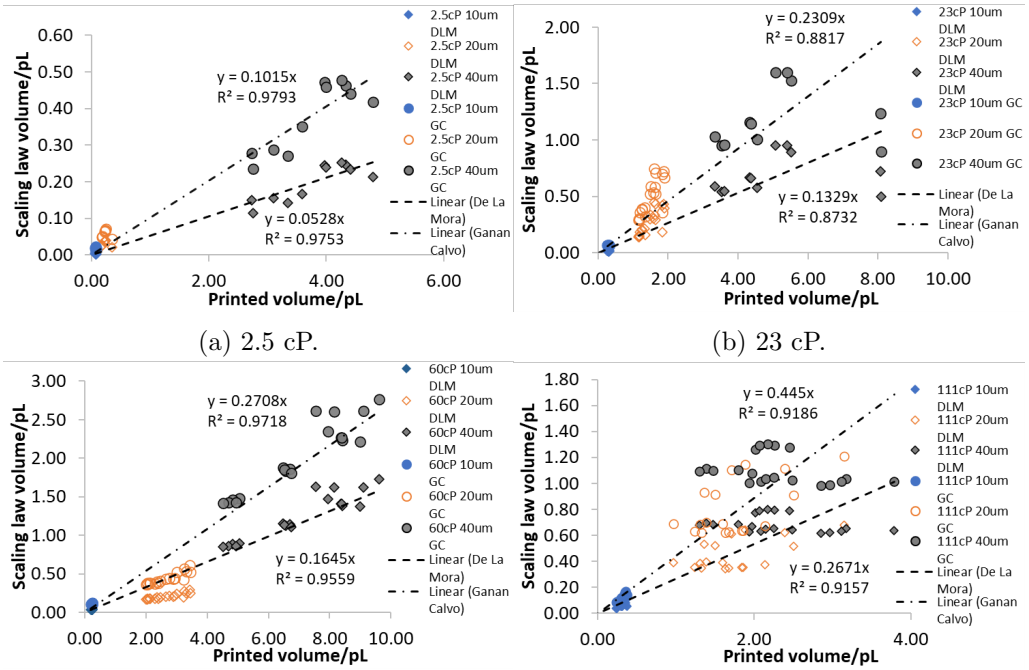

(a) 2.5 cP.

(b) 23 cP.

(c) 60 cP.

(d) 111 cP.

Figure 4.8: Scaling law volumes against printed volumes for a range of viscosity solutions at a conductivity of 60 μS cm^{-1}, on a 10, 20 and 40 μm emitter. The trend lines represent the scaling by De La Mora and Loscertales [1994] and Ganan-Calvo et al. [1997].

However, on increasing the viscosity the correlation of the linear fit generally decreases. The lowest R^2 of 0.88 at 23 cP relates to a large deviation from the trends at the highest volume printed. It should be noted that there was a difference in the size of the deposit. The reduction in the slope shows how there can be variation between how the transient data relates to the printed volume. Therefore, the scaling laws cannot be used across all viscosities to reliably calculate trends for flow rates and volumes.

4.3.3 Discussion

In constant voltage operation where the transients have had to be recorded over a stationary substrate, results have shown that at smaller ESDs build-up of liquid affects the volume calculated from the scaling laws. Therefore, in relation to pulsations when a constant voltage is applied it is being concluded that only data at an ESD of 1.0 cm and above should be used. It has been shown that in both constant and pulsed voltage operation both scaling laws give a good fit to the data, as shown in Figures 4.7 and 4.8, where the R^2 is > 0.88.

A previous study by Paine et al. [2007b] in nanoelectrospray compared the volume from the measured flow rate and frequency in pulsations given by Equation 2.3.19, with those from the scaling by De La Mora and Loscertales [1994] given by Equation 2.3.20. In pulsed voltage operation Paine et al. [2007b] showed that the scaling law gave a 1.2 to 2.1 times underestimate in the volume compared to that calculated from the printed deposit using Equation 2.4.6. In the present work this scaling gives a 3.3 times underestimate. The work by Paine et al. [2007b] was limited to a small range of liquid properties and emitter sizes, where it was suggested more tests were required to confirm the reliability of using the scaling law.

In the present work the scaling law also underestimates the volume from being 2 to 10 times smaller depending on the viscosity. In switched voltage operation it has been suggested that there could be a possible role of inertia (Paine [2009]). In majority of the present data $\delta_\mu < 1$, therefore viscosity is more dominant than inertia, however at 2.5 cP δ_μ is close to 1 at 0.8. It is thought that for the lower viscosity solution the inertia could be causing a larger droplet to be ejected in comparison to what is recorded from the current transient. More investigations would be required to conclude this. However, in both constant and pulsed voltage operation the scaling by Ganan-Calvo et al. [1997] gives a closer estimate of the ejected volume at being on average 3.7 times smaller than the printed volume compared to 9.0 times given by the De La Mora and Loscertales [1994] scaling,

and is therefore going to be used in this thesis.

5

DC voltage nanoelectrospray

This chapter focuses on the effects of liquid properties (viscosity and conductivity), and process parameters (applied voltage and emitter geometry) on nanoelectrospray behaviour, in continuous voltage operation. This work is investigating how each variable affects the spray mode/pulse shape, pulsation frequency and current. These values have been calculated directly from the recorded current transients, which were measured using a stationary substrate as discussed in Chapter 3, Section 3.2.1.1. The flow rate has been calculated from the current measurements using established scaling laws, as discussed in Chapter 4, Section 4.3, and the volume from the flow rate and on-time of the ejection.

5.1 Nanoelectrospray modes and the effect of the applied voltage

It was discussed in Chapter 2, Section 2.3 that an electrospray ejects liquid in different modes which depend on the liquid properties, and the process parameters (voltage, emitter geometry etc). The applied voltage is one of the key process parameters, which when increased, causes transitions from one mode to another. However, as discussed in Section 2.3 not all modes are observed in all conditions. The interplay between the viscosity (μ), conductivity (K), surface tension (γ), voltage, variable flow rate (Q) and emitter geometry are important in understanding the modes which are observed.

Figure 5.1 shows an example of different pulsation modes, where the main mode of interest is that of the natural pulsations/mode II ejections. Using a glycerol

and water solution, with a viscosity of 60 cP, conductivity of 60 μS cm^{-1} and an emitter outer diameter (OD) of 20 μm, Figure 5.1 shows the effect that the applied voltage has on the ejection process. Below a threshold voltage of 1.715 kV no liquid was ejected or current was observed. At a voltage of 1.899 kV, axial mode II ejections were recorded with a constant frequency of 1.41 kHz, and an amplitude of $\sim$ 34 nA. Increasing the voltage to 2.078 kV causes the time between pulsations to decrease, and the frequency of the pulsations to increase to 4.04 kHz, with an increase in amplitude to $\sim$ 49 nA. The increase in voltage from 1.899 to 2.078 kV shows a jump in the base line current from 0 to 12 nA. On a further increase in voltage to 2.155 kV, axial mode II pulsations collapsed to axial mode III with a constant current of $\sim$ 35 nA.

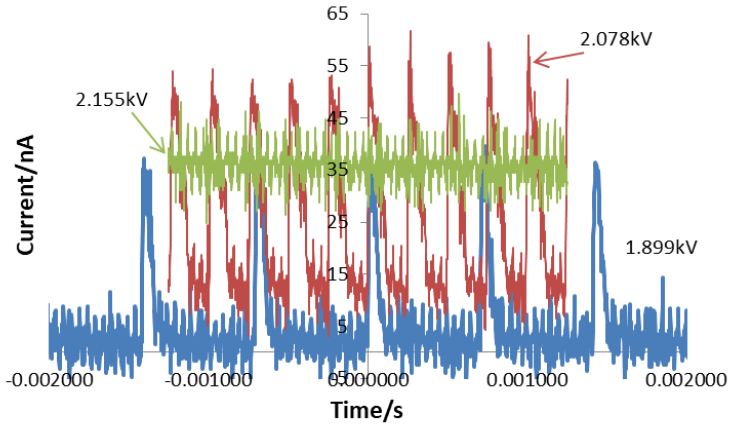

Figure 5.1: Current against time graph for a glycerol and water solution at 60 cP, 60 μS cm^{-1}, and on a 20 μm emitter, showing the effect of the voltage on the current transients.

In the majority of the solutions tested in these experiments, the spray modes observed followed the trend of Figure 5.1. However, the 2.5 cP solutions at 60 and 600 μS cm^{-1}, on a 20 μm emitter, showed a different behaviour with applied voltage. Instead of just axial mode II ejections before cone-jet mode, there were axial mode I and high frequency pulsations. High frequency pulsations were also observed for the 23 cP solution at 600 μS cm^{-1}, also on a 20 μm emitter. Figure 5.2 shows another example of how the spray modes observed vary with applied voltage, this time using a glycerol and water solution with a viscosity of 2.5 cP, conductivity of 600 μS cm^{-1} and an emitter OD of 20 μm. Below a threshold

voltage of 1.729 kV no liquid was ejected or current was measured. On increasing the voltage above 1.729 kV more regularly ejections were observed. Not shown in Figure 5.2 due to the low pulsation frequency compared to the other voltages, at 1.862 kV, axial mode II was observed at a frequency of 1.15 kHz, increasing the voltage further axial mode I ejections with two pulses per ejection event were observed. At a voltage of 1.955 kV, axial mode I ejections occurred with low frequency pulsations at 13.8 kHz, made up of three higher frequency pulsations. Axial mode I ejections were only recorded at 2.5 cP, and consisted of either two or three pulsations per ejection event. Sometimes this mode was preceded by a single ejection. At 1.974 kV, there was a sudden increase in the frequency to 75.5 kHz, as high frequency single ejections were observed. Increasing the voltage to 2.070 kV, very high frequency pulsations at 145 kHz, with a base line of 20 nA were recorded. After a further increase in the applied voltage to 2.167 kV, the high frequency pulsations collapsed to leave axial mode III with a constant current of 40 to 45 nA.

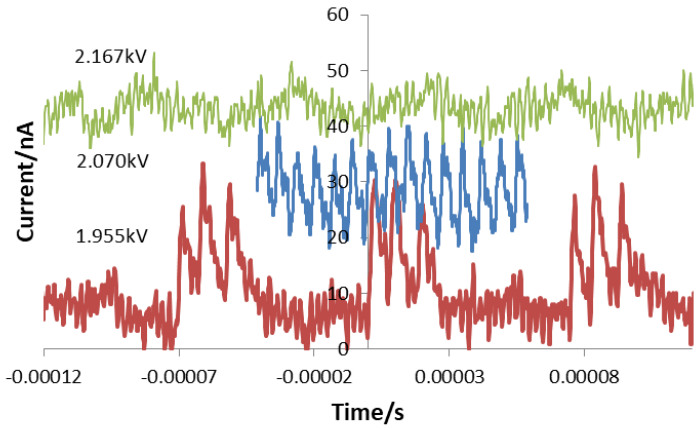

Figure 5.2: Current against time graph for a glycerol and water solution at 2.5 cP, 600 μS cm^{-1}, and on a 20 μm emitter, showing the effect of the voltage on the current transients.

Previous literature in nanoelectrospray has shown that the spray modes entered depend on the balance between the liquid properties and set-up geometry. Using a range of water, triethylene glycol and ethylene glycol solutions, at a range of conductivities, Paine et al. [2007a] observed that axial mode I ejections were not observed in all conditions. It was reported that axial mode I ejections were

only observed for a water solution, with a conductivity of 8.0x10^{-4} S m^{-1} on a 30 μm emitter, and for ethylene glycol with conductivity 2.7x10^{-2} S m^{-1} on a 150 μm emitter, where again water had the lower viscosity. It was also observed that for the ethylene glycol solution only a few pulses per packet were ejected, whereas many pulsations in a packet were observed for water. In other work, Alexander et al. [2006] observed that using triethylene glycol at a conductivity of 2x10^{-2} S m^{-1} on a 50 μm emitter (OD), and a water solution with conductivity 7x10^{-4} S m^{-1} on a 10 to 15 μm emitter (OD), axial mode I was not observed at all. This shows how important the balance between the set-up parameters is on the mode/performance. In the present work the effect of parameters on axial mode II ejections are being considered, as shown in Figure 5.1. This will however include the high frequency pulsations described in Figure 5.2.

Considering one solution with a viscosity of 23 cP, a conductivity of 60 μS cm^{-1}, and an emitter OD of 20 μm, Figure 5.3 shows the effect of applied voltage on the different current values measured, where the current comes from the flow of electrically charged ions which are collected at the substrate, when the droplets that detach from the jet impact (I_{on}, I_{ave}, $I_{\text{cone-jet}}$). The current has been measured over the pulsation range through to cone-jet mode ($I_{\text{cone-jet}}$). Each data set shows a linear relationship of current to voltage, showing that in both mode II and cone-jet mode the electrospray system follows ohmic behaviour, with a constant resistance for each spray mode, where Ohm's law is given by

$$V = IR_{\Omega}, \tag{5.1.1}$$

where V is the voltage and R_{Ω} is the resistance. This is in agreement with previously published literature (Alexander et al. [2006]; Wang and Stark [2010c]). In nanoelectrospray liquid is only ejected above the onset voltage (V_{onset}), which also means that current is only measured above this value. The onset voltage for initial ejections (V_{onset}) is being calculated from the equation of the line through the I_{ave} data, and it is when I_{ave} reduces to 0. Setting I_{ave} to 0 and rearranged

for the voltage, V_{onset} is calculated by

$$V_{\text{onset}} = (0 - c)\left(\frac{\mathrm{d}V}{\mathrm{d}I_{\text{ave}}}\right), \tag{5.1.2}$$

where c is the value of I_{ave} when the applied voltage is 0.

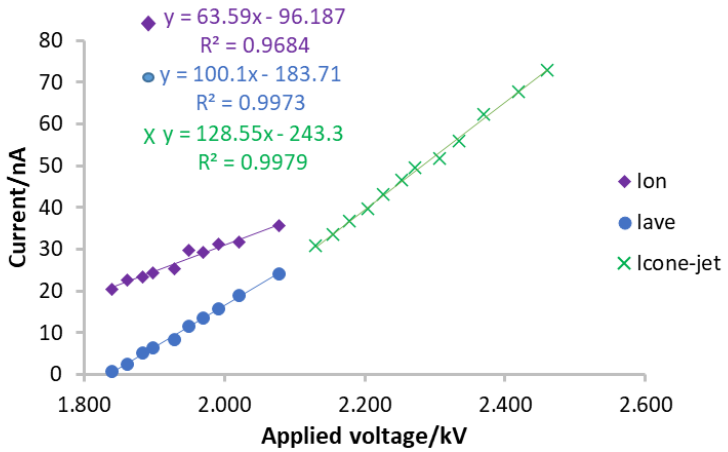

Figure 5.3: I_{on}, I_{ave} and $I_{\text{cone-jet}}$ against applied voltage for a glycerol and water solution at 23 cP, 60 μS cm^{-1}, and on a 20 μm emitter.

Comparing I_{ave} and I_{on} for pulsations in Figure 5.3, results show that I_{on} is always larger than I_{ave}. However, as the voltage increases the magnitude of the difference between I_{ave} and I_{on} decreases. With I_{on} being 30 times larger than I_{ave} at the lowest voltage, and decreasing to 1.5 times at the highest voltage. Figures 5.1 and 5.2 show that increasing the voltage decreases the time between the pulsations, which can be used to explain the decrease in the magnitude difference. As the off-time (τ_{off}) decreases there is less of a charging current within I_{ave}, where I_{ave} is given by Equation 2.3.4. The integral gets closer to being equal to the calculation for I_{on} which is given by Equation 2.3.5. Figure 5.4 shows the overlap of current transients at 1.840 kV, 1.949 kV and 2.078 kV. The time base has been reduced to observe the effect on the pulse shape, which is why the lowest voltage of 1.840 kV has only one pulse, due to the lower frequency. The overlapping of the pulses at time equal to zero shows how increasing the voltage causes the base current of the pulse to increase from 0 to 12 nA, between 1.840 and 2.078 kV. There is also an increase in I_{peak} between 1.840 and 2.078 kV, where I_{peak} increases from 35 to 50 nA. From observing the traces in Figure 5.4, τ_{on} increases by 1.3 times

between 1.840 and 2.078 kV. This might explain why I_{on} has a lower $\mathrm{d}I/\mathrm{dk}V$ compared to that of I_{ave} and $I_{\text{cone-jet}}$ because the shape of the pulse is changing very little over the 240 V range.

Figure 5.3 shows a transition between I_{ave} and $I_{\text{cone-jet}}$, where the $I_{\text{cone-jet}}$ value measured is 1.3 times that of the highest I_{ave} value. Stark et al. [2014] observed this same effect, however the transition from I_{ave} to $I_{\text{cone-jet}}$ was more prominent with $I_{\text{cone-jet}}$ being $\sim$ 2.0 times I_{ave}. The greater increase in I_{ave} observed by Stark et al. [2014] is mostly due to using a much larger capillary with an OD of 115 μm, which is almost 6.0 times the 20 μm OD used in the present tests. In terms of I_{on} there is a decrease in entering cone-jet mode, where $I_{\text{cone-jet}}$ is 0.85 times I_{on}. This is in agreement with measurements by Stark et al. [2014], where it was observed that I_{on} decreased on transitioning from axial mode II to mode IIb, with a further decrease in the current on entering cone-jet mode.

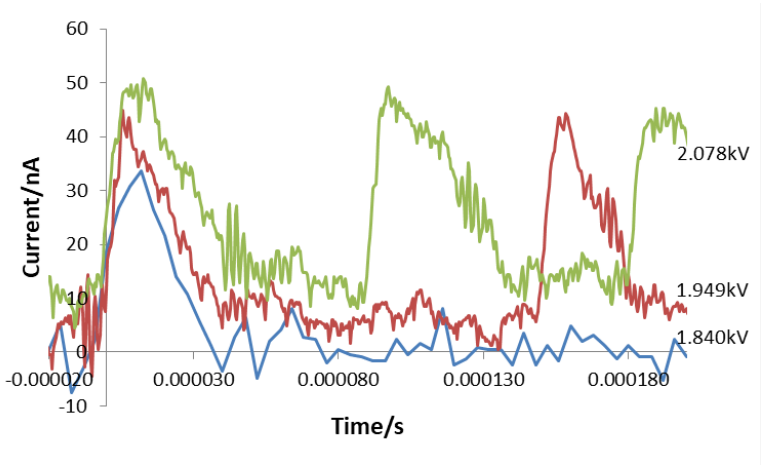

Figure 5.4: Current against time graph for a glycerol and water solution at μ=23 cP, 60 μS cm^{-1}, and on a 20 μm emitter, showing the effect of the voltage on the current transients.

Figure 5.5 shows the effect of V_{step} on the pulsation frequency, where

$$V_{\text{step}} = V_{\text{applied}} - V_{\text{onset}}, \tag{5.1.3}$$

and V_{applied} refers to the applied voltage. To compare data over a range of variables in following sections, V_{step} is going to be considered instead of V_{applied}.

Results show that for the 23 cP, 60 μS cm^{-1} solution on a 20 μm emitter, the frequency increases linearly with V_{step} ($R^2 = 0.98$), where the rate of change of frequency with voltage is 46.04 kHz kV^{-1}. Previous results by Paine et al. [2007a] and Wang and Stark [2010c] have also shown a linear increase in frequency with voltage.

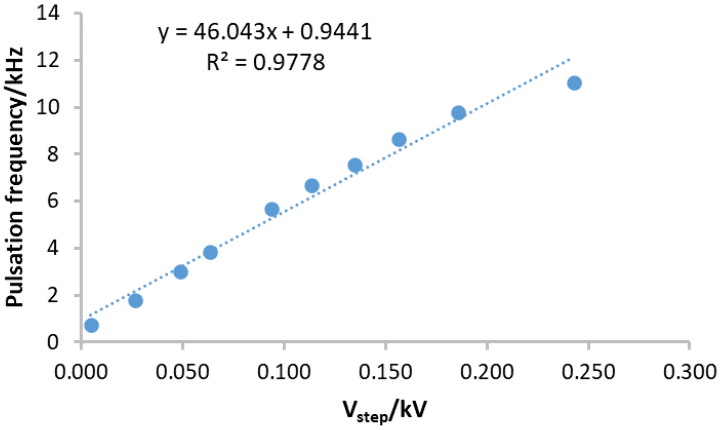

Figure 5.5: Pulsation frequency against V_{step} for a glycerol and water solution at 23 cP , 60 μS cm^{-1}, and on a 20 μm emitter.

5.1.1 Calculated flow rate and volume

Using the process described in Section 4.3, where the current/ejected charge is related to the nanoelectrospray flow rate or ejection volume, the results in Figure 5.6 show the response of the average flow rate through the jet during the on-time (Q_{jet}) with an increase in V_{step}. In cone-jet mode however, Q_{jet} has been calculated from $I_{\text{cone-jet}}$ since liquid is continuously being ejected. Figure 5.6 shows a decrease in the flow rate when transitioning from pulsations to cone-jet mode.

Previous literature has shown that the flow rate increases linearly with the applied voltage (Smith et al. [2006b]; Smith et al. [2006a]; Ryan et al. [2014]), fitting a linear trend through both the pulsation and cone-jet mode data, results in Figure 5.6 show a good correlation with $R^2 > 0.97$. The gradient of the trend $m_Q = \mathrm{d}Q_{\text{jet}}/\mathrm{d}V_{\text{step}}$ represents the sensitivity of the flow rate to voltage, in Figure

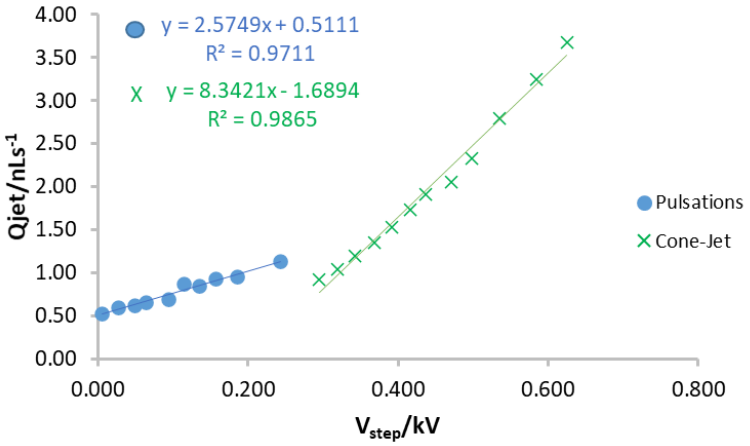

Figure 5.6: Q_{jet} against V_{step} for a glycerol and water solution at 23 cP, 60 μS cm^{-1} and on a 20 μm emitter.

5.6, m_Q= 2.57 nL s^{-1} kV^{-1} in pulsations and 8.34 nL s^{-1} kV^{-1} in cone-jet mode. In previous literature m_Q has been shown to range from 1 to 20 nL s^{-1} kV^{-1}, where it has been shown that m_Q is independent of the spray mode. In the experiments by Ryan et al. [2014] the in-line flow rate was measured, whereas in the present results the difference could be down to use of scaling laws based on cone-jet mode data and not physically measured values.

Figure 5.7 shows the effect that increasing V_{step} has on the relative scale of the ejected volume of liquid from the jet during an entire pulsation event, where an increase in V_{step} gives an increase in the ejected volume. Scaling has been presented (Chen et al. [2006]) for the minimum drop volume ejected from the cone during a pulsation event, which gives an estimated volume for the test conditions of 0.06 pL, which is approximately 3.0 times larger than the smallest volume calculated from the transients, as shown in Figure 5.7. It is concluded the estimate in the present work is smaller but of the same order of magnitude as the scaling.

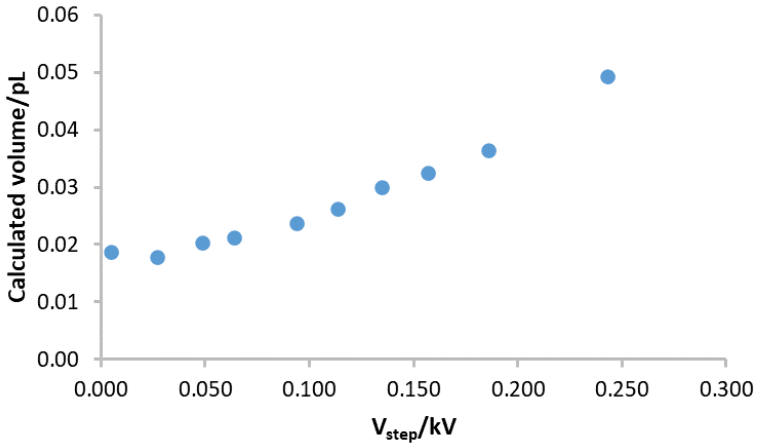

Figure 5.7: Calculated volume against V_{step} for a glycerol and water solution at 23 cP , 60 μS cm^{-1}, and on a 20 μm emitter.

5.2 Effect of viscosity

This section is investigating the effect of viscosity across a range of solutions from 2.5 to 111 cP. Throughout this section a constant conductivity of 60 μS cm^{-1}, emitter outer diameter of 20 μm, and an emitter-to-substrate distance of 1.0 cm have been used.

5.2.1 Transient characteristics

The effect of the viscosity on the pulsation frequency, with varying V_{step}, is shown in Figure 5.8. Results show that increasing the viscosity decreases the range of frequencies achieved, especially in terms of the maximum frequency. Comparing the different frequency data, at 2.5 cP there is a sudden jump in the frequency at V_{step}=0.090 kV. This is caused by a change in spray mode from axial mode I, with two pulses, to a high frequency mode with a non-zero minimum current, as shown in Figure 5.2.

Fitting a linear trend through each of the data sets in Figure 5.8, shows a good fit to the data with $R^2 \geq 0.95$. For the 2.5 cP solution, only the high frequency mode II data has been considered. This is because axial mode II ejections are

of interest in these experiments, and only mode II ejections were observed at the other viscosities tested. The rate of change of frequency with V_{step} is clearly dependent on the viscosity with $\mathrm{d}f/\mathrm{d}V_{\text{step}}$ decreasing from 327 kHz kV^{-1} at 2.5 cP to 7.89-12.76 kHz kV^{-1} at 111 cP, showing a decreasing sensitivity to voltage as viscosity increases.

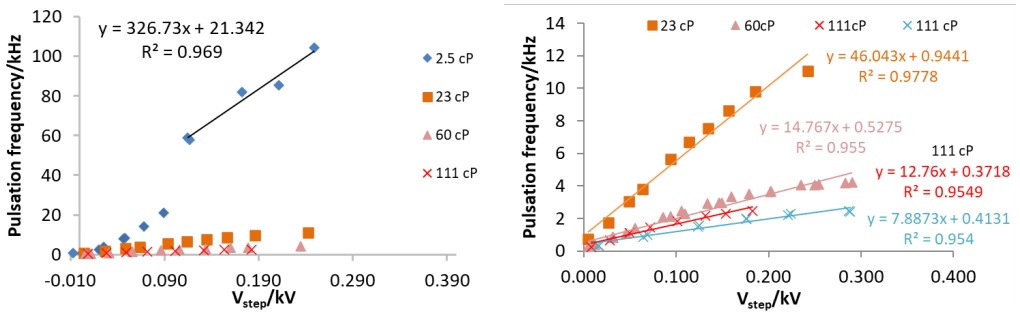

(a) All viscsoity data.

(b) Viscosity above 23cP.

Figure 5.8: Pulsation frequency against V_{step} for a range of glycerol and water solutions at different viscosities, with K=60 μS cm^{-1}, and emitter OD=20 μm. Errors are in the range of 2-20 % at low V_{step} values and all other errors are <1 %.

To illustrate the effect of viscosity, the frequency has been plotted against viscosity at differing V_{step} values as shown in Figure 5.9, where the frequency at each V_{step} has been calculated from the trend lines in Figure 5.8 to get a relative effect of increasing V_{step} at each viscosity. Results show that as V_{step} increases so does $\mathrm{d}f/\mathrm{d}\mu$ from 19.4 to 253 kHz cP^{-1}. The power law exponent of the viscosity on the frequency decreases from -0.64 at a V_{step} of 0.050 kV, to a dependence of approximately -1.00 at a V_{step} of 0.150 kV and above. At the maximum frequency where V_{step} is not necessarily constant across each viscosity $f \sim \mu^{-1}$. The data at the lowest V_{step} value is less reliable since it is close to V_{onset}, and therefore might not be fully stable. For 2.5 cP at both 0.050 and 0.100 kV the frequency was measured from mode I ejections.

The effect of the viscosity on the power law exponent in Figure 5.9 could have been expected as the viscous time is given by $\tau_\mu = \mu d_i/\gamma$, which would give $f \sim \mu^{-1}$ since $f = 1/\tau$ (Jaworek and Krupa [1999a]; Ismail et al. [2018]). This result is also in agreement with the scaling law given by Chen et al. [2006], which

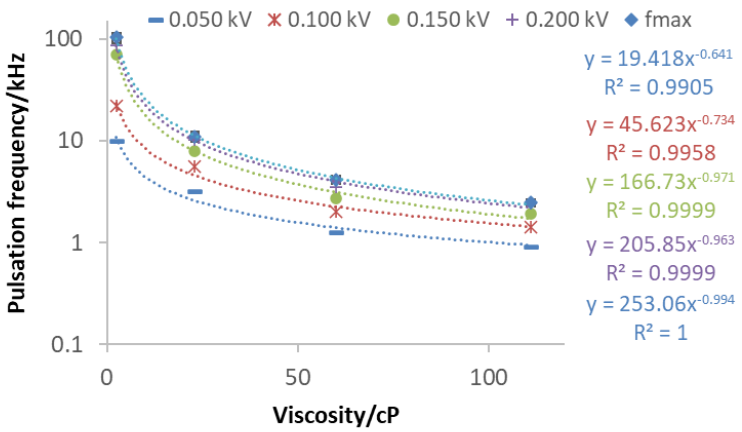

Figure 5.9: Pulsation frequency against viscosity for a range of glycerol and water solutions, with K=60 μS cm^{-1}, and emitter OD=20 μm, at a range of V_{step} values including the maximum pulsation frequency.

relates different parameters to an upper frequency estimate, and assuming that viscosity is the only parameter being altered the scaling suggests that $f \sim \mu^{-1}$. In the work presented in this section the only parameters which change slightly with viscosity are, ϵ, ρ and γ, but not by orders of magnitude compared to the viscosity.

The effect of viscosity on the average current measured over an entire pulsation cycle has shown an interesting result, in that I_{ave} is independent of the viscosity, as shown in Figure 5.10. This has been shown for both pulsation and cone-jet modes. Table 5.1 shows the values of $\mathrm{d}I_{\text{ave}}/\mathrm{d}V_{\text{step}}$ for each viscosity in both the pulsation and cone-jet regime, where the results show no correlation with viscosity. The value of $\mathrm{d}I_{\text{ave}}/\mathrm{d}V_{\text{step}}$ for cone-jet mode are 1.2 to 1.7 times larger than that for pulsations, with the increase being more significant as the viscosity decreases. This could be due to a different high frequency pulsation mode observed at 2.5 cP, but again no real trend. Therefore, the results show that I_{ave} increases with V_{step} and is independent of viscosity.

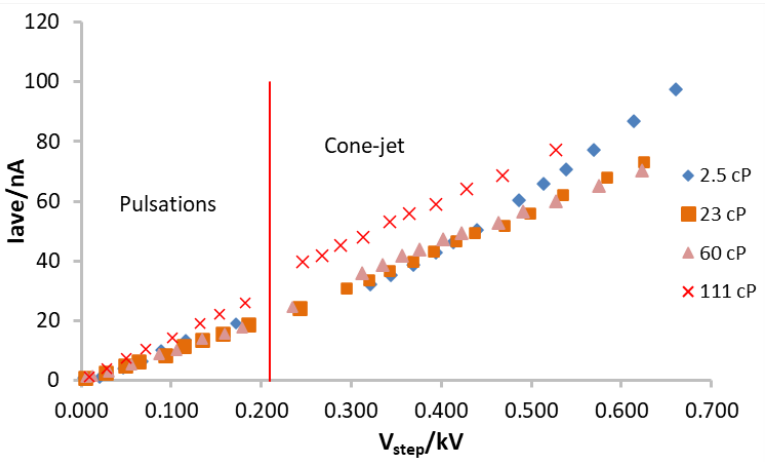

Figure 5.10: I_{ave} against V_{step} in both pulsation and cone-jet modes for a range of glycerol and water solutions at different viscosities, with K=60 μS cm^{-1}, and emitter OD=20 μm.

Viscosity/cP	Pulsations/nA kV^{-1}	CJM/nA kV^{-1}
2.5	116.9	193.7
23	100.1	128.6
60	98.46	109.2
111	107.2	133.5

Table 5.1: Values of dI_{ave}/dV_{step} for pulsation and cone-jet modes for a range of viscsoities, with K=60 μS cm^{-1} and emitter OD=20 μm.

The average current comes from measuring over an entire pulsation cycle, and has been shown to be independent of viscosity. Figure 5.11 shows a pulsation cycle which has been split up into the current measured during liquid ejection (I_{on}), and the current measured during charge/liquid replenishment (I_{charge}). The horizontal line at 13.5 nA represents where the current fits the criteria of $I \geq 0.25(I_{\text{peak}} - I_{\text{base}}) + I_{\text{base}}$ (Paine et al. [2007a]).

Figure 5.12a shows the effect of V_{step} on I_{on}, where for each viscosity I_{on} increases with increasing V_{step}. The trend of I_{on} with V_{step} is shown to be largely independent of viscosity. There is a slight decrease in I_{on} at 2.5 cP which could be due to different transient characteristics, such as a single pulse before mode I and high frequency pulsations. All the other viscosity data is

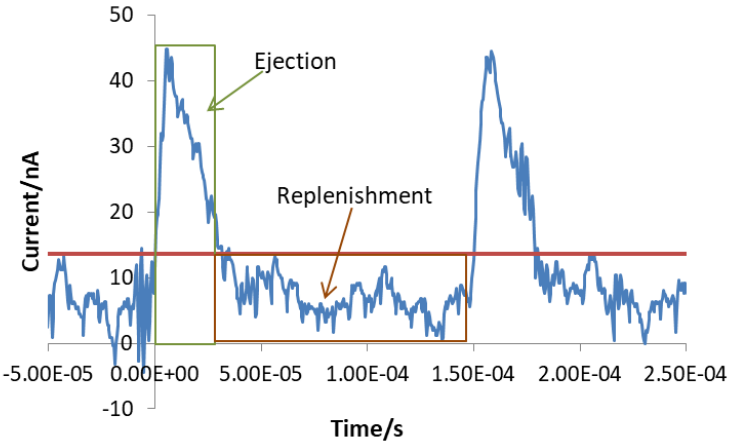

Figure 5.11: Current against time graph to show where the ejection and replenishment phases occur during a pulsation cycle.

scattered around similar I_{on} values starting at 20 to 25 nA. The effect of viscosity on the current transferred during the off-time is shown by Figure 5.12b, where I_{Charge} increases linearly with V_{step}, and is also shown to be independent of viscosity. The current and viscosity results are showing that all current values are independent of viscosity.

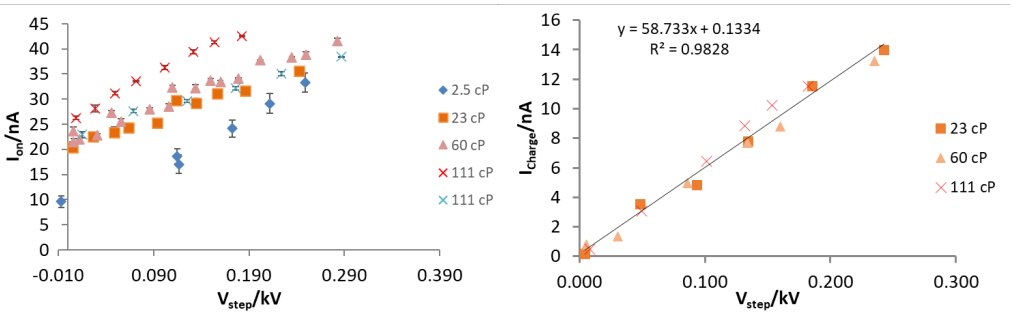

(a) I_{on} against V_{step}. (b) I_{charge} against V_{step}.

Figure 5.12: Current during liquid ejection and replenishment against V_{step} for a range of glycerol and water solutions at different viscosities, with K=60 μS cm^{-1} and emitter OD=20 μm.

Figure 5.13 shows the effect of V_{step} on both the charge emitted and the on-time of the pulse, where both results show the same trend in that they both increase with viscosity. At 2.5 cP, the charge emitted increases from 0.12 to 0.22 pC, whereas at 111 cP there is an increase from 3.04 to 8.63 pC. The charge emitted during an ejection is related to I_{on} by the equation $q_{\text{emit}} = I_{\text{on}}\tau_{\text{on}}$, where q_{emit} comes from integrating under the pulse in the current transient as shown in Figure 5.11. For

I_{on} to be constant there must be a balance between an increase in q_{emit} with the increase in τ_{on}.

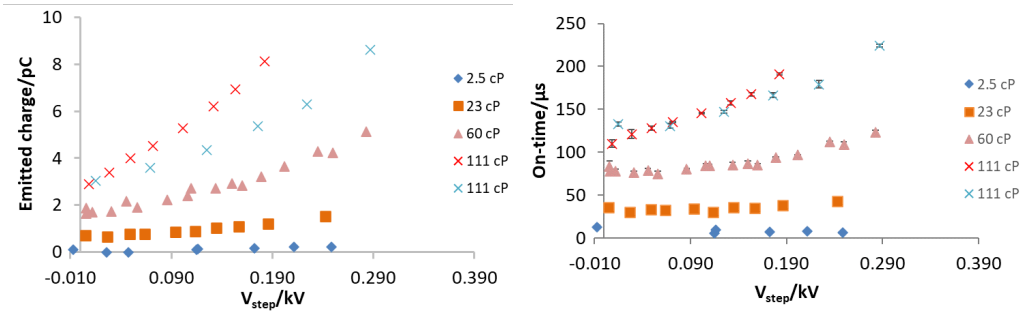

(a) Emitted charge against V_{step}. (b) On-time against V_{step}.

Figure 5.13: Emitted charge and on-time against V_{step} for a range of glycerol and water solutions at different viscosities, with K=60 μS cm^{-1}, and emitter OD=20 μm.

Figure 5.14 shows transients for all four viscosities at a constant V_{step} of 0.120±0.005 kV. At 2.5 cP, I_{peak} is 25 nA and τ_{on} is 5.4 μs. Compared to all the other viscosities, increasing from 23 cP, I_{peak} is constant at approximately 42 nA, whereas τ_{on} increases from 30 μs to 145 μs. At a constant V_{step}, the transients show agreement with previous suggestions by Paine et al. [2007a], where it was observed that the on-time of the pulse decreased when the solution had a lower viscosity.

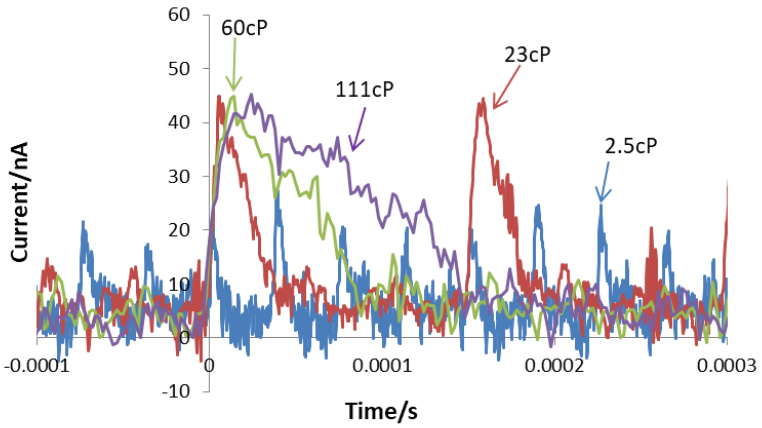

Figure 5.14: Current against time data for each viscsoity at a constant V_{step}=(0.120±0.005) kV, showing the effect on pulse shape, for a range of glycerol and water solutions at different viscosities, with K=60 μS cm^{-1}, and emitter OD=20 μm.

During the charge/replenishment phase the total charge transferred has been

measured for each viscosity except for the 2.5 cP solution, since there is no clear off-time between the ejections, however there is still a clear effect over the other viscosity ranges. Figure 5.15 shows that for each viscosity the amount of charge built up during a single ejection is relatively constant, and independent of V_{step}. This is in agreement with previous work by Stark et al. [2014]. Figure 5.15 shows that increasing the viscosity results in a greater amount of charge being transferred between pulsations, which would be expected since more charge is ejected per pulse. The time during the replenishment phase increases with viscosity, and is shown for a constant V_{step} in Figure 5.14.

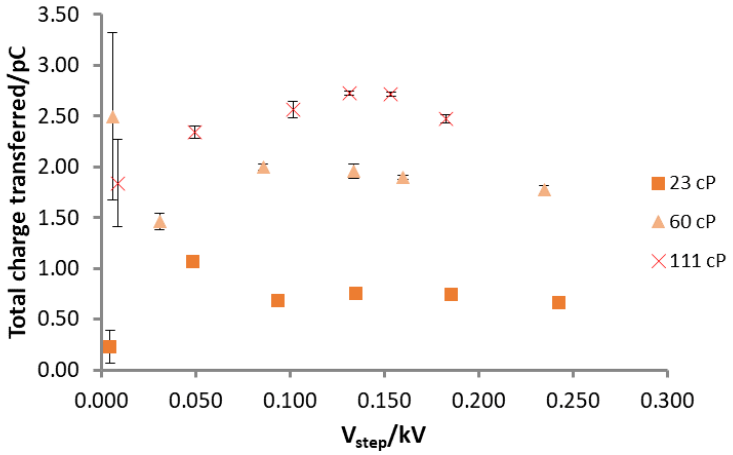

Figure 5.15: Charge transferred during off-time against V_{step} for a range of glycerol and water solutions at different viscosities, with K=60 μS cm^{-1}, and emitter OD=20 μm.

Figure 5.16 shows the pulsation frequency for each viscosity against I_{Charge}. The results show that the frequency increases linearly with an increase in I_{Charge}, and that increasing the viscosity decreases $\mathrm{d}f/\mathrm{d}I_{\text{Charge}}$.

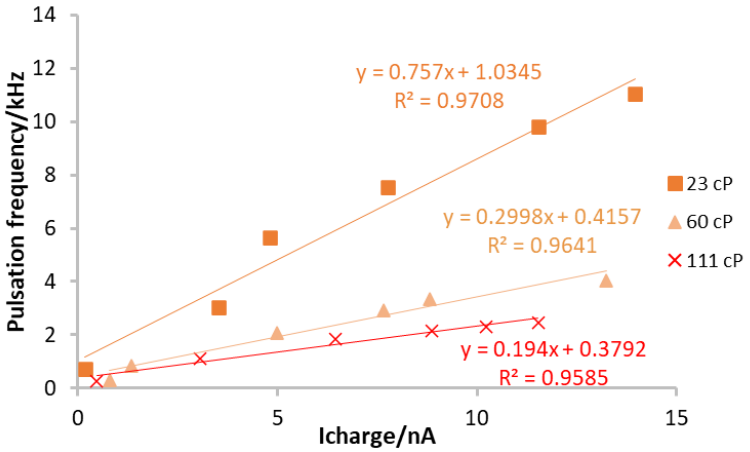

Figure 5.16: Pulsation frequency against I_{Charge} for a range of glycerol and water solutions at different viscosities, with K=60 μS cm^{-1} and emitter OD=20 μm.

5.2.2 Calculated flow rate and volume

As discussed in Section 4.3, combining the current data with scaling laws enables an estimation of the nanoelectrospray flow rate and volume ejected during a pulsation. The effect of V_{step} on the flow rate through the jet at a range of viscosities, in both pulsation and cone-jet modes is shown in Figure 5.17. Figure 5.17 shows that Q_{jet} increases with an increase in V_{step}, but there is no correlation with viscosity. The 2.5 cP high frequency data has a slightly lower Q_{jet} in pulsation mode than the 111 cP data, but in relation to the change in the order of magnitude of the viscosity, this is insignificant. The same can be said for the variation of Q_{jet} in cone-jet mode, where there is a decrease in flow rate when going from pulsations to cone-jet mode, but that is the same for all viscosities.

Calculating the volume ejected from Q_{jet} and the on-time, the effect of V_{step} on the volume at a range of viscosities is shown in Figure 5.18. Results show that increasing the viscosity of the solution increases the volume ejected during a pulsation event.

The predicted minimum volumes, using the approach from Chen et al. [2006]

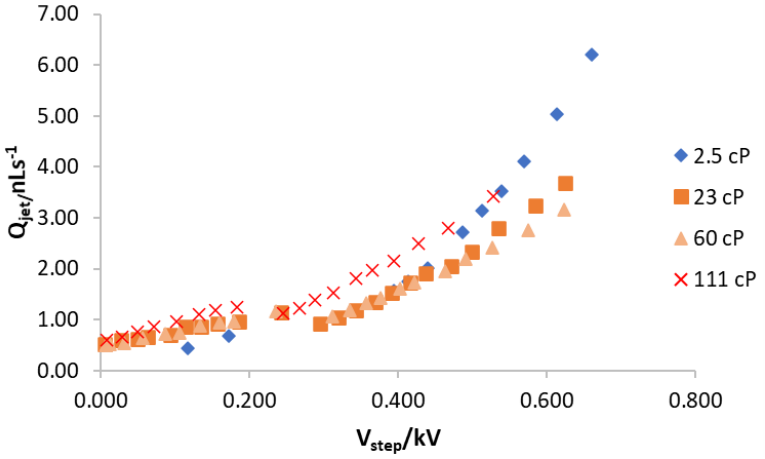

Figure 5.17: Q_{jet} in both pulsation and cone-jet modes against V_{step} for a range of glycerol and water solutions at different viscosities, with K=60 μS cm^{-1} and emitter OD=20 μm.

are, 0.075 pL at 2.5 cP, 0.056 pL at 23 cP, 0.051 pL at 60 cP, and 0.048 pL at 111 cP. Taking the minimum volumes in Figure 5.18, results show that the scaling gives a relatively good order of magnitude estimate at 23 cP and above, with the scaling ranging from being 0.7 to 2.9 times the minimum volume calculated from the current transients. In Section 4.3 it was shown that the scaling by Ganan-Calvo et al. [1997] gave an underestimate of the ejected volume by ~1.3 times when applying a constant voltage, which is within the magnitude difference range given. However, at 2.5 cP the Chen et al. [2006] scaling is 19 times larger than the smallest volume at 0.004 pL, since the scaling does not include a term for viscosity, it is therefore not giving a good representation to the data presented in Figure 5.18.

In previous literature Guo et al. [2018] performed a systematic study using glycerol and water solutions to investigate the effect of viscosity on drop volume. In these results, it was shown that when applying a constant voltage, increasing the viscosity also increased the drop volume, which is in agreement with the data in Figure 5.18. However, Guo et al. [2018] observed that increasing the applied voltage decreased the ejected volume. Results from Figure 5.18, show a clear disagreement with this result. In the work presented by Guo et al. [2018], the viscosity ranged from 40 to 80 cP and the conductivity

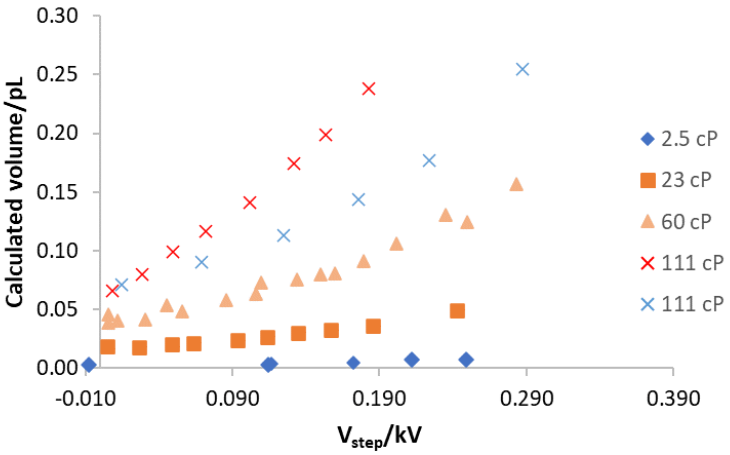

Figure 5.18: Calculated volume against V_{step} for a range of glycerol and water solutions at different viscosities with K=60 μS cm^{-1} and emitter OD=20 μm.

ranged from 2 to 10 μS cm^{-1} which are similar to those tested here. The main difference is in the size of the emitter geometry. Guo et al. [2018] used emitters with an OD of 260 μm and an ID of 160 μm, which is 13 times larger than the 20 μm emitters used for the data in Figure 5.18. Another difference is that the drop volumes calculated by Guo et al. [2018] were from the printed drops and the spherical cap equation, rather than from transients. Chapter 4 showed how the volumes from the transients related to the physical deposits, where the same observation of an increase in volume with V_{step} was recorded.

When using the scaling laws to calculate a relative value for the flow rate, Figure 5.17 suggests that the viscosity does not affect the average flow rate through the jet. This result contradicts those of previous studies where it has been suggested or shown that in unforced/nanoelectrospray the flow rate follows that of Poiseuille flow where

$$Q = \frac{P_D + P_e}{R_T} \qquad\qquad R_T = \frac{8\mu L}{\pi {r_i}^4},$$

(Smith et al. [2006a]; Choi et al. [2008]; Ryan et al. [2009]; Guo et al. [2018]) where P_D is the external pressure from the head height/back pressure, and P_e is the pressure from the electric field. In the present work, since a constant head pressure has been used, it would therefore be expected that as the viscosity

increased the flow rate would decrease, giving $Q \sim \mu^{-1}$. This reduction in flow rate with viscosity was shown in relation to cone-jet mode by Smith et al. [2006a], where by measuring the flow rate using an in-line flow rate meter the higher viscosity triethylene glycol solution (40 cP) had a smaller $\mathrm{d}(m_Q/Q_{\mathrm{on}})\%/\mathrm{d}Q_{\mathrm{on}}$ of 60.02 s nL^{-1}, compared to 116.86 s nL^{-1} for the lower viscosity ethylene glycol solution (21 cP). Concluding that the increase in viscosity increases the hydraulic resistance. However, when taking into account the resistance to flow and taking m_{pe} ($m_{pe} = m_Q R_T$) the data collapsed.

In the experiments in this section and those by Smith et al. [2006a] both had a constant head pressure applied, the difference is that the work by Smith et al. [2006a] had an initial flow rate (Q_{nom}). The only reason there was no initial flow rate in the present experiments was because the surface tension was greater than the head pressure, therefore an applied voltage was required to overcome the surface tension.

As shown in Figure 5.12a, I_{on} is largely independent of the viscosity except for a slight reduction at 2.5 cP which could be due to a different high frequency spray mode, or being close to having $\delta_\mu > 1$, meaning inertia starts to become important. Taking the average q_{emit} and τ_{on} for each solution the magnitude increase in both parameters is largely constant with increased viscosity, for example going from 2.5 to 23 cP q_{emit} increases by ~ 2.6 times and τ_{on} by ~ 2.4 times, and from 60 to 111 cP q_{emit} increases by ~ 2.1 times and τ_{on} by ~ 1.7 times. Therefore concluding that I_{on} is independent of viscosity.

Therefore, using I_{on} and the scaling by Ganan-Calvo et al. [1997] to calculate a representation for the instantaneous flow rate through the jet, since in the scaling $I \propto Q^{0.5}$ and there is no term for viscosity, the scaling will yield a flow rate independent of viscosity. The scaling by Ganan-Calvo et al. [1997] is based on cone-jet mode, in Figures 5.10 and 5.17 cone-jet mode data was included which shows the same outcome as that for pulsations. However, each of these experiments were taken in the absence of flow rate measurements, as due to the

set-up described in Section 3.2 an in-line flow rate meter could not be used to confirm the observations.

5.3 Effect of conductivity

This section is investigating the effect of conductivity across a range of solutions from 6 to 600 μS cm^{-1}. Throughout this section a constant viscosity of 23 cP, emitter outer diameter of 20 μm, and an emitter-to-substrate distance of 1.0 cm have been used.

5.3.1 Transient characteristics

The effect of the conductivity on the pulsation frequency, with varying V_{step}, is shown in Figure 5.19. Results show that increasing the conductivity increases the pulsation frequency. At low V_{step} values the frequencies are similar for each conductivity up to 0.090 kV, where the frequencies then start to deviate. By this stage the 6 μS cm^{-1} data has already entered cone-jet mode. It is clearly shown in Figure 5.19 that there is a large difference in V_{step} as the conductivity increases. The voltage step range over which the pulsations are observed increases by three times between 6 and 60 μS cm^{-1}, and two times between 60 and 600 μS cm^{-1}. In terms of the onset voltage there is a slight variation of a couple of hundred volts, but no real trend, with the values being 1.925 kV at 6 μS cm^{-1}, 1.835 kV at 60 μS cm^{-1} and 2.008 kV at 600 μS cm^{-1}.

A linear trend has been fitted to each of the data sets to determine the dependence of the frequency on V_{step}. Figure 5.19 shows that increasing the conductivity increases the rate of change in frequency with V_{step} from 35.87 kHz kV^{-1} at 6 μS cm^{-1} to 80.67 kHz kV^{-1} at 600 μS cm^{-1}, therefore concluding that a higher conductivity solution has a greater frequency sensitivity to voltage. This is beneficial as it means that one solution can have a greater range of ejection/print speeds.

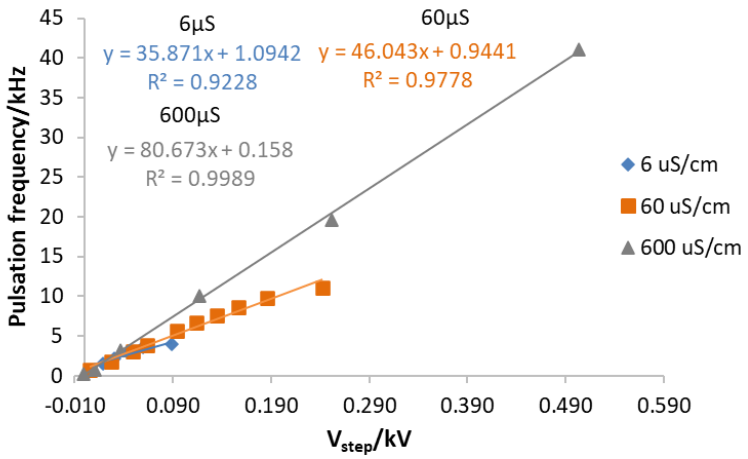

Figure 5.19: Pulsation frequency against V_{step} at a range of conductivities, at μ=23 cP and on a 20 μm emitter.

The dependence of the frequency on the conductivity has been calculated for a range of V_{step} values using the same method as discussed in Section 5.2.1, and for the maximum frequency as shown in Figure 5.20. The only data set which is not included at each of the V_{step} values is that of 6 μS cm^{-1}, due to this conductivity solution entering cone-jet mode at a much lower V_{step} value. However, a power law has still been fitted to each of the data sets. Results in Figure 5.20 show that increasing V_{step} causes an increase in the power law exponent of K from 0.08 at 0.050 kV, to 0.21 at 0.200 kV. Also plotted is the maximum pulsation frequency where $f \sim K^{0.49}$. In each of the data sets there is a fluctuation in $\mathrm{d}f/\mathrm{d}K$ between V_{step} values of 0.150 and 0.200 kV. However, between the highest V_{step} and the maximum frequency the value of $\mathrm{d}f/\mathrm{d}K$ reduces by more than half.

The scaling given by Chen et al. [2006], which predicts the upper bound on the frequency, gives $f \sim K$, if all other parameters are constant. Guo et al. [2018] also reported the dependence of f on K, and found that the average value of the power law exponent for a range of viscosities was $K^{0.58}$. In both experiments the jet impinged on the substrate, with the main difference being the emitter size and emitter-to-substrate distance. Chen et al. [2006] used a 50 μm ID emitter, at an emitter-to-substrate distance of 110 μm, whereas Guo et al. [2018] had a 160 μm emitter ID at a distance of 2.5 mm. Comparing the results from Chen et al. [2006] and Guo et al. [2018], the data in Figure 5.20 is in closer agreement

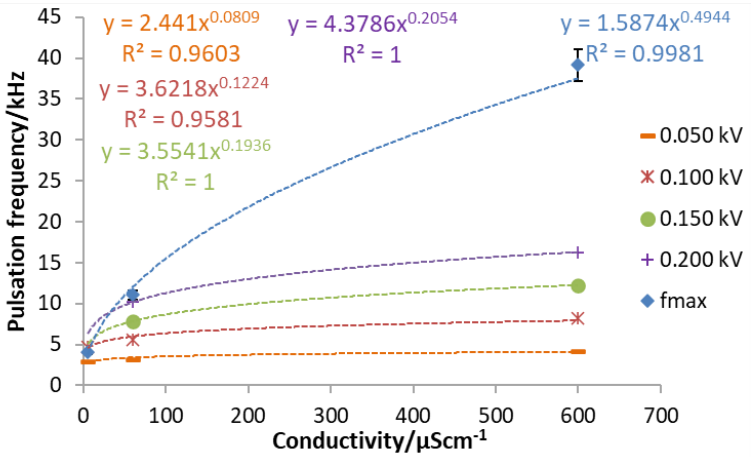

Figure 5.20: Pulsation frequency against conductivity at a range of V_{step} values and the maximum frequency.

to the result given by Guo et al. [2018].

Figure 5.21 shows the average current against V_{step} for each conductivity. Each of the data sets shows that I_{ave} increases linearly with V_{step}, and that each of the different conductivity values overlap. The 6 μS cm^{-1} data cuts off before cone-jet mode at ~6 nA, 60 μS cm^{-1} at ~25 nA and 600 μS cm^{-1} at ~55 nA. Figure 5.21 shows that there is only a slight change in $\mathrm{d}I_{\text{ave}}/\mathrm{d}V_{\text{step}}$ with increase in conductivity.

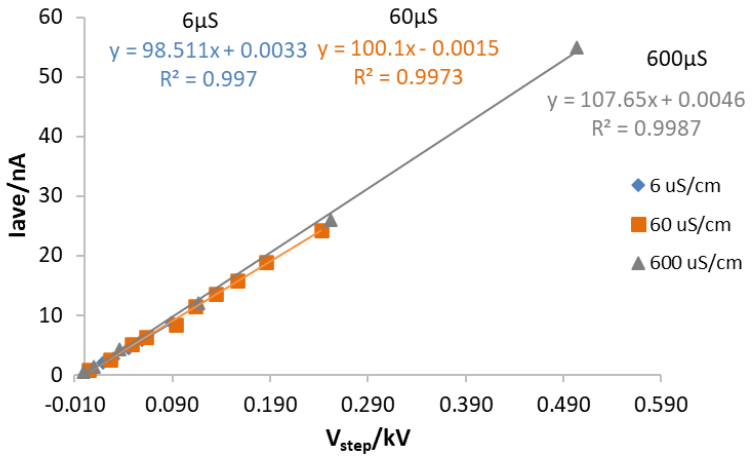

Figure 5.21: I_{ave} against V_{step} at a range of conductivities at μ=23 cP and on a 20 μm emitter.

The effect of V_{step} on I_{on} is shown in Figure 5.22, where results show that an increase in conductivity results in an increase in I_{on}. The current emitted during

an ejection approximately doubles between 6 and 60 μS cm^{-1}, whereas going from 60 and 600 μS cm^{-1} I_{on} increases by approximately 1.4 times.

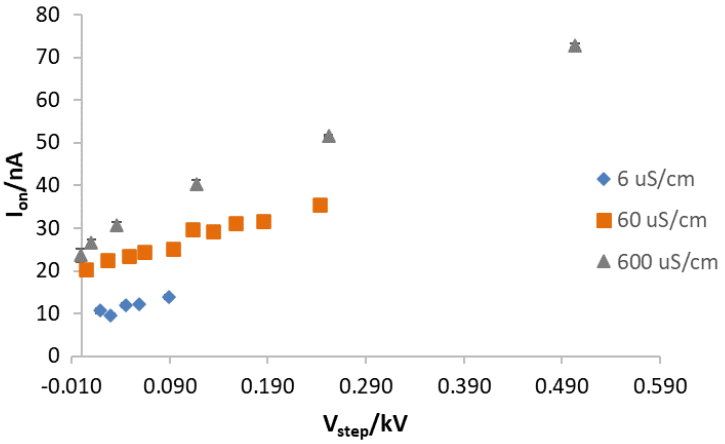

Figure 5.22: I_{on} against V_{step} at a range of conductivities, at μ=23 cP and on a 20 μm emitter.

Figure 5.23a shows the effect of V_{step} on the charge emitted during an ejection event. Generally all conductivities tested showed an increase in emitted charge with V_{step}, with the emitted charge approximately doubling over the V_{step} range. Taking the average on-time of each ejection over the V_{step} range, and plotting against conductivity, Figure 5.23b shows a decrease in the on-time with an increase in conductivity. Over the conductivity range tested $\tau_{on} \sim K^{-0.36}$, and falls from ~85 μs at 6 μS cm^{-1} to ~15 μs at 600 μS cm^{-1}.

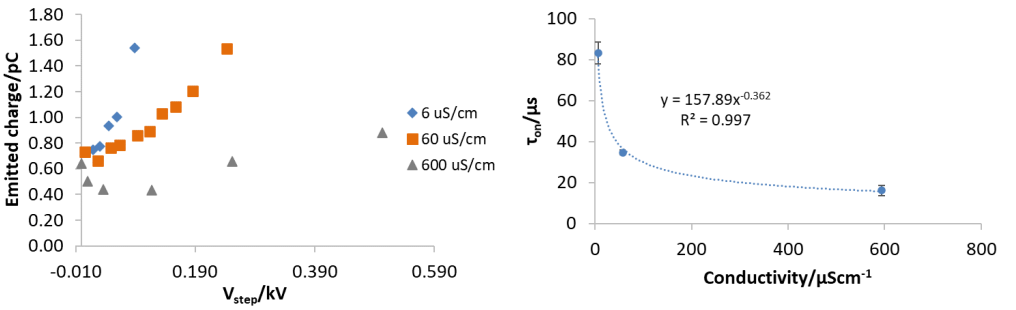

(a) Emitted charge against V_{step}.

(b) On-time against conductivity.

Figure 5.23: Transient characteristics from the pulsations during liquid ejection at a range of conductivities, at μ=23 cP and on a 20 μm emitter.

In previous literature it was shown that the on-time decreased with conductivity where $\tau_{on} \sim K^{-1}$, where it was suggested that the on-time was related to the

charge relaxation time ($t_e = \epsilon\epsilon_0/K$) (Stark et al. [2014]). In the present work results show the same in that there is a decrease in τ_{on} with increase in conductivity, however the conductivity has a power law that is approximately three times smaller. In the work by Stark et al. [2014] the conductivity also ranged over two orders of magnitude from 29 to 2319 μS cm^{-1}.

Figure 5.24 shows overlapping current transients at each conductivity, where V_{step} is selected to be as close as possible from the recorded data. The values of V_{step} are 0.045 kV at 6 μS cm^{-1}, 0.049 kV at 60 μS cm^{-1} and 0.036 kV at 600 μS cm^{-1}. The main effects of increasing the conductivity is on the on-time, as shown in Figure 5.23b, and on increasing the peak current from ~20 nA at 6 μS cm^{-1} to ~50 nA at 600 μS cm^{-1}. Over the V_{step} range tested the duty cycle of the pulsations at each conductivity ranges from 10 to 29% at 6 μS cm^{-1}, 2.3 to 47% at 60 μS cm^{-1} and 0.5 to 50% at 600 μS cm^{-1}. Increasing the conductivity has been shown to produce a greater duty cycle range, before entering a duty cycle of 100% at cone-jet mode.

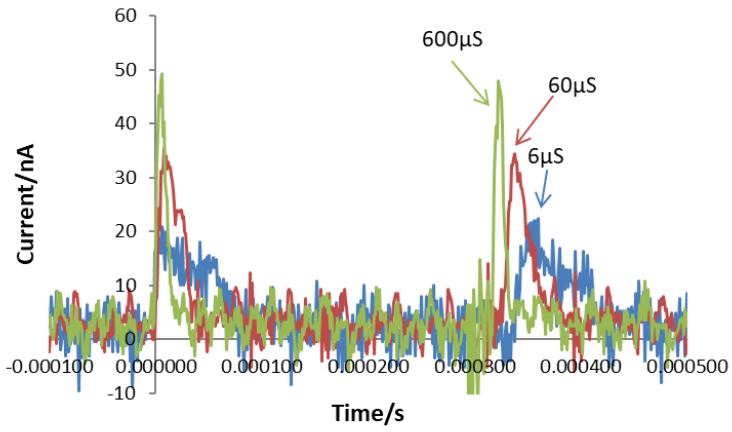

Figure 5.24: Current against time transients for each conductivity, showing the effect on pulse shape at a range of conductivities, with V_{step}=(0.041±0.003) kV, μ=23 cP and on a 20 μm emitter.

Figure 5.25a shows that the conductivity does not have an influence on the recharging current. Taking a trend through all the data sets $\mathrm{d}I_{\text{charge}}/\mathrm{d}V_{\text{step}}$ equals 74.81 nA kV^{-1}, with an R^2 = 0.98. Figure 5.25b shows the amount of charge that has been transferred between each ejection. For each conductivity

the charge transferred is independent of V_{step}, it is also independent of the conductivity. Previous literature has also reported that the charge transferred between ejections is independent of the conductivity of the solution (Stark et al. [2014]).

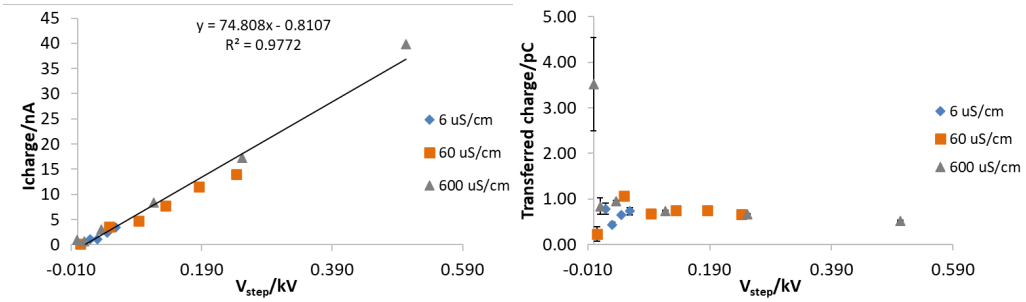

(a) I_{charge} against V_{step}. (b) Charge transferred against V_{step}.

Figure 5.25: Transient characteristics from the pulsations during liquid and charge replenishment, at μ=23 cP and on a 20 μm emitter.

Combining data from Figures 5.22 and 5.25a, the pulsation frequency has been plotted against the different sets of current data. Figure 5.26a shows that increasing the conductivity causes an increase in I_{on}, and therefore suggests that the conductivity affects how the frequency is dependent on I_{on}. Whereas Figure 5.26b shows that the frequency increases linearly with I_{charge} and each of the data sets collapse onto the same trend. Fitting a linear trend through all the data gives a $\mathrm{d}f/\mathrm{d}I_{\text{charge}}$ of 1.00 kHz nA^{-1}. This is in agreement with previous literature by Stark et al. [2014], where $\mathrm{d}f/\mathrm{d}I_{\text{charge}}$ was 0.47 kHz nA^{-1}, and it was suggested that the collapsing of the data meant that the conductivity was not dominating the relationship between the frequency and I_{charge}. Therefore, it can be concluded that the conductivity affects the ejection process.

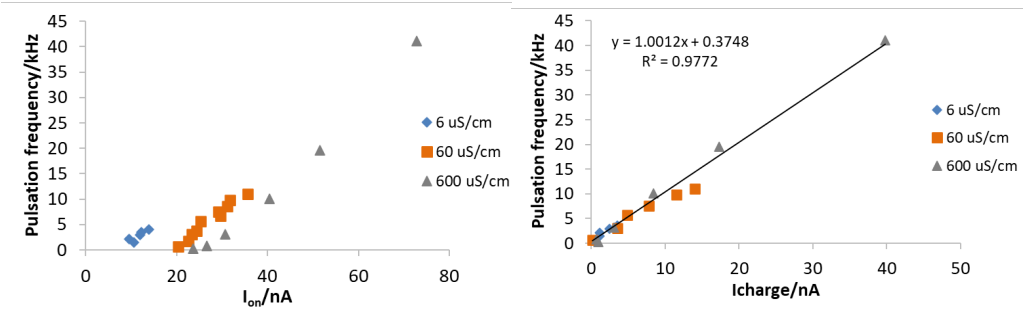

(a) Frequency against I_{on}.

(b) Frequency against I_{charge}.

Figure 5.26: Pulsation frequency against I_{on} and I_{charge}, at μ=23 cP and on a 20 μm emitter.

5.3.2 Calculated flow rate and volume

Figure 5.27 shows the effect of the conductivity on the flow rate through the jet over a range of V_{step} values. At 6 μS cm^{-1}, Q_{jet} increases by approximately 1.2 times over the range of V_{step}, whereas both 60 and 600 μS cm^{-1} increase by ~2.0 to 2.5 times. The results show that an increase in conductivity causes a decrease in flow rate, where Q_{jet} reduces by approximately 20 times between 6 and 600 μS cm^{-1}.

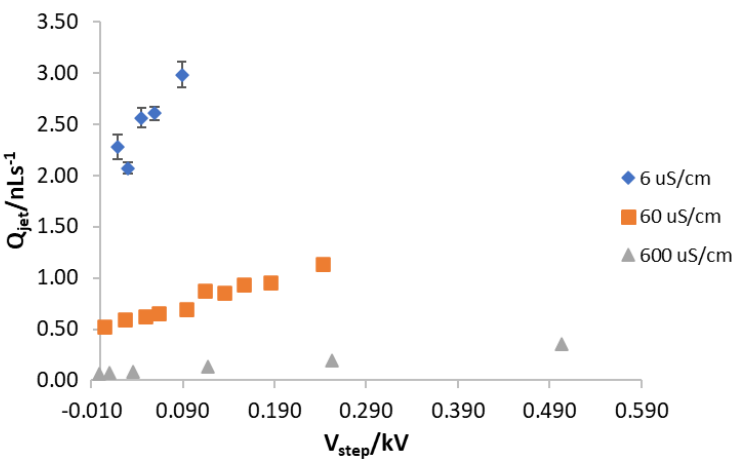

Figure 5.27: Q_{jet} against V_{step} at a range of conductivities, at μ=23 cP and on a 20 μm emitter.

In previous literature Ryan et al. [2014] showed using ethylene glycol (EG), with a conductivity of 0.23 S m^{-1}, and 1-ethyl-3-methylimidazolium tetrafluoroborate (EMI BF_4) with a conductivity of 1.4 S m^{-1} that the higher conductivity solution

had a lower flow rate. The other liquid properties of pure EG are ρ=1110 kg m^{-3}, μ=21 cP, and γ=47.8 mN m^{-1}, compared to ρ=1297 kg m^{-3}, μ=38 cP, and γ=48.2 mN m^{-1} for pure EMI BF_4 (Shamsipur et al. [2010]). It is therefore being assumed that since the conductivity is the most prominent liquid property changing, it was shown that for EG the flow rate ranged from ∼0.60 to 1.40 nL s^{-1} , whereas EMI BF_4 ranged from ∼0.05 to 0.25 nL s^{-1}. This is in agreement with the present work showing that one order of magnitude increase in K, can cause a decrease in the order of magnitude in Q.

In contrast Guo et al. [2018] suggested that the supplied flow rate followed Poiseuille flow, and that the conductivity did not affect the supplied flow rate. In the present work the effect of conductivity on the flow rate has been tested over a range of two orders of magnitude in K.

Figure 5.28 shows the calculated volume against V_{step}. The results show that an increase in the conductivity causes a reduction in the ejected volume. Using the approach by Chen et al. [2006], the predicted minimum volumes range from 0.56 pL at 6 μS cm^{-1} to 0.0056 pL at 600 μS cm^{-1}. In the present work the minimum volumes are 0.16 pL at 6 μS cm^{-1} and 0.0021 pL at 600 μS cm^{-1}. Compared to the viscosity, this scaling is shown to give a good order of magnitude estimate for the effect of conductivity on the ejected volume, and therefore gives a good representation to the data in Figure 5.28.

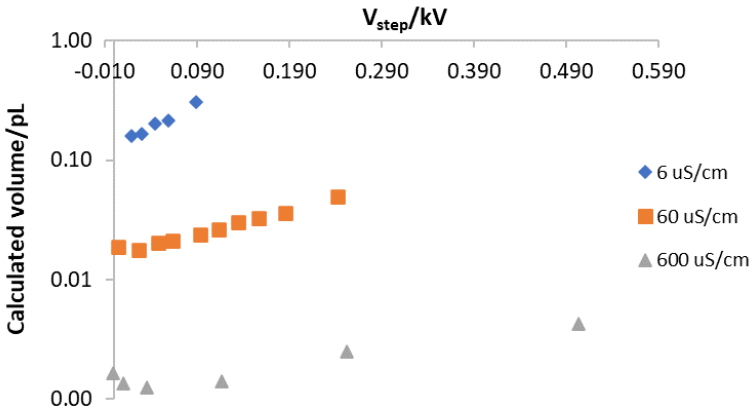

Figure 5.28: Calculated volume against V_{step} at a range of conductivities, at μ=23 cP and on a 20 μm emitter.

5.4 Effect of emitter geometry

This section is investigating the effect of the emitter outer diameter (OD) using sizes 10, 20, and 40 μm. A single solution has been tested which has a viscosity of 60 cP, a conductivity of 60 μS cm^{-1} and an emitter-to-substrate distance of 1.0 cm.

5.4.1 Transient characteristics

The effect of the emitter geometry on the pulsation frequency is shown in Figure 5.29a, where an increase in emitter size shows a decrease in the pulsation frequency with V_{step}. Fitting a linear trend to each of the data sets, results show a reduction in $\mathrm{d}f/\mathrm{d}V_{\text{step}}$, which decreases from 25.87 kHz kV^{-1} at 10 μm to 8.24 kHz kV^{-1} at 40 μm. Therefore, concluding that for an increase in voltage there is a reduced response in the frequency increasing when a larger emitter is used.

The dependence of the pulsation frequency with emitter OD at differing V_{step} values, shows that increasing the size of the emitter decreases the pulsation frequency, as shown in Figure 5.29b. Fitting a power law to each of the data

sets, results show that the power law exponent is approximately constant. The value of the exponent would be expected from the capillary time scale where $t_c = \sqrt{\rho d_n^3/\gamma}$, therefore giving $f \sim d_n^{-3/2}$. However, for the maximum frequency the power law exponent increases giving $f \sim d_n^{-0.23}$. The main difference here is that the maximum frequency does not have the same V_{step} value for each emitter size.

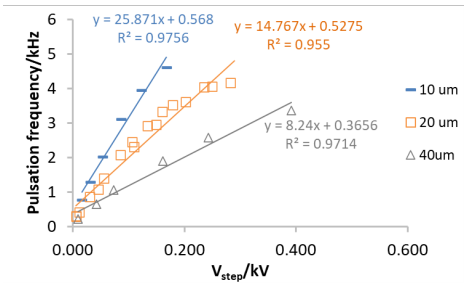

(a) Pulsation frequency against V_{step}.

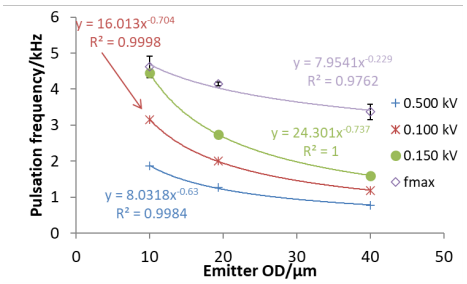

(b) Frequency data at same V_{step} and the maximum.

Figure 5.29: Effect of emitter geometry on the pulsation frequency in terms of V_{step}, at μ=60 cP and K=60 μS cm^{-1}.

Unlike for the viscosity and conductivity data in the previous sections, changing the size of the emitter has a significant effect on the applied voltage, where the onset voltages are: 1.250 kV at 10 μm, 1.803 kV at 20 μm and 1.893 kV at 40 μm. To allow for better comparison of the trends, the data will be plotted against the change in electric field, where the equation to describe an infinite wire opposite an infinite flat counter electrode has been used, which is given by Equation 2.3.12.

Figure 5.30a shows the effect of the pulsation frequency against the change in electric field (E_{step}), where results show that the frequency increases with E_{step} but is independent of the emitter OD. Fitting a linear relationship to each of the data sets results show no real correlation in $\mathrm{d}f/\mathrm{d}E_{\text{step}}$, concluding that the emitter OD does not affect the sensitivity of the pulsation frequency, but does affect the maximum frequency and electric field strength range.

Compared to V_{step}, the 40 μm data at the highest E_{step} overlaps with the maximum frequency value, as shown in Figure 5.30b. The maximum frequency decreases with an increase in emitter OD, where $d_n^{-0.23}$, as was shown for V_{step}.

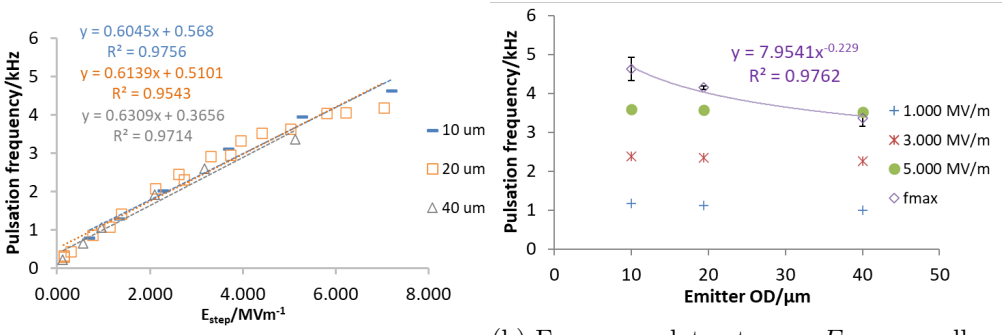

(a) Pulsation frequency against E_{step}.

(b) Frequency data at same E_{step} as well as the maximum.

Figure 5.30: Effect of emitter geometry on the pulsation frequency in terms of E_{step}, at μ=60 cP and K=60 μS cm^{-1}.

Compared to previous literature, Chen et al. [2006] suggested scaling for the maximum pulsation frequency, where it was shown that the frequency and emitter ID scaled as $f \sim d_i^{5/2}$. This suggests that the maximum frequency that should be achievable increases with an increase in emitter ID, which is in disagreement with the maximum frequency in the present work, as well as work by others such as Paine et al. [2007a].

Choi et al. [2008] on the other hand gives $f \sim d_n^{-3/4}$, which suggests a decrease in the frequency with increased emitter. This scaling has come from the balance between surface tension and electrostatic forces, along with the anchoring of the meniscus. The field equation also takes into account the emitter geometry and was given by Equation 2.3.12. The scaling for the maximum frequency derived by Choi et al. [2008] is 3.0 times that measured in the present data, however they show the same dependence with a larger emitter producing a smaller frequency.

Figure 5.31 shows the effect of both V_{step} and E_{step} on I_{ave} during an entire pulsation cycle. Results show that all emitter ODs have a linear response with V_{step} and E_{step}. In terms of I_{ave} with V_{step}, as shown in Figure 5.31a, the trend with emitter OD is not clear. The main observation is that the 10 μm data has a smaller dI_{ave}/dV_{step} at 56 nA kV^{-1}, compared to the 20 and 40 μm at 97 to 99 nA kV^{-1}. Plotting the data against E_{step} as in Figure 5.31b, there is a clear trend in that increasing the size of the emitter increases the change in

dI_{ave}/dE_{step}. The values for dI_{ave}/dE_{step} are: 1.31 nAm MV^{-1} (R^2=0.98) at 10 μm, 3.91 nAm MV^{-1} (R^2=0.99) at 20 μm and 7.60 nAm MV^{-1} (R^2=0.99) at 40 μm.

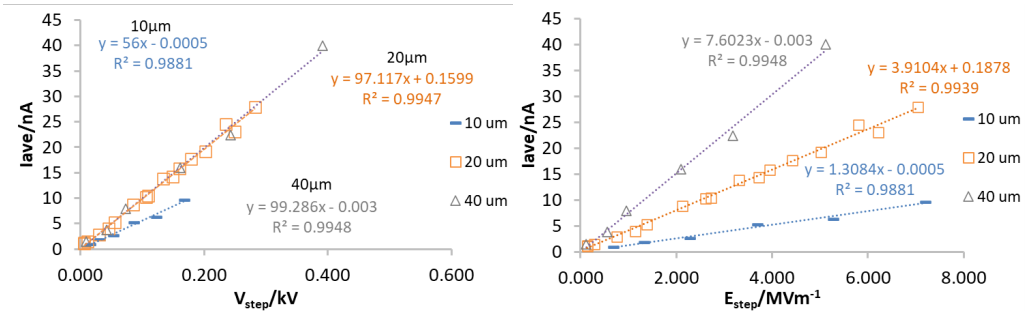

(a) I_{ave} against V_{step}.

(b) I_{ave} against E_{step}.

Figure 5.31: Effect of emitter geometry on I_{ave}, at μ=60 cP and K=60 μS cm^{-1}.

The current emitted during the on-time is shown in Figure 5.32a, where I_{on} increases with an increase in E_{step}. The current emitted during the on-time increases over the E_{step} range tested for each emitter, increasing by 1.4 times at 10 μm, 1.6 times at 20 μm and 1.8 times at 40 μm. Increasing the emitter OD increases I_{on}, with an approximate doubling between 10 and 20 μm, and an increase of ~1.5 times between 20 and 40 μm. The same trend with increasing emitter OD is observed with the charge emitted as shown in Figure 5.32b, where the increase between 10 and 20 μm is ~3.0 times and between 20 and 40 μm is ~2.0 times.

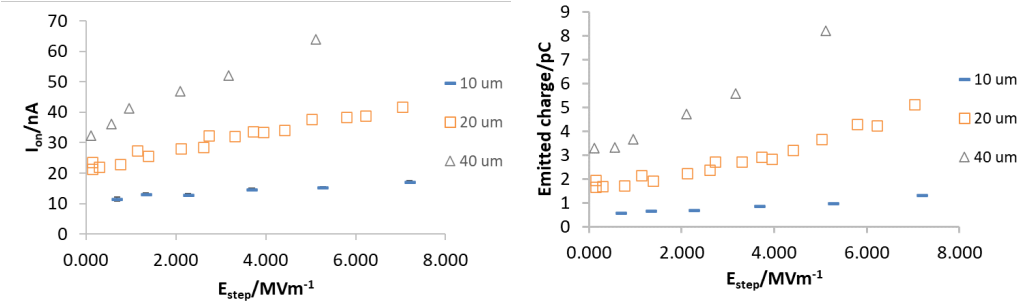

(a) I_{on} against E_{step}.

(b) Charge emitted during liquid ejection against E_{step}.

Figure 5.32: Current and charge values during liquid ejection, at μ=60 cP and K=60 μS cm^{-1}.

Figure 5.33 shows transients at similar values of E_{step}, with 2.370 MV m^{-1} at

10 μm, 2.070 MV m^{-1} at 20 μm and 2.118 MV m^{-1} 40 μm. It is shown that a larger emitter OD produces a higher peak current, from approximately 18 nA at 10 μm to 68 nA at 40 μm. There is also an increase in the base current with emitter OD. Figure 5.33 shows that the frequency is reduced for the larger emitter geometry, however the larger emitter has a larger on-time. For this E_{step} value the on-time increases from 49 μs at 10 μm to 99 μs at 40 μm.

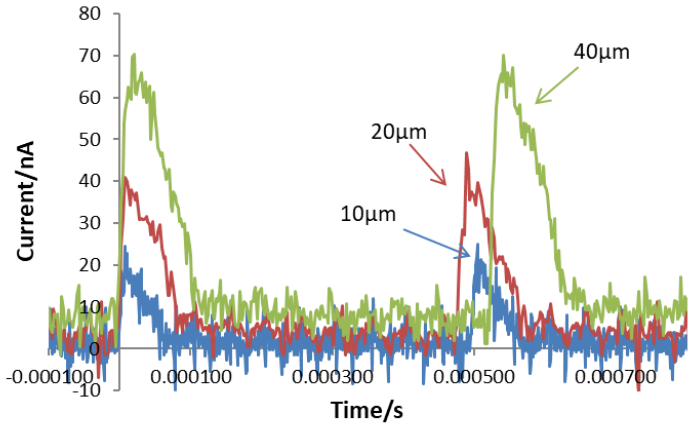

Figure 5.33: Current against time data for each emitter OD, showing the effect on pulse shape at a range of emitter ODs with μ=60 cP and K=60 μS cm^{-1}.

The effect of the emitter on the current during the off-time is shown in Figure 5.34a. Each of the trends shows a linear response to an increase in E_{step}, where the rate of the increase reduces from 3.98 nAm MV^{-1} at 40μm to 0.70 nAm MV^{-1} at 10 μm. I_{charge} shows a similar trend to I_{ave}. The main difference is that $\mathrm{d}I/\mathrm{d}E_{\text{step}}$ for I_{ave} is approximately 1.9 times that for I_{charge}. Figure 5.34b shows the amount of charge transferred for the next ejection, which is also larger for a bigger emitter OD.

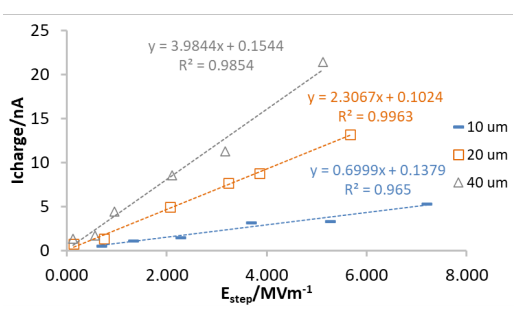

(a) I_{charge} against E_{step}.

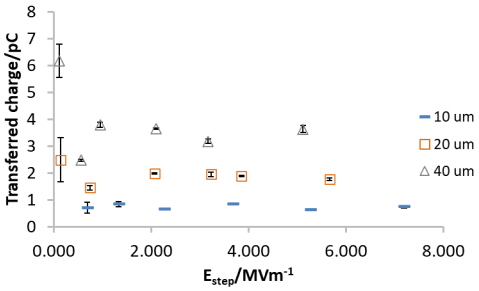

(b) Charge transferred during liquid replenishment against E_{step}.

Figure 5.34: Transient characteristics from the pulsations during liquid and charge replenishment, at μ=60 cP and K=60 μS cm^{-1}.

Figure 5.35 shows how I_{charge} relates to the frequency with emitter OD. The data shows that I_{charge} has a greater effect on the frequency at 10 μm with a $\mathrm{d}f/\mathrm{d}I_{\text{charge}}$ of 0.83 kHz nA^{-1} compared to 0.15 kHz nA^{-1} at 40 μm.

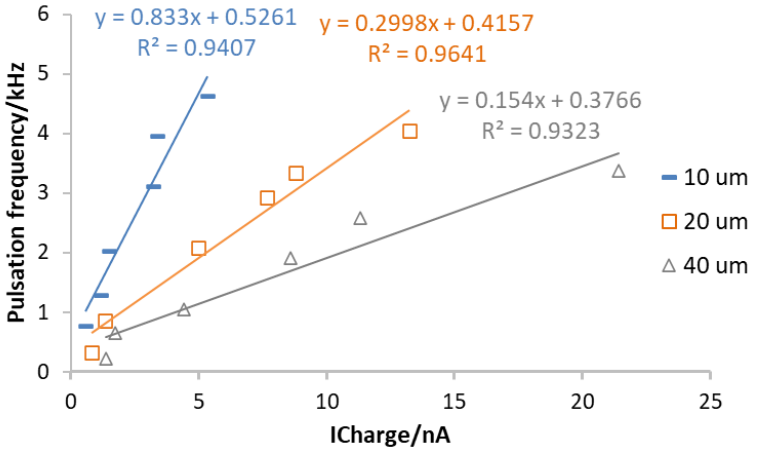

Figure 5.35: Pulsation frequency against I_{charge}, at μ=60 cP and K=60 μS cm^{-1}.

5.4.2 Calculated flow rate and volume

Figure 5.36 shows the flow rate through the jet against E_{step}. The greatest increase in Q_{jet} with E_{step} is that at 40 μm, where there is an increase in Q_{jet} of 2.6 times compared to a 1.5 times increase at 10 μm. At initial E_{step} values, Q_{jet} approximately doubles from 10 to 20 μm and from 20 to 40 μm up to an E_{step} value of 2.000 MV m^{-1}. The 20 μm and especially 40 μm flow rates then start

to increase at a greater rate.

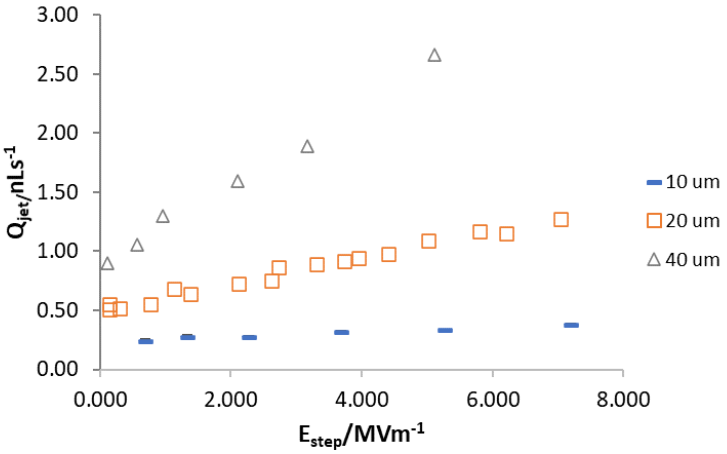

Figure 5.36: Q_{jet} against E_{step}, at μ=60 cP and K=60 μS cm^{-1}.

The calculated drop volume during an ejection is shown in Figure 5.37, where there is a clear increase in volume with emitter size. Equation 2.3.17 estimates the minimum volume for each emitter giving: 0.018 pL at 10 μm, 0.051 pL at 20 μm and 0.14 pL at 40 μm, which gives a good representation of the data in Figure 5.37.

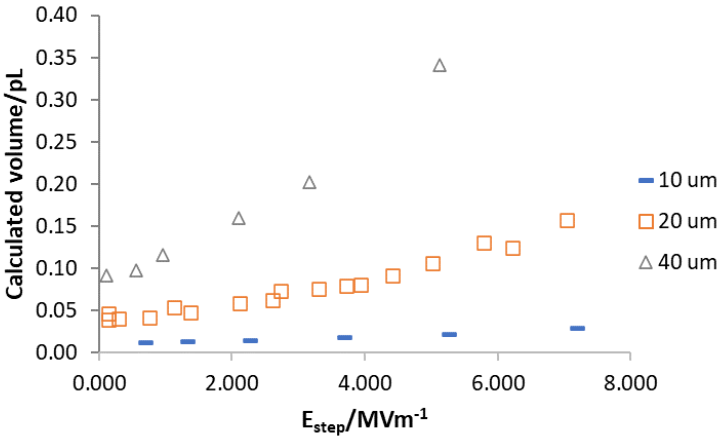

Figure 5.37: Calculated ejected volume against E_{step}, at μ=60 cP and K=60 μS cm^{-1}.

5.5 Non-dimensional analysis

In Sections 5.1 to 5.4 the relationship that varying the voltage, viscosity, conductivity and emitter OD has on processes such as the frequency of the ejection, the current and charge were shown for individual data sets. To characterise the effect that varying a range of parameters has on the pulsation process plotting the data in dimensionless form will be explored. Two important processes to consider are the pulsation frequency which relates to the rate of consecutive ejections, and the emitted charge which relates to the amount of liquid ejected during the process.

For a range of viscosity, conductivity and emitter OD experiments, Figure 5.38 shows the effect that increasing the electrical bond number (Bo_e) has on the pulsation frequency made dimensionless as the ratio to the capillary frequency ($f_c = \sqrt{\gamma/\rho d_n^3}$). In forced flow electrospray and using micro-dripping mode Hijano et al. [2015] plotted $(f/f_c)^2$ against Bo_e at a range of constant flow rates, $(f/f_c)^2$ increased with Bo_e. Results in Figure 5.38 show a continual increase in $(f/f_c)^2$ against Bo_e, but with a reducing slope at higher Bo_e values. There are differences between the experiments in Figure 5.38 and those by Hijano et al. [2015] in that in the present work the data uses mode II pulsations, and the flow rate is also increasing with Bo_e which might give rise to the difference in slope observed. In Figure 5.38, data has been included from the papers by Alexander et al. [2006] and Stark et al. [2014], where results show that both of these sets of data fit within the data ranges of the experiments in the present study.

It is shown in Figure 5.38 that when plotting $(f/f_c)^2$ against Bo_e for a range of parameters the data does not fully collapse onto a single trend. In general the 40 μm data requires a smaller Bo_e to achieve similar values of $(f/f_c)^2$, however the trend with other parameters is not as clear.

For the first ejected droplet Gañán-Calvo et al. [2016] showed that by plotting a log-log plot of the dimensionless charge (q/q_0) against ζ_q, where $\zeta_q = \delta_\mu^{-2/3}\epsilon^{7/12}$,

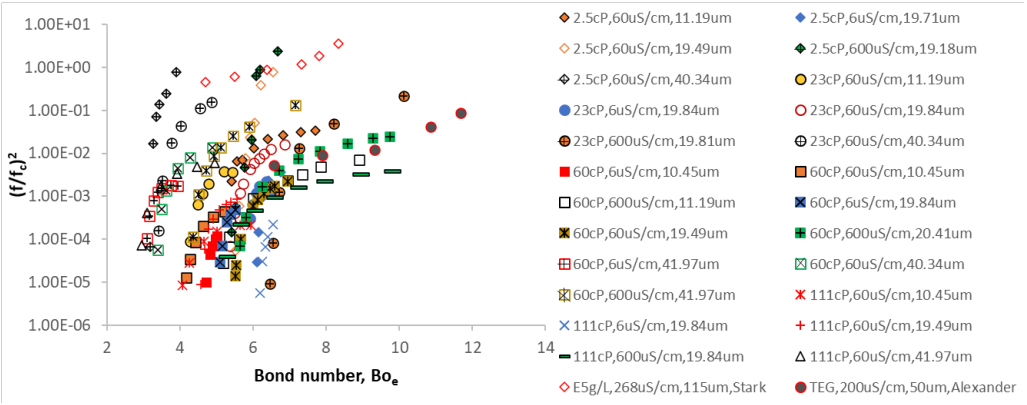

Figure 5.38: Square of the dimensionless frequency $((f/f_c)^2)$ against the electrical bond number (Bo_e), for a range of glycerol and water solutions on a range of emitter ODs. Data from Alexander et al. [2006] and Stark et al. [2014] have been included where TEG=triethylene glycol and E=ethylene glycol.

the data collapsed to scale as $q/q_0 = 0.2\zeta_q$. Figure 5.39 shows the same plot in relation to mode II pulsations, where results show that over the range of parameters tested ζ_q increases with conductivity and viscosity, and q/q_0 increases with an increase in each parameter varied. The best fit through the data follows a power law relationship giving $q/q_0 = 51.56\zeta_q^{1.89}$. The effect of increasing Bo_e is not captured in the dimensionless parameter q/q_0 and so leads to a larger variance and poorer R^2 value. Calculating the average q/q_0 value for each set of data, fitting a power law relationship gives $q/q_0 = 93.19\zeta_q^{1.75}$, which leads to an increased correlation with an R^2 value of 0.88.

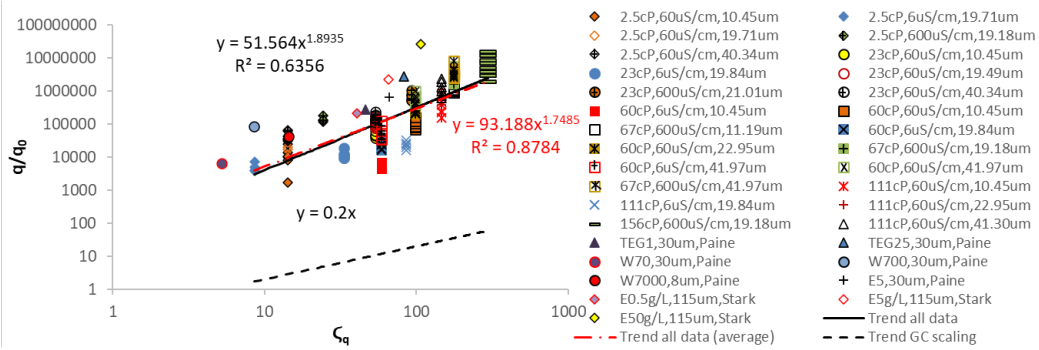

Figure 5.39: Dimensionless charge (q/q_0) against ζ_q, where $\zeta_q = \delta_\mu^{-2/3}\epsilon^{7/12}$ for a range of glycerol and water solutions on a range of emitter ODs. Data from Paine et al. [2007a] and Stark et al. [2014] have been included where TEG=triethylene glycol, E=ethylene glycol and W=water.

The dashed line represents the scaling by Gañán-Calvo et al. [2016] where results

show that q/q_0 from the present data is several orders of magnitude greater. The main difference between the experiments is that Gañán-Calvo et al. [2016] focused on the first droplet from a transient jet, which could represent a small fraction of the total charge emitted during a pulsation event, whereas the present work focuses on an entire pulsation event which is most likely due to the production of multiple droplets per pulsation. To confirm the trend observed in Figure 5.39 for a pulsation event, charge data from other nanoelectrospray pulsation tests have been included (Paine et al. [2007a]; Stark et al. [2014]) where results show that the solutions in those experiments also fit with the data from the present work. Therefore, concluding that during an entire pulsation cycle the value of $\mathrm{d}(q/q_0)/\mathrm{d}\zeta$ is greater than that for the first ejected droplet, also that the ejected charge in nanoelectrospray can be predicted from the plot given particular liquid properties.

5.6 Summary

This chapter shows the effects that varying the viscosity, conductivity, and emitter geometry have on nanoelectrospray pulsations. The pulsation frequency has been shown to increase linearly with V_{step}, where $\mathrm{d}f/\mathrm{d}V_{\mathrm{step}}$ was shown to reduce with an increase in viscosity and emitter OD, and increase with conductivity. The maximum frequency and therefore the quickest rate at which the ejection process can occur was shown to be related to each of the parameters by $f_{\max} \sim \mu^{-1}$, $f_{\max} \sim K^{0.49}$, and $f_{\max} \sim d_n^{-0.23}$. Over the parameter range tested results show that changing the viscosity has a greater influence on the pulsation frequency. The non-dimensional frequency ($(f/f_c)^2$) against Bo_e results showed a difference in slope as $(f/f_c)^2$ increased with Bo_e, and that generally a smaller Bo_e was required the larger the emitter OD.

The charge emitted during the ejection process was shown to be dependent on each parameter, with a greater charge being measured for a higher viscosity and larger emitter OD, but smaller in relation to a higher conductivity. The non-

dimensional charge (q/q_0) against ζ_q fitted to a power law relationship, where taking the average q/q_0 to account for the increase in Bo_e, $q/q_0 = 93.19\zeta_q^{1.75}$.

Combining current data with the scaling laws has been shown to give an estimation for the flow rate and the ejected volume. Results have shown that Q_{jet} is largely independent of viscosity, and as discussed so was I_{on}. The scaling does not have a term for viscosity, and since $I \propto Q^{0.5}$, no effect on the flow rate was calculated. Having a lower conductivity and larger emitter OD showed an increase in flow rate. The scale for the ejected volume which relates to the resolution showed that to achieve the smallest volume a low viscosity, high conductivity and small emitter are required.

6

Pulsed voltage nanoelectrospray: Constant emitter-to-substrate distance

This chapter focuses on the effects of liquid properties (viscosity and conductivity), and process parameters (magnitude of the pulsed voltage and emitter geometry) on nanoelectrospray behaviour in pulsed voltage operation. The emitter-to-substrate distance has been kept to a constant distance of 1.0 cm. This work is investigating how each variable affects the spray mode/pulse shape, the formation time, and the ejected volume. The main interest is the behaviour of the first ejection, which was isolated by altering the frequency (f) and duty cycle (D_c) of the voltage pulse. As discussed in Chapter 5 the flow rate has been calculated from current measurements using established scaling laws, and the volume calculated from the flow rate and on-time of the ejection.

6.1 Pulsed voltage modes and the effect of the applied voltage

Similar to constant voltage nanoelectrospray as discussed in Chapter 5, Section 5.1, the magnitude and duration of the voltage pulse can affect the spray mode, where both axial mode II pulsations and cone-jet mode can be observed. As an example, Figure 6.1 shows the influence of V_2 on the current transients, for a duration of 5.00 ms (f=100 Hz, D_c=50%), where the emitter was held at a constant voltage (V_1 1.723 kV). V_1 and V_2 were defined in Chapter 3 as the

base/resting voltage and the ejection voltage. Figure 6.1 shows the effect of varying V_2 for a 111 cP, 60 μS cm^{-1} glycerol and water solution on a 20 μm emitter. At V_2=2.260 kV, with a switching amplitude of 0.537 kV, a current peak is observed at around 0.40 ms after pulsing to V_2, which is followed by a gradual relaxation of the current until plateauing at a steady cone-jet current for the remaining pulse duration. On reducing V_2 to 2.218 kV, with a voltage amplitude of 0.495 kV, there is again an initial pulse on switching which then relaxes to cone-jet mode, before two pulses are ejected starting at approximately 4.00 ms. At V_2=2.215 kV, cone-jet mode transitions to pulsations at 2.00 ms after the initial switching of the voltage, with the number of pulses doubling from those measured at 2.218 kV. Reducing the voltage further to 2.211 kV only pulsations are observed, with the initial pulse at approximately 0.50 ms. This shows that the number of pulses can be very sensitive to a small change in V_2, from 2 pulses at 2.218 kV to only pulsations at 2.211 kV, a difference of only 0.007 kV.

In this work the main interest is in the magnitude of the voltage pulse (V_{pulse}) or jump in bond number (ΔBo_e) required to achieve full pulsations as shown in Figure 6.1d, where the duration of the single voltage pulse was 5.00 ms (f=100 Hz, DC=50%). Once in this condition the frequency and duty cycle were altered to isolate the first pulsation event. The V_2 voltage was then decreased and the frequency and duty cycle altered accordingly to continue to isolate the first pulse, as described in Section 3.2.1.2.

To use electrospray for printing one of the key parameters to understand is the formation time (T_{form}) (Paine [2009]), or the time it takes for the initial ejection to occur. This will determine the speed of the ejections and therefore the maximum print speed. Figure 6.2 shows the effect of V_2 on the formation time, from the highest V_2 at which only pulsations were recorded. Results show that for a greater V_2 value, the first ejection requires a shorter time to form than for smaller voltages, which agrees with previous literature (Paine et al. [2007b]; Paine [2009]; Lee et al. [2012b]). The time decreased from 2.78 ms at 1.907 kV to 0.39 ms at 2.211 kV, which is a reduction in the formation time by an order of magnitude.

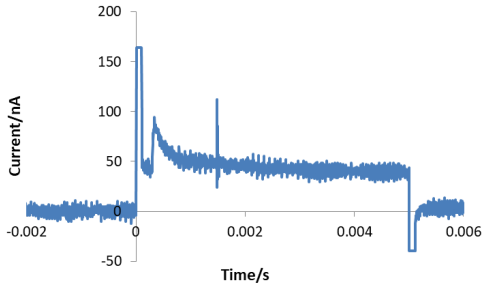

(a) V_2=2.260 kV

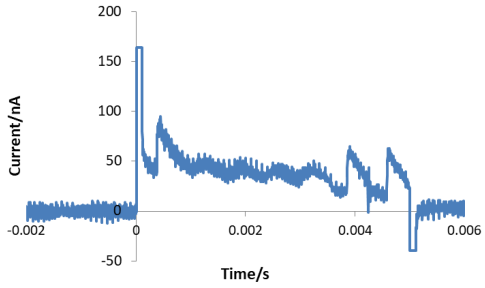

(b) V_2=2.218 kV

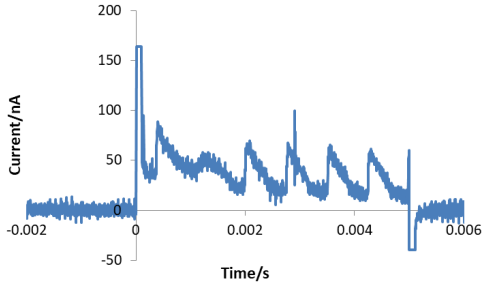

(c) V_2=2.215 kV

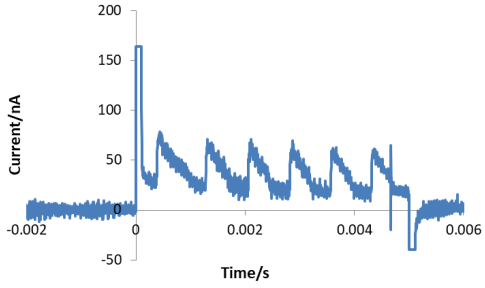

(d) V_2=2.211 kV

Figure 6.1: Current against time graphs for a glycerol and water solution at 111 cP, 60 μS cm^{-1}, and on a 20 μm emitter, showing the effect of voltage on the current transients. Each voltage pulse has a duration of 5.00 ms and V_1=1.723 kV.

Fitting a power law to the data shows that $T_{\text{form}} \sim V_2^{-12}$.

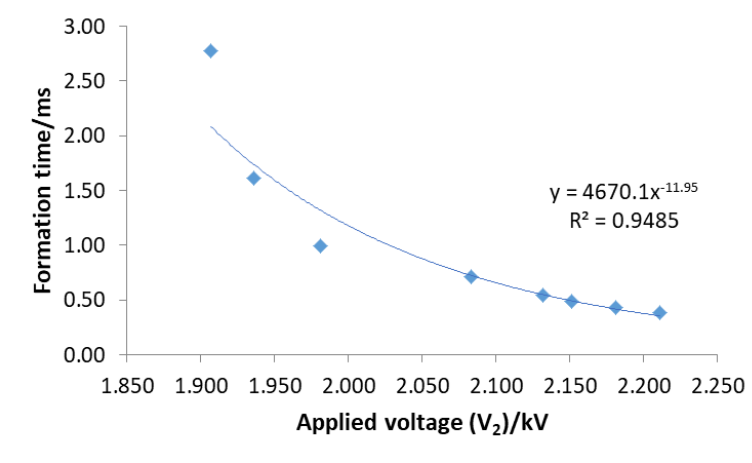

Figure 6.2: Formation time against the applied voltage (V_2) for a glycerol and water solution at 111 cP, 60 μS cm^{-1}, and on a 20 μm emitter (V_1=1.723 kV).

As discussed in Chapter 5, the data presented in this section is plotted against V_{pulse}, where

$$V_{\text{pulse}} = V_2 - V_1. \tag{6.1.1}$$

Figure 6.3 shows the effect of V_{pulse} on the formation time where $T_{\text{form}} \sim V_{\text{pulse}}^{-2.37}$.

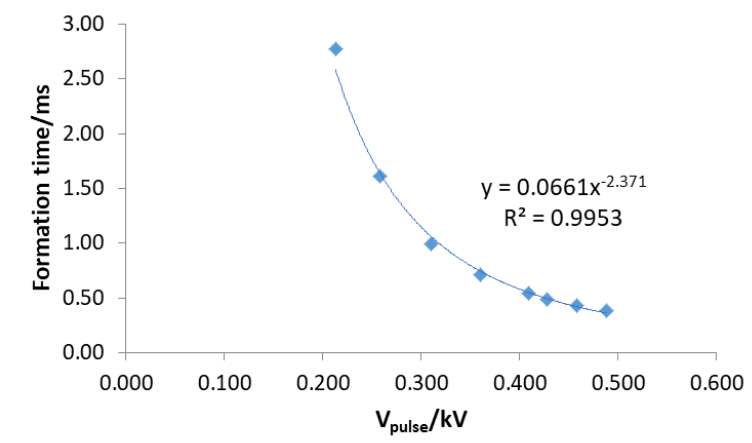

Figure 6.3: Formation time against V_{pulse} for a glycerol and water solution at 111 cP, 60 μS cm^{-1}, and on a 20 μm emitter.

Similarly to that calculated for a single pulse during constant voltage nanoelectrospray, the peak current and the current during the ejection process can be calculated. Figure 6.4 shows the variation of I_{peak} and I_{on} with an increase in V_{pulse}, where I_{peak} is found to be approximately 1.5 times greater

than I_{on}. As was also observed in constant voltage operation, the current increases linearly with V_{pulse}. It is shown that I_{peak} has a greater dI_{peak}/dV_{pulse} of 138 nA kV^{-1}, compared to that of I_{on} where dI_{on}/dV_{pulse}=103 nA kV^{-1}.

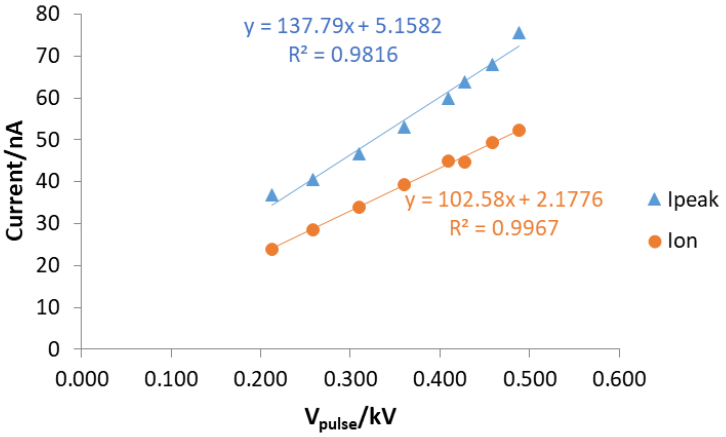

Figure 6.4: I_{peak} and I_{on} against V_{pulse} for a glycerol and water solution at 111 cP, 60 μS cm^{-1}, and on a 20 μm emitter.

Figure 6.5a shows the emitted charge against V_{pulse}. The charge emitted increases from 6.4 to 30.6 pC, which is an increase of approximately 5.0 times over the V_{pulse} range tested. Figure 6.5b shows the on-time against V_{pulse}, where the on-time increases with increasing V_{pulse}. Over the V_{pulse} range tested the on-time approximately doubles from 268 to 592 μs.

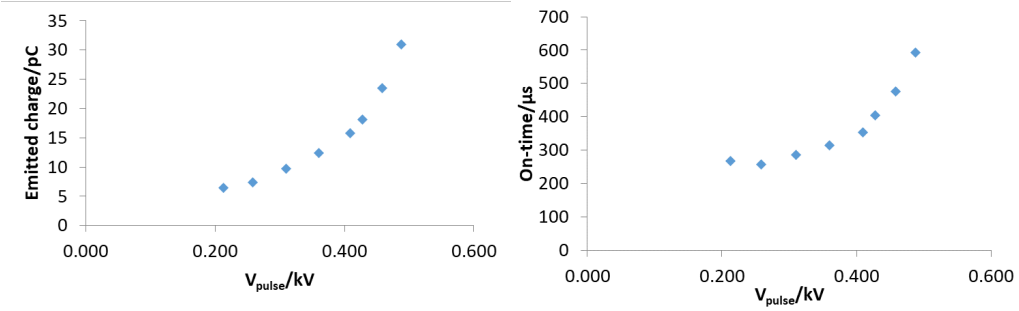

(a) Emitted charge.

(b) On-time.

Figure 6.5: Emitted charge and on-time against V_{pulse} for a glycerol and water solution at 111 cP, 60 μS cm^{-1} and on a 20 μm emitter.

6.1.1 Calculated flow rate and volume

Figure 6.6a shows that Q_{jet} increases with V_{pulse}. The dependence of the ejected volume on V_{pulse} is shown in Figure 6.6b, where results show that the ejected volume increases as V_{pulse} increases. The ejected volumes range from 0.15 to 1.06 pL over a V_{pulse} range of 0.275 kV.

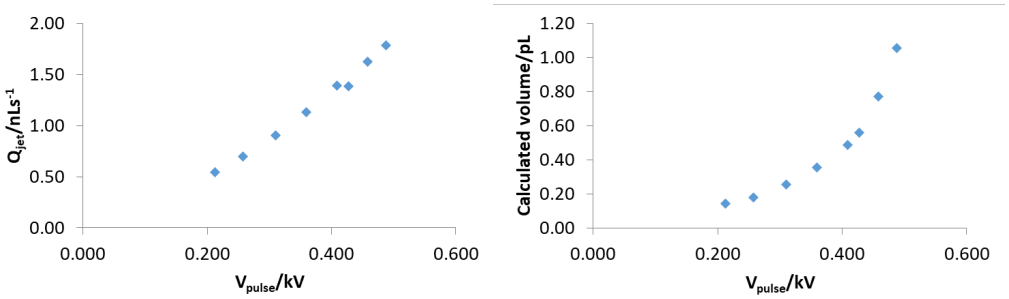

(a) Q_{jet}. (b) Calculated volume.

Figure 6.6: Q_{jet} and calculated volume against V_{pulse} for a glycerol and water solution at 111 cP, 60 μS cm^{-1} and on a 20 μm emitter.

Figure 6.7 shows a comparison between the ejected volume at similar applied/V_2 voltages, in both continuous and pulsed voltage operation. Results show that a larger volume is ejected when the voltage is pulsed rather than constant. The ejected volume in pulsed voltage operation ranges from being approximately 1.4 times greater at ~1.950 kV, to 2.7 times at ~2.200 kV.

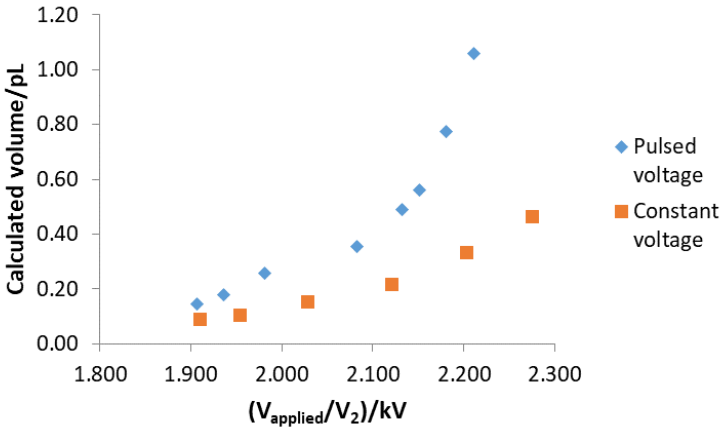

Figure 6.7: Calculated volume against the applied voltage/V_2 for a glycerol and water solution at 111 cP, 60 μS cm^{-1}, and on a 20 μm emitter.

6.2 Effect of viscosity and conductivity

This section focuses on the effect of viscosity (2.5 to 156 cP) and conductivity (60 and 600 μS cm^{-1}) on isolating and controlling the first pulsation event. Each data set was measured on a 20 μm emitter. At 600 μS cm^{-1}, the viscosity of both the 60 and 111 cP solutions was slightly higher at 67 and 156 cP.

6.2.1 Transient characteristics

As discussed in Section 6.1, different spray modes are observed depending on the magnitude of the voltage pulse. In Figure 6.1, it was shown that at a viscosity of 111 cP, and a conductivity of 60 μS cm^{-1}, a small reduction in V_{pulse} from 0.537 to 0.488 kV was required to go from cone-jet mode to full pulsations.

Figure 6.8 shows the effect of V_{pulse} for a solution with a viscosity of 2.5 cP, and conductivity of 60 μS cm^{-1}. Results show that decreasing the value of V_2 causes cone-jet mode to transition into pulsations. Figures 6.8b and 6.8c show that in between the transition from cone-jet mode to pulsations, the length of time over which cone-jet mode was observed reduces, and the number of pulsations gradually increases. The individual pulses cannot be observed due to the high frequency of the pulsations compared to the time scale at which the traces were measured. At V_{pulse}=0.267 kV, the duration of the pulse was reduced to 1.00 ms (f=500 Hz, D_c=50%) to make it easier to determine when cone-jet mode had fully transitioned to pulsations. In Section 5.2, it was shown that at a lower viscosity a higher pulsation frequency was observed, showing that the effect of viscosity on the frequency is similar in both continuous and pulsed voltage operation. At 2.5 cP, it is shown that a smaller V_{pulse} of 0.267 kV was needed to achieve pulsations, compared to 0.488 kV at 111 cP in the previous section.

Figure 6.9 shows the effect of V_{pulse} on the formation time at a conductivity of 60 μS cm^{-1}, and at a range of viscosities, where the formation time decreases for an increase in V_{pulse}. The 2.5 cP data is indicating that a smaller V_{pulse} is required

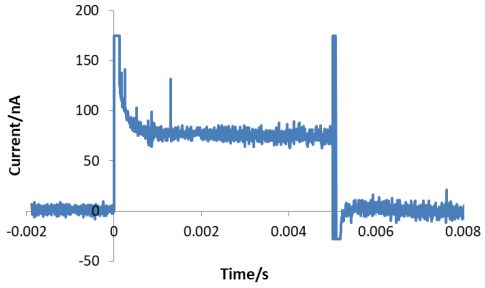

(a) V_2=2.414 kV, V_{pulse}=0.704 kV.

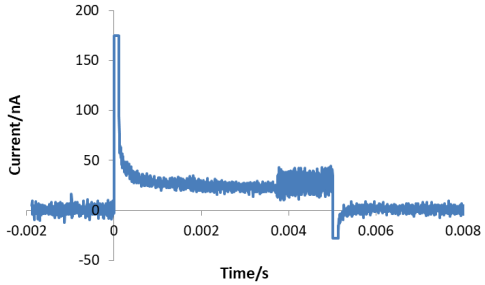

(b) V_2=2.122 kV, V_{pulse}=0.412 kV.

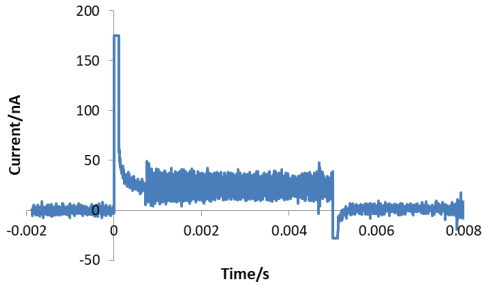

(c) V_2=2.059 kV, V_{pulse}=0.349 kV.

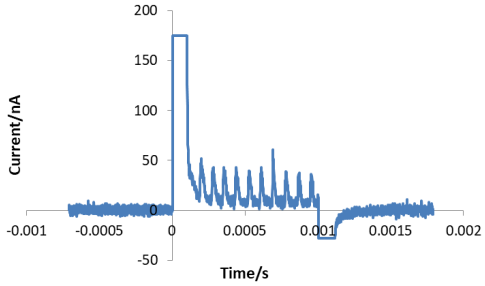

(d) V_2=1.977 kV, V_{pulse}=0.267 kV.

Figure 6.8: Current against time graphs for a glycerol and water solution at 2.5 cP, 60 μS cm^{-1}, and on a 20 μm emitter, showing the effect of voltage on the current transients where V_1=1.710 kV.

to isolate a single ejection compared to a higher viscosity. There are fewer data points at 2.5 cP as during the experiments it was found to be more difficult to control this solution, as when it was thought that the last pulse/first ejection was out of the initial discharging curve, reducing V_2 would sometimes then cause another ejection to come out of the switch ahead of what was thought to be the first ejection. The stability of this solution when pulsing the voltage was not as clear as for the higher viscosity solutions. Fitting a power law to the data in Figure 6.9, results show that at 60 and 111 cP there is no significant effect of the viscosity on the power law exponent, with 60 cP = -2.43 and 111 cP = - 2.37. At 2.5 cP, the data point V_{pulse}=0.109 kV is indicating that there would be an increase in the formation time. However, further investigations are required over a greater V_{pulse} range to fit an accurate trend to the data. There is a slight increase in $\mathrm{d}T_{\text{form}}/\mathrm{d}V_{\text{pulse}}$ from 0.044 ms kV^{-1} at 60 cP to 0.066 ms kV^{-1} at 111 cP.

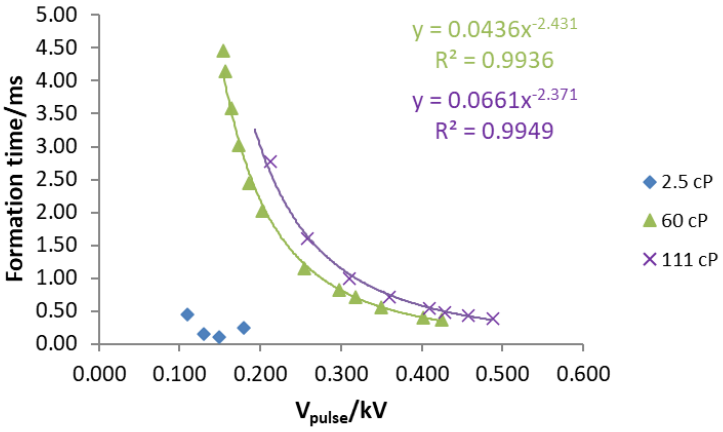

Figure 6.9: Formation time against V_{pulse} for a glycerol and water solution at 60 μS cm^{-1}, and on a 20 μm emitter.

Figure 6.10 shows the effect of V_{pulse} on spray modes at viscosities of 23 and 67 cP, at a conductivity of 600 μS cm^{-1}. Figures 6.10a and 6.10b show the effect at a V_{pulse} of 0.689 kV at 23 cP, and 0.605 kV at 67 cP, results show that both viscosities entered cone-jet mode before entering pulsations at approximately 1.00 ms. For these values of V_{pulse}, applying a pulse of 5.00 ms does not allow individual pulses to be distinguished, as discussed previously V_2 was reduced to

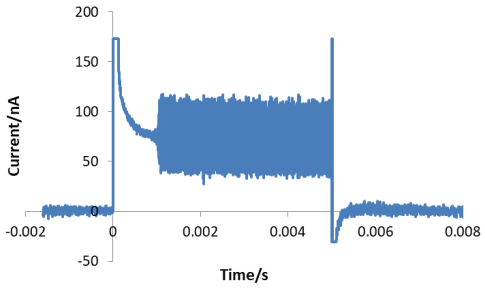

(a) 23 cP, V_2=2.491 kV, V_{pulse}=0.689 kV.

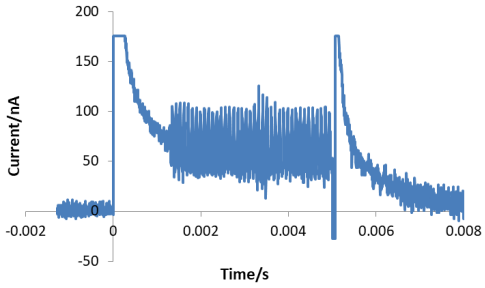

(b) 67 cP, V_2=2.407 kV, V_{pulse}=0.605 kV.

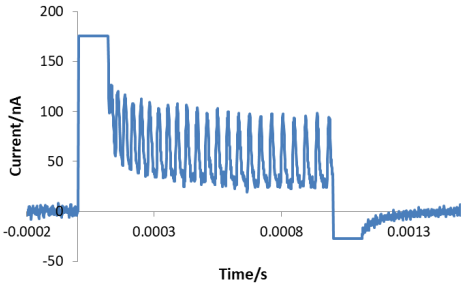

(c) 23 cP, V_2=2.359 kV, V_{pulse}=0.557 kV.

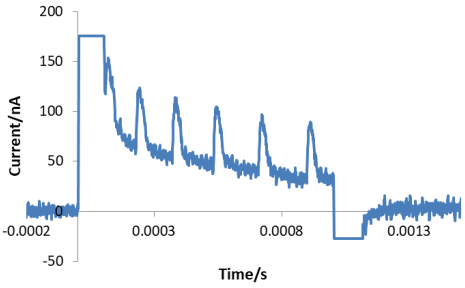

(d) 67 cP, V_2=2.074 kV, V_{pulse}=0.272 kV.

Figure 6.10: Current against time graphs at 23 and 67 cP, at 600 μS cm^{-1}, and on a 20 μm emitter, showing the effect of voltage on the current transients where V_1=1.802 kV.

a duration of 1.00 ms to observe the individual pulses, as shown in Figures 6.10c and 6.10d. Between the pulsations at 67 cP the peak of each ejection is observed, whereas at 23 cP the pulsations are closer together that each ejection is not distinguishable, due to the lower viscosity having a higher pulsation frequency.

Figures 6.10c and 6.10d show the maximum V_{pulse} required to achieve full pulsations. To achieve pulsations the lower viscosity solution required a V_{pulse} that is approximately double that of the higher viscosity. In both figures it is shown that the pulsations are not fully out of the current response from pulsing the voltage from V_1 to V_2. To achieve the shortest formation time for the first pulsation event a V_2= 2.085 kV (V_{pulse}=0.283 kV) was required at 23 cP, and V_2= 1.996 kV (V_{pulse}=0.194 kV) at 67 cP. This shows that a greater reduction in the magnitude of the voltage, was required for the lower viscosity solution to make sure that the first pulse was recorded.

The effect of V_{pulse} on the formation time at a range of viscosities and conductivity

of 600 μS cm^{-1} is shown in Figure 6.11, where results show that for all viscosities as V_{pulse} increases the formation time is shown to decrease. The effect of viscosity on the formation time with increasing V_{pulse} is not as clear as at 60 μS cm^{-1}. At 60 μS cm^{-1}, to achieve a given formation time a larger V_{pulse} was required for an increase in viscosity. At 600 μS cm^{-1}, the same trend is not observed mainly due to the formation time of the 67 cP solution having similar V_{pulse} values to the 2.5 cP solution. Fitting a power law to the data in Figure 6.11, there is no clear correlation between the viscosity and the power law exponent. The power law exponent at 23 cP is -3.73, which is slightly smaller than the -2.50 and -2.76 at 67 and 156 cP. There is an increase $\mathrm{d}T_{\text{form}}/\mathrm{d}V_{\text{pulse}}$ from 0.0011 nA kV^{-1} at 23 cP to 0.0104 nA kV^{-1} at 156 cP.

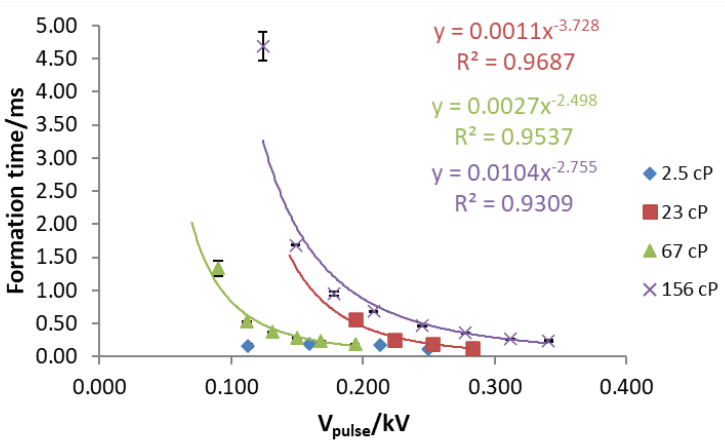

Figure 6.11: Formation time against V_{pulse} for a glycerol and water solution at 600 μS cm^{-1}, and on a 20 μm emitter.

The effect of conductivity on the formation time shows that the power law exponent decreases slightly with conductivity, from -2.43 to -2.50 at 60-67 cP, and from -2.37 to -2.76 at 111-156 cP. A clearer trend is observed in relation to $\mathrm{d}T_{\text{form}}/\mathrm{d}V_{\text{pulse}}$, where there is an order of magnitude decrease from 0.0436 to 0.0027 ms kV^{-1} at 60-67 cP, compared to a smaller reduction from 0.0661 to 0.0104 ms kV^{-1} at 111-156 cP. This is indicating that in relation to the formation time with change in V_{pulse}, the conductivity has a greater effect than viscosity at 60-67 and 111-156 cP.

Figure 6.12 shows how I_{on} increases with V_{pulse} for a range of viscosities, at both

60 and 600 μS cm^{-1}. At 60 μS cm^{-1}, results show that I_{on} generally increases with V_{pulse}, as shown in Figure 6.12a. However, not all of the data sets show the same relationship between I_{on} and V_{pulse}. Fitting a linear trend through the data at 60 and 111 cP, the value of dI_{on}/dV_{pulse} is greater for the higher viscosity solution, going from 42 nA kV^{-1} at 60 cP, to 103 nA kV^{-1} at 111 cP.

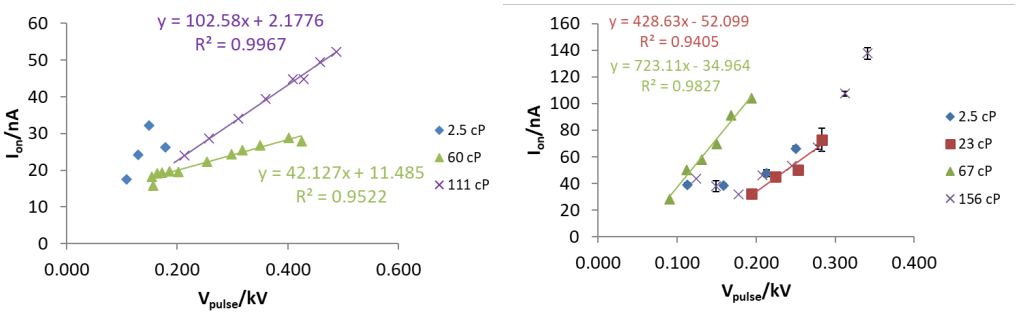

(a) 60 μS cm^{-1}. (b) 600 μS cm^{-1}.

Figure 6.12: I_{on} against V_{pulse} at a range of viscosities and conductivities on a 20 μm emitter.

Figure 6.12b shows I_{on} against V_{pulse} at 600 μS cm^{-1}, where only the 23 and 67 cP data show a linear relationship between I_{on} and V_{pulse}. However, in relation to the 23 cP case, more data is required over a larger V_{pulse} range to fully conclude the trend. Taking into account the values of dI_{on}/dV_{pulse}, the 67 cP data has a greater value at 723 nA kV^{-1} compared to 429 nA kV^{-1} at 23 cP. This is showing a similar relationship to that at 60 μS cm^{-1}, where it was shown that the higher viscosity had the greater dI_{on}/dV_{pulse}.

Comparing the magnitude of the current in Figures 6.12a and 6.12b results show that increasing the conductivity increases the current range. The value of dI_{on}/dV_{pulse} can be compared at 60-67 cP, where there is an order of magnitude increase, from 42 to 723 nA kV^{-1}.

Figure 6.13 shows how the on-time varies with increasing V_{pulse}, at 60 and 600 μS cm^{-1}. At 60 μS cm^{-1}, Figure 6.13a shows that the 2.5 cP solution has an on-time that is at least an order of magnitude smaller than that at 60 and 111 cP. However, there is no clear difference in the on-time between 60 and 111 cP. A clearer trend is observed at 600 μS cm^{-1} as shown in Figure 6.13b,

where the on-time increases with an increase in viscosity, although the on-time at each viscosity is approximately constant. The on-time at 156 cP is approximately 3.0 times that at 2.5 cP.

Comparing across both of the conductivities results show that the higher conductivity solution has a smaller on-time which varies with viscosity. At 600 μS cm^{-1}, all of the on-times are below 100 μs. At 2.5 cP, the on-time for 600 μS cm^{-1} is approximately half that of 60 μS cm^{-1}, whereas at 60-67 and 111-156 cP the on-time at 600 μS cm^{-1} is almost an order of magnitude smaller, over the V_{pulse} range measured.

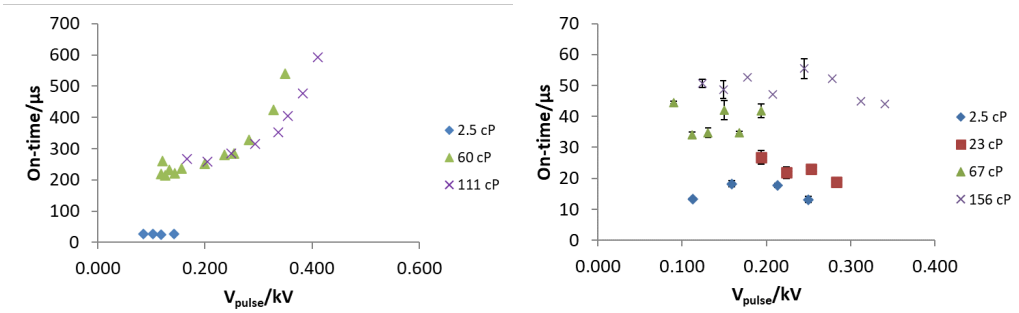

(a) 60 μS cm^{-1}. (b) 600 μS cm^{-1}.

Figure 6.13: On-time against V_{pulse} at a range of viscosities and conductivities on a 20 μm emitter.

The effect of V_{pulse} on the emitted charge at a range of viscosities is shown in Figure 6.14, at both 60 and 600 μS cm^{-1}. At 60 μS cm^{-1}, Figure 6.14a shows that the emitted charge increases with V_{pulse}, where the amount of charge emitted increases with increasing viscosity. At 600 μS cm^{-1}, Figure 6.14b shows that the trend is not as clear. Above V_{pulse}=0.130 kV the charge emitted at 67 cP is greater than that at 156 cP.

Varying the conductivity shows that over the V_{pulse} range from 0.110 to 0.340 kV a greater charge is emitted at 60 μS cm^{-1}, especially at 60-67 and 111-156 cP. In Section 5.3 it was shown that when a constant voltage is applied a greater charge is emitted the smaller the conductivity of the solution. The same observation has been shown in terms of pulsed voltage operation.

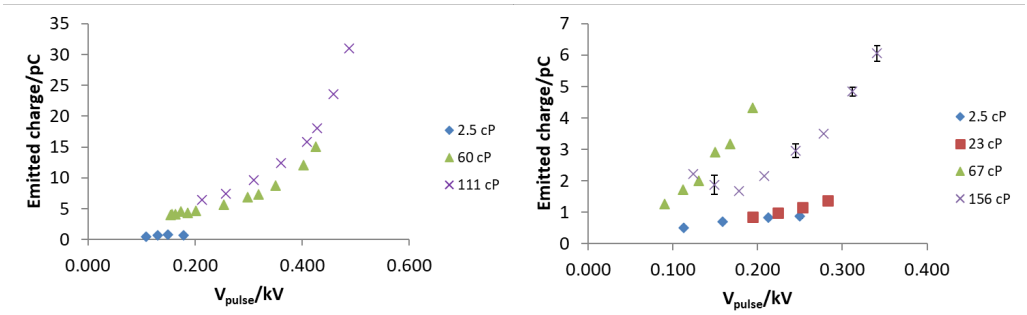

(a) 60 μS cm^{-1}. (b) 600 μS cm^{-1}.

Figure 6.14: Emitted charge against V_{pulse} at a range of viscosities and conductivities on a 20 μm emitter.

The current, on-time and charge are calculated from the current transients. To try and understand some of the observations described in this section, current transients at similar values of V_{pulse} have been plotted. Figure 6.15 shows transients at 60 μS cm^{-1}. Figures 6.15a and 6.15b, show current transients at a V_{pulse} of 0.149 to 0.154 kV, where there is an increase in the formation time with increasing viscosity. To compare the 60 and 111 cP data a greater V_{pulse} of 0.402 and 0.409 kV were chosen, as this is at a V_{pulse} in the middle of both data sets. As shown in Figures 6.15c and 6.15d, the 60 cP solution has a shorter formation time compared to 111 cP.

Similar to the data at 60 μS cm^{-1}, the 600 μS cm^{-1} data also shows differences in isolating a single ejection, especially in terms of the base current. At 600 μS cm^{-1}, the effect of the viscosity on the formation time was not as clear as it was at 60 μS cm^{-1}, where it was shown that a smaller V_{pulse} was required at 67 cP to achieve a similar formation time to that at 23 cP. Figure 6.16 takes current transients for values of V_{pulse} that are as close to each other as possible for the data measured. The values for the V_{pulse} range from 0.213 kV at 2.5 cP, 0.194 kV at 23 and 67 cP, to 0.208 kV at 156 cP, and 0.213 kV at 2.5 cP. Figures 6.16a and 6.16c show little variation in the formation time between 2.5 and 67 cP.

Figures 6.15 and 6.16 show that the duration of the voltage pulse is not necessarily constant for each solution when applying the same V_{pulse}, which is dependent on the on-time and frequency of the pulsations. The transients show examples of the

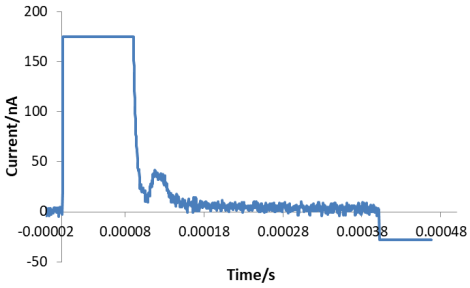

(a) 2.5 cP, V_{pulse}=0.149 kV.

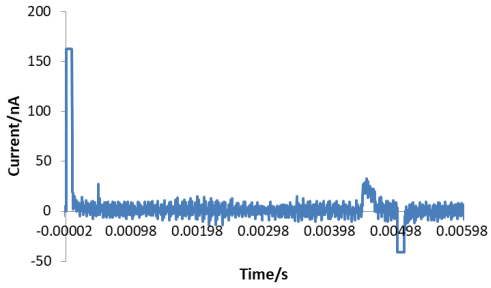

(b) 60 cP, V_{pulse}=0.154 kV.

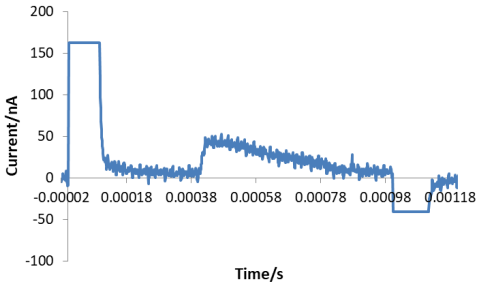

(c) 60 cP, V_{pulse}=0.402 kV.

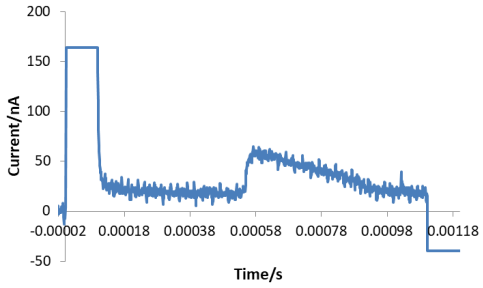

(d) 111 cP, V_{pulse}=0.409 kV.

Figure 6.15: Current against time graphs at a range of glycerol and water solutions, at 60 μS cm^{-1}, and on a 20 μm emitter.

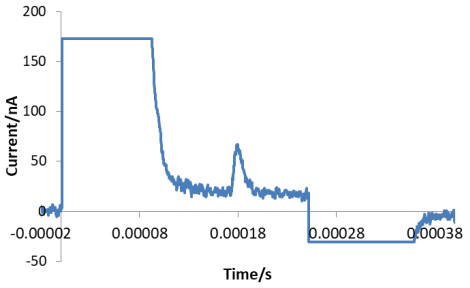

(a) 2.5 cP, V_{pulse}=0.213 kV.

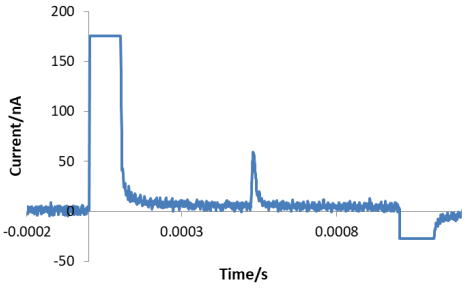

(b) 23 cP, V_{pulse}=0.194 kV.

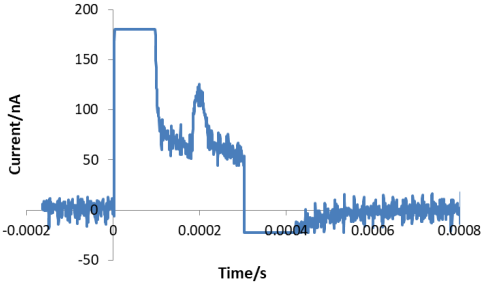

(c) 67 cP, V_{pulse}=0.194 kV.

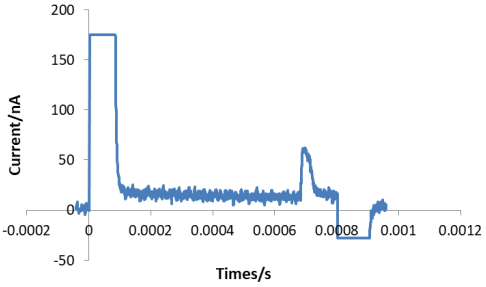

(d) 156 cP, V_{pulse}=0.208 kV.

Figure 6.16: Current against time graph at a range of glycerol and water solutions, at 600 μS cm^{-1}, and on a 20 μm emitter.

ejection process and the response to pulsing the voltage from V_1 to V_2, showing how the current varies with time, which is then used to calculate the charge and ejected volume, which are relevant for the resolution in printing applications.

6.2.2 Calculated flow rate and volume

Figure 6.17 shows the effect of V_{pulse} on the flow rate through the jet, where it is shown that as V_{pulse} increases so does Q_{jet}. The effect of viscosity on Q_{jet} shows there is no clear correlation at both 60 and 600 μS cm^{-1}. At 60 μS cm^{-1}, Figure 6.17 shows that the 111 cP data has a greater flow rate range from 0.55 to 1.79 nL s^{-1}, compared to 0.35 to 0.73 nL s^{-1} at 60 cP. The 2.5 cP data has a greater flow rate than that at both 60 and 111 cP, for the small range of V_{pulse} values over which the 2.5 cP data was recorded. At 600 μS cm^{-1}, Figure 6.17 shows that there is no real correlation between an increase in viscosity and the calculated flow rate, as the 67 cP data does not quite follow the same trend as the other viscosities, which show Q_{jet} is independent of viscosity. Therefore, the effect of viscosity on Q_{jet} at both 60 and 600 μS cm^{-1} is not as conclusive, as that observed in Section 5.2.

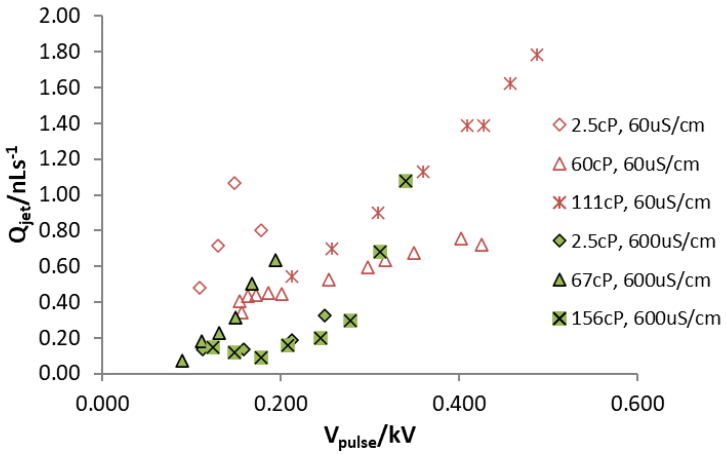

Figure 6.17: Q_{jet} against V_{pulse} at a range of viscosities and conductivities on a 20 μm emitter.

Comparing the effect of conductivity, Figure 6.17 shows a reduction in Q_{jet} with an increase in the conductivity. The slight discrepancy is that at a V_{pulse} of

0.166 kV, the 67 cP data at 600 μS cm^{-1} starts to become greater than that at 60 μS cm^{-1}, where it has been discussed that this could be due to having a non-zero base current in response to the pulsing of the voltage as shown in Figure 6.16c.

Figure 6.18 shows the calculated volume against V_{pulse}, where the volume increases with V_{pulse}. At 60 μS cm^{-1}, there is an increase in volume with viscosity especially for V_{pulse} greater than 0.360 kV, where between 60 and 111 cP the calculated volume increases by approximately 1.5 times. A similar trend is observed at 600 μS cm^{-1}, except for the 67 cP data increases at a greater rate compared with the other viscosities.

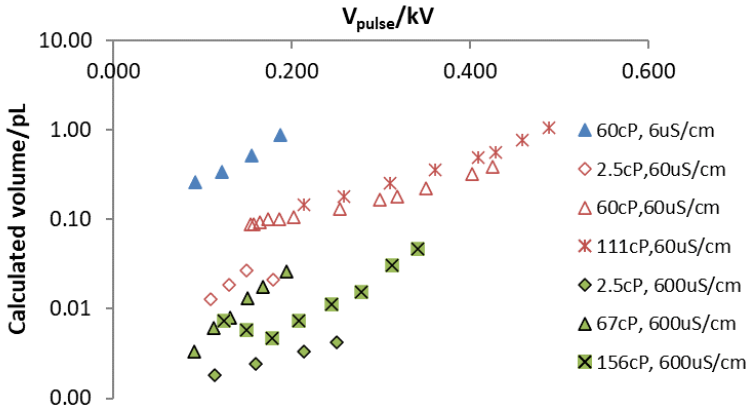

Figure 6.18: Calculated volume against V_{pulse} at a range of viscosities and conductivities on a 20 μm emitter.

At 60 cP there are calculated volumes from tests at a conductivity of 6 μS cm^{-1} for comparison, where results show that the 6 μS cm^{-1} data has a greater volume than that at both 60 and 600 μS cm^{-1}. At a constant V_{pulse} of 0.155 kV, the ejected volume decreases from 0.52 pL at 6 μS cm^{-1}, to 0.105 pL at 60 μS cm^{-1}, and then to 0.017 pL at 600μS cm^{-1}. In Chapter 5, it was shown that the ejected volume decreased with an increase in the conductivity. Therefore, the general trend for both continuous and pulsed voltage operation, is that to achieve a smaller volume a higher conductivity is required.

6.3 Effect of viscosity and emitter geometry

This section focuses on the effect of viscosity (2.5 to 111 cP) and emitter outer diameter (10 to 40 μm) on isolating and controlling the first ejection. Each data set was measured at a conductivity of 60 μS cm^{-1}.

6.3.1 Transient characteristics

To compare the effect of the emitter geometry in pulsed voltage operation the data is going to be plotted against the jump in electrical bond number (ΔBo_e), where Bo_e is given by Equation 2.3.43. The effect of the viscosity with ΔBo_e is shown in Figures 6.19 and 6.20, on both a 10 and 40 μm emitter. Results on a 20 μm emitter were shown and discussed Section 6.2 in relation to V_{pulse}. All three emitter geometries show that the formation time decreases for an increase in $V_{\text{pulse}}/\Delta Bo_e$, where a power law fits to each of the data sets.

Plotting the formation time against ΔBo_e at a range of viscosities when using a 10 μm emitter is shown in Figure 6.19. Fitting a power law to each of the data sets results indicate that a slightly higher ΔBo_e should be needed the higher in viscosity the solution. The exponent of the power law decreases from -2.01 at 23 cP to -3.11 at 111 cP, whereas the value of $\mathrm{d}T_{\text{form}}/\mathrm{d}\Delta Bo_e$ shows no clear correlation with an increase in viscosity.

Figure 6.20 shows the formation time against ΔBo_e when using a 40 μm emitter, where results also show that generally as the viscosity increases a greater ΔBo_e is required to achieve a similar formation time as a lower viscosity solution. The 2.5 cP solution requires a smaller ΔBo_e to achieve a formation time below 1.00 ms compared to the other viscosities. At ΔBo_e of 1.5, the 23, 60 and 111 cP data sets all have similar formation times of 0.40 to 0.50 ms. Fitting a power law to each of the data sets, results show no clear correlation between the exponent and the viscosity. The value of the exponent at 23 and 60 cP are -2.25 and -2.23, where at 2.5 and 111 cP the exponents equal -3.14 and -2.86. In terms of the

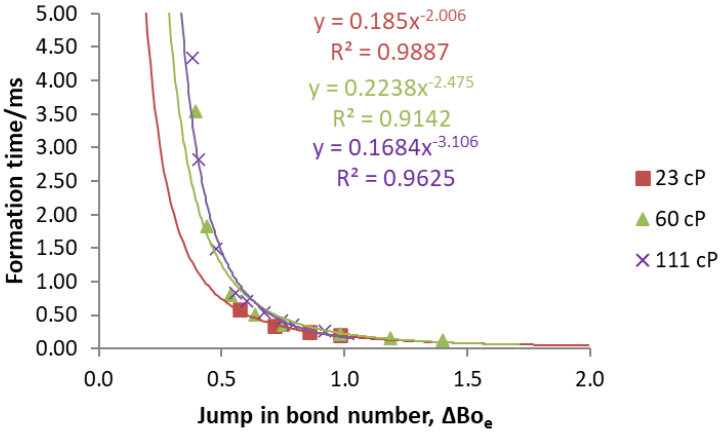

Figure 6.19: Formation time against ΔBo_e for a glycerol and water solution at 60 μS cm^{-1}, and on a 10 μm emitter.

effect of viscosity on $\mathrm{d}T_{\mathrm{form}}/\mathrm{d}\Delta Bo_e$, the 2.5 cP solution has the smallest value of 0.24 ms, but there is no clear trend between 23 and 60 cP, with an increase to 2.66 ms at 111 cP.

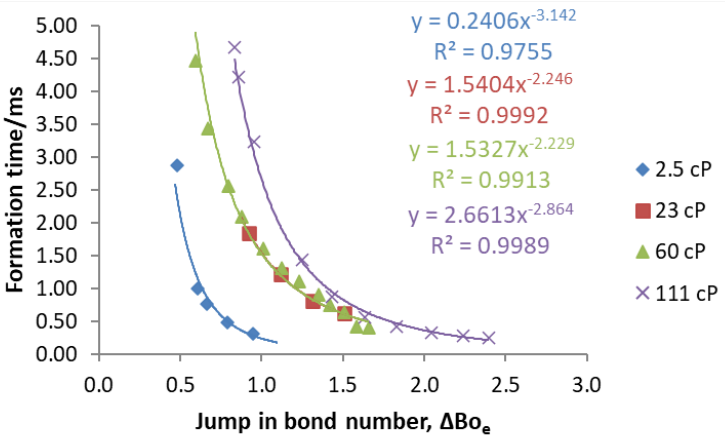

Figure 6.20: Formation time against ΔBo_e for a glycerol and water solution at 60 μS cm^{-1}, and on a 40 μm emitter.

Comparing the power law fitted to each of the data sets across all three emitter geometries, results show that there is little effect of the emitter size on the power law exponent. Across all three emitter sizes, the power law exponent for the 60 cP data are -2.48 at 10 μm, -2.27 at 20 μm, and -2.23 at 40 μm, this is showing that the exponent is approximately independent of the emitter OD. A similar result was observed at 111 cP with the power law exponent equalling -3.18 at 10 μm, -2.18 at 20 μm, and -2.86 at 40 μm. However, even though the 23 cP data only

has data at 10 and 40 μm, there is little effect on the power law exponent, with -2.01 at 10 μm and -2.25 at 40 μm. Therefore, results are indicating that the emitter OD has little effect on the power law exponent when a constant V_1 is applied. The effect of the emitter OD on $\mathrm{d}T_{\mathrm{form}}/\mathrm{d}\Delta Bo_e$ is not conclusive either. Across all three emitters from 10 to 40 μm $\mathrm{d}T_{\mathrm{form}}/\mathrm{d}\Delta Bo_e$ generally increases with viscosity, however at 60 cP on the 20 μm emitter $\mathrm{d}T_{\mathrm{form}}/\mathrm{d}\Delta Bo_e$ is 2.38 ms which is greater than at 40 μm.

The effect of ΔBo_e on I_{on} is shown in Figure 6.21 using both a 10 and 40 μm emitter. Results show that in both experimental conditions, I_{on} increases linearly with ΔBo_e, and generally increases with viscosity. On the 10 μm emitter, Figure 6.21a shows that $\mathrm{d}I_{\mathrm{on}}/\mathrm{d}\Delta Bo_e$ increases with viscosity from 8.84 nA at 23 cP to 19.09 nA at 111 cP. In Figure 6.21b on the 40 μm emitter the trend with $\mathrm{d}I_{\mathrm{on}}/\mathrm{d}\Delta Bo_e$ is not as clear, with the 2.5 and 60 cP solutions having similar values of $\mathrm{d}I_{\mathrm{on}}/\mathrm{d}\Delta Bo_e$ at 16.55 and 17.09 nA, compared with 27.97 nA at 23 cP and 31.44 nA at 111 cP.

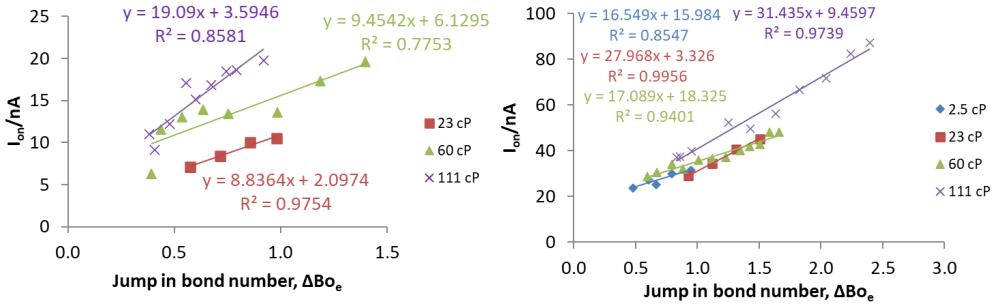

(a) 10 μm. (b) 40 μm.

Figure 6.21: I_{on} against ΔBo_e at a range of viscosities and emitter geometries at a conductivity of 60 μS cm^{-1}.

For each viscosity, as the emitter increases the value of I_{on} also increases for the range of ΔBo_e values over which the data was measured. Increasing the size of the emitter from 10 to 20 μm decreases the values of $\mathrm{d}I_{\mathrm{on}}/\mathrm{d}\Delta Bo_e$ from 9.45 to 7.49 nA at 60 cP, and from 19.09 to 17.22 nA at 111 cP. An increase in $\mathrm{d}I_{\mathrm{on}}/\mathrm{d}\Delta Bo_e$ is observed from 20 to 40 μm, from 7.49 to 17.09 nA at 60 cP, and from 17.22 to 31.44 nA at 111 cP.

On both a 10 and 40 μm emitter Figure 6.22 shows the effect of ΔBo_e on the on-time of the pulse. Using a 10 μm emitter, Figure 6.22a shows that for each viscosity there is no trend between the on-time and ΔBo_e. However, it is shown that generally a smaller on-time is produced for a higher viscosity solution. A similar observation is found in Figure 6.22b, this time on a 40 μm emitter. Results show that the 111 cP data has a smaller on-time then the 23 and 60 cP solutions. At 2.5 cP, the on-time is similar to that at 111 cP, except the data has been measured over a smaller ΔBo_e range.

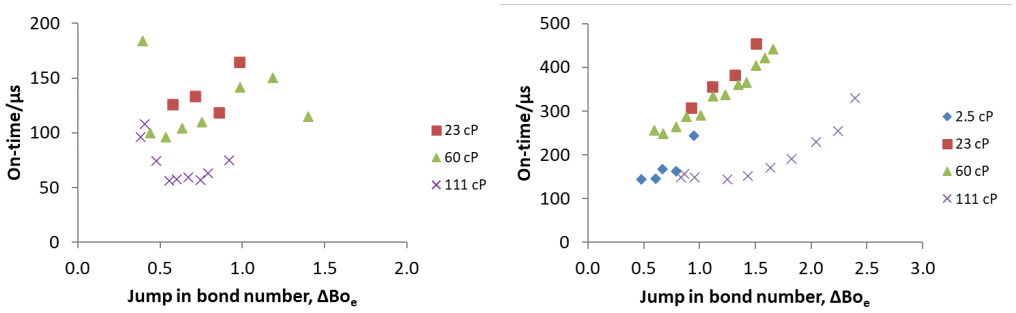

(a) 10 μm. (b) 40 μm.

Figure 6.22: On-time against ΔBo_e at a range of viscosities and emitter geometries at a conductivity of 60 μS cm^{-1}.

To understand the effect of emitter geometry, Figure 6.23 shows the on-time against ΔBo_e at 60 and 111 cP. Both sets of results show agreement in that the 10 μm data has the shortest on-time. This result agrees with that shown in Section 5.4, when the emitter OD was varied and a constant voltage was applied. However, there is disagreement between the 20 and 40 μm sets of data. At 60 cP, the trend follows that in Section 5.4, where it was shown that the on-time increases with an increase in the emitter OD. The 111 cP data on the other hand shows the opposite, in that the 20 μm data set has a larger on-time than that at 40 μm. Comparing the 2.5 cP data between 20 and 40 μm, the results are in agreement with the 60 cP data set, in that the 40 μm emitter has the larger on-time. At 2.5 cP, the on-time at 20 μm ranges from 25 to 27 μs, and from 142 to 243 μs at 40 μm. This is in agreement with what would be expected from when a constant voltage/field strength was applied.

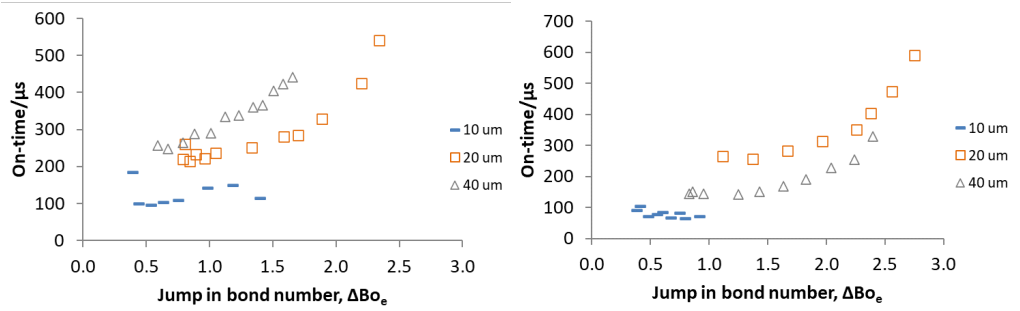

(a) 60 cP. (b) 111 cP.

Figure 6.23: On-time against ΔBo_e at a range of viscosities and emitter geometries at a conductivity of 60 μS cm^{-1}.

Figure 6.24 shows current transients for the 111 cP solution, at ΔBo_e=1.2±0.2 and 2.3±0.1, on a 20 and 40 μm emitter. There is a transient at 10 μm at an ΔBo_e of 1.2±0.2, but not at 2.3±0.1 due to the smaller range of ΔBo_e values at 10 μm. At ΔBo_e=1.2±0.2, Figure 6.24a shows that the 40 μm emitter has a pulse with a greater peak current of approximately 80 nA compared to 49 nA at 20 μm, and 33 nA at 10 μm. Each trace has a base current in the range of 0 to 12 nA. Between the 20 and 40 μm data sets there is a clear difference in the shape of the pulse. Figure 6.24b shows current transients at ΔBo_e=2.3±0.1, where again the 40 μm data has a greater peak current of 125 nA compared to 62 nA at 20 μm. However, compared to ΔBo_e of 1.2±0.2 there is a difference in the base current with I_{base} being 2.5 times greater at 40 μm. As discussed in Section 6.2, results have shown no clear correlation in which variables affect the non-zero base current at higher values of $V_{\text{pulse}}/\Delta Bo_e$.

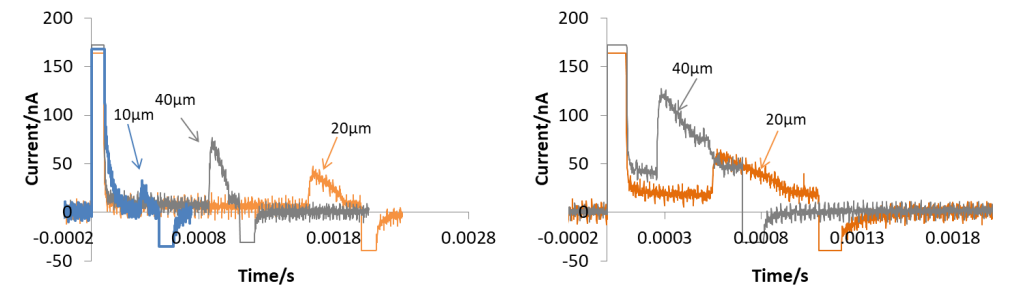

(a) ΔBo_e=1.2±0.2. (b) ΔBo_e=2.3±0.1.

Figure 6.24: Current against time graphs for a glycerol and water solution with μ=111 cP, and K=60 μS cm^{-1}.

The emitted charge against ΔBo_e is shown in Figure 6.25, for both a 10 and 40 μm emitter. Across each of the emitter sizes, the effect of viscosity is not consistent on the amount of charge emitted. On the 10 μm emitter, results in Figure 6.25a are showing no clear effect of viscosity on the emitted charge. In Section 6.2, it was shown that on a 20 μm emitter the amount of charge emitted increased the higher in viscosity the solution. Whereas on the 40 μm emitter results in Figure 6.25b show no clear variation, with the 2.5 and 111 cP solutions having the lowest emitted charge, compared with that at 23 and 60 cP.

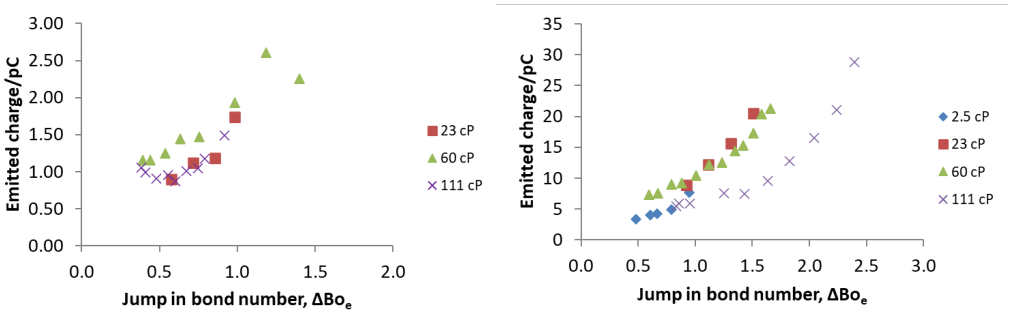

(a) 10 μm. (b) 40 μm.

Figure 6.25: Emitted charge against ΔBo_e at a range of viscosities and emitter geometries at a conductivity of 60 μS cm^{-1}.

Taking both the 60 and 111 cP data, where there are results across all three emitters, Figure 6.26b shows the effect of emitter geometry. Both the 60 and 111 cP solutions show that the 10 μm emitter emits less charge compared with that at 20 and 40 μm. This is consistent with the effect of emitter geometry on the emitted charge during the application of a constant voltage. Similar to the on-time, the 111 cP data does not continue to follow this trend, where results show little variation in the emitted charge between the 20 and 40 μm emitter.

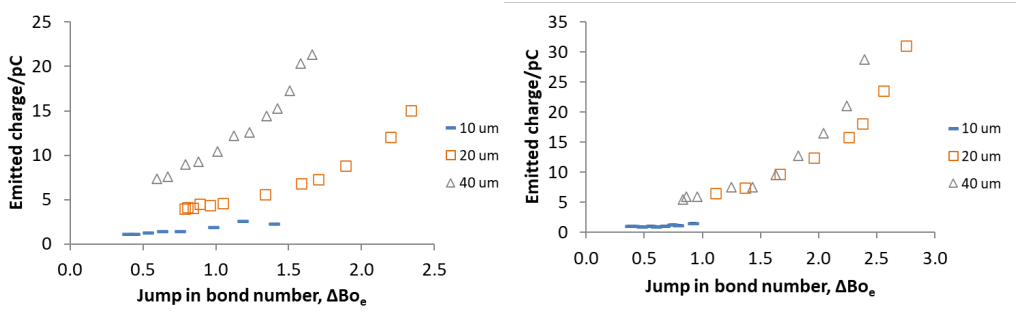

(a) 60 cP. (b) 111 cP.

Figure 6.26: Emitted charge against ΔBo_e at a range of viscosities and emitter geometries at a conductivity of 60 μS cm^{-1}.

6.3.2 Calculated flow rate and volume

The effect of ΔBo_e on Q_{jet} for a range of viscosities and emitter ODs is shown in Figure 6.27, where an increase in ΔBo_e results in an increase in Q_{jet}. Results show that for each emitter OD the effect of viscosity on Q_{jet} is not conclusive. On both the 10 and 20 μm emitters, Q_{jet} increases with viscosity, especially at higher values of ΔBo_e, whereas at 40 μm Q_{jet} is largely independent of viscosity. An increase in emitter increases Q_{jet}.

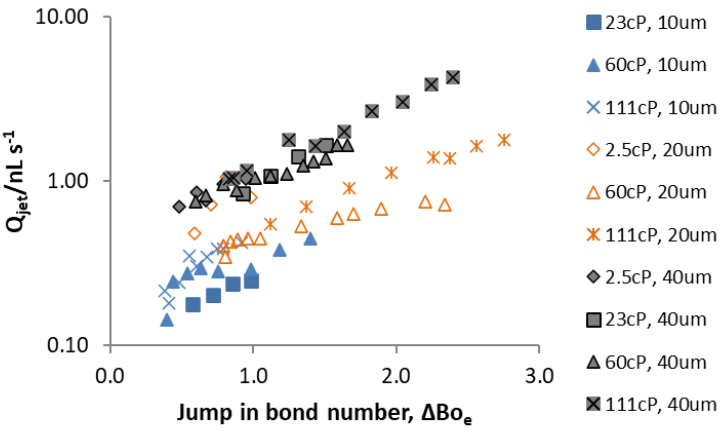

Figure 6.27: Q_{jet} against ΔBo_e at a range of viscosities and emitter geometries at a conductivity of 60 μS cm^{-1}.

Figure 6.28 shows the calculated volume against ΔBo_e, where results show that at each viscosity and on each emitter the smallest volume ejected is at the lowest ΔBo_e. The effect of viscosity on the volume is not as conclusive for each emitter

size. However, results show that increasing the size of the emitter increases the ejected volume.

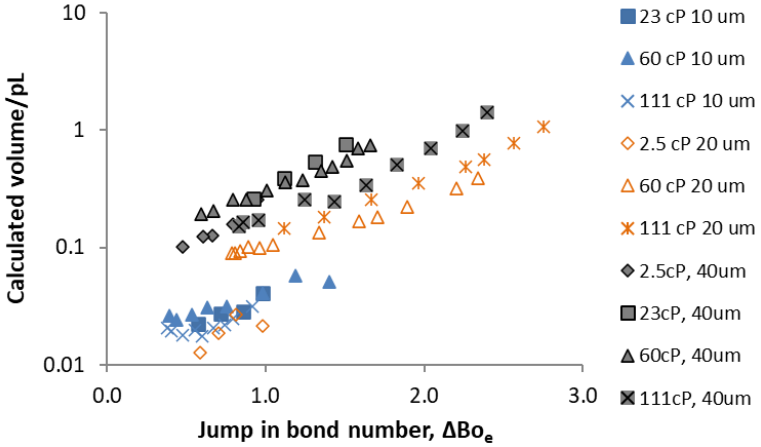

Figure 6.28: Calculated volume against ΔBo_e at a range of viscosities and emitter geometries at a conductivity of 60 μS cm^{-1}.

6.4 Effect of conductivity and emitter geometry

This section focuses on the effect of conductivity (6 and 600 μS cm^{-1}) and emitter geometry (10 to 40 μm) on isolating and controlling the first ejection. Each data set was measured at a viscosity of 60-67 cP. At 600 μS cm^{-1}, the viscosity of the 60 cP solution increased slightly to 67 cP.

6.4.1 Transient characteristics

The effect of ΔBo_e on the formation time on a range of emitter ODs is shown in Figure 6.29, where it is shown that the formation time decreases for an increase in ΔBo_e. Figure 6.29a shows the effect of emitter OD on the formation time at 6 μS cm^{-1}. Fitting a power law to each of the data sets, results show that the exponent increases from -3.92 to -2.29 as the emitter OD increases. However, more data points are required at 10 and 20 μm to fully conclude the trend being observed. The values of $\mathrm{d}T_{\mathrm{form}}/\mathrm{d}\Delta Bo_e$ show that as the emitter is increased, $\mathrm{d}T_{\mathrm{form}}/\mathrm{d}\Delta Bo_e$ increases from 0.04 ms at 10 μm to 0.83 ms at 40 μm.

Figures 6.29b and 6.29c show the effect of ΔBo_e on the formation time on a range of emitter ODs at 60 and 600 μS cm^{-1}. At 60 μS cm^{-1}, the power law exponent of ΔBo_e increases with emitter OD from -2.48 to -2.23, whereas at 600 μS cm^{-1} there is a reduction from -2.44 to -2.81. Both data sets generally show an increase in $\mathrm{d}T_{\mathrm{form}}/\mathrm{d}\Delta Bo_e$ with emitter OD, except on the 20 μm data set at 60 μS cm^{-1} which has a slightly greater $\mathrm{d}T_{\mathrm{form}}/\mathrm{d}\Delta Bo_e$.

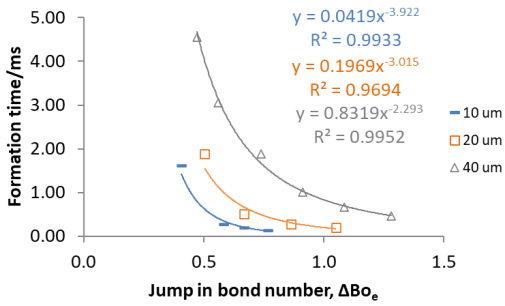

(a) 6 μS cm^{-1}.

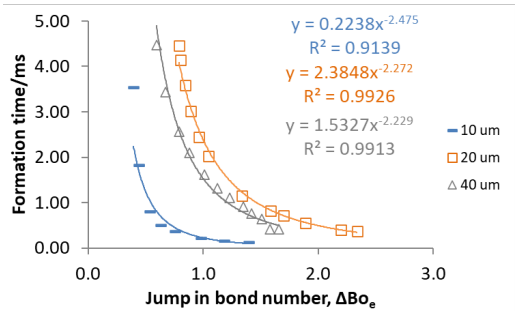

(b) 60 μS cm^{-1}.

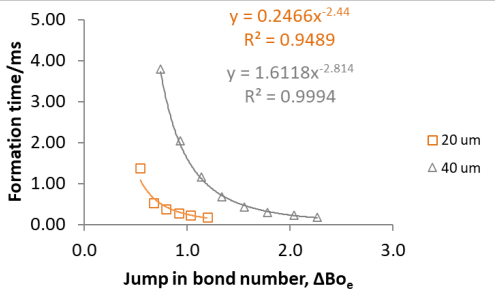

(c) 600 μS cm^{-1}.

Figure 6.29: Effect of emitter geometry and conductivity on the formation time against ΔBo_e at μ=60-67 cP.

Results in Figure 6.29 show slightly different trends in the power law exponent and $\mathrm{d}T_{\mathrm{form}}/\mathrm{d}\Delta Bo_e$ with the change in conductivity. Taking the power law exponents across each emitter separately, both the 10 and 20 μm data sets show an increase in the exponent as the conductivity increases from 6 to 60 μS cm^{-1}, with a slight decrease on the 20 μm at 600 μS cm^{-1}. At 40μm, there is no variation in the power law exponent between 6 and 60 μS cm^{-1}, with a slight decrease observed at 600 μS cm^{-1}. Increasing the conductivity from 6 to 60 μS cm^{-1}, results show an increase in $\mathrm{d}T_{\mathrm{form}}/\mathrm{d}\Delta Bo_e$ on the 20 and 40 μm emitters. The same trend is not observed when going from 60 to 600 μS cm^{-1} on the 20 μm emitter, whereas at 40 μm $\mathrm{d}T_{\mathrm{form}}/\mathrm{d}\Delta Bo_e$ increases.

The effect of ΔBo_e on I_{on} is shown in Figure 6.30, where results show that for each emitter OD and conductivity I_{on} increases linearly with ΔBo_e. At each conductivity and similar values of ΔBo_e the 10 μm data has the smallest I_{on}. Generally I_{on} increases with emitter OD except at 6 μS cm^{-1} above ΔBo_e=0.8, and at 600 μS cm^{-1}. Across each of the conductivities tested there is no clear conclusion as to the effect of the emitter OD on dI_{on}/dΔBo_e, with there being fluctuations in trend depending on the conductivity.

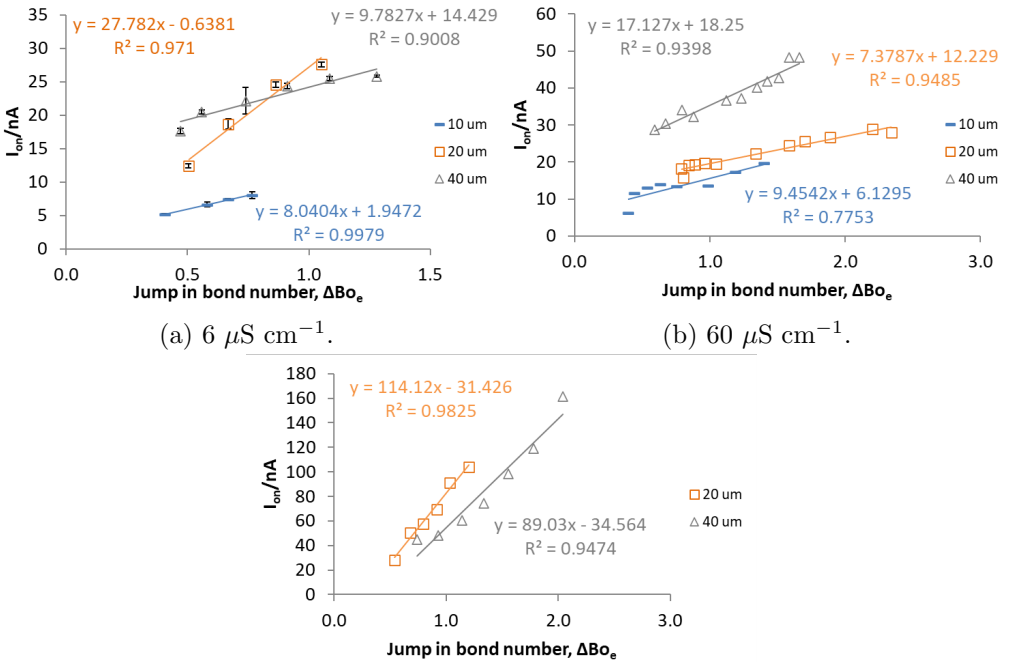

(a) 6 μS cm^{-1}. (b) 60 μS cm^{-1}.

(c) 600 μS cm^{-1}.

Figure 6.30: Effect of emitter geometry and conductivity on I_{on} against ΔBo_e at μ=60-67 cP.

Results show that increasing the conductivity generally increases the I_{on} range achieved for the jump in bond numbers tested. Except for the 20 μm, results at 10 μm indicate an increase in dI_{on}/dΔBo_e, whereas at 40 μm there is a clear increase in dI_{on}/dΔBo_e with conductivity.

The effect of ΔBo_e on the on-time at a range of emitter ODs is shown in Figures 6.23a and 6.31, where the trends show that the on-time is greater for the larger emitter OD. Results also show that the on-time does not always increase with increasing ΔBo_e. There is no correlation between process parameters as to how

and if the on-time will increase with ΔBo_e. Results show that the on-time can fluctuate especially at smaller values of ΔBo_e.

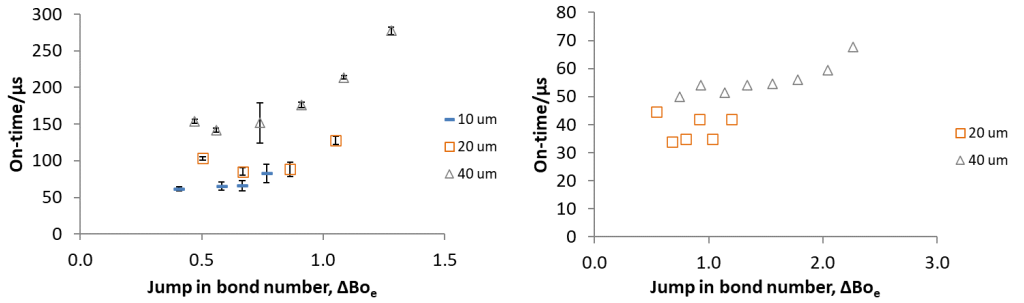

(a) 6 μS cm^{-1}. (b) 600 μS cm^{-1}.

Figure 6.31: Effect of emitter geometry and conductivity on the on-time against ΔBo_e at μ=60-67 cP.

Figures 6.26a and 6.32 show the emitted charge against ΔBo_e at each conductivity, where the general trend shows that the charge emitted increases with an increase in both ΔBo_e and the emitter OD.

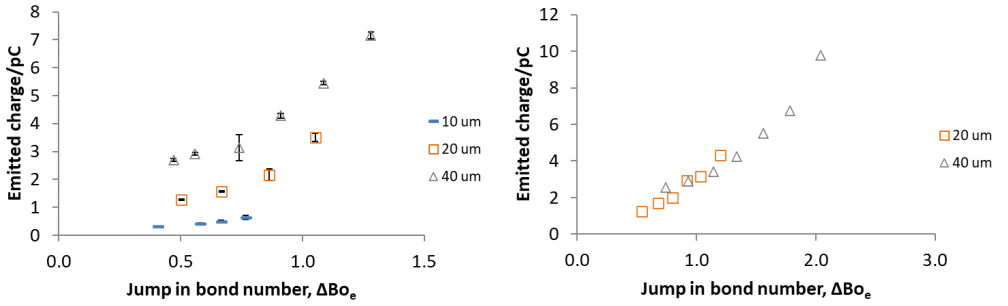

(a) 6 μS cm^{-1}. (b) 600 μS cm^{-1}.

Figure 6.32: Effect of emitter geometry and conductivity on the emitted charge against ΔBo_e at μ=60-67 cP.

6.4.2 Calculated flow rate and volume

The flow rate through the jet against ΔBo_e is shown in Figure 6.33. Independent of the variation in conductivity, the general trends show that Q_{jet} increases with an increase in both ΔBo_e and the emitter OD. The effect of the conductivity shows that over each of the ΔBo_e ranges tested, Q_{jet} decreases for an increase in the conductivity. Both of these observations in pulsed voltage operation are in agreement with trends shown in Chapter 5, when a constant voltage was applied.

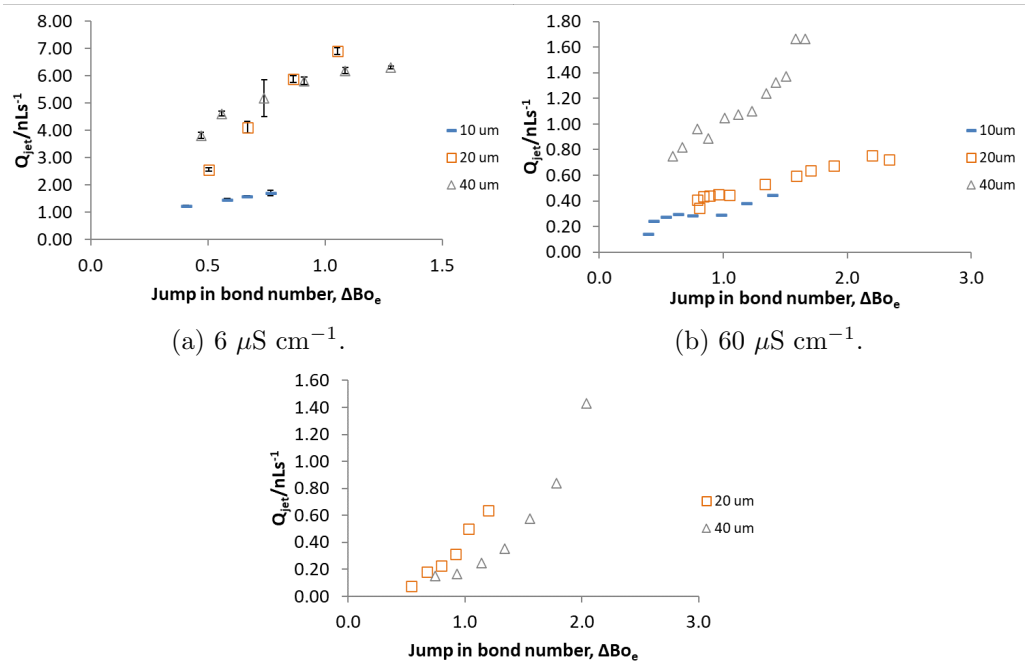

(a) 6 μS cm^{-1}.

(b) 60 μS cm^{-1}.

(c) 600 μS cm^{-1}.

Figure 6.33: Effect of emitter geometry and conductivity on Q_{jet} against ΔBo_e at μ=60-67 cP.

The calculated volume also shows that at a constant conductivity, the volume increases with increasing ΔBo_e and emitter OD as shown in Figure 6.34. Comparing the effect of the conductivity on the ejected volume, Figure 6.34 shows that for the range of ΔBo_e values tested, a smaller volume is ejected the higher in conductivity the solution, reducing by at least an order of magnitude. The same effect of a smaller ejected volume for a smaller emitter OD, and higher conductivity was also reported in Chapter 5.

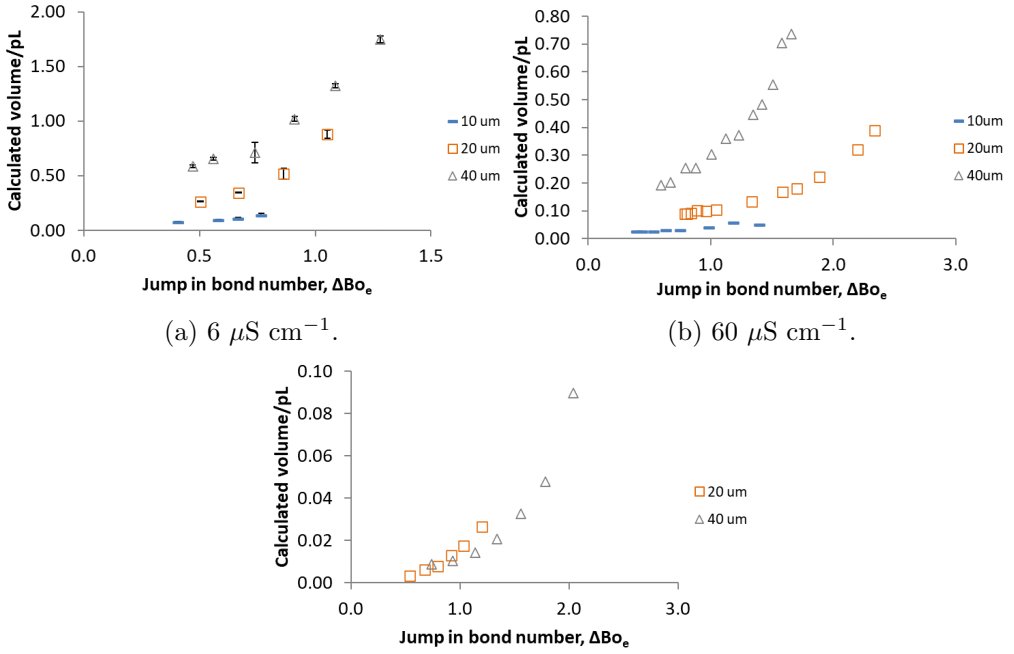

(a) 6 μS cm^{-1}.

(b) 60 μS cm^{-1}.

(c) 600 μS cm^{-1}.

Figure 6.34: Effect of emitter geometry and conductivity on the calculated volume against ΔBo_e at μ=60-67 cP.

6.5 Non-dimensional analysis

As shown in Section 5.5 in constant voltage operation, the charge can be plotted in non-dimensional form, Figure 6.35 shows q/q_0 against ζ_q in pulsed voltage operation. As discussed in Section 5.5 the non-dimensional values do not account for the change in ΔBo_e, which when plotting the best fit through all of the data leads to a poor R^2 value of 0.30, and $q/q_0 = 2169\zeta_q^{1.22}$. Taking the average q/q_0 there is still a poor R^2 value of 0.47, with $q/q_0 = 2276\zeta_q^{1.20}$. In pulsed voltage operation $\mathrm{d}q/q_0/\mathrm{d}\zeta_q$ is several orders of magnitude greater that shown by the Gañán-Calvo et al. [2016] scaling. As discussed for constant voltage operation the work by Gañán-Calvo et al. [2016] focuses on the first drop from the transient, whereas in the present work the focus is on the entire pulsation process, and the total emitted charge.

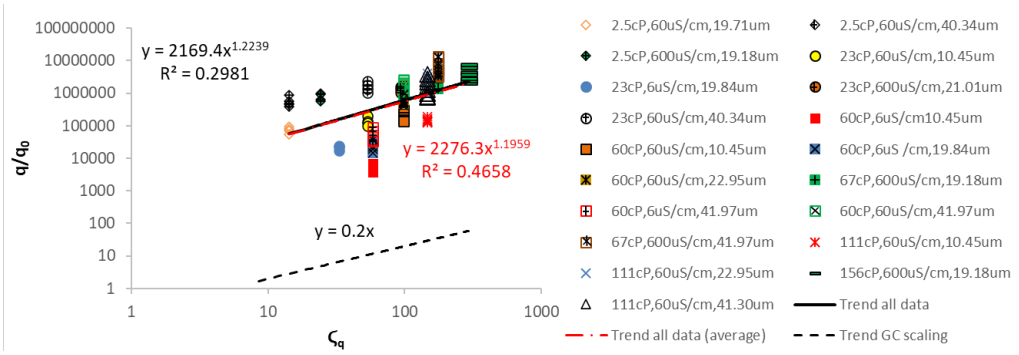

Figure 6.35: Dimensionless charge (q/q_0) against ζ_q, where $\zeta_q = \delta_\mu^{-2/3}\epsilon^{7/12}$ for a range of glycerol and water solutions on a range of emitter ODs.

6.6 Summary and discussion

This chapter has shown the effects that varying the viscosity, conductivity, and emitter geometry have on controlling the spray mode/ejection process during pulsed voltage nanoelectrospray operation. Results have shown that the magnitude of the voltage is important in both the spray mode of the ejection, and the formation time. Across all solutions tested, results have shown that the formation time decreases for an increase in V_2, and therefore $V_{\text{pulse}}/\Delta Bo_e$. This is in agreement with previous literature in both forced and unforced electrospray operation (Paine et al. [2007b]; Paine [2009]; Lee et al. [2012b]; Obata et al. [2015]).

In the present results it was shown that the power law exponent ranged from -2.00 to -3.18, but there was no clear correlation as to the effect of each of the variables. In majority of cases the power law exponent was constant and around -2.20 to -2.40.

In Sections 6.2 and 6.3, results showed that generally $\mathrm{d}T_{\text{form}}/\mathrm{d}V_{\text{pulse}}$ and $\mathrm{d}T_{\text{form}}/\mathrm{d}\Delta Bo_e$ increased with an increase in viscosity. Increasing the conductivity, as shown in Sections 6.2 and 6.4 results showed there was generally a reduction in $\mathrm{d}T_{\text{form}}/\mathrm{d}V_{\text{pulse}}(\Delta Bo_e)$, except at 60 cP between 6 and 60 μS cm^{-1}, where an increase in $\mathrm{d}T_{\text{form}}/\mathrm{d}\Delta Bo_e$ was observed. Results in Sections 6.3 and 6.4 showed that the effect of the emitter OD on $\mathrm{d}T_{\text{form}}/\mathrm{d}\Delta Bo_e$

was not as conclusive. It has been discussed before that to fully conclude and build upon the results discussed in this chapter a wider range of viscosities, conductivities and emitter geometries need to be tested. This will give a much broader range of parameters to clarify the behaviours discussed above.

It has been shown that in general an increased $V_{\text{pulse}}/\Delta Bo_e$ is required to start ejections/achieve ejections for a given formation time, for an increase in viscosity and emitter OD. Paine [2009] suggested that there could be a role of inertia when switching the voltage. It was shown that a lower V_2 was required for a smaller V_1. It was suggested that due to the meniscus being less deformed, there would be a greater momentum due to the meniscus having further to move to form a jet. The Reynold's number gives the ratio between inertia and viscous forces and is given by

$$R_e = \frac{\rho Q}{\pi r \mu}, \tag{6.6.1}$$

(Zhang and Basaran [1996]). For a flow rate of 2 nL s^{-1}, using a triethylene glycol solution on an emitter with r_c=15 μm, and using $r = r_j$, Paine [2009] calculated the Reynold's number to be 0.55. It was suggested that inertia might be starting to play a role in deforming the meniscus. For the present experiments comparing the Reynold's number at the lowest and highest viscosity, across emitters, where $Q = Q_{\text{jet}}$ and $r = r_j$ calculated from Equation 2.3.33. At 2.5 cP, R_e ranges from 0.36 to 0.49 on a 20 μm emitter, and from 0.46 to 0.59 on a 40 μm emitter. At 111 cP, R_e ranges from 0.006 to 0.009 on a 10 μm emitter, 0.011 to 0.024 on a 20 μm emitter, and from 0.017 to 0.044 on a 40 μm emitter. Physically it would be expected that for inertia to be more dominant $R_e > 1$, however it does show that the viscous forces reduce the lower the viscosity of the solution which would be expected from Equation 6.6.1. In the present experiments since Q_{jet} is largely independent of the viscosity $R_e \sim \mu^{-1}$. In terms of the emitter OD, Q_{jet} is dependent on the emitter OD therefore $R_e \sim Q/r$.

Calculated volume

In this chapter the effect of viscosity, conductivity and emitter geometry have been shown to affect the ejected volume, where the volume has been calculated from the current transients. Results have shown that the volume increases for an increase in $V_{\text{pulse}}/\Delta Bo_e$.

The effect of viscosity on the calculated volume depends on the conductivity and emitter OD. On a 20 μm emitter increasing the viscosity generally increased the ejected volume, whereas on a 10 and 40 μm emitter there was no clear correlation. The effect of conductivity on the ejected volume, showed a very clear result across all different combinations of viscosity and conductivity. During pulsed voltage nanoelectrospray, results showed that increasing the conductivity reduced the size of the deposit. The effect of the conductivity, and the emitter geometry showed a clear trend in that a larger emitter ejected a larger volume across all parameter combinations tested.

This chapter has shown that in nanoelectrospray a single ejection can be controlled for a range of viscosities, conductivities and emitter geometries. The formation time, pulse characteristics and ejected volume all depend on the combination of these parameters, with an important parameter being that of the magnitude of the pulsed voltage. There have been clear trends observed for certain variables, however further investigations are required at a larger range of viscosities and emitter geometries to understand some of the trends observed. This will help with further optimisation for using nanoelectrospray for controlled ejections.

7

Pulsed voltage nanoelectrospray: Effect of emitter-to-substrate distance and nanoelectrospray printing

This chapter focuses on the effect of the emitter-to-substrate distance (ESD) on nanoelectrospray behaviour, in pulsed voltage operation. The liquid properties (viscosity, and conductivity) and emitter geometry have been varied, with the main focus being on the trends with a change in the emitter-to-substrate distance. This work is investigating how the emitter-to-substrate distance affects the spray mode/pulse shape, the formation time, and the ejected volume. The main interest is the behaviour of the first ejection, which was isolated by altering the frequency (f) and duty cycle (D_c) of the voltage pulse. As discussed in Chapter 5 the flow rate has been calculated from current measurements using established scaling laws, and the volume calculated from the flow rate and the on-time of the ejection. In Section 3.2.1.2 it was discussed how the substrate was monitored to avoid a large build-up of liquid, and at an ESD where a discrete droplet was produced the substrate was moved between each deposit.

7.1 Effect of the emitter-to-substrate distance and the effect of the applied voltage

This section focuses on the effect of the ESD on the formation time, the flow rate, and the calculated volume, that have been calculated from the current transients.

A range of different viscosity and conductivity solutions, on both a 20 and 40 μm emitter have been selected, where the main interest is on the trends with ESD, rather than the effect of the liquid properties, and emitter geometry.

7.1.1 Transient characteristics

At each ESD, Figure 7.1 shows that the formation time decreases for an increase in E_{pulse}. In Figure 7.1a at an ESD of 499±5 μm and below, a greater E_{pulse} is required to start ejections at a T_{form} of 5.00 ms. Whereas in Figure 7.1b, it is the 1.0±0.2 cm and the 190±3 μm which require a greater E_{pulse} to achieve the same T_{form} values as the other ESDs. However, in Figure 7.1c results show that the 1.0±0.2 cm ESD requires the largest E_{pulse} to achieve the same T_{form} values as the other ESDs. Each of the data sets fits to a power law with an R^2 >0.97. Comparing the power law exponent across each ESD, results show that there is no clear correlation between the power law exponent, and the ESD across all three data sets. In Figures 7.1a and 7.1b, for a change in the ESD the power law exponent ranges from -2.02 to -2.44, which is a difference of 19%. A similar result is shown in Figure 7.1c, except there is a slightly larger range of power law exponents from -1.90 to -2.80, which is a difference of 38%. However, there is still no clear correlation between decreasing the ESD and the value of the power law exponent. Figure 7.1 shows that $\mathrm{d}T_{\text{form}}/\mathrm{d}E_{\text{pulse}}$ tends to decrease at an ESD below 1.0±0.2 cm, but then starts to increase again at an ESD of 499±5 μm and below, therefore showing no clear trend with decreasing ESD.

Collapsing the data in Figure 7.1 in relation to the jump in bond number (ΔBo_e), Figure 7.2 shows that there is no clear correlation with difference in ESD, viscosity, conductivity and emitter OD. Fitting a trend line through all of the data, results show the data fits to a power law relationship with $T_{\text{form}} = 1.53\Delta Bo_e^{-1.46}$, with an $R^2 = 0.79$. In the work by Paine [2009], $\mathrm{d}T_{\text{form}}/\mathrm{d}\Delta Bo_e$ and the power law exponent were shown to be dependent on V_1. In the present work since the data is largely independent with change in process

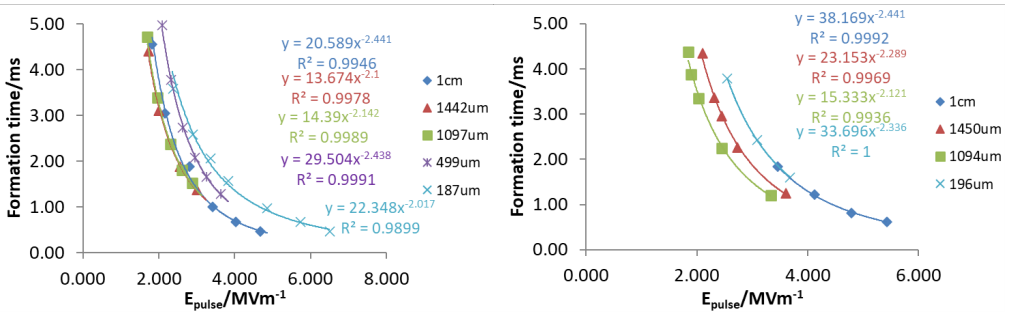

(a) 60 cP, 6 μS cm^{-1}, and on a 40 μm emitter.

(b) 23 cP, 60 μS cm^{-1}, and on a 40 μm emitter.

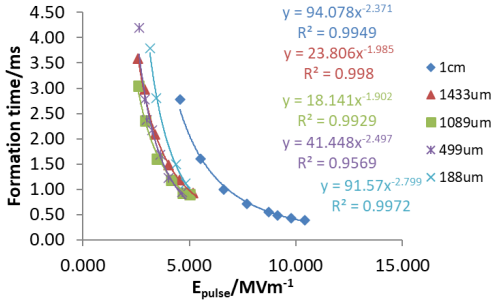

(c) 111 cP, 60 μS cm^{-1}, and on a 20 μm emitter.

Figure 7.1: Formation time against E_{pulse} at a range of emitter-to-substrate distances.

parameters it suggests that V_1 is constant. This would be expected since in each experimental condition V_1 was set to be 5% below V_{onset}. Results are also suggesting that the effect of ΔBo_e on the formation time is independent of the viscosity, conductivity, emitter OD and ESD, for a constant percentage below V_{onset}.

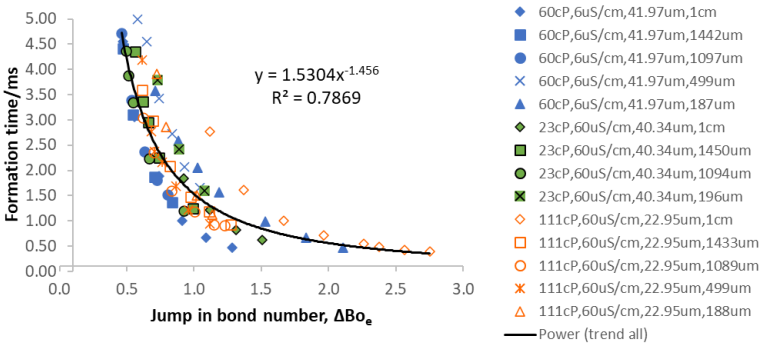

Figure 7.2: Formation time against ΔBo_e for a range of glycerol and water solutions at varying emitter-to-substrate distances.

The effect of the ESD on the current during an ejection is shown in Figure 7.3,

where results show that I_{on} increases with increasing E_{pulse}. At similar values of E_{pulse}, there is a clear trend in that at an ESD of 1.0±0.2 cm a smaller current is measured. However, there is no clear correlation with change in ESD values at 1442±5 μm and below.

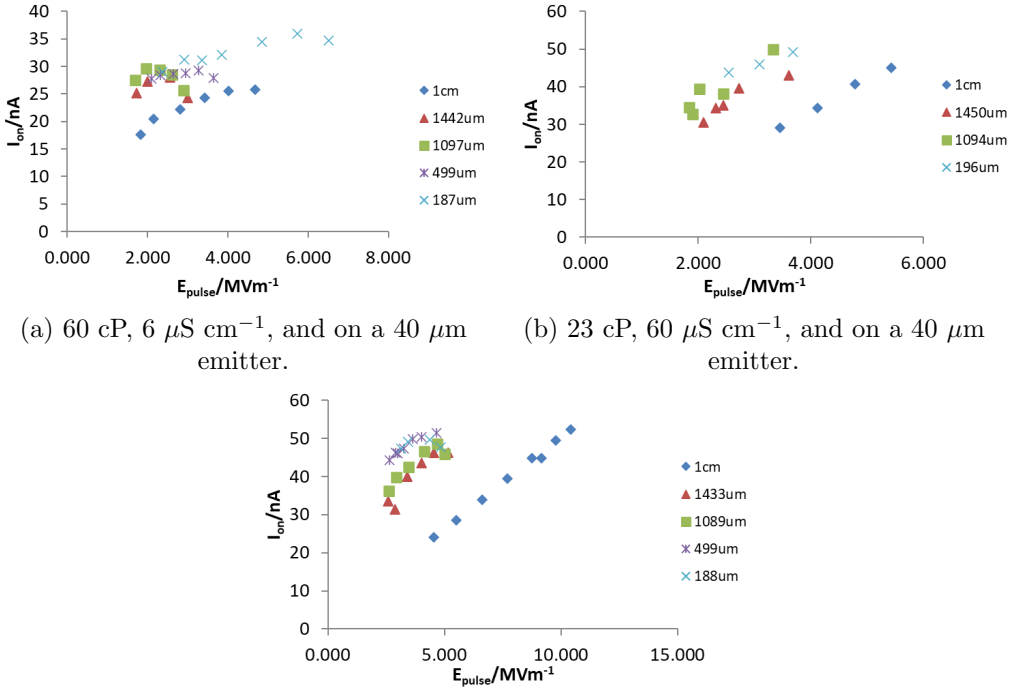

(a) 60 cP, 6 μS cm^{-1}, and on a 40 μm emitter.

(b) 23 cP, 60 μS cm^{-1}, and on a 40 μm emitter.

(c) 111 cP, 60 μS cm^{-1}, and on a 20 μm emitter.

Figure 7.3: I_{on} against E_{pulse} at a range of emitter-to-substrate distances.

Figure 7.4 shows current transients at similar values of E_{pulse}, at a range of ESDs. Results show that decreasing the ESD causes a change in the shape of the pulsations, with the clearest being at an ESD of 1.0±0.2 cm, where a much smaller pulse is observed. From an ESD of 1.0±0.2 cm to 1442±5 μm, the on-times increases by approximately 3.0 times in Figures 7.4a and 7.4b, and by 1.6 times in Figure 7.4c. There is also an increase in the peak current between an ESD of 1.0±0.2 cm and 1442±5 μm, which increases from ∼40 to 49 nA in Figure 7.4a, and from ∼35 to 49 nA in Figure 7.4b. Comparing the on-time at an ESD of 1.0±0.2 cm to that at 190±3 μm, the on-time increases by approximately 2.8 times at 190±3 μm. Results show that by having a smaller ESD, liquid is being ejected for a longer duration than that at an ESD of 1.0±0.2 cm.

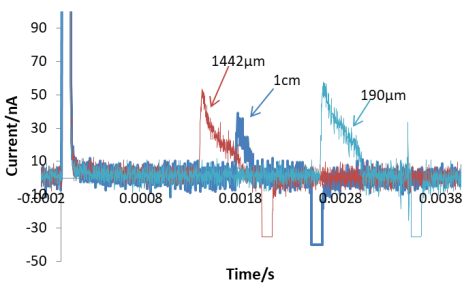

(a) 60 cP, 6 μS cm^{-1}, and on a 40 μm emitter. E_{pulse}=2.814 to 3.004 MV m^{-1}.

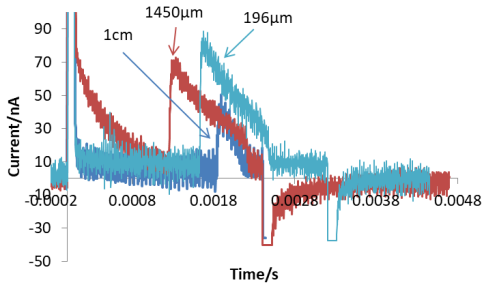

(b) 23 cP, 60 μS cm^{-1}, and on a 40 μm emitter. E_{pulse}=3.461 to 3.684 MV m^{-1}.

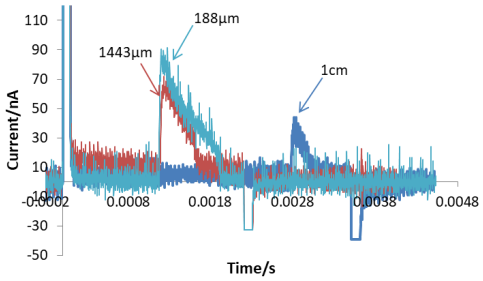

(c) 111 cP, 60 μS cm^{-1}, and on a 20 μm emitter. E_{pulse}=4.544 to 4.823 MV m^{-1}.

Figure 7.4: Current against time graphs for a range of glycerol and water solutions at a range of emitter-to-substrate distances.

7.1.2 Calculated flow rate and volume

The effect of E_{pulse} on the flow rate through the jet at a range of ESDs is shown in Figure 7.5, where results show an increase in Q_{jet} with E_{pulse}. For a given value of E_{pulse}, results clearly show that at the largest ESD of 1.0±0.2 cm, the smallest Q_{jet} is recorded, while there is slight scatter between Q_{jet} values at each of the other ESDs. The smaller Q_{jet} at 1.0±0.2 cm relates to there being a smaller I_{on} value, as this current was used to calculate the flow rate. The effect of the ESD on the flow rate is also shown in Figure 7.4, as the peak current represents the maximum flow rate, where results show reducing the ESD increases I_{peak} therefore increasing the maximum flow rate.

The effect of E_{pulse} on the calculated volume at a range of ESDs is shown in Figure 7.6, where results show at each ESD value an increase in volume with an increase in E_{pulse}. For a given E_{pulse}, results show that the smallest ejected

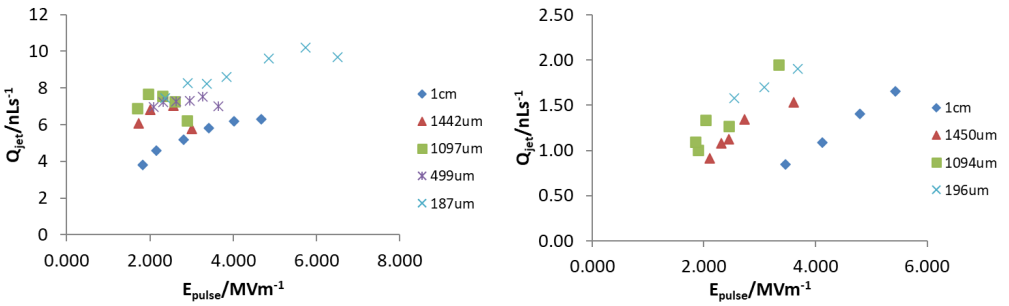

(a) 60 cP, 6 μS cm^{-1}, and on a 40 μm emitter.

(b) 23 cP, 60 μS cm^{-1}, and on a 40 μm emitter.

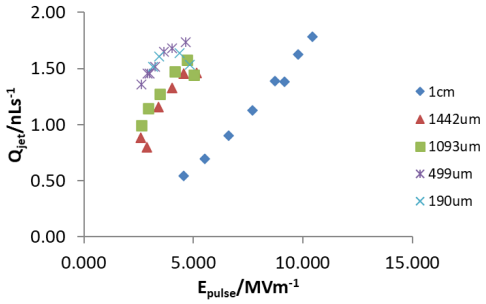

(c) 111 cP, 60 μS cm^{-1}, and on a 20 μm emitter.

Figure 7.5: Q_{jet} against E_{pulse} at a range of emitter-to-substrate distances.

volumes are from an ESD of 1.0±0.2 cm, where the variation in volume reduces as the ESD decreases. Figures 7.6a and 7.6c show that the largest volumes ejected are from the lowest ESDs, at values of 499±5 and 190±3 μm. This result could have been expected from the results shown in Figures 7.4 and 7.5, where it was shown that the duration of the pulse and the flow rate through the jet increase with a reduction in the ESD. However, the general trend shows that to achieve a smaller volume, a greater ESD is required.

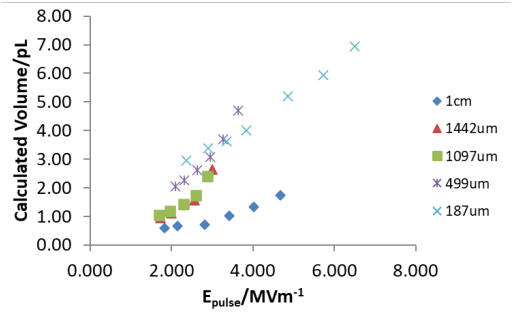

(a) 60 cP, 6 μS cm^{-1}, and on a 40 μm emitter.

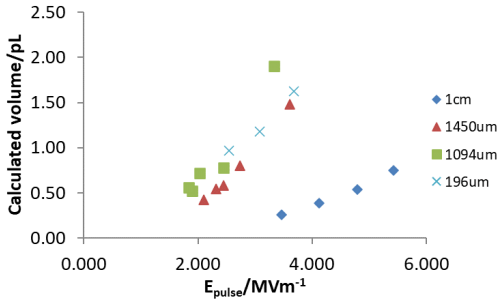

(b) 23 cP, 60 μS cm^{-1}, and on a 40 μm emitter.

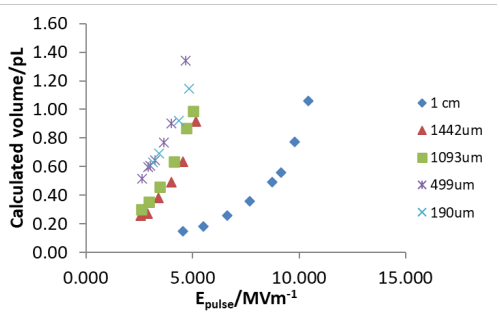

(c) 111 cP, 60 μS cm^{-1}, and on a 20 μm emitter.

Figure 7.6: Calculated volume against E_{pulse} at a range of emitter-to-substrate distances.

7.2 Effect of process parameters on the maximum emitter-to-substrate distance to achieve a discrete drop

In Section 7.1 it was shown that to achieve the smallest drop volumes a greater ESD is required. Electrohydrodynamic jet printing requires the ESD to be small enough that the spray coalesces on the substrate, the jet impinges on the substrate to form a drop, or the drops that detach from the jet impact onto the substrate. The ESD from the substrate at which a spray becomes a droplet depends on the interplay between liquid properties and emitter geometry. Figures 7.7 and 7.8 show examples of the effect that reducing the ESD has on achieving an individual droplet.

Figure 7.7 shows droplets printed using a solution with a viscosity of 23 cP, a

conductivity of 60 μS cm^{-1}, and on a 10 μm emitter. Each of the deposits was printed from a single pulse of the voltage, where the highest V_2 for pulsations was used, which corresponds to an E_{pulse} of 3.138 MV m^{-1} at 194 μm, 3.541 MV m^{-1} at 152 μm, and 4.470 MV m^{-1} at 145 μm. The stage was moved across ~50 μm before the next ejection, as shown by the scale bar in Figure 7.7. Results show that at an ESD of 194 μm, there is a large spray area on one side of each of the droplets, with a small amount of spray around the rest of the drop. On decreasing the ESD to 152 μm, Figure 7.7 shows a reduction in the spray area around the bottom edge of the droplet. On a further reduction to 145 μm, the spray at the bottom of the droplet is almost negligible compared to the rest of the droplet. Since the spray area is mainly on the bottom half of the droplet, this could suggest that the meniscus is not fully symmetrical, which could have caused the jet to whip in the same direction as the non-symmetrical meniscus as the voltage pulse switches off. Imaging of the jet during printing was not possible to establish exactly the mode of ejection (varicose or whipping).

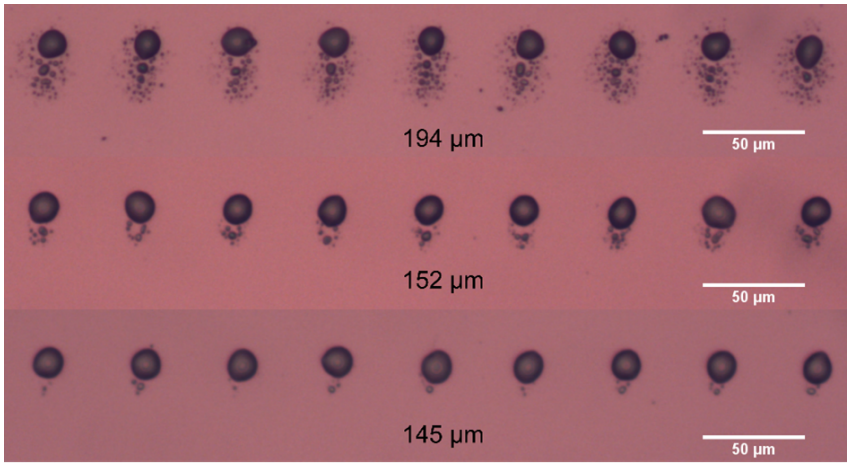

Figure 7.7: Droplets of glycerol and water at 23 cP, 60 μS cm^{-1} and on a 10 μm emitter, printed at a range of emitter-to-substrate distances.

Figure 7.8 shows another example of the transition from a spray to an individual droplet, using a solution with a viscosity of 156 cP, a conductivity of 600 μScm^{-1}, and on a 20 μm emitter. Drops were printed at the highest V_2 voltage to achieve pulsations, which corresponds to an E_{pulse} of 5.074 MV m^{-1} at 119 μm, 4.173 MV m^{-1} at 107 μm, and 4.311 MV m^{-1} at 86 μm. Results

show that at an ESD of 119 μm, the jet has broken up into a spray with a diameter of approximately 47 μm. The spacing between depositions was $\sim$50 μm, where at an ESD of 119 μm, results show a slight overlap between the edges of each spray area. Reducing the ESD to 107 μm, results show that not only has the spray area reduced to having a diameter of $\sim$33 μm, but there is a centralised droplet within each of the spray areas. This suggests that the jet has broken up before reaching the substrate, as the height of the spray would have reduced leading to a smaller spray area. The droplet in the middle is most likely due to smaller droplets within the spray area coalescing to form one large deposit. Reducing the ESD even further to 86 μm, results show that there is a negligible amount of spray around each of the droplets, with the drop in the middle having a diameter of $\sim$11 μm. This suggests that at 86 μm, the jet is getting close to touching the substrate.

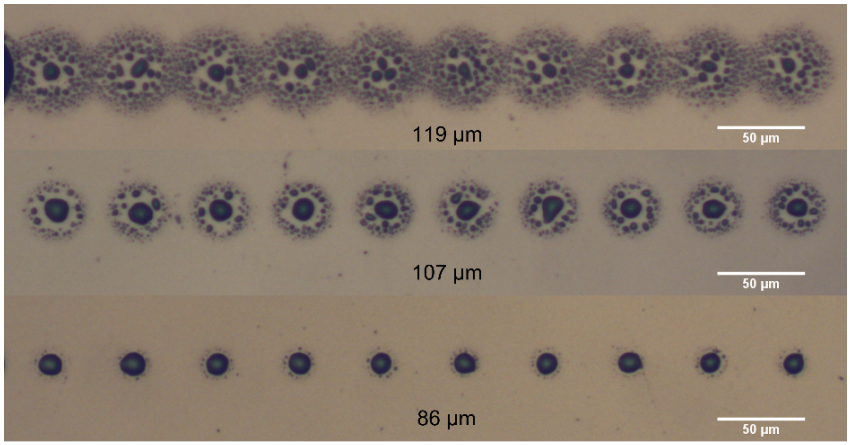

Figure 7.8: Droplets of glycerol and water at 156 cP, 600 μS cm^{-1} and on a 20 μm emitter, printed at a range of emitter-to-substrate distances.

Understanding what affects the maximum ESD is important for high resolution printing, as the interplay between the liquid properties and emitter geometry will determine how far from the substrate the user needs to be to achieve an individual droplet. A systematic study has been performed to understand the effect that each of these parameters has on the maximum ESD, showing how important each variable is on the distance at which the operator can print.

The maximum ESD as discussed above, has been calculated using the highest

V_2 required to achieve pulsations for a given solution. With the variation in ESD, as well as liquid properties and emitter geometry, there can be variations in the values of E_{pulse}. Further investigations would be required to understand the effects of the magnitude of the pulsed voltage on the maximum ESD. Therefore, for these results it is being assumed that the change in liquid properties and emitter geometry will be more significant than that of E_{pulse}.

Figure 7.9 shows a chart of the maximum ESD at a range of viscosities and conductivities. Taking each conductivity separately, results show that the maximum ESD increases from 2.5 to 60-67 cP, before decreasing at 111-156 cP. The higher viscosities of 67 and 156 cP are at a conductivity of 600 μS cm^{-1}. The magnitude increase in the ESD between 2.5 and 60-67 cP for each conductivity is approximately, 1.3 times at 6 μS cm^{-1} and 60 μS cm^{-1} and 1.4 times at 600 μS cm^{-1}. This is showing that when using the maximum V_2 value, the maximum ESD is weakly dependent on the viscosity.

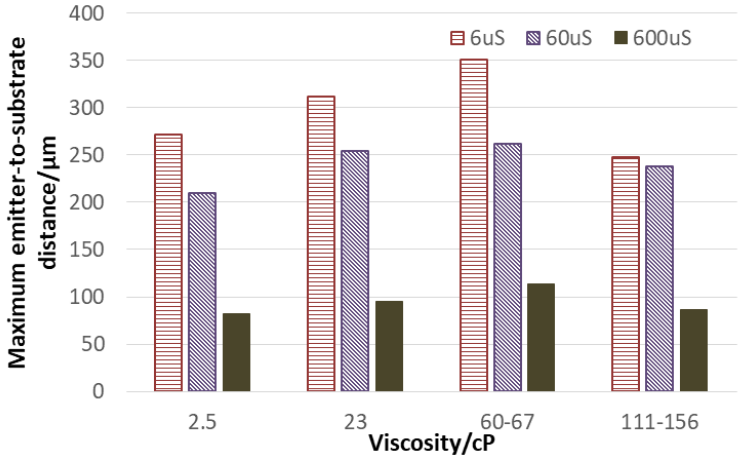

Figure 7.9: Effect of viscosity and conductivity, on the maximum emitter-to-substrate distance to achieve a discrete droplet, using a constant emitter geometry of 20 μm.

Comparing the effect of conductivity at each viscosity a much clearer trend is observed, in that decreasing the conductivity increases the maximum ESD. Figure 7.9 shows that for each viscosity the maximum ESD increases by approximately 3.0 times between 6 and 600 μS cm^{-1}. The magnitude increase in the maximum ESD at 6 μS cm^{-1} compared to 60 μS cm^{-1} is approximately, 1.3 times at 2.5 cP,

1.2 times at 23 cP, 1.3 times at 60 cP, and 1.1 times at 111 cP. Other than at 111 cP the magnitude increase in the maximum ESD at 6 μS cm^{-1} compared to 60 μS cm^{-1} is approximately constant with viscosity. The increase in the maximum ESD from 600 to 60 μS cm^{-1} is approximately, 2.6 times at 2.5 cP, 2.68 times at 23 cP, 2.3 times at 60-67 cP, and 2.8 times at 111-156 cP. This is showing that when decreasing the conductivity by the same magnitude for each viscosity, the magnitude increase of the ESD is approximately independent of the viscosity.

Figure 7.10 shows the effect of both the viscosity and the emitter geometry on the maximum ESD. Results show that across each viscosity for each emitter geometry there is a peak observed in the maximum ESD. At 10 μm, the peak in the maximum ESD is at 2.5 cP where the maximum ESD is at ~180 μm. The peak in the maximum ESD is not as clear on the 20 μm emitter, but is around 23 to 60 cP, with the maximum ESD being equal to ~255 to 262 μm. At 40 μm, the peak in the maximum ESD is at 23 cP, where the maximum ESD is ~344 μm.

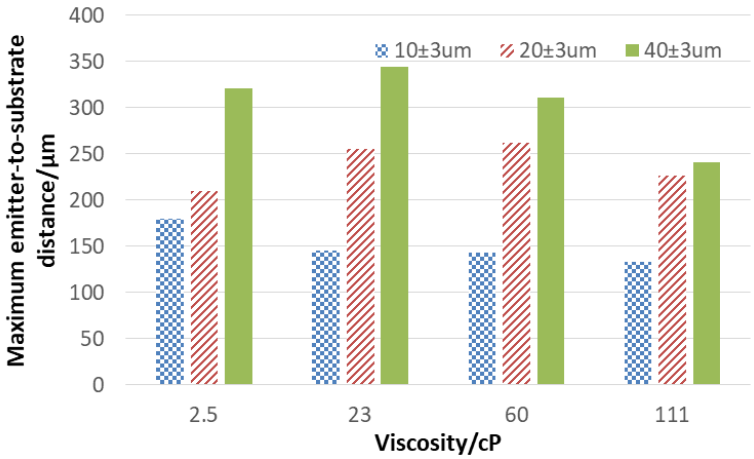

Figure 7.10: Effect of viscosity and emitter geometry, on the maximum emitter-to-substrate distance to achieve a discrete droplet, at a constant conductivity of 60 μS cm^{-1}.

At a constant viscosity, increasing the size of the emitter OD increases the maximum ESD required to achieve a discrete droplet. Figure 7.10 shows that the effect of the emitter OD on the maximum ESD depends on the viscosity of the solution. The magnitude increase in the maximum ESD between 10 and

20 μm is approximately, 1.2 times at 2.5 cP, 1.8 times at 23 to 111 cP. The magnitude difference in the maximum ESD between 10 and 20 μm is less at 2.5 cP, but is relatively constant at 23 cP and above. Between 20 and 40 μm the magnitude difference in the maximum ESD is approximately, 1.5 times at 2.5 cP, 1.4 times at 23 cP, 1.2 times at 60 cP, and 1.1 times at 111 cP.

The effect of conductivity and emitter geometry is shown in Figure 7.11, where results show that increasing the conductivity reduces the maximum ESD on each emitter OD. On a 10 μm emitter, the magnitude increase in the ESD with decrease in conductivity is by approximately 1.3 times at 6 μS cm^{-1} compared 60 μS cm^{-1}, and 1.6 times at 60 μS cm^{-1} compared to 600 μS cm^{-1}. At 20 and 40 μm, the magnitude difference on decreasing the conductivity ranges from 1.3 to 1.4 times between 6 and 60 μS cm^{-1}, and 2.3 to 2.4 times between 60 and 600 μS cm^{-1}.

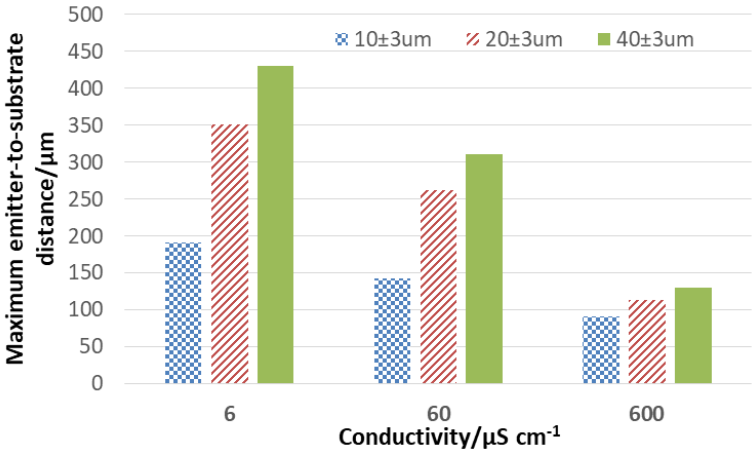

Figure 7.11: Effect of conductivity and emitter geometry, on the maximum emitter-to-substrate distance to achieve a discrete droplet, at a constant viscosity of 60-67 cP.

Figure 7.11 shows that increasing the emitter OD increases the maximum ESD. The magnitude increase in the maximum ESD between emitters at 6 μS cm^{-1} is approximately 1.8 times from 10 to 20 μm, and 1.2 times from 20 to 40 μm, compared to 1.2 times from 10 to 20 μm, and 1.1 times from 20 to 40 μm at 600 μS cm^{-1}. This shows that the difference in the maximum ESD is marginally greater between 10 and 20 μm, however there is little effect on the magnitude difference between increasing the emitter OD with conductivity.

There is little previous literature on the effect that process parameters have on pulsed voltage nanoelectrospray operation, and the distance to achieve a discrete droplet. In majority of literature where an unforced/nanoelectrospray has been applied to printing applications, emitters with an ID of less than 30 μm have been used, which has required an ESD of less than 100 μm (Park et al. [2008]), with 30 μm being used in a wide range of applications (Kim et al. [2010]; Poellmann and Johnson [2013]; Poellmann and Johnson [2014]).

In this section results have shown how process parameters affect the length of the jet and therefore jet breakup. The conductivity and emitter OD have been shown to have the greatest effect on the maximum ESD, with a lower conductivity and larger emitter required to achieve the greatest ESD. The findings in these results show that by optimising the combination of viscosity, conductivity, and emitter geometry a wide range of ESDs can be achieved. The findings here have shown that just because a smaller emitter is being used, does not necessarily mean that the operator is limited to an ESD of 30 to 50 μm. Using an emitter with an OD of 10 μm if the combination of liquid properties match then an ESD of almost 200 μm can be used, as shown in Figure 7.11. This could improve the use of electrospray printing, as by being able to operate further away from the substrate means that if the substrate deforms it will have less effect on the ejection process and cause less chance of the emitter breaking.

7.3 Scaling laws for the length of the jet and transition from whipping to varicose mode

Scaling laws for the length of the jet in the viscid and inviscid limit were discussed in Section 2.3.5.2, where the radius of the jet was given by Equation 2.3.34 and limited to the conditions given by Equation 2.3.35. Figure 7.12 shows the maximum ESDs from Section 7.2 which fit at least one of the criteria, where the flow rate has been calculated from I_{on} and the scaling by Ganan-Calvo et al.

[1997] as discussed previously.

Figure 7.12 shows that the non-dimensional breakup length against $6\mu/Z_v d_n$, where both have been made dimensionless in relation to the emitter OD. The dashed line represents the theoretical value where the data in Ismail et al. [2018] showed that from Equation 2.3.36 that when $Re < 5$ the data fitted to give $k_v = 7$. Majority of the data from Section 7.2 is shown not to follow the same trend and shows a lot of scatter, however each of the data sets fits the criteria of $Re < 5$.

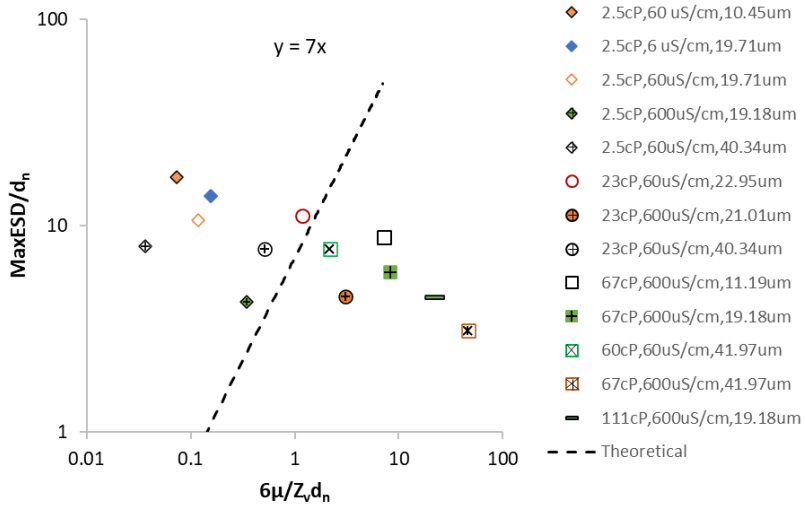

Figure 7.12: Non-dimensional breakup length (L_b/d_n) against $6\mu/Z_v d_n$, for a range of solutions which fit the criteria $\alpha_\rho >> \alpha_\mu^{1/4}, \alpha_\rho/(\epsilon - 1) >> 1$. The dashed line represents the theoretical value.

There are differences between the measurements in the present work and those by Ismail et al. [2018] with the main difference being that Ismail et al. [2018] imaged the jet to measure the length, and the focus was on varicose breakup. In Section 7.2 the maximum ESD was measured from observing the deposits that had been printed, as discussed in Section 3.2.1.2. This method could mean that the maximum ESD is greater than the actual jet length, as depending on the mode of breakup (varicose or whipping) the droplet could have detached from the jet and impacted the substrate from a distance greater than the jet length. The length of the cone would also be included in the maximum ESD, where the effect of this in relation to the jet length would vary depending on conductivity

and emitter OD.

In the present experiments it is not known whether jet breakup was in varicose or whipping mode due to not having a high speed camera to monitor the ejection process. As discussed in Section 2.3.5.2, Xia et al. [2019] developed scaling laws to determine the criteria required to transition from varicose to whipping. To be able to fit all of the data in Section 7.2, the data which did not fit the criteria for the radius of the jet given previously fitted the criteria for Equation 2.3.54. This data fitted to the scaling for viscous forces and electrostatic suction being dominant (VE) compared to inertia and electrostatic suction being dominant (IE).

Having calculated $G = \Gamma^2 \delta_\mu^{-0.33}$ for when $\delta_\mu << 1$ and $G = \Gamma^2$ for values greater than 1, Figure 7.13 shows the mode of ejection that could be expected for the data in this section. The horizontal lines in Figure 7.13 at G=145 and 165 represent where the transition between varicose and whipping should occur (Xia et al. [2019]). Results suggest that majority of jet breakup should be in varicose mode. The vertical dot dashed line represents where $\delta_\mu = 1$ and is the transition between viscosity and inertia being dominant, where viscous forces are important when $\delta_\mu < 1$.

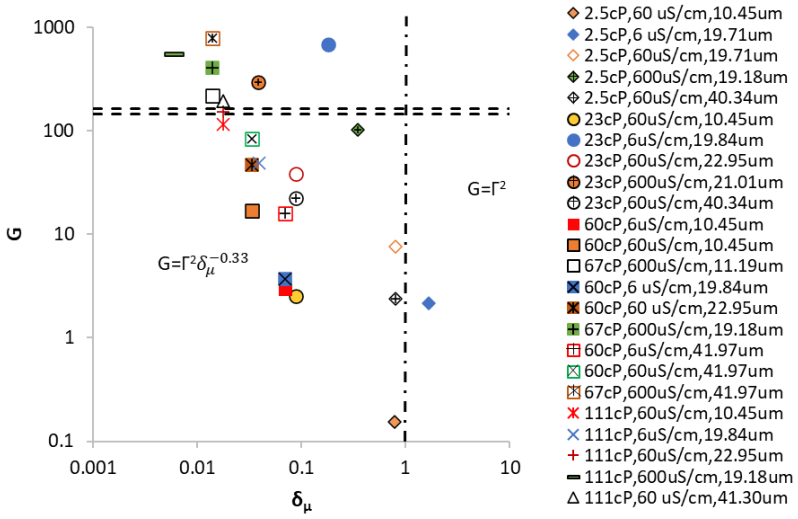

Figure 7.13: Transition between varicose and whipping modes by plotting G against δ_μ. The dashed lines at G=145 and 165 are the seperation between modes given in Figure 7 by Ismail et al. [2018].

Figure 7.13 might explain some of the divergence from theory observed in Figure 7.12. All of the data to the right and including the 23 cP, 600 μS cm^{-1}, 21.01 μm condition are suggested to be produced in whipping mode, where the scaling laws are for varicose mode. The other data that diverges is the 2.5 cP data, where the 2.5 cP, 6 μS cm^{-1}, 19.71 μm data is the only one where $\delta_\mu > 1$, suggesting that inertia is more dominant, and the other data at this viscosity has a δ_μ close to 1.

7.4 Nanoelectrospray printing

In the previous section it was shown that the ESD required to achieve a discrete droplet depended on the liquid properties, and the emitter geometry. This section is focusing on examples of physically printed droplets and the effect of the magnitude of the pulsed voltage, liquid properties, and emitter geometry.

Figure 7.14 shows droplets printed at a range of V_{pulse} values where V_1=0.851 kV, using a 23 cP solution, at 60 μS cm^{-1}, on a 20 μm emitter. Results show that reducing the magnitude of the voltage pulse reduces the size of the deposit. At a V_{pulse} of 0.175 kV, the volume measured using the spherical cap equation (Equation 2.4.9)(v_{print}) is 1.77 pL, compared to 1.20 pL at a V_{pulse} of 0.093 kV. This is a 1.5 times difference in the calculated volume over the 0.100 kV range. Figure 7.15 shows the difference between the volumes calculated from the printed droplets and those calculated from the current transients. Results clearly show that the current transient underestimates the volume by approximately 1.00 pL, this was discussed in Section 4.3. However, it shows that for this solution the difference between the drops at different V_{pulse} values has a constant difference between v_{print} and $v_{\text{transient}}$. The calculated error in the measurements are similar in size to the data points. The error in multiple current transients ranges from 1.6 to 3.3 %.

Figure 7.16 shows the effect of viscosity at similar values of V_{pulse}, for solutions at 2.5, 60 and 111 cP, where a conductivity of 60 μS cm^{-1}, and an emitter OD

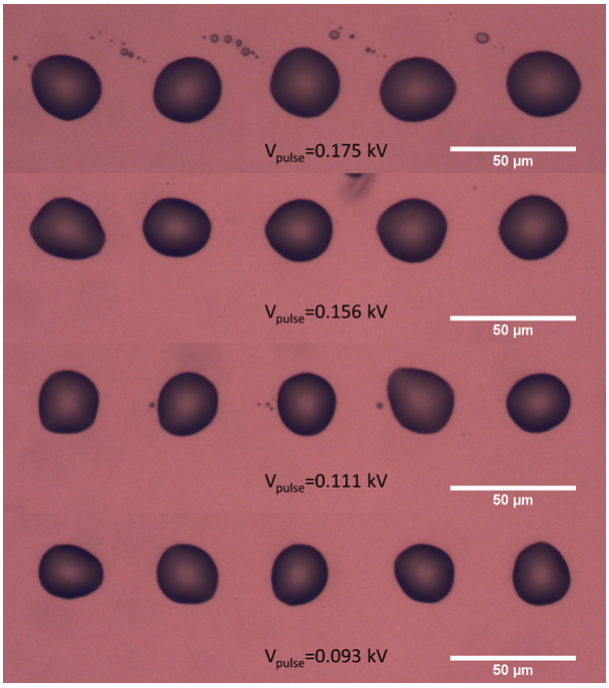

Figure 7.14: Droplets of glycerol and water at 23 cP, 60 μS cm^{-1} on a 20 μm emitter, printed at a range of V_{pulse} values.

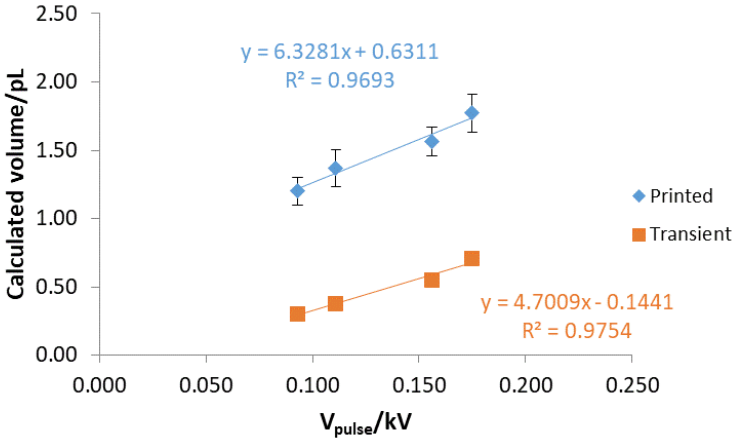

Figure 7.15: Calculated volume against V_{pulse} at μ=23 cP, 60 μS cm^{-1} on a 20 μm emitter.

of 40 μm were used. At 2.5 cP, the initial droplet is slightly larger and at a V_{pulse} of 0.118 kV, the transient relating to this ejection showed that this droplet was ejected in cone-jet mode. Therefore, V_{pulse} was reduced to 0.114 kV, where a single ejection was produced, printing four reproducible droplets. The average volume for the four single ejected droplets is 4.26±0.56 pL. At 60 cP, there is a slight increase in v_{print} to 4.81±0.15 pL, which could also be due to a slight increase in

the V_{pulse} as discussed above. In an increase in viscosity to 111 cP, Figure 7.16 shows a reduction in the drop volume with v_{print} equal to 2.18±0.12 pL.

There is again a difference between v_{print} and $v_{\text{transient}}$, with $v_{\text{transient}}$ equalling 0.42 pL at 2.5 cP, 1.43 pL at 60 cP and 1.02 pL at 111 cP. The percentage errors in $v_{\text{transient}}$ are 4% at 2.5 cP, and 1% at 60 to 111 cP. Therefore, v_{print} ranges from being 10 times greater than $v_{\text{transient}}$ at 2.5 cP, to 2.0 times at 111 cP. This is indicating that the scaling fits closer the higher in viscosity the solution. It was shown in Chapter 4, Section 4.2 that for a 4.00 pL droplet with a 30%wt glycerol content, it could take approximately 77 minutes for the glycerol to evaporate, and for a 2.00 pL droplet at 85%wt glycerol, it could take approximately 152 minutes for the glycerol to evaporate. Therefore, with no longer than 15 minutes between printing an imaging the droplets it is being assumed that the contact line will remain relatively constant, especially for the 85% glycerol solution.

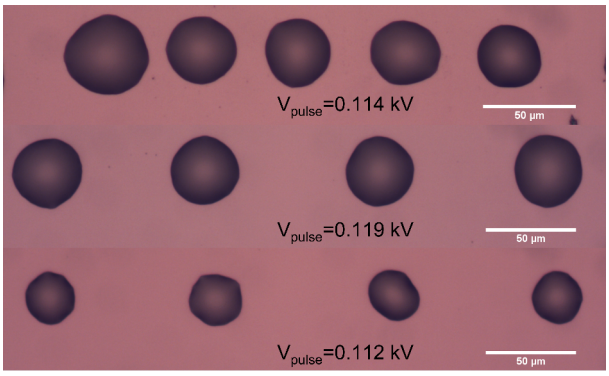

Figure 7.16: Droplets of glycerol and water at 60 μS cm^{-1} on a 40 μm emitter, printed at a range of viscosities from 2.5 cP(top), 60 cP and 111 cP (bottom).

Figure 7.17 shows the effect of conductivity on the size of droplets printed, where the ESD was kept constant at 81±3 μm. Results show that at a relatively constant V_{pulse} increasing the conductivity varies the size of the print, from a v_{print} of 0.20±0.01 pL at 6 μS cm^{-1}, 0.42±0.08 pL at 60 μS cm^{-1}, and 0.04 to 0.20 pL at 600 μS cm^{-1}. There is an increase in volume between 6 and 60 μS cm^{-1}, with a clearer decrease at 600 μS cm^{-1}. The reason for the large range in values at 600 μS cm^{-1} is shown in Figure 7.17, where results show that there is a variation in drop size compared to 6 and 60 μS cm^{-1}. The reason for the difference in drop

size can be shown by the current transients measured for each of the droplets.

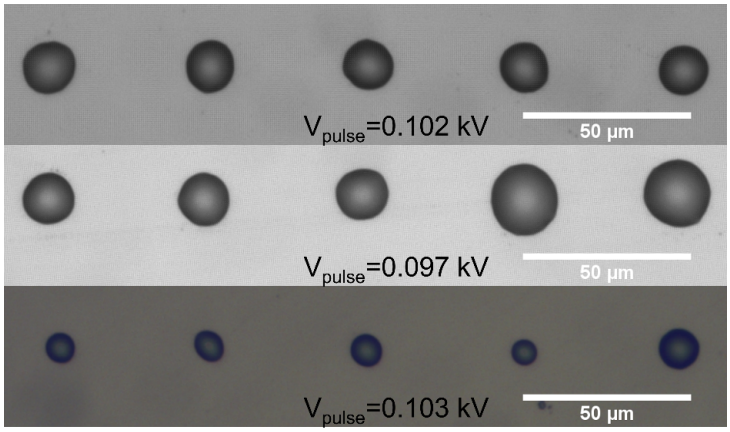

Figure 7.17: Droplets of glycerol and water at 2.5 cP, and on a 20 μm emitter, printed at a range of conductivities from 6 μS cm^{-1}(top), 60 μS cm^{-1} and 600 μS cm^{-1} (bottom).

At 600 μS cm^{-1}, it was not as easy to isolate a single ejection, due to the high frequency of the pulsations, as was discussed in Chapter 5. Figure 7.18 shows example transients for droplets one and two starting from the right hand side of the image. Figure 7.18a refers to the larger drop furthest to the right, where the current transient shows that this droplet is made up from two ejections. Whereas in Figure 7.18b which refers to the second drop from the right, it is shown that this droplet is made up from a single ejection, hence the smaller volume. There is the start of another ejection after the first, but then the voltage switch turns off and the pulse does not finish. Since this droplet is smaller than the droplet to the right from two ejections, it can be assumed that the second ejection did not continue.

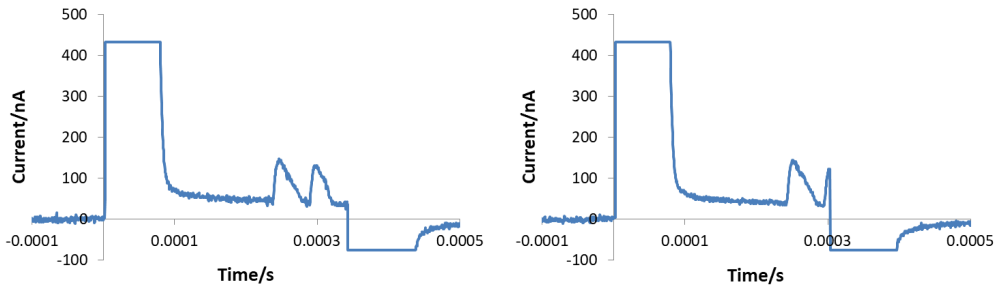

(a) (b)

Figure 7.18: Current against time graphs for glycerol and water solutions at μ=2.5 cP, K= 600 μS cm^{-1}, and on a 20 μm emitter.

Figure 7.19 shows the effect of the emitter OD on the size of the deposits printed. As discussed previously the change in electric field (E_{pulse}) has been used, where it was shown that the size of the emitter affects the voltage. The 10 μm data was printed at 80 μm, compared to 188 μm at 20 and 40 μm. By using the field strength it reduces the effect of the emitter OD and the ESD on the voltage, making the data comparable. It also means the main effect being observed is that of the emitter OD. The maximum percentage difference in E_{pulse} is 25% between 10 and 40 μm. However, the difference in v_{print} is much greater at 190%. At 10 μm, v_{print} equals 0.24±0.01 pL ($v_{\text{transient}}$=0.12 pL), 3.29±0.12 pL ($v_{\text{transient}}$=0.55 pL) at 20 μm, and 8.99±0.54 pL ($v_{\text{transient}}$=2.65 pL) at 40 μm. The percentage errors in $v_{\text{transient}}$ are 2.6% at 10μm, 3.0% at 20 μm and 3.8% at 40 μm.

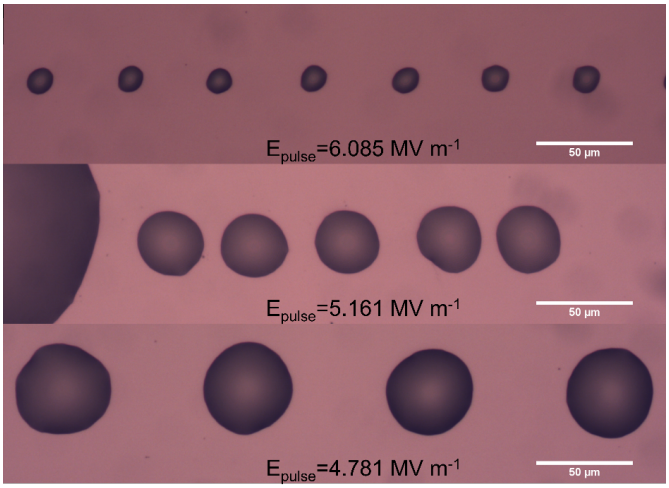

Figure 7.19: Droplets of glycerol and water at 60 cP, and at a conductivity of 60 μS cm^{-1}, printed on a range of emitter sizes from 10 μm(top), 20 μm and 40 μm (bottom).

Further investigations are needed at a larger range of $V_{\text{pulse}}/E_{\text{pulse}}$, viscosity, conductivity and emitter OD to fully understand the behaviour of single ejections on the printed volume. It has been shown that the difference between v_{print} and $v_{\text{transient}}$ depends on the solution properties, and the process parameters. By having a broader range of test variables, it might be possible to produce a scaling factor that can be used across each parameter to account for differences in the printed volume and that calculated from the current transient. It was previously

noted by Paine et al. [2007b] that the scaling laws give a good order of magnitude estimate, but it was also noted that the estimated volume was smaller than the physical values. However, for tests where the flow rate is not measured this method can give a prediction for the order of magnitude of the flow rate and volume.

7.5 Summary

This chapter has shown that there is no clear correlation between decreasing the ESD, and the dependence of E_{pulse} on reducing the formation time. Current transients showed that reducing the ESD increased the on-time and the peak current, where this result was also shown in relation to the calculated ejected volumes. Results showed that smaller volumes were ejected at an ESD of 1.0±0.2 cm. In Figure 7.15 and from other printed results it was shown that the current transient estimated a smaller volume than that calculated from the physically printed droplets. The magnitude difference between $v_{\text{transient}}$ and v_{print} was shown to be dependent on the combination of liquid properties and emitter geometry.

The ESDs shown in this chapter are much less than those used in ink-jet printing, where the distance ranges from 2 to 3 mm (Derby [2010]). To achieve an ESD in the mm range when printing using electrospray pulsations, previous research suggests that emitters with an OD of a few hundred microns are required, as these have been used for printing from 1 to 5 mm away from the substrate (Lee et al. [2012b]; Yuan et al. [2015]; Guo et al. [2018]). Results in this chapter have shown that at the highest V_2 values the maximum ESD required to achieve a discrete droplet, depends on the liquid properties and emitter geometry. It has been shown that a larger emitter ejects a larger volume, reducing the print resolution, but also increases the ESD. This shows that there is a trade off between using a larger emitter and achieving a greater ESD, or having a higher print resolution.

8

Conclusion and future work

8.1 Conclusions

In nanoelectrospray the flow rate is modulated by the applied voltage, understanding the interplay between the liquid properties, emitter geometry and emitter-to-substrate distance (ESD) is vital to understanding the affect that each parameter has on the characteristics of the ejection. To further our understanding as to the effect that changing a given parameter has on the ejection characteristics, a systematic approach was used. A key aim to this work has been to use the current transients, along with established scaling laws (De La Mora and Loscertales [1994]; De La Mora [1996]; Ganan-Calvo et al. [1997]) to calculate the flow rate and therefore the ejected volume, since in these tests the flow rate was not measured directly. The effect of each parameter was investigated by applying both a continuous and pulsed voltage.

These experiments have shown that a range of parameters can be tested, and that nanoelectrospray pulsations can be controlled and utilised using a simple set-up with no pumps or valves just a glass capillary with a metal pin within the solution to apply the voltage, positioned opposite a counter electrode. This design is ideal for printing applications which require a small amount of solution.

Pulsation data was repeated for several solutions in different set-up conditions, several months apart giving the same dependence as previous tests. Results have been shown to fit with other nanoelectrospray data when plotted in dimensionless form, confirming the trends in the present work. This set-up has only been tested using solutions with high surface tensions greater than 60 mN m^{-1}, where the initial head pressure from the 3.0 cm head height is not large enough to overcome the surface tension, and the amount of solution was adequate for the

flow rates to perform each of the tests. If using solutions with a much lower surface tension around 25 mN m^{-1}, or using emitters that are hundreds of microns in diameter, adjustments in the amount of solution and back pressure may be required. However, it would be expected that similar results would be obtained to those discussed in the present work.

DC voltage nanoelectrospray

In continuous voltage operation, and using a single variable it has been shown that the pulsation frequency is largely dependent on both the viscosity and the conductivity of the solution. At a constant value of V_{step} results showed that as V_{step} increased, the pulsation frequency was shown to be related to the viscosity by $f \sim \mu^{-1}$, which is in agreement with the scaling given by Chen et al. [2006]. The effect of conductivity at a constant V_{step} showed that the power law exponent of K increased from 0.08 at 0.050 kV, to 0.49 at the maximum frequency recorded, which is close to that reported by Guo et al. [2018] where $f \sim K^{0.58}$. By varying the emitter OD and plotting the data against E_{step} instead of V_{step}, each of the data sets collapsed onto similar trends. Results showed little variation in the pulsation frequency at similar values of E_{step} for each emitter OD, however there was a decrease in the maximum frequency with increase in emitter size, with $f \sim d_n^{-0.23}$. It was shown that by plotting the dimensionless frequency $((f/f_c)^2)$ against the electrical bond number (Bo_e), data from a range of parameters could be plotted together. Results showed that the largest emitter required the smallest Bo_e, however there was no clear trend with other variables.

Plotting the dimensionless charge (q/q_0) against ζ_q results showed that even though q/q_0 did not account for the increase in Bo_e, the data collapsed to scale as $q/q_0 = 51.56\zeta_q^{1.89}$. Taking the average values for q/q_0 to account for the effect of Bo_e, the data scaled as $q/q_0 = 93.19\zeta_q^{1.75}$. This scaling is greater than the $q/q_0 = 0.2\zeta_q$ given by Gañán-Calvo et al. [2016], however other nanoelectrospray data from Paine et al. [2007a] and Stark et al. [2014] fitted with the present

data. It was concluded that the difference was possibly due to Gañán-Calvo et al. [2016] calculating the charge for the first droplet ejected, and therefore capturing a small fraction of the total charge emitted, compared to multiple ejections over a full pulsation event as measured in the present work.

Pulsed voltage nanoelectrospray: Constant emitter-to-substrate distance.

Controlling a single ejection event is important in using an electrospray for printing. It was shown that the magnitude of the switched voltage was important to controlling the ejections and the spray mode produced. It was shown that increasing the magnitude of the voltage pulse decreased the formation time, where the formation time decreased in a power law relationship with $V_{\text{pulse}}/\Delta Bo_e$. The dependence of $V_{\text{pulse}}/\Delta Bo_e$ on the power law was not always clear, however it was shown that values of $V_{\text{pulse}}/\Delta Bo_e$ required to achieve ejections at similar values of formation time, were dependent on the viscosity, conductivity and emitter OD.

As with constant voltage operation q/q_0 against ζ_q was shown to collapse the data for a range viscosity and conductivity solutions on emitters 10 to 40 μm. Taking the average value for q/q_0 the data scaled as $q/q_0 = 2276\zeta_q^{1.20}$, which is several orders of magnitude greater than that given by Gañán-Calvo et al. [2016] for the same reasons as discussed above.

Pulsed voltage nanoelectrospray: Effect of emitter-to-substrate distance and nanoelectrospray printing.

The ESD is important in whether a droplet or a spray is deposited on the substrate. It has been shown that there is little dependence of the ESD on the reduction of the formation time with E_{pulse}. A key observation was that the ESD affected the shape of the measured pulsations, with the height and width

of the pulses increasing as the ESD decreased. This increase in the shape of the pulse was shown when investigating the effect of the ESD on the calculated ejected volume, where it was clearly shown that the smallest volumes were ejected at the greatest ESD of 1.0±0.1 cm. At this ESD the jet would have broken up into a spray. It was later shown that at the greatest V_2 for pulsations, the maximum ESD required to print a droplet ranged from approximately 100 μm, to just over 400 μm depending on the combination of liquid properties.

8.1.1 Future work

Future work includes building upon the results discussed in this thesis by increasing the range of process parameters tested, to build a further understanding on the effect of each parameter.

The characteristics of the substrate are important in achieving the highest print resolution, as the substrate affects the contact angle and therefore the wetting characteristics. A hydrophilic substrate would cause the droplets to spread out, increasing the drop diameter and reducing the print resolution, compared to a hydrophobic substrate which would do the opposite. There is also the possibility that the properties of the substrate would affect the impact dynamics of the droplet/s, and whether the drops breakup on impact or not, as this would reduce the resolution of the print.

Effects on vibrations of the nozzle were reduced by having a vibration table in which the equipment was mounted. Any form of vibration during printing could cause droplets to be positioned off axis which would reduce the accuracy of the printed image.

In continuous voltage operation an interesting result was observed in that the flow rate is independent of the viscosity, over a range of conductivity and emitter geometries. Further investigations are required as it was noted that the scaling law used does not include a term for viscosity, and that flow rate measurements

were not possible to clarify the results. Further experiments including flow rate measurements would be required to either confirm or disprove the result given by the scaling law, as this is not possible from the results at present.

In pulsed voltage operation and the application for nanoelectrospray printing the combination of liquid properties and process parameters has been shown to be important in isolating and controlling a single ejection, and in the ESD required to print a discrete droplet. A few interesting observations were shown in relation to the effect of viscosity, in that a smaller viscosity generally requiring a smaller $V_{\text{pulse}}/\Delta Bo_e$ to achieve an ejection. It was noted that further investigations were required at a lower viscosity range to produce a more conclusive answer. It might also open up further information into the possibility in whether there is a role of inertia that is causing the trend observed so far.

The ESD is important in achieving a droplet or a spray. Further experiments could be designed to develop the effect of parameters on the maximum ESD at a range of voltage magnitudes to determine whether this changes the maximum ESD, with an idea to develop a print window for nanoelectrospray operation. This will help the operator to determine the ESD, emitter OD and the range of voltages required to achieve the ideal print for a specific solution, and ideally being able to control the ejections to print a range of designs without the need for testing a range of parameters.

Bibliography

Matthew S Alexander, Mark D Paine, and John PW Stark. Pulsation modes and the effect of applied voltage on current and flow rate in nanoelectrospray. *Analytical chemistry*, 78(8):2658–2664, 2006.

Seongpil An, Min Wook Lee, Na Young Kim, Changmin Lee, Salem S Al-Deyab, Scott C James, and Sam S Yoon. Effect of viscosity, electrical conductivity, and surface tension on direct-current-pulsed drop-on-demand electrohydrodynamic printing frequency. *Applied Physics Letters*, 105(21):214102, 2014.

Glycerine Producers' Association et al. *Physical properties of glycerine and its solutions*. Glycerine Producers' Association, 1963.

A Barrero, AM Ganan-Calvo, J Davila, A Palacios, and E Gomez-Gonzalez. The role of the electrical conductivity and viscosity on the motions inside taylor cones. *Journal of electrostatics*, 47(1-2):13–26, 1999.

Kira Barton, Sandipan Mishra, K Alex Shorter, Andrew Alleyne, Placid Ferreira, and John Rogers. A desktop electrohydrodynamic jet printing system. *Mechatronics*, 20(5):611–616, 2010.

David B Bober and Chuan-Hua Chen. Pulsating electrohydrodynamic cone-jets: from choked jet to oscillating cone. *Journal of Fluid Mechanics*, 689:552–563, 2011.

Edward Bormashenko, Albina Musin, and Michael Zinigrad. Evaporation of droplets on strongly and weakly pinning surfaces and dynamics of the triple line. *Colloids and Surfaces A: Physicochemical and Engineering Aspects*, 385 (1-3):235–240, 2011.

M Brugnara. Contact angle, 2004-2006. URL `https://imagej.nih.gov/ij/plugins/contact-angle.html(accessed:2018-2020)`.

William Carter, George C Popell, Johnson Samuel, and Sandipan Mishra. A fundamental study and modeling of the micro-droplet formation process in near-field electrohydrodynamic jet printing. *Journal of Micro and Nano-Manufacturing*, 2(2), 2014.

C-H Chen, DA Saville, and Ilhan A Aksay. Scaling laws for pulsed electrohydrodynamic drop formation. *Applied Physics Letters*, 89(12):124103, 2006.

Hong Kyoon Choi, Jang-Ung Park, O Ok Park, Placid M Ferreira, John G Georgiadis, and John A Rogers. Scaling laws for jet pulsations associated with high-resolution electrohydrodynamic printing. *Applied Physics Letters*, 92(12):123109, 2008.

M Cloupeau and B Prunet-Foch. Electrostatic spraying of liquids in cone-jet mode. *Journal of electrostatics*, 22(2):135–159, 1989.

Michel Cloupeau and Bernard Prunet-Foch. Electrohydrodynamic spraying functioning modes: a critical review. *Journal of Aerosol Science*, 25(6):1021–1036, 1994.

Robert T Collins, Michael T Harris, and Osman A Basaran. Breakup of electrified jets. *Journal of Fluid Mechanics*, 588:75–129, 2007.

Gerard Cummins and Marc PY Desmulliez. Inkjet printing of conductive materials: a review. *Circuit World*, 38(4):193–213, 2012.

S David, K Sefiane, and L Tadrist. Experimental investigation of the effect of thermal properties of the substrate in the wetting and evaporation of sessile drops. *Colloids and Surfaces A: Physicochemical and Engineering Aspects*, 298 (1-2):108–114, 2007.

J Fernández De La Mora and Ignacio González Loscertales. The current emitted

by highly conducting taylor cones. *Journal of Fluid Mechanics*, 260:155–184, 1994.

Juan Fernández De La Mora. On the outcome of the coulombic fission of a charged isolated drop. *Journal of colloid and interface science*, 178(1):209–218, 1996.

Brian Derby. Inkjet printing of functional and structural materials: fluid property requirements, feature stability, and resolution. *Annual Review of Materials Research*, 40:395–414, 2010.

H Yildirim Erbil. Evaporation of pure liquid sessile and spherical suspended drops: A review. *Advances in colloid and interface science*, 170(1-2):67–86, 2012.

Amin Famili, Saurabh A Palkar, and William J Baldy Jr. First drop dissimilarity in drop-on-demand inkjet devices. *Physics of Fluids (1994-present)*, 23(1): 012109, 2011.

Alfonso M Ganan-Calvo. Cone-jet analytical extension of taylor's electrostatic solution and the asymptotic universal scaling laws in electrospraying. *Physical review letters*, 79(2):217, 1997.

Alfonso M Gañán-Calvo. On the general scaling theory for electrospraying. *Journal of Fluid Mechanics, 507, 203-212a..*, 2004.

Alfonso M Gañán-Calvo, N Rebollo-Muñoz, and JM Montanero. The minimum or natural rate of flow and droplet size ejected by taylor cone–jets: physical symmetries and scaling laws. *New Journal of Physics*, 15(3):033035, 2013.

Alfonso M Ganán-Calvo, José M López-Herrera, Miguel A Herrada, Antonio Ramos, and José M Montanero. Review on the physics of electrospray: from electrokinetics to the operating conditions of single and coaxial taylor cone-jets, and ac electrospray. *Journal of Aerosol Science*, 125:32–56, 2018.

Alfonso Miguel Gañán-Calvo, José María López-Herrera, Noelia Rebollo-Muñoz, and JM Montanero. The onset of electrospray: the universal scaling laws of the first ejection. *Scientific reports*, 6(1):1–9, 2016.

AM Ganan-Calvo, J Davila, and A Barrero. Current and droplet size in the electrospraying of liquids. scaling laws. *Journal of Aerosol Science*, 28(2):249–275, 1997.

Graham TT Gibson, Samuel M Mugo, and Richard D Oleschuk. Nanoelectrospray emitters: trends and perspective. *Mass Spectrometry Reviews*, 28(6):918–936, 2009.

Lei Guo, Yongqing Duan, YongAn Huang, and Zhouping Yin. Experimental study of the influence of ink properties and process parameters on ejection volume in electrohydrodynamic jet printing. *Micromachines*, 9(10):522, 2018.

RD Harrison and H Ellis. Revised nuffield advanced science book of data, 1984.

RPA Hartman, DJ Brunner, DMA Camelot, JCM Marijnissen, and B Scarlett. Jet break-up in electrohydrodynamic atomization in the cone-jet mode. *Journal of aerosol science*, 31(1):65–95, 2000.

FJ Higuera. Current/flow-rate characteristic of an electrospray with a small meniscus. *Journal of Fluid Mechanics*, 513:239, 2004.

AJ Hijano, IG Loscertales, SE Ibáñez, and FJ Higuera. Periodic emission of droplets from an oscillating electrified meniscus of a low-viscosity, highly conductive liquid. *Physical Review E*, 91(1):013011, 2015.

Hua Hu and Ronald G Larson. Evaporation of a sessile droplet on a substrate. *The Journal of Physical Chemistry B*, 106(6):1334–1344, 2002.

Zishuai Huang, Wei Hua, Dominique Verreault, and Heather C Allen. Salty glycerol versus salty water surface organization: bromide and iodide surface propensities. *The Journal of Physical Chemistry A*, 117(29):6346–6353, 2013.

A Said Ismail, J Yao, HH Xia, and JPW Stark. Breakup length of electrified liquid jets: Scaling laws and applications. *Physical Review Applied*, 10(6): 064010, 2018.

A Jaworek and A Krupa. Classification of the modes of ehd spraying. *Journal of Aerosol Science*, 30(7):873–893, 1999a.

A Jaworek and A Krupa. Jet and drops formation in electrohydrodynamic spraying of liquids. a systematic approach. *Experiments in fluids*, 27(1):43–52, 1999b.

ATSA Jaworek and Arkadiusz Tomasz Sobczyk. Electrospraying route to nanotechnology: An overview. *Journal of electrostatics*, 66(3-4):197–219, 2008.

SN Jayasinghe and MJ Edirisinghe. Effect of viscosity on the size of relics produced by electrostatic atomization. *Journal of Aerosol Science*, 33(10): 1379–1388, 2002.

R Juraschek and FW Röllgen. Pulsation phenomena during electrospray ionization. *International journal of mass spectrometry*, 177(1):1–15, 1998.

Bong Hoon Kim, M Serdar Onses, Jong Bin Lim, Sooji Nam, Nuri Oh, Hojun Kim, Ki Jun Yu, Jung Woo Lee, Jae-Hwan Kim, Seung-Kyun Kang, et al. High-resolution patterns of quantum dots formed by electrohydrodynamic jet printing for light-emitting diodes. *Nano letters*, 15(2):969–973, 2015.

Joonghyuk Kim, Hyuncheol Oh, and Sang Soo Kim. Electrohydrodynamic drop-on-demand patterning in pulsed cone-jet mode at various frequencies. *Journal of Aerosol Science*, 39(9):819–825, 2008.

Kyoungtae Kim, Byung Uk Lee, Gi Byung Hwang, Jun Hyun Lee, and Sangsoo Kim. Drop-on-demand patterning of bacterial cells using pulsed jet electrospraying. *Analytical chemistry*, 82(5):2109–2112, 2010.

Samuel Haedong Kim, Heuiseok Kang, Kyungtae Kang, Sang Ho Lee, Kwan Hyun Cho, and Jun Young Hwang. Effect of meniscus damping ratio on drop-on-demand electrohydrodynamic jetting. *Applied Sciences*, 8(2):164, 2018.

MM Laurila, B Khorramdel, A Dastpak, and M Mäntysalo. Statistical analysis

of e-jet print parameter effects on ag-nanoparticle ink droplet size. *Journal of Micromechanics and Microengineering*, 27(9):095005, 2017.

MW Lee, DK Kang, NY Kim, Ho Young Kim, SC James, and SS Yoon. A study of ejection modes for pulsed-dc electrohydrodynamic inkjet printing. *Journal of Aerosol Science*, 46:1–6, 2012a.

Seungmi Lee, Junyoung Song, Ho Kim, and Jaewon Chung. Time resolved imaging of electrohydrodynamic jetting on demand induced by square pulse voltage. *Journal of aerosol science*, 52:89–97, 2012b.

Ioan Marginean, Peter Nemes, Lida Parvin, and Akos Vertes. How much charge is there on a pulsating taylor cone? *Applied physics letters*, 89(6):064104, 2006.

Ioan Marginean, Peter Nemes, and Akos Vertes. Astable regime in electrosprays. *Physical Review E*, 76(2):026320, 2007.

Glen McHale, Sanaa Aqil, NJ Shirtcliffe, MI Newton, and H Yildirim Erbil. Analysis of droplet evaporation on a superhydrophobic surface. *Langmuir*, 21 (24):11053–11060, 2005.

JR Melcher and GI Taylor. Electrohydrodynamics: a review of the role of interfacial shear stresses. *Annual review of fluid mechanics*, 1(1):111–146, 1969.

Sandipan Mishra, Kira L Barton, Andrew G Alleyne, Placid M Ferreira, and John A Rogers. High-speed and drop-on-demand printing with a pulsed electrohydrodynamic jet. *Journal of Micromechanics and Microengineering*, 20(9):095026, 2010.

Robert Moerman, Johannes Frank, Johannes CM Marijnissen, Thomas GM Schalkhammer, and Gijs WK van Dedem. Miniaturized electrospraying as a technique for the production of microarrays of reproducible micrometer-sized protein spots. *Analytical chemistry*, 73(10):2183–2189, 2001.

Tuan AH Nguyen, Anh V Nguyen, Marc A Hampton, Zhi Ping Xu, Longbin Huang, and Victor Rudolph. Theoretical and experimental analysis of droplet

evaporation on solid surfaces. *Chemical engineering science*, 69(1):522–529, 2012.

Daichi Obata, Hiroshi Tasaka, Sunao Katsuki, and Hidenori Akiyama. Formation of liquid cone jet dependent on rise time of driving voltage. *Journal of Electrostatics*, 76:274–277, 2015.

Mark D Paine. Transient electrospray behaviour following high voltage switching. *Microfluidics and nanofluidics*, 6(6):775–783, 2009.

Mark D Paine, Matthew S Alexander, and John PW Stark. Nozzle and liquid effects on the spray modes in nanoelectrospray. *Journal of colloid and interface science*, 305(1):111–123, 2007a.

MD Paine, MS Alexander, KL Smith, M Wang, and JPW Stark. Controlled electrospray pulsation for deposition of femtoliter fluid droplets onto surfaces. *Journal of Aerosol Science*, 38(3):315–324, 2007b.

Jaehong Park, Beomsoo Kim, Sang-Yoon Kim, and Jungho Hwang. Prediction of drop-on-demand (dod) pattern size in pulse voltage-applied electrohydrodynamic (ehd) jet printing of ag colloid ink. *Applied Physics A*, 117(4):2225–2234, 2014.

Jang-Ung Park, Jung Heon Lee, Ungyu Paik, Yi Lu, and John A Rogers. Nanoscale patterns of oligonucleotides formed by electrohydrodynamic jet printing with applications in biosensing and nanomaterials assembly. *Nano letters*, 8(12):4210–4216, 2008.

Lida Parvin, Marsha C Galicia, Jennifer M Gauntt, Leah M Carney, Ann B Nguyen, Eunyoung Park, Linda Heffernan, and Akos Vertes. Electrospray diagnostics by fourier analysis of current oscillations and fast imaging. *Analytical chemistry*, 77(13):3908–3915, 2005.

Thanh Huy Phung, Seora Kim, and Kye-Si Kwon. A high speed electrohydrodynamic (ehd) jet printing method for line printing. *Journal of Micromechanics and Microengineering*, 27(9):095003, 2017.

Michael J Poellmann and Amy J Wagoner Johnson. Characterizing and patterning polyacrylamide substrates functionalized with n-hydroxysuccinimide. *Cellular and Molecular Bioengineering*, 6(3):299–309, 2013.

Michael J Poellmann and Amy J Wagoner Johnson. Multimaterial polyacrylamide: fabrication with electrohydrodynamic jet printing, applications, and modeling. *Biofabrication*, 6(3):035018, 2014.

Lei Qian, Hongbo Lan, and Guangming Zhang. A theoretical model for predicting the feature size printed by electrohydrodynamic jet printing. *Applied Physics Letters*, 112(20):203505, 2018.

Khalid Rahman, Arshad Khan, Nguyen Minh Nam, Kyung Hyun Choi, and Dong-Soo Kim. Study of drop-on-demand printing through multi-step pulse voltage. *International Journal of Precision Engineering and Manufacturing*, 12(4):663–669, 2011.

AK Ray, B Devakottai, A Souyri, and JL Huckaby. Evaporation characteristics of droplets coated with immiscible layers of nonvolatile liquids. *Langmuir*, 7 (3):525–531, 1991.

CN Ryan, KL Smith, MS Alexander, and JPW Stark. Effect of emitter geometry on flow rate sensitivity to voltage in cone jet mode electrospray. *Journal of Physics D: Applied Physics*, 42(15):155504, 2009.

CN Ryan, KL Smith, and JPW Stark. The influence of geometry on the flow rate sensitivity to applied voltage within cone-jet mode electrospray. *Journal of Applied Physics*, 112(11):114510, 2012.

CN Ryan, KL Smith, and JPW Stark. The flow rate sensitivity to voltage across four electrospray modes. *Applied Physics Letters*, 104(8):084101, 2014.

K Sefiane, L Tadrist, and M Douglas. Experimental study of evaporating water–ethanol mixture sessile drop: influence of concentration. *International journal of heat and mass transfer*, 46(23):4527–4534, 2003.

Mojtaba Shamsipur, Ali Akbar Miran Beigi, Mohammad Teymouri, Sayed Mahdi Pourmortazavi, and Mohsen Irandoust. Physical and electrochemical properties of ionic liquids 1-ethyl-3-methylimidazolium tetrafluoroborate, 1-butyl-3-methylimidazolium trifluoromethanesulfonate and 1-butyl-1-methylpyrrolidinium bis (trifluoromethylsulfonyl) imide. *Journal of Molecular Liquids*, 157(1):43–50, 2010.

Kazuyo Shigeta, Ying He, Erick Sutanto, Somi Kang, An-Phong Le, Ralph G Nuzzo, Andrew G Alleyne, Placid M Ferreira, Yi Lu, and John A Rogers. Functional protein microarrays by electrohydrodynamic jet printing. *Analytical chemistry*, 84(22):10012–10018, 2012.

David PH Smith. The electrohydrodynamic atomization of liquids. *IEEE transactions on industry applications*, (3):527–535, 1986.

Katharine L Smith, Matthew S Alexander, and John PW Stark. The sensitivity of volumetric flow rate to applied voltage in cone-jet mode electrospray and the influence of solution properties and emitter geometry. *Physics of Fluids*, 18(9):092104, 2006a.

KL Smith, MS Alexander, and JPW Stark. Voltage effects on the volumetric flow rate in cone-jet mode electrospraying. *Journal of applied physics*, 99(6): 064909, 2006b.

John PW Stark, Matthew S Alexander, and Katherine L Smith. Electrospray pulsation: A diagnostic to understand cone-jet stability and minimum flow. *Journal of Applied Physics*, 115(4):044905, 2014.

J Stringer and B Derby. Limits to feature size and resolution in ink jet printing. *Journal of the European Ceramic Society*, 29(5):913–918, 2009.

E Sutanto, K Shigeta, YK Kim, PG Graf, DJ Hoelzle, KL Barton, AG Alleyne, PM Ferreira, and JA Rogers. A multimaterial electrohydrodynamic jet (e-jet) printing system. *Journal of Micromechanics and Microengineering*, 22(4): 045008, 2012.

Koichi Takamura, Herbert Fischer, and Norman R Morrow. Physical properties of aqueous glycerol solutions. *Journal of Petroleum Science and Engineering*, 98:50–60, 2012.

Geoffrey Ingram Taylor. Disintegration of water drops in an electric field. *Proceedings of the Royal Society of London. Series A. Mathematical and Physical Sciences*, 280(1382):383–397, 1964.

Gary J Van Berkel and Vilmos Kertesz. Using the electrochemistry of the electrospray ion source. *Analytical chemistry*, 79(15), 2007.

S Verdoold, LLF Agostinho, CU Yurteri, and JCM Marijnissen. A generic electrospray classification. *Journal of Aerosol Science*, 67:87–103, 2014.

K Wang and JPW Stark. Deposition of colloidal gold nanoparticles by fully pulsed-voltage-controlled electrohydrodynamic atomisation. *Journal of Nanoparticle Research*, 12(3):707–711, 2010a.

Ke Wang and John Stark. Nozzle size effects on the nanoelectrospraying of au nanocolloid in a fully voltage-controlled form. *Sensors and Actuators A: Physical*, 165(2):338–341, 2011.

Ke Wang and John Stark. Dispersion of nano-au suspension using novel pulsed jet nanoelectrospraying approach. *Materials Letters*, 123:120–123, 2014.

Ke Wang and John PW Stark. Direct fabrication of electrically functional microstructures by fully voltage-controlled electrohydrodynamic jet printing of silver nano-ink. *Applied Physics A*, 99(4):763–766, 2010b.

Ke Wang and John PW Stark. Voltage effects on the nanoelectrospray characteristics in fully voltage-controlled atomisation of gold nanocolloids. *Analytica chimica acta*, 679(1-2):81–84, 2010c.

Ke Wang, Mark D Paine, and John PW Stark. Fully voltage-controlled electrohydrodynamic jet printing of conductive silver tracks with a sub-100 μ m linewidth. *Journal of applied physics*, 106(2):024907, 2009.

Yunshan Wang, Ming K Tan, David B Go, and Hsueh-Chia Chang. Electrospray cone-jet breakup and droplet production for electrolyte solutions. *EPL (Europhysics Letters)*, 99(6):64003, 2012.

Junfei Wei, Wenqing Shui, Feng Zhou, Yu Lu, Kankai Chen, Guobing Xu, and Pengyuan Yang. Naturally and externally pulsed electrospray. *Mass spectrometry reviews*, 21(3):148–162, 2002.

Matthias Wilm and Matthias Mann. Analytical properties of the nanoelectrospray ion source. *Analytical chemistry*, 68(1):1–8, 1996.

HH Xia, A Ismail, J Yao, and JPW Stark. Scaling laws for transition from varicose to whipping instabilities in electrohydrodynamic jetting. *Physical Review Applied*, 12(1):014031, 2019.

Osamu Yogi, Tomonori Kawakami, Masayo Yamauchi, Jing Yong Ye, and Mitsuru Ishikawa. On-demand droplet spotter for preparing pico-to femtoliter droplets on surfaces. *Analytical chemistry*, 73(8):1896–1902, 2001.

Milim Yu, Kyung Hyun Ahn, and Seung Jong Lee. Design optimization of ink in electrohydrodynamic jet printing: Effect of viscoelasticity on the formation of taylor cone jet. *Materials & Design*, 89:109–115, 2016.

Xin Yuan and Zhenhua Xiong. High frequency pulsed electrohydrodynamic printing with controllable fine droplets. *Journal of Micromechanics and Microengineering*, 28(9):095008, 2018.

Xin Yuan, Zhengyu Ba, and Zhenhua Xiong. Fine droplet generation using tunable electrohydrodynamic pulsation. *Journal of Micromechanics and Microengineering*, 25(7):075028, 2015.

John Zeleny. Instability of electrified liquid surfaces. *Physical review*, 10(1):1, 1917.

Xiaoguang Zhang and Osman A Basaran. Dynamics of drop formation from a capillary in the presence of an electric field. *Journal of Fluid Mechanics*, 326: 239–263, 1996.

Menghua Zhu, Yongqing Duan, Nian Liu, Hegeng Li, Jinghui Li, Peipei Du, Zhifang Tan, Guangda Niu, Liang Gao, YongAn Huang, et al. Electrohydrodynamically printed high-resolution full-color hybrid perovskites. *Advanced Functional Materials*, 29(35):1903294, 2019.